Coarse Analysis of Microscopic Models using Equation-Free Methods

Marschler, Christian

Publication date:
2014

Document Version
Publisher's PDF, also known as Version of record

Coarse Analysis of Microscopic Models using Equation-Free Methods

Christian Marschler

Kongens Lyngby 2014
PhD-2014-342

Technical University of Denmark
Applied Mathematics and Computer Science
Building 322, DK-2800 Kongens Lyngby, Denmark
Phone +45 45253031, Fax +45 45881399
compute@compute.dtu.dk
www.compute.dtu.dk PhD-2014-342

Summary

Mathematical models of real-world problems from physics, biology and chemistry have become very complex over the last three decades. Although increasing computational power allows to solve even larger systems of differential equations, the number of differential equations is still a main limiting factor for the complexity of models, e.g., in real-time applications. With the increasing amount of data generated by computer simulations a challenge is to extract valuable information from the models in order to help scientists and managers in a decision-making process. Although the dynamics of these models might be high-dimensional, the properties of interest are usually macroscopic and low-dimensional in nature. Examples are numerous and not necessarily restricted to computer models. For instance, the power output, energy consumption and temperature of engines are interesting quantities for engineers, although the models they base their design on are described for the gas mixture (a system with many degrees-of-freedom) inside a combustion engine. Since good models are often not available on the macroscopic scale the necessary information has to be extracted from the microscopic, high-dimensional models.

The goal of this thesis is to investigate such high-dimensional multiscale models and extract relevant low-dimensional information from them. Recently developed mathematical tools allow to reach this goal: a combination of so-called equation-free methods with numerical bifurcation analysis is used and further developed to gain insight into high-dimensional systems on a macroscopic level of interest. Based on a switching-procedure between a detailed microscopic and a coarse macroscopic level during simulations it is possible to obtain a closure-on-demand for the macroscopic dynamics by only using short simulation bursts of computationally-expensive complex models. Those information is subsequently

used to construct bifurcation diagrams that show the parameter dependence of solutions of the system.

The methods developed for this thesis have been applied to a wide range of relevant problems. Applications include the learning behavior in the barn owl's auditory system, traffic jam formation in an optimal velocity model for circular car traffic and oscillating behavior of pedestrian groups in a counter-flow through a corridor with narrow door. The methods do not only quantify interesting properties in these models (learning outcome, traffic jam density, oscillation period), but also allow to investigate unstable solutions, which are important information to determine basins of attraction of stable solutions and thereby reveal information on the long-term behavior of an initial state.

Resumé

Matematiske modeller til at svare på spørgesmål fra fysik, biologi og kemi er blevet meget komplekse gennem de sidste tre årtier. Selvom en øget beregningskraft hjælper til at løse endnu større systemer af differentialligninger, er antallet af differentialligninger stadig en limiterende faktor, hvis komplekse modeller skal løses, f.eks. i real-tids anvendelser. Med den større mængde af computer-genereret data får vi derudover nye udfordringer med at ekstrahere vigtige oplysninger fra modellerne til at hjælpe forskere og managere i beslutningsprocesser. Selvom dynamikken i modellerne kan være højdimensional, plejer interessante egenskaber at være makroskopiske og lavdimensionale. Der findes mange eksempler, som ikke nødvendigvis er begrænset til computersimuleringer. F.eks. er effekten og temperaturen af motorer interessante værdier for ingeniører, selvom deres modeller er baseret på beskrivelser af gasblandingen (et system med mange frihedsgrader) i en forbrændningsmotor. Eftersom gode modeller ofte ikke er til rådighed på en makroskopisk skala, må den nødvendige information udledes fra mikroskopiske højdimensionale modeller.

Målet med denne afhandling er at undersøge disse højdimensionale multiskala modeller og ekstrahere relevante, lavdimensionale oplsyninger fra dem. Nye værktøjer indenfor matematik gør det muligt at nå dette mål: en kombination af såkaldte ligningsfrie metoder med numerisk bifurkationsanalyse bruges til at få indsigt i højdimensionale systemer på det interessante makroskopiske niveau. Baseret på en procedure der veksler mellem en detaljeret mikroskopisk og et grovt makroskopisk niveau under simuleringer, er det muligt at få en closure-on-demand for den makroskopiske dynamik gennem korte simuleringer, dvs. simulation bursts, af beregninsintensive, komplekse modeller. Disse oplysninger er bagefter brugt til at konstruere bifurkationsdiagrammer, som viser parameterafhængigheden af løsninger til systemet.

Metoderne, som blev udviklet til denne afhandling, blev anvendt til mange forskellige slags problemer. Anvendelser omfatter læringsadfærd af det auditoriske system hos sløruglen, dannelsen af trafikpropper i en optimal hastighedsmodel for ringtrafik og oscillerende løsninger i fodgængergrupper i modstrøm gennem en smal korridor. Metoderne ikke kun kvantificerer spændende egenskaber i modellerne (læringssuccess, trafikproptæthed, oscilleringsperiode), men finder også ustabile løsninger, som supplerer med vigtige oplsyninger om attraktionsområder af stabile løsninger og dermed bestemmer langtidsadfærd af en begyndelsestilstand.

Preface

The work on this PhD project started at the Department of Mathematics. It has been continued at the Department of Applied Mathematics and Computer Science after a restructering of the department structure at the Technical University of Denmark. The thesis is written in fullfilment of the requirements for aquiring a PhD degree in Mathematics. Associate Professor Jens Starke, Technical University of Denmark, Department of Applied Mathematics and Computer Science, has been the supervisor of this thesis.

The thesis deals with the macroscopic analysis of multiscale systems using equation-free methods and diffusion map investigations. It builds up on very successful techniques developed in dynamical systems theory. Namely, bifurcation theory and later on numerical bifurcation analysis are the tools of choice to analyze qualitative changes in system behavior. This theory is well-developed in the context of low-dimensional dynamical systems. The reasoning behind these considerations is based on the center manifold theorem, stating that the only non-trivial dynamics happens on a (usually low-dimensional) center manifold. Subsequently, the concepts of center manifold theory have been extended to systems with a separation of time scales. The analog of the center manifold is a slow manifold, where the interesting dynamics takes place on. In the case of a normally attracting slow manifold the long term dynamics on the slow manifold decides on the behavior of the system after initial (fast) transients have settled. Here, the equation-free framework comes in and opens up for the possibility of a macroscopic analysis of high-dimensional systems on this slow manifold. Diffusion maps are another method to obtain a low-dimensional description of a data set or trajectory of a dynamical system in diffusion map space where Euclidean distances are replaced by a so-called diffusion distance.

The thesis consists of an introductory part on dynamical systems with multiple time scales, a review on equation-free methods and diffusion maps and a discussion of the main application areas investigated in this work. Following this review the five scientific papers, written during the PhD project, have been added in the appendix. The introductory part is meant as a short review of existing work and to point out the connection between the state of the art of equation-free methods and diffusion maps with the work presented in the scientific papers in the appendix. The new results from this PhD project are presented in the scientific papers in the appendix and are the main part for judgement of the scientific achievements. Due to this way of presentation, I hope to give a good overview about the field of equation-free methods while avoiding unnecessary repetitions from the articles.

Christian Marschler
Lyngby, 31-July-2014

Acknowledgements

I would like to thank a number of people who helped and supported me throughout the time as a PhD student at DTU. The importance of every single person can not be quantified, since this thesis would not exist in this shape without any of those. Therefore, I would like to thank my colleagues, friends and family in a random order.

First, I would like to thank my supervisor Jens Starke for his support throughout the last three years. He helped me getting a good start in Denmark and I will certainly never forget the numerous discussions with him about science and more specifically about our research. The relationship with Jens goes far beyond a normal student-teacher interaction. I would also like to thank him for motivating me to start running and for introducing me to new taste-experiences with his expertise in food and cooking. Thank you very much for your time and effort!

I am also grateful to all my colleagues at DTU who made my time so enjoyable. Morten Andersen, as my "mentor" and office mate, introduced me to everyone at DTU Matematik on my first day. He also shared uncountable many cups of coffee with me. This thesis would certainly look different without him! I would also like to thank my part-time office mates, Michael Elmegård and Irene Heilmann. The endless discussions with Michael about dynamical systems in particular and science in general helped me through many hard times when one was close to loosing faith in the modern definition of science. Michael is also a great ambassador for Denmark and I learned so much about the country and local habits from him. Irene always helped to add another point-of-view to our discussions about dynamical systems and other unrelated topics. Sharing an office with you was a great experience. You are all not only colleagues, but very

good friends to me!

Further, I would like to thank Øistein Wind-Willassen, Kristoffer Hoffmann, Peter Nørtoft and Frank Vinther for our common time at DTU. You all helped me incredibly much to settle in Denmark and understand the Danish society, culture and language! Tusind tak skal I have.

More thanks go to all organizers and members of the numerous clubs at the department, especially to Frank Schilder and Fernando Piñero. The social events in the beer club, cake club and football club helped me to rest my brain from a hard day of work together with great company.

Further, I would also like to thank all my collaborators Ioannis G. Kevrekidis, Jan Sieber, J. Leo van Hemmen, Poul G. Hjorth, Rainer Berkemer, Atsushi Kawamoto, Carmen Faust-Ellsässer and Ping Liu. I really enjoyed discussing and working with you. I hope we can continue our work in the future. For the financial support for my extended research stay at Princeton University and for a conference participation I am grateful to Otto Mønsteds Fond.

Last, but definitely not least, I would like to thank my family for all their moral support. As in every scientific work, there have been ups and many downs and I would especially thank my fiancé Kathrin for not only standing me, but also building me up when times were hard. You even moved to Denmark because of me and I can only hope to be as good a support for you as you have been for me. I am also very grateful to my parents, Brigitte and Andreas Marschler, and my brother David. They always gave me a new perspective in times were a strict focus on mathematics does not solve any problems. Thank you so much for helping me staying down to earth.

To my family

Contents

List of Symbols

General

$\mathbb{R}$	real numbers
C, K	constants
i, j	indices
I	identity matrix
rank	rank of a matrix
Re, Im	real and imaginary part of a complex number

Dynamical Systems

$f, (f_\varepsilon)$	vector field (of slow-fast system with time scale separation ε)
$\phi, (\phi_\varepsilon)$	flow for the vector field $f, (f_\varepsilon)$
F	macroscopic vector field
Φ	macroscopic flow on the manifold $\mathcal{M}_\varepsilon$
Φ_*	correct flow on $\mathcal{M}_\varepsilon$
$x \in \mathbb{R}^{n_f}, n_f$	fast variable in explicit slow-fast systems with dimension n_f
$y \in \mathbb{R}^{n_s}, n_s$	slow variable in explicit slow-fast systems with dimension n_s
$p \in \mathbb{R}^m, m$	system parameters with dimension m
$\mathcal{M}_0, (\mathcal{M}_\varepsilon)$	slow manifold for $\varepsilon = 0$ ($\varepsilon > 0$)
E^s, E^c, E^u	stable, center and unstable eigenspaces
$W^s_{loc}, W^c_{loc}, W^u_{loc}$	local stable, center and unstable manifolds
W^s, W^c, W^u	stable, center and unstable manifolds

A_s, A_c, A_u	stable, center and unstable matrices
B_s, B_c, B_u	stable, center and unstable nonlinearities
γ	infinitesimal small perturbation
Df	Jacobian of f
λ_i, v_i	eigenvalues and eigenvectors of linearized system
T	period of periodic solutions
π_ε	stable fiber projection
ψ	test function
g, h	graphs of the center/slow manifold
G	extended continuation problem
ξ	extended continuation variable (u, p)
η	predictor in continuation problem
g_j	auxiliary conditions in numerical continuation
r, ∂_r	space variable and its partial derivative in PDE descriptions
Equation-Free	
$\mathcal{L}$	lifting operator
$\mathcal{R}$	restriction operator
P	lift-evolve-restrict scheme
$u, v \in \mathbb{R}^n$	microscopic variable with dimension n
$U, V \in \mathbb{R}^N$	macroscopic variable with dimension N
s	iterative step size for ZDP
L_m	map for m-th ZDP
d	highest derivative in the gap-tooth scheme
H	discretization for spatial grid
Time	
t_{skip}	healing time
δ	time on the slow manifold
τ	macroscopic time
t	time, fast time scale in explicit slow-fast systems
ε	time scale separation
Δt	time step for projective integration
$\frac{d}{dt} = \dot{}$, $(\frac{d}{d\tau} = ')$	derivative with respect to t, (τ)

Diffusion Maps

x_i, X	data point and data set in diffusion map algorithm
w_k	weights in PCA
$T = (t_{ik})$	scores and score matrix in PCA
U, W	orthogonal matrices in SVD
σ_i, Σ	singular values and matrix of singular values
d_{ij}	Euclidean norm of data points
A_{ij}	soft-thresholded distance matrix
M_{ij}	Markov matrix for diffusion map
Ψ_i	diffusion map eigenvector

Chapter 1

Introduction to Dynamical Systems with Multiple Time Scales

"To doubt everything and to believe everything are two equally convenient solutions; each saves us from thinking."
H. Poincaré, Science and Hypothesis, 1905.

Recently-developed methods for the macroscopic analysis of multi-scale systems, namely the equation-free framework and diffusion maps, are discussed, further developed and applied in this thesis. The methods are based on the theory of dynamical systems with multiple time scales, which is introduced in this chapter.

The study of differential equations has a long history and dates back to the independent work of Newton [New87, Smi08] and Leibniz [Par89]. They developed the ideas about infinitesimal calculus and thereby built the foundation for the study of differential equations. As the greatest mathematicians and philosophers of their time they developed a plethora of techniques and methods, e.g., the notion of derivatives and integrals, which have been applied to numerous problems ever since. In particular, the field of mechanics has been of great importance for the development of differential equations (see the work of Lagrange

[Lag88] and Hamilton [Ham34]). The very fruitful interaction between experiments and theory is outstanding. Later on, the discovery of electromagnetism and the mathematical formalization of fluid mechanics (see the work by Maxwell [Max65], Rayleigh [SR79], Euler [Eul56] and Gauss [Gau30, Gau67]) resulted naturally in a description by (partial) differential equations. In the 19th century the ongoing research in the field of thermodynamics by Boltzmann [Bol71], Maxwell [Max67] and others led to the description of high-dimensional dynamical systems, i.e., gases, by low-dimensional quantities, e.g., temperature, free energy and pressure, via statistical methods. Until then, most systems known from physics were formulated using conservation laws. The most prominent ones being the conservation of energy, mass and momentum. Emmy Noether proved that these conservation laws are related to symmetries in the system [Noe18]. In the beginning of the 20th century physics has been dealing with the new field of quantum mechanics. Deep discussions between Einstein and Bohr [Boh49], Heisenberg and Schrödinger [Hei25, Sch26] and Planck [Pla00] shed light on the quantum nature of electrons and photons, that needed both a description by classical mechanics and a statistical interpretation (wave-particle duality). Despite the controversy of quantum mechanics, the theory was still formulated in terms of Hamiltonians, i.e., energy-conserving systems. The existence of a Hamiltonian assures the possibility to apply tools from mechanics and mathematics that have been developed over more than 300 years.

It was about the same time as quantum mechanics arose, when scientists started thinking about general non-linear systems including studies of dissipative problems that go beyond classical friction problems, e.g., Coulomb friction and Stokes law. Suddenly, all the techniques to solve conservative equations could not be used to study these systems. Especially non-linear systems posed many open questions for existence and uniqueness of solutions leading to the theorem of Peano and the theorem of Picard-Lindelöf [Lin94, Mei07]. It was with the rise of non-linear dissipative systems, that the field of dynamical systems was founded. Instead of giving explicit analytical solutions to problems, dynamical systems theory provides a qualitative analysis of extremely complicated systems, e.g., it answers questions about the existence of fixed points, periodic orbits and chaotic behavior. Henri Poincaré was the first one who studied dynamical systems with qualitative methods and can be seen as the founder of modern dynamical systems theory. His famous idea to study periodic solutions as intersections with a section in phase space is now known as the technique of Poincaré sections [Poi90]. Further on, dynamical systems theory has been developed by many scientists from many different fields, e.g., mathematics [Sma67, HDS74, Fei78, AL88], radio transmission [vdP26], non-linear oscillations [Duf18], meteorology [Lor63], and computer science [Man83] to only name a few. It is the contribution by so many different fields and researchers, that make dynamical systems theory a very fruitful theory that is useful for applications, since almost all theory has been developed alongside real-world applications.

A milestone in the analysis of dynamical systems is *bifurcation theory*. Bifurcation analysis deals with the qualitative change of system behavior when parameters are changed. Bifurcation analysis reduces the high complexity of systems to diagrams showing the qualitative parameter dependence of the systems, i.e., bifurcation diagrams. The success of bifurcation analysis became more established with computers which allow one to perform *numerical bifurcation analysis*. Nowadays, a lot of software packages are available for numerical continuation of solutions and bifurcation analysis, e.g., AUTO [DK86], CoCo [DS13]. Despite its success, bifurcation analysis is limited to relatively low-dimensional systems or more specifically to systems with a low-dimensional center manifold. A rather complete classification of bifurcations can only be found for generic two-dimensional systems. Usually, this restriction is not crucial, since the interesting dynamics often happens on low-dimensional manifolds (see the center manifold theorem in Sec. 1.1). Nevertheless, it has shown to be difficult to analyze high-dimensional systems with respect to their bifurcation structure if the intrinsic dimension of the center manifold is large. The main focus of this thesis is to gain insight into the intrinsic low-dimensional dynamics of high-dimensional systems using equation-free methods.

Throughout the thesis we use the terms high-dimensional system, microscopic system and fine-scale dynamics synonymously. On the other hand, the terms low-dimensional system, macroscopic system and coarse dynamics are used equivalently. The notation does not specifically refer to any physical interpretation of the variables, e.g., macroscopic variables are not necessarily derived from microscopic dynamics as statistical quantities. In particular, dimensionality always denotes the dimension of the dynamical systems, such that a PDE would be an infinite-dimensional system. If solutions to PDEs are denoted as macroscopic solutions, e.g., density of a pedestrian crowd, opposed to microscopic solutions, e.g., positions of pedestrians, this is clearly denoted to avoid confusion.

To begin with, it is worth noticing that many high-dimensional systems behave essentially low-dimensional. Examples reach from molecular dynamics [AW59] to reaction kinetics [MM13] and modes in mechanical systems extracted from a *finite element analysis* [ZM71]. After initialization of the system at an arbitrary point in phase space the dynamics quickly approaches a low-dimensional object, the so-called slow manifold. The dynamics on the slow manifold has a time scale of $\mathcal{O}(\varepsilon)$ compared to the dynamics off the slow manifold, i.e., there exists a spectral gap. Furthermore, we assume that the manifold is normally attracting as it is usually the case in dissipative systems. The slow manifold plays the same role as the center manifold in the sense, that all the long-term behavior happens on this manifold. Nevertheless, the dynamics on the slow manifold can be arbitrarily complex depending on the dimension of the manifold. Often observed cases are the convergence to a fixed point, periodic orbits or even

chaotic motion.

It is observed in many experiments that high-dimensional or microscopic systems with many degrees-of-freedom behave essentially low-dimensional or macroscopic after transients have settled. Often, these transients are not important and the high-dimensional dynamics is not the focus of research. A good example for such a reduction of dimensionality can be found in the thermodynamics of an ideal gas. While one is interested in the temperature and pressure of the gas, single trajectories of molecules are not of any significance. Therefore, it is enough for (equilibrium) thermodynamics to investigate low-order moments of particle distributions. The advantage of this statistical approach is, that it is versatile and can be applied to various systems without re-defining the macroscopic variables for the interesting dynamical features in every single application.

A different approach is taken by recently developed multi-scale methods. A prominent one is the so-called *equation-free approach* (see Chap. 2 for a detailed introduction) for studying the not directly accessible macroscopic dynamics. In the equation-free framework, it is assumed that a microscopic description or simulation of the system is available. These simulators typically depend on some system parameters, whose influence on the solutions should be studied. Additionally, two operators are required: the restriction operator, defining the macroscopic variables of interest, and the lifting operator, constructing a microscopic state from a macroscopic one. Using the framework, the interesting macroscopic dynamics can be extracted from the microscopic system and tools from numerical bifurcation analysis can be used to analyze these systems on a macroscopic level without deriving the coarse equations.

Equation-free methods have been applied to many different problems reaching from chemistry and physics ([ZVG+12, KS09]) over social sciences (Paper I, Paper II and [AHS14]) to biology (Paper III and Paper IV and [Ell08]). Common classes of dynamical systems suitable for equation-free computations are many-particle or agent-based systems. In general, equation-free methods prove useful for systems with a mesoscopic dimension: low-dimensional systems can usually be handled directly and in the case of infinitely many particles or equations a continuum limit formulation or averaging and homogenization methods can be applied instead.

In this thesis, focus is put on the mathematically clear formulation of *implicit* equation-free methods introduced in Chap. 2 and Paper I that are applied to an optimal velocity model for traffic jams on a ring road. Paper II gives a non-mathematical overview of equation-free methods and investigates the applicability both in traffic models and pedestrian flow. Furthermore, it is investigated how equation-free methods can be applied to weakly-stochastic systems, i.e., systems with a noisy microscopic dynamics that show deterministic macro-

scopic behavior. An example is the neuronal network model that is presented and analyzed in Paper III and Paper IV. Furthermore, the diffusion map algorithm described in Chap. 3 is investigated with respect to its application to pedestrian problems in Paper V. The combination of diffusion maps with the equation-free framework is a possibility to perform a fully automatic equation-free bifurcation analysis in future work (see the discussion in Sections 2 and 3 for details). We start our discussion with a review on dynamical systems theory in Sec. 1.1 and present a short introduction to bifurcation theory in Sec. 1.2 and dynamical systems with time scale separation in Sec. 1.3.

1.1 Background from Dynamical Systems

In this section a short introduction to the theory of dynamical systems is given in order to set the scene for the recent developments in equation-free computations presented in Chap. 2. This section will also form the basis for Sec. 1.2 on bifurcation theory and for Sec. 1.3 on dynamical systems with time scale separation. Since the purpose of this section is to introduce notation the results are presented without rigorous mathematical proof. Instead, references to standard textbooks are given wherever necessary. Furthermore, only concepts that will be used in the research articles in Appendix A are introduced. Hence, this section is not an exhaustive overview of the field of dynamical systems and the interested reader is rather referred to well-established textbooks (see e.g., [GH83, Wig03, Mei07]) for a detailed introduction to dynamical systems.

The field of dynamical systems deals with the analysis of differential equations. Here, we define a *dynamical system* as

$$\dot{u} := \frac{d}{dt}u = f(u,p), \qquad u \in \mathbb{R}^n,\ p \in \mathbb{R}^m,\ f : \mathbb{R}^n \times \mathbb{R}^m \to \mathbb{R}^n, \tag{1.1}$$

where u is the dependent variable, i.e., the *state* of the system, p are possible parameters and $t \in \mathbb{R}$ is the independent variable, i.e., the time. Further, the *vector field* f is assumed to be sufficiently smooth. Here, we only deal with *autonomous* dynamical systems where the right-hand side f does not explicitly depend on time t. Note, that often the parameter dependence is suppressed for notational convenience, i.e., we write $f(u)$ for $f(u,p)$, if the parameters are fixed. In order to have existence and uniqueness of solutions for the *initial value problem*

$$\dot{u} = f(u), \qquad u(t_0) = u_0 \tag{1.2}$$

in a neighborhood $U \subset \mathbb{R}^n$ containing u_0, i.e., $u_0 \in U$, and time interval $[t_0 - \tau; t_0 + \tau]$, f has to be at least Lipschitz-continuous. Usually, we will assume

that f is C^1. In general, system (1.1) is solved by the *flow* $\phi(t;u)$ defined as

$$\frac{d}{dt}\phi(t;u) = f(\phi(t;u)).$$

The flow constitutes a group with group properties i) $\phi(0;\cdot) = I$ and ii) $\phi(t+s;\cdot) = \phi(t;\cdot)\circ\phi(s;\cdot)$ where I denotes the $n\times n$ identity matrix. In particular, the flow gives a solution to the initial value problem (1.2) as $u(t) = \phi(t;u_0)$.

In many applications, the long-term behavior of the system, i.e., the *ω-limit set*, is of big relevance. Here, two types of solutions are most important:

$$u(t) = \tilde{u} \qquad \forall t, \qquad \textit{fixed points}, \tag{1.3}$$

$$u(t) = u(t+T) \qquad \forall t,\ T>0 \text{ fixed}, \qquad \textit{periodic solutions}. \tag{1.4}$$

A fixed point $\tilde{u}$ is also called *equilibrium* and $T\in\mathbb{R}^+$ is the *period* of the solution (1.4), if it is the smallest number with this property. Fixed points are the simplest solutions of dynamical systems and are usually the starting point for a more detailed analysis. More complicated solutions are usually obtained by studying bifurcation diagrams and especially the points where solutions bifurcate from a branch of equilibria (see Sec. 1.2). Periodic solutions are of particular interest in periodically forced systems, where periodic solutions naturally arise. Nevertheless, periodic solutions can also be found in unforced systems, e.g., van der Pol oscillator [vdP26] and predator-prey cycles [Lot10], and usually emerge in a Hopf bifurcation (see (1.13) in Sec. 1.2).

Not only the type of solution is important but also its stability. The concept of stability can be understood intuitively: a fixed point or periodic solution is stable, if solutions that are initially close stay close as time proceeds. The mathematical formulation of stability is a little more involved (see for example the definition for Lyapunov stability in [Kuz04]). Since we are interested in Appendix A in the stability of fixed points against perturbations we introduce the notion of stability of the linearized system. Assume, $\gamma(t)$ is a small perturbation to the solution $u(t)$. Further assume, that $u(t)=\tilde{u}$ is a fixed point, i.e., $\dot{u} = f(\tilde{u}) = 0$. A Taylor expansion of the perturbed solution $u(t)+\gamma(t)$ to second order yields

$$\frac{d}{dt}(u(t)+\gamma(t)) = \dot{u}(t)+\dot{\gamma}(t) = f(\tilde{u}+\gamma) = f(\tilde{u}) + Df(\tilde{u})\gamma + \mathcal{O}(\gamma^2), \tag{1.5}$$

where $Df(\tilde{u})$ is the Jacobian of f evaluated at $\tilde{u}$. Using the assumptions and neglecting higher-order terms of $\mathcal{O}(\gamma^2)$ results in the *linearized system*

$$\dot{\gamma}(t) = Df(\tilde{u})\gamma. \tag{1.6}$$

This system is solved by an exponential function and the eigenvalues $\lambda_1,\dots,\lambda_n$ of $Df(\tilde{u})$ give information about the decaying, neutral or growing eigendirections $v_1,\dots,v_n$. Note, that the eigenvalues are assumed to be non-degenerate,

i.e., $\lambda_i \neq \lambda_j$ for $i \neq j$. Otherwise, we would have to deal with generalized eigenvectors, which would complicate the clear presentation but not pose serious mathematical problems. We say an eigendirection v_i is (asymptotically) *stable*, if the corresponding real part of eigenvalue $\operatorname{Re}\lambda_i < 0$ and *unstable* for $\operatorname{Re}\lambda_i > 0$. Eigendirections v_i with $\operatorname{Re}\lambda_i = 0$ constitute a special case, where higher-order terms in the Taylor expansion (1.5) are needed to make a statement about the stability. Furthermore, these eigenvalues are connected to bifurcations (see Sec. 1.2). Fixed points $\tilde{u}$ with $\operatorname{Re}\lambda_i < 0\,\forall i$ are called *stable* or *sinks*. All other fixed points are called *unstable*. In general, if both positive and negative real parts of eigenvalues exist, $\tilde{u}$ is called a *saddle*. In the case of only positive real parts of eigenvalues, $\tilde{u}$ is called *source*. Similar classifications can be found for periodic solutions by studying Poincaré sections. Since we are not using these methods in the papers, the reader is referred to standard textbooks (see e.g., [GH83, Mei07]) for an introduction to stability analysis of periodic solutions. Note, that an unstable solution cannot be observed in real-world applications without further ado.

For the linearized system (1.6), we define several subspaces

$$\begin{aligned}
E^s &= \operatorname{span}\{v_i \in \mathbb{R}^n \mid Df(\tilde{u})v_i = \lambda_i v_i,\ \operatorname{Re}\lambda_i < 0\},\\
E^u &= \operatorname{span}\{v_i \in \mathbb{R}^n \mid Df(\tilde{u})v_i = \lambda_i v_i,\ \operatorname{Re}\lambda_i > 0\},\\
E^c &= \operatorname{span}\{v_i \in \mathbb{R}^n \mid Df(\tilde{u})v_i = \lambda_i v_i,\ \operatorname{Re}\lambda_i = 0\},
\end{aligned}$$

where E^s and E^u denote the stable and unstable eigenspaces, respectively. E^c is called the *center eigenspace*. If $E^c = \emptyset$ the fixed point $\tilde{u}$ is called *hyperbolic*. Otherwise, it is *non-hyperbolic*. The interesting set in terms of the dynamics is the center eigenspace. While perturbations in the stable and unstable eigenspaces approach or leave the fixed point exponentially in time, the linear stability analysis reveals no information about the behavior of perturbations in the center directions. In the fully non-linear case the eigenspaces E^s, E^u, E^c have nonlinear analogs. Locally, we define the two invariant sets in a neighborhood U of $\tilde{u}$:

$$\begin{aligned}
W^s_{loc}(\tilde{u}) &= \{u \in U \subset \mathbb{R}^n \mid \phi(t;u) \to \tilde{u} \text{ for } t \to \infty,\ \phi(t;u) \in U\ \forall\ t \geq 0\},\\
W^u_{loc}(\tilde{u}) &= \{u \in U \subset \mathbb{R}^n \mid \phi(t;u) \to \tilde{u} \text{ for } t \to -\infty,\ \phi(t;u) \in U\ \forall\ t \leq 0\}.
\end{aligned}$$

W^s_{loc} and W^u_{loc} are the local stable and unstable manifolds, respectively. The global manifolds W^s and W^u can be constructed by following the flow of the local sets and compute the union as

$$W^s = \bigcup_{t \leq 0} \phi(t; W^s_{loc}(\tilde{u})), \qquad W^u = \bigcup_{t \geq 0} \phi(t; W^u_{loc}(\tilde{u})).$$

The *stable manifold theorem* assures the existence of local stable and unstable manifolds for a hyperbolic fixed point $\tilde{u}$. The manifolds are as smooth as f and

have the same dimensions as the corresponding linear subspaces. Additionally, W^s_{loc} and W^u_{loc} are tangent at $\tilde{u}$ to E^s and E^u, respectively (see e.g., Theorem 1.3.2 in [GH83]).

In the case of a hyperbolic fixed point $\tilde{u}$, the dynamics in a suitable neighborhood of $\tilde{u}$ can be completely understood by its linearization. This is the statement of the *theorem by Hartman-Grobman* (see e.g., Theorem 4.13 in [Mei07]). From that point of view the only interesting case is a non-hyperbolic fixed point, i.e., $\dim(E^c) \neq 0$, where linearization fails to describe the dynamics close to this fixed point. In the non-hyperbolic case, the *center manifold theorem* assures the existence of an invariant center manifold W^c that is tangent to E^c at the fixed point $\tilde{u}$ but in general is not unique (see e.g., Figure 3.2.1 in [GH83] for an example). Furthermore, the smoothness of the center manifold is C^{r-1} for a C^r vector field f. Since the dynamics away from the invariant center manifold W^c is known and W^c can be locally described as a graph over E^c it is possible to reduce the high-dimensional problem to the dynamics on the center manifold. Consider a transformation in the neighborhood of a fixed point of the general system (1.1) to

$$\begin{aligned} \dot{x} &= A_c x + B_c(x, y, z), \\ \dot{y} &= A_s y + B_s(x, y, z), \\ \dot{z} &= A_u z + B_u(x, y, z), \end{aligned} \tag{1.7}$$

where A_s and A_u are stable and unstable matrices, respectively, i.e., all eigenvalues of A_s (A_u) have real part smaller (larger) than zero, and A_c is the center matrix with eigenvalues with real part zero. The functions B_c, B_s, and B_u denote the non-linear parts with $B_i(0,0,0) = 0$ and $DB_i(0,0,0) = 0$ for $i \in \{s, u, c\}$, i.e., the origin is a fixed point and linear stability is determined by A_s, A_c, and A_u. We now define two maps $g : E^c \to E^s$ and $h : E^c \to E^u$ such that on W^c we have $y = g(x)$ and $z = h(x)$. The center manifold is thus given as

$$W^c = \{(x, g(x), h(x))\}.$$

The *non-hyperbolic Hartman-Grobman theorem* now states (see [Mei07]), that the dynamics close to the fixed point 0 is topologically conjugate to the system

$$\begin{aligned} \dot{x} &= A_c x + B_c(x, g(x), h(x)), \\ \dot{y} &= A_s y, \\ \dot{z} &= A_u z. \end{aligned} \tag{1.8}$$

Note, that the dynamics in the y- and z-component is trivial and that we only have to study the dynamics in x, which is decoupled from the rest. This is the key insight of the *center manifold reduction*, which reduces the dynamics of the system close to a non-hyperbolic fixed point to the dynamics in a low-dimensional space (usually $\dim(E^c) \ll n$). The center manifold reduction is

very useful in the study of high-dimensional systems close to non-hyperbolic fixed points. A similar reasoning is the basis for the slow manifold reduction used in systems with time scale separation (see Sec. 1.3). The existence of at least one eigenvalue of the linearization with real part zero also opens up for the field of bifurcation theory, which studies the influence of system parameters on the dynamics of the system. Intuitively, it is clear that non-hyperbolic fixed points are not persistent, since small perturbations move the eigenvalue away from the imaginary axis. The essentials of bifurcation theory will be reviewed in the next section.

1.2 Bifurcation Analysis and Numerical Continuation

Bifurcation analysis deals with the qualitative change of system behavior under parameter changes. It is one of the most successful subfields of dynamical systems theory and has attracted much attention not only from mathematicians but also from applied scientists and engineers. The reason is that bifurcation analysis allows predicting system behavior and helps to determine boundaries between basins of attraction for different solutions. As such, it helps to design a good set of working parameters for devices and gives valuable information about the robustness of systems to parameter perturbations. In this section some basic concepts from bifurcation theory will be reviewed. The focus lies on local bifurcations of fixed points in low-dimensional systems. Those bifurcations are important as they are the main focus of the research papers on equation-free methods in Appendix A. Further, the theory is quite well-developed in the one- and two-dimensional case. Global bifurcations, e.g., heteroclinic and homoclinic bifurcations, are not considered here. For a detailed introduction to bifurcation theory the reader is referred to standard textbooks, see e.g., [HK91, Kuz04].

The outcome of every bifurcation analysis is a *bifurcation diagram* that shows the parameter dependence of solutions of the underlying system (1.1), e.g., in (u, p)- or $(\|u\|, p)$-space. Local bifurcations are classified by the way how the eigenvalues of the linearized system cross the imaginary axis with parameter changes. Since bifurcations describe a fundamental change in system dynamics they can not happen at hyperbolic fixed points. An infinitesimally small perturbation in the parameters from p to $p + \delta p$ cannot shift eigenvalues over the imaginary axis and hence the corresponding flows will be *topologically equivalent*, i.e., there exists a homeomorphism h and a map τ, monotonically-increasing with t, such that $h(\phi_{p+\delta p}(\tau(u,t);u)) = \phi_p(t;h(u))$. Topologically equivalent systems have the same qualitative dynamics. Consequently, local bifurcations can only happen on center manifolds and the center manifold reduction (1.8) justifies the

investigation of low-dimensional systems, i.e., the linear system (1.6) typically possesses one or two eigenvalues on the imaginary axis.

First, we consider the case of a single real eigenvalue crossing zero with all other eigenvalues having non-vanishing real part. The center manifold reduction leads us to the study of a one-dimensional system.

One-dimensional systems For the simplest case of fixed points $\tilde{u}$ in a one-dimensional system with $f(\tilde{u}, p) = 0$ the bifurcation diagram shows the equilibria in dependence on the parameter p (cf. Fig. 1.1). Therefore, the bifurcation diagram is the union of all points (u, p) for which $f(u, p) = 0$. Further, we restrict ourselves to local bifurcations, i.e., bifurcations that can be understood by investigating the vicinity of equilibria in phase space. The connected components in the bifurcation diagram are called *branches*, which are divided into *stable* and *unstable* branches depending on the stability properties of the linearized system (1.6). Before studying what happens when bifurcations are present, we would first like to understand the behavior when bifurcations are absent. Assume we have already found a solution $(\tilde{u}, \tilde{p})$ such that $f(\tilde{u}, \tilde{p}) = 0$. If $\partial f/\partial u|_{(\tilde{u},\tilde{p})} \neq 0$ the *implicit function theorem* tells us that there exists a unique function $u(p)$ for some interval around $\tilde{p}$ such that $f(u(p), p) = 0$ and $u(\tilde{p}) = \tilde{u}$. Consequently, there can be no local bifurcation close to $\tilde{p}$ and a necessary condition for the existence of a bifurcation is that the system is singular, i.e., $\partial f/\partial u|_{(\tilde{u},\tilde{p})} = 0$. Note, that this is equivalent to our assumption, that a real eigenvalue crosses zero. We also remark that the argumentation with the implicit function theorem is not sufficient in higher dimensions: in the case of a Hopf bifurcation (see (1.13)) the implicit function theorem guarentees the existence of a unique curve of fixed points although a bifurcation, i.e., the birth of a limit cycle, happens.

In the following, the presentation is restricted to the description of *codimension one* bifurcations, i.e., one parameter has to be changed in order to observe the bifurcation. Codimension one bifurcations are usually observed in real-world applications and correspond to the crossing of the imaginary axis of a real eigenvalue or a pair of complex eigenvalues. For bifurcations with higher codimension, e.g., cusp bifurcation, the reader is referred to [HK91, Kuz04]. In order to begin the classification of some bifurcations, we recall, that bifurcations happen at *critical or bifurcation points* where the linear flow is singular. Hence, all bifurcation points $(\tilde{u}, \tilde{p})$ have the *singularity conditions*

$$f(\tilde{u}, \tilde{p}) = 0 \qquad \text{and} \qquad \partial f/\partial u|_{(\tilde{u},\tilde{p})} = 0. \tag{1.9}$$

Consequently, the classification is done via higher-order derivatives, i.e., via the type of nonlinearity. The simplest case of a *nondegeneracy condition* is that the

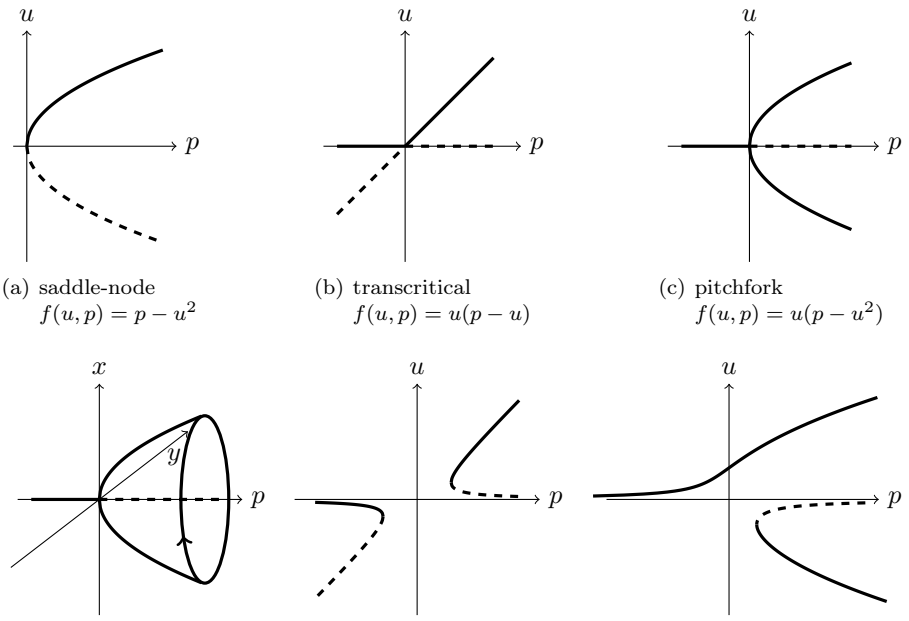

(a) saddle-node $f(u,p) = p - u^2$

(b) transcritical $f(u,p) = u(p-u)$

(c) pitchfork $f(u,p) = u(p-u^2)$

(d) Hopf

(e) Perturbed transcritical $f(u,p) = u(p-u) + \varepsilon$

(f) Perturbed pitchfork $f(u,p) = u(p-u^2) + \varepsilon$

Figure 1.1: Bifurcation diagrams. Full (dashed) lines correspond to stable (unstable) branches.

quadratic term in the Taylor expansion (1.5) is non-vanishing, i.e.,

$$\partial^2 f/\partial u^2|_{(\tilde{u},\tilde{p})} \neq 0. \tag{1.10}$$

Further, assume the *transversality condition*

$$\partial f/\partial p|_{(\tilde{u},\tilde{p})} \neq 0 \tag{1.11}$$

is fulfilled. Then, the system undergoes a *saddle-node* or *fold* bifurcation at $(\tilde{u},\tilde{p})$. The saddle-node bifurcation is shown in Fig. 1.1(a) and connects a stable with an unstable branch. Note, that the implicit function theorem can be applied to obtain a function $p(u)$ due to condition (1.11). It is easiest to understand bifurcations in their corresponding *normal form*, which is the simplest vector field giving rise to the respective bifurcation. The normal form for the saddle-node bifurcation is

$$\dot{u} = p - u^2 \qquad \text{saddle-node.}$$

It is easily seen that the number of fixed points depends on the parameter p, such that there are no fixed points for $p < 0$, one (degenerate) fixed point for

$p = 0$ and two fixed points for $p > 0$. At the bifurcation point $(\tilde{u}, \tilde{p}) = (0, 0)$ the singularity conditions (1.9) are fulfilled. Furthermore, $\partial^2 f/\partial u^2|_{(\tilde{u},\tilde{p})} = -2 \neq 0$ and $\partial f/\partial p|_{(\tilde{u},\tilde{p})} = 1 \neq 0$ supplement the sufficient conditions (1.10) and (1.11) for a saddle-node bifurcation.

If the vector field has certain symmetries or certain special properties there are more codimension one bifurcations that occur frequently. These dynamical systems are usually encountered in models from physics. The most common additional bifurcations are the *transcritical bifurcation* with conditions

$$\left.\begin{aligned} f(\tilde{u}, \tilde{p}) &= 0 \\ \partial f/\partial u|_{(\tilde{u},\tilde{p})} &= 0 \\ \partial f/\partial p|_{(\tilde{u},\tilde{p})} &= 0 \end{aligned}\right\} \quad \text{(singularity)},$$
$$\partial^2 f/\partial u^2|_{(\tilde{u},\tilde{p})} \neq 0, \quad \text{(nondegeneracy)},$$
$$\partial^2 f/\partial u \partial p|_{(\tilde{u},\tilde{p})} \neq 0, \quad \text{(transversality)},$$

and the *pitchfork bifurcation* with conditions

$$\left.\begin{aligned} f(\tilde{u}, \tilde{p}) &= 0 \\ \partial f/\partial u|_{(\tilde{u},\tilde{p})} &= 0 \\ \partial f/\partial p|_{(\tilde{u},\tilde{p})} &= 0 \\ \partial^2 f/\partial u^2|_{(\tilde{u},\tilde{p})} &= 0 \end{aligned}\right\} \quad \text{(singularity)},$$
$$\partial^3 f/\partial u^3|_{(\tilde{u},\tilde{p})} \neq 0, \quad \text{(nondegeneracy)},$$
$$\partial^2 f/\partial u \partial p|_{(\tilde{u},\tilde{p})} \neq 0, \quad \text{(transversality)}.$$

The transcritical bifurcation has the special property that $u = 0$ is a fixed point for all values of the parameter p with symmetry $f(-u, -p) = f(u, p)$. The transcritical bifurcation is also known as an *exchange of stability*, since the branches continue in the same direction with a mere exchange of stability (see Fig. 1.1(b)). The pitchfork bifurcation is a special bifurcation in systems with symmetry $f(-u, p) = -f(u, p)$, see Fig. 1.1(c). The pitchfork is further classified as *supercritical* for $\partial^3 f/\partial u^3|_{(\tilde{u},\tilde{p})} < 0$ and *subcritical* for $\partial^3 f/\partial u^3|_{(\tilde{u},\tilde{p})} > 0$. The normal forms are given as

$$\begin{aligned} \dot{u} &= u(p - u) && \text{transcritical} \\ \dot{u} &= u(p - u^2) && \text{pitchfork} \end{aligned} \tag{1.12}$$

and it is easily checked that the conditions for the respective bifurcation are fulfilled at the bifurcation point $(\tilde{u}, \tilde{p}) = (0, 0)$. The study of bifurcations in dynamical systems with symmetry is a whole field on its own and would go far beyond the scope of this short review (see e.g., [GSS88, WR02] for further reading). Note, that both the transcritical and the pitchfork bifurcation are structurally unstable as they perturb to ordinary saddle-node bifurcations under general perturbations of the vector field f (cf. Fig. 1.1(e) and Fig. 1.1(f)

where a constant has been added to the vector fields in (1.12)). On the other hand, the saddle-node bifurcation is structurally stable, e.g., adding a constant merely translates the bifurcation point, and is therefore often encountered in applications.

Two-dimensional systems So far, the presented bifurcations were codimension one with a one-dimensional state variable. Another very important bifurcation in applications is the *Hopf* or *Andronov-Hopf* bifurcation (see Fig. 1.1(d)). In contrast to the other bifurcations, where a real eigenvalue crosses zero at the bifurcation, the Hopf bifurcation requires a pair of complex eigenvalues crossing the imaginary axis. Hence, in order to observe a Hopf bifurcation, the phase space has to be at least two-dimensional. The importance of the (supercritical) Hopf bifurcation stems from the fact that a stable equilibrium loses stability and gives rise to a stable limit cycle. This behavior can be observed in many physical systems and is therefore studied in great detail. Before presenting the general theorem for existence of a Hopf bifurcation, it is instructive to consider the system

$$\begin{aligned} \dot{x} &= -y + x(p + a(x^2 + y^2)), \\ \dot{y} &= x + y(p + a(x^2 + y^2)), \end{aligned} \tag{1.13}$$

where we write $u = (x, y) \in \mathbb{R}^2$. At the bifurcation point $(\tilde{u}, \tilde{p}) = ((0, 0), 0)$ it is easily verified that $f(\tilde{u}, \tilde{p}) = 0$ and

$$D_u f|_{(\tilde{u},\tilde{p})} = \begin{pmatrix} p + 3ax^2 + ay^2 & -1 + 2axy \\ 1 + 2axy & p + ax^2 + 3ay^2 \end{pmatrix}\Bigg|_{(\tilde{u},\tilde{p})} = \begin{pmatrix} 0 & -1 \\ 1 & 0 \end{pmatrix}. \tag{1.14}$$

The eigenvalues of (1.14) are $\lambda_\pm = \pm \mathrm{i}$ and purely imaginary. The implicit function theorem guarentees the existence of a smooth curve of equilibria $u(p)$ going through the origin and the eigenvalues $\lambda_\pm(p)$ vary smoothly with p. Moreover, we compute

$$\frac{d}{dp}(\operatorname{Re} \lambda_\pm(p))\Big|_{(\tilde{u},\tilde{p})} = 1 \neq 0, \tag{1.15}$$

such that the eigenvalues cross the imaginary axis transversally. The conditions (1.14) and (1.15) add the sufficient conditions for a Hopf bifurcation: assume we have an equilibrium $(\tilde{u}, \tilde{p})$ for which $D_u f|_{(\tilde{u},\tilde{p})}$ has a simple pair of imaginary eigenvalues and no other eigenvalues with real part zero. Further assume, that the pair of imaginary eigenvalues fulfills the condition (1.15). Then, the *Hopf theorem* implies that the dynamical system undergoes a Hopf bifurcation at $(\tilde{u}, \tilde{p})$. Additionally, the bifurcation is supercritical for $a < 0$ and subcritical for $a > 0$ in (1.13).

Knowledge of bifurcation diagrams gives valuable information about the behavior of the system for different parameter values. The computation of bifurcation

diagrams is complicated by the fact that, in general, branches cannot be computed analytically. For this case, *numerical continuation* is the method of choice to obtain a discrete approximation of branches in bifurcation diagrams. In the remainder of this section, the concepts of numerical continuation that have been used in the papers in Appendix A will be introduced. For a broader introduction to numerical continuation and bifurcation analysis the interested reader is referred to e.g., [Kuz04, DS13].

The main ingredient in numerical continuation is the implicit function theorem. The strategy in a numerical continuation scheme is to use the existence of smooth branches in order to find connected components where the linearized system is not singular. At singular points the continuation process would ideally classify the type of bifurcation and continue all branches emanating from this bifurcation point. Additionally, the stability of branches should be determined during the continuation process. If we restrict ourselves to find bifurcation diagrams for equilibria the outcome of a numerical continuation would be the zero set $\{(u,p) \mid f(u,p) = 0\}$. Note, that a continuation method only finds connected components. In order to detect disconnected branches, the continuation process has to be initialized on another branch.

Basically all continuation schemes are composed of two steps: a *predictor* and a *corrector* step (we neglect issues concerning step size control). In the predictor step a potentially new equilibrium $(\hat{u}, \hat{p})$ is predicted from a previous one. The prediction typically introduces an error, because $(\hat{u}, \hat{p})$ is not exactly on the branch. This error is corrected in the corrector step by solving $f(u,p) = 0$ in a suitable subspace. For this purpose, one usually uses Newton iterations, but the corrector step can also be formulated as a bisection or false position method (see, e.g., [CHS12] and Paper IV).

Before explaining details about continuation techniques, we note that it is useful to consider the *one-parameter continuation problem* in the form

$$G(\xi) = 0, \qquad G : \mathbb{R}^{n+1} \to \mathbb{R}^n$$

where $\xi = (u,p)$. The level set $G(\xi) = f(u,p) = 0$ defines the parameter-dependent equilibria and the implicit function theorem guarentees the existence of a smooth curve for a regular system, i.e., $\operatorname{rank} DG = n$. The goal is to trace branches in the bifurcation diagram by finding a sequence of subsequent points $\xi_1, \xi_2, \ldots$ starting from an initial solution ξ_0. The initial solution can either be known analytically or it can be obtained by an initial guess with subsequent Newton corrections. The starting point of each continuation step is the choice of a good candidate for ξ_{j+1} from previous states $\xi_j, \xi_{j-1}, \ldots, \xi_0$. A popular choice is the *tangent predictor*

$$\hat{\xi}_{j+1} = \xi_j + h_j \eta_j, \tag{1.16}$$

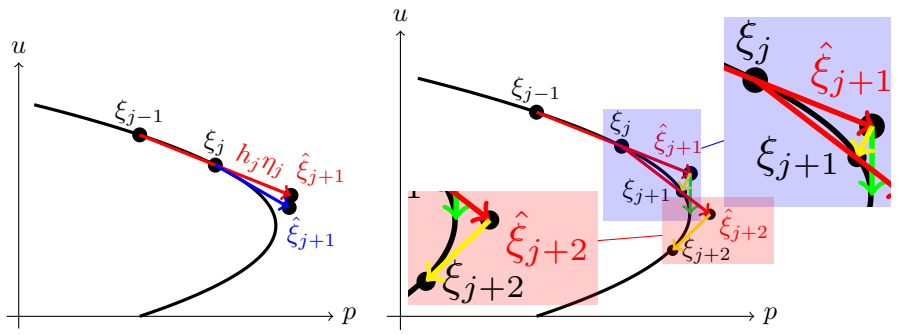

(a) Predictor step (b) Corrector step

Figure 1.2: Numerical continuation scheme. (a) Sketch for different predictor steps. The secant predictor (red) uses information from the two previous points ξ_{j-1} and ξ_j, while the tangent predictor (blue) only uses local information at ξ_j. (b) Predictor-corrector method. The blue box shows the comparison between natural continuation (fixed parameter value, green arrow) and pseudo-arclength continuation (orthogonal to prediction, yellow arrow). The red box shows a second corrector step that visualizes how pseudo-arclength continuation is able to continue branches around fold points.

where h_j is the step size and η_j the normalized tangent vector to the branch at ξ_j (see Fig. 1.2(a)). The tangent is found by solving

$$DG|_{\xi=\xi_j} \cdot \eta_j = 0. \tag{1.17}$$

Another choice is the *secant predictor* that uses two previous points on the branch to find the predicted point $\hat{\xi}^{j+1}$. Here, the same equation (1.16) is used with

$$\eta_j = \frac{\xi_j - \xi_{j-1}}{\|\xi_j - \xi_{j-1}\|}.$$

This has the advantage that it is not necessary to solve (1.17), which can be computationally expensive for large systems.

Since $G(\hat{\xi}_{j+1}) \neq 0$ in general, the subsequent correction step uses Newton iterations to solve $G(\xi_{j+1}) = 0$ starting from the predicted point $\hat{\xi}_{j+1}$. Since Newton iterations require the system to have square Jacobian, i.e., as many equations as unknowns, we have to choose another scalar condition $g_j(\xi) = 0$ for the corrector step. *Natural continuation* seeks an equilibrium for a fixed parameter value p. Denoting $\hat{\xi}_{j+1} = (\hat{u}_{j+1}, \hat{p}_{j+1})$, natural continuation uses

$$g_j(\xi) = p - \hat{p}_{j+1} \tag{1.18}$$

as auxiliary condition. Consequently, the Newton iteration solves the system

$$\begin{aligned} G(\xi_{j+1}) &= 0 \\ g(\xi_{j+1}) &= 0 \end{aligned} \quad \Rightarrow \quad \begin{aligned} f(u_{j+1}, p_{j+1}) &= 0 \\ p_{j+1} - \hat{p}_{j+1} &= 0 \end{aligned}$$

in $n+1$ unknowns (u, p) and $n+1$ equations (n for G and 1 for g) in a subspace orthogonal to the parameter axis (see green arrow in Fig. 1.2(b)). The biggest disadvantage of natural continuation is, that it is incapable of continuing branches around fold points. A prediction beyond the fold point prevents the Newton iteration to converge. Therefore, a frequently-used technique is *pseudo-arclength continuation*. The only difference to natural continuation is the choice of the auxiliary scalar equation or geometrically-speaking the choice of the suitable subspace. Instead of (1.18) we use

$$g_j(\xi) = \langle \xi - \hat{\xi}_{j+1}, \eta_j \rangle,$$

where $\langle \cdot \rangle$ is the inner product (in $\mathbb{R}^{n+1}$). Effectively, the system $G(\xi) = 0$ is solved in a subspace orthogonal to the predictor (see yellow arrow in Fig. 1.2(b)). Therefore, it is possible for pseudo-arclength continuation to continue branches around folds. Note that the stability of the branches can be extracted as a by-product of the Newton iterations at the converged point ξ_{j+1}. Further, standard criteria from Newton iterations can be used to check for convergence, e.g., convergence of the residual.

Another important ingredient in numerical continuation is the numerical detection of bifurcations in the continuation process. This is usually accomplished with *test functions* ψ: scalar-valued functions that cross zero at the bifurcation point. In the case of a saddle-node bifurcation one way to construct a test function is

$$\psi(u, p) = \prod_{i=1}^{n} \lambda_i(u, p), \tag{1.19}$$

where $\lambda_i(u, p)$ are the eigenvalues of the linear dynamics at the point (u, p) on the branch. At a regular fold point exactly one eigenvalue changes stability, i.e., crosses zero, and therefore a fold is detected along the branch if

$$\psi(\xi_j)\psi(\xi_{j+1}) < 0.$$

It can be tedious in applications to compute all eigenvalues for the linearized flow and instead of (1.19), one often uses the test function

$$\psi(u, p) = \det\left(\frac{\partial f(u, p)}{\partial u}\right). \tag{1.20}$$

In general, one has to be careful when using test functions. For example, if two real eigenvalues cross zero the same time, i.e., a non-generic fold, the test

functions (1.19) and (1.20) would not detect the fold. Similar test functions also exist for other bifurcations, e.g., Hopf bifurcations (see [Kuz04] for details).

We stop the introduction to bifurcation analysis and numerical continuation at this point since we have presented all the results necessary to understand the relevant parts in the research papers in Appendix A. This short presentation only scratches the surface of (numerical) bifurcation analysis. Much more has to be said about continuation of periodic orbits with methods such as (multiple) shooting and collocation. Further, continuation of bifurcations and in general continuation in more than one parameter has to be discussed as well. Also, methods for branch switching at certain bifurcation points, e.g., Hopf bifurcations and pitch-fork bifurcations, have not been discussed here. This list is not at all complete and we would like to conclude this section with a brief remark on available software packages for numerical continuation and bifurcation analysis.

Many different packages are available as open source projects and their capabilities differ substantially. Powerful packages are AUTO [DK86] (written in Fortran), MatCont [DGK03] (written in Matlab) and CoCo [DS13] (written in Matlab). Furthermore, there exists also software for specialized applications. DDE-Biftool [ELS01] focusses on the bifurcation analysis of delay-differential equations and Sympercon [Sym] analyzes symmetric systems. HomCont [DCF+98] is specialized in continuation of homoclinic and heteroclinic orbits.

In the next section, special dynamical systems with time scale separation are discussed. This constitutes the foundation for the analysis of such systems with the equation-free framework (cf. Chap. 2).

1.3 Time Scale Separation

The importance of systems with time scale separation has been elaborated on in the introduction. Time scale separation is also observed in applications in the Appendix A, e.g., speed of pedestrians vs. oscillation period (Paper II and Paper V), car speed vs. speed of traffic jams (Paper I and Paper II) and neuron dynamics vs. map formation time scale (Paper III and Paper IV). Here, we like to give a short overview of the existing mathematical theory and concepts. Details can be found in the research papers in Appendix A, in particular in Paper I. This section follows the ideas of Fenichel's geometric singular perturbation theory [Fen79, Wig94] in its general form. Along the general discussion, we also give the results for explicit slow-fast systems (based on the lecture notes by Christopher Jones [Jon95]) in order to visualize the concepts and build up

intuition. It is assumed that the reader is familiar with dynamical systems theory and concepts from geometry, e.g., manifolds, graphs, and we use common meanings without strict definition.

Assume we have a dynamical system

$$\dot{u} = f_\varepsilon(u), \qquad u \in \mathbb{R}^n, \qquad f_\varepsilon : \mathbb{R}^n \to \mathbb{R}^n, \tag{1.21}$$

with time scale separation ε and flow ϕ_ε for the smooth right-hand side f_ε. Assume further, that ε is a *singular perturbation parameter*, i.e., for $\varepsilon = 0$ there exists an invariant critical slow manifold M_0 such that the flow $\phi_0(t; u) = u$ for all $u \in M_0$ and $t \in \mathbb{R}$. This means, that M_0 solely consists of fixed points and $f_0(u) = 0$ for all $u \in M_0$. To simplify the discussion, we assume further that M_0 is compact. Although the time scale separation in applications can often not be influenced directly it is of theoretical interest to study the limit $\varepsilon \to 0$. The strategy is to establish results for the case $\varepsilon = 0$ and then study how they persist for $\varepsilon > 0$. To build up intuition, it is beneficial to study explicit slow-fast systems. Although an explicit splitting into slow and fast variables is unnecessary for Fenichel's results, it helps to better understand the theorems.

An *explicit slow-fast system* is given as

$$\begin{aligned} \dot{x} &= f(x, y, \varepsilon), \\ \dot{y} &= \varepsilon g(x, y, \varepsilon), \end{aligned} \tag{1.22}$$

where $\dot{} = d/dt$ denotes the time-derivative with respect to the *fast time* t and $x \in \mathbb{R}^{n_f}$ and $y \in \mathbb{R}^{n_s}$ are the *fast and slow variables*, respectively. f and g are smooth in $U \times I$, where $U \subset \mathbb{R}^n = \mathbb{R}^{n_f} \times \mathbb{R}^{n_s}$ and I is an interval containing zero. For $\varepsilon \neq 0$, the *fast system* (1.22) can be transformed into the equivalent *slow system*

$$\begin{aligned} \varepsilon x' &= f(x, y, \varepsilon), \\ y' &= g(x, y, \varepsilon). \end{aligned} \tag{1.23}$$

Here, $' = d/d\tau$ is the time-derivative with respect to the *slow time* $\tau = \varepsilon t$. In the case of infinite time scale separation, i.e., $\varepsilon = 0$, the slow and fast systems are no longer equivalent but have both their interesting properties. We first consider the slow system (1.23), that is turned into a differential algebraic equation

$$\begin{aligned} 0 &= f(x, y, 0), \\ y' &= g(x, y, 0), \end{aligned} \tag{1.24}$$

which is only defined on $0 = f(x, y, 0)$. This constraint can be used in the implicit function theorem, assuming non-degeneracy, to find a function $x = h(y)$ such that $f(h(y), y, 0) = 0$. Therefore, h defines (at least locally) a graph

$$M_0 = \{(x, y) \in \mathbb{R}^n \mid x = h(y)\},$$

which is the *critical manifold*. On M_0 the dynamics is given by

$$y' = g(h(y), y, 0)$$

and describes the slow dynamics. This constitutes a dimensionality reduction from $n = n_f + n_s$ to n_s dimensions. A disadvantage of system (1.24) is, that the dynamics is not defined off M_0.

Looking at the singular case for system (1.22) results in

$$\dot{x} = f(x, y, 0), \tag{1.25a}$$
$$\dot{y} = 0. \tag{1.25b}$$

This ODE also defines a flow away from M_0, but the dynamics on M_0 is trivial as all points on M_0 are fixed points of (1.25a) (note, that $f(x, y, 0) = 0$ on M_0). Comparing with the general approach in (1.21), M_0 is the critical manifold that has been stated to exist in singular perturbed systems. It is the goal of *geometric singular perturbation theory* to study those systems for a small but finite time scale separation $\varepsilon \neq 0$.

Before discussing Fenichel's results, we investigate the linearized flow Df_0 on M_0 for the general system (1.21). Df_0 has at least n_s zero eigenvalues, since (1.25b) is identically zero and therefore all directions tangential to M_0 have zero eigenvalue. The best we can hope for is that M_0 is *normally hyperbolic*, i.e., the linearized flow on M_0 has exactly n_s eigenvalues zero and all the remaining n_f eigenvalues are non-vanishing. In the remaining part of this section we will assume that M_0 is normally hyperbolic.

Since M_0 contains fixed points, it is natural to define the invariant stable and unstable manifolds to those fixed points $u_0 \in M_0$ in the usual manner

$$W_0^s(u_0) = \{u \in \mathbb{R}^n \mid \lim_{t\to\infty} \phi_0(t; u) = u_0\},$$
$$W_0^u(u_0) = \{u \in \mathbb{R}^n \mid \lim_{t\to-\infty} \phi_0(t; u) = u_0\}.$$

In this context, $W_0^s(u_0)$ and $W_0^u(u_0)$ are also called the *stable* and *unstable fibers* for the *basepoint* u_0. The union of the stable and unstable fibers build the stable and unstable manifolds for M_0, respectively, i.e.,

$$W_0^s(M_0) = \bigcup_{u_0 \in M_0} W_0^s(u_0),$$
$$W_0^u(M_0) = \bigcup_{u_0 \in M_0} W_0^u(u_0).$$

In equation-free computations, we assume that the slow manifolds are normally attracting, i.e., $\dim(W_0^u(M_0)) = 0$. Then, the *stable fiber projection* $\pi_0 : U \to$

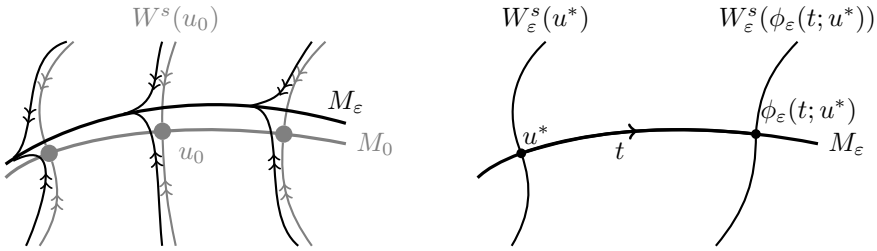

(a) Persistence of the slow manifold. (b) Invariance as a family.

Figure 1.3: Visualizations of the main results of Fenichel's theory. (a) The critical manifold M_0 (gray) of fixed points persists for $\varepsilon > 0$. The flow on the slow manifold M_ε (black) is different from the flow on M_0 which consists solely of fixed points (gray dots). (b) Fibers persist as a family according to Fenichel's third theorem (cf. also (1.26)).

$M_0, \pi_0(u) = u_0$ assigns to each $u \in U$ in a neighborhood of M_0 its basepoint u_0. The natural question to ask is: what happens to the manifolds M_0, $W_0^{s/u}(u_0)$ and $W_0^{s/u}(M_0)$ if ε is non-zero but small? The answer is given by Fenichel and we will briefly discuss his main theorems in the remainder of this section.

We consider now the system (1.21) for $\varepsilon > 0$. Fenichel's first theorem states that under the conditions of smooth f_ε and a normally hyperbolic, compact M_0 there exists a *slow manifold* M_ε, also compact, that is i) locally invariant under f_ε, ii) diffeomorphic to M_0 and iii) $\mathcal{O}(\varepsilon)$-close to M_0. Note that, although M_ε is diffeomorphic to M_0, the dynamics are fundamentally different. Usually, M_ε does not consist of fixed points only (see Fig. 1.3(a)) and the dynamics on M_ε can be as complicated as in any other dynamical system. The persistence of the slow manifold forms the basis for equation-free computations (see Chap. 2). It is also the reason, why pattern formation is observed in many physical systems (see also the slaving principle [Hak83]).

Additionally, Fenichel's second theorem states that also the stable and unstable manifolds persist: there exists stable/unstable manifolds $W_\varepsilon^{s/u}(M_\varepsilon)$ that are i) locally invariant under f_ε, ii) diffeomorphic to $W_0^{s/u}(M_0)$ and iii) $\mathcal{O}(\varepsilon)$-close to $W_0^{s/u}(M_0)$. At first sight it seems counter-intuitive to talk about the stable and unstable manifolds $W_\varepsilon^{s/u}(M_\varepsilon)$, since M_ε does not consist of fixed points. It is in a similar manner as in Fenichel's first theorem: the dynamics on the manifold $W_\varepsilon^{s/u}(M_\varepsilon)$ is changed, but the approach to the slow manifold M_ε happens with an exponential rate for points in the stable and unstable manifolds $W_\varepsilon^{s/u}(M_\varepsilon)$

in positive and negative time, respectively (see, e.g., [Jon95] for the estimates).

Furthermore, it is intuitively clear, that individual fibers $W_0^{s/u}(u_0)$ cannot persist as such, since the basepoint u_0 on the manifold, which is fixed in the case $\varepsilon = 0$ is moving on M_ε. Nevertheless, Fenichel's third theorem states the persistence of the fibers in a certain way: for all $u^* \in M_\varepsilon$ there exist manifolds $W_\varepsilon^{s/u}(u^*)$ which are i) invariant as a family under f_ε, ii) diffeomorphic to $W_0^{s/u}(u^*)$ and iii) $\mathcal{O}(\varepsilon)$-close to $W_0^{s/u}(u^*)$. *Invariant as a family* means, that after a time t the fibers for the basepoint u^* are a subset of the fibers of the basepoint u^* after time t, i.e.,

$$\phi_\varepsilon(t; W_\varepsilon^{s/u}(u^*)) \subset W_\varepsilon^{s/u}(\phi_\varepsilon(t; u^*)). \tag{1.26}$$

This is visualized in Fig. 1.3(b).

The results of Fenichel provide the mathematical basis for the development of equation-free methods. In equation-free methods, a dynamical system is assumed to possess a normally-attracting slow manifold. The dynamics on this manifold decides about the long-term behavior of the system and is therefore of interest for applications. Usually, the equations of motion on the slow manifold are not given in closed form and a splitting into slow and fast variables is also not available in an obvious manner. We will introduce equation-free methods in the next section.

Chapter 2

Equation-Free Methods

"Someone told me that each equation I included in the book would halve the sales."

S. Hawking, A brief history of time, 1988.

We introduced the notion of dynamical systems with time scale separation in Chap. 1. These systems are frequently observed in nature, e.g., in quasi-geostrophic flow [Lor86] in meteorology; in the van der Pol oscillator [vdP20] and celestial mechanics [Hol90] in physics; and in Michaelis-Menten kinetics [MM13] (see [JG11] for a translation into English) in chemistry and biology. The time scale separation often results in pattern formation, see e.g., the Belousov-Zhabotinsky reaction [Bel59, Zha64, FN74]. This list of applications is far from being complete and all the examples are interesting in their own right. Therefore, there is a strong demand to understand the relevant coarse dynamics of systems with time scale separation.

In this chapter the so-called equation-free approach, proposed and analyzed by Kevrekidis and coworkers, is discussed (see [KGH+03, KGH04] and [KS09] for a recent review on equation-free methods). First, a short overview on the methodology of equation-free analysis is presented in Sec. 2.1, followed by an introduction of the newly-developed implicit equation-free methods in Sec. 2.2 (cf. also [MSB+14] and Paper I). Afterwards, important higher-level tasks, e.g., coarse-

projective integration and coarse bifurcation analysis, employing the equation-free methodology are introduced in Sec. 2.3. Furthermore, existing methods and applications based on these higher-level tasks are presented in Sec. 2.4. The chapter concludes with a discussion about critical issues in equation-free computations in Sec. 2.5.

2.1 The Equation-Free Idea

One main idea behind the analysis of multi-scale systems originating in physics is that the long-term evolution of these systems happens on a low-dimensional slow manifold $\mathcal{M}_\varepsilon$ which is normally attracting. For singularly perturbed systems in explicit slow-fast form the critical slow manifold $\mathcal{M}_0$ can be explicitly constructed as a graph in the case of infinite time scale separation, i.e., $\varepsilon = 0$. Fenichel's theory [Fen79] guarantees the persistence of this manifold $\mathcal{M}_\varepsilon$ for small $\varepsilon > 0$ (cf. Sec. 1.3 for details). In the normally attracting case after a (short) initial transient the dynamics are well-described by the flow ϕ_ε reduced to $\mathcal{M}_\varepsilon$. Usually, the dimension of $\mathcal{M}_\varepsilon$ is much smaller than the dimension of the full phase space, making the coarse analysis of multi-scale systems tractable. In real-world problems, it is not always possible to derive the dynamics on this slow manifold, although many phenomena are known to be inherently low-dimensional, e.g., pattern formation. This is due to a modeling that often takes place on a microscopic level and consequently equations of motion for the interesting macroscopic scale are not available in closed form. A method to gain insight into the dynamics on $\mathcal{M}_\varepsilon$ without deriving explicit evolution equations is therefore very desirable. Here, the *equation-free idea* comes into play.

Assume, that a microscopic model for our problem is available. In general, these models are high-dimensional systems, e.g., ordinary, partial or stochastic differential equations. For the sake of simplicity, we assume the microscopic model to be an autonomous ordinary differential equation with sufficiently smooth right-hand side

$$\dot{u} = f_\varepsilon(u, p), \qquad u \in \mathbb{R}^n, \qquad f_\varepsilon : \mathbb{R}^{n+m} \to \mathbb{R}^n. \tag{2.1}$$

Usually, the problem depends on a set of (real) parameters $p \in \mathbb{R}^m$. The subscript ε denotes the time scale separation which is not necessarily known in applications. Note, that (2.1) is not required to be in the explicit form for slow-fast systems, i.e., the splitting into slow and fast variables can be unknown. The solution of (2.1) after time t for initial condition $u(t_0)$ is determined by

$$u(t_0 + t) = \phi_\varepsilon(t; u(t_0)), \tag{2.2}$$

where ϕ_ε is the flow of (2.1). In the numerical implementation of equation-free methods a discretized-in-time version of ϕ_ε is called the *microscopic time stepper*.

Further, the equations of motion on the slow manifold $\mathcal{M}_\varepsilon$ are known to exist but might be unknown. Formally, we define the macroscopic dynamics to be described by

$$\dot{U} = F(U, p), \qquad U \in \mathbb{R}^N, \qquad F : \mathbb{R}^{N+m} \to \mathbb{R}^N. \tag{2.3}$$

Here, F is the macroscopic vector field and U denotes the macroscopic, low-dimensional variables (typically $N \ll n$). Again, we formally assume that a solution to (2.3) exists and is given by the macroscopic flow Φ:

$$U(t_0 + t) = \Phi(t; U(t_0)). \tag{2.4}$$

The idea is now to approximate the macroscopic flow Φ in order to gain information on the macroscopic scale. Since the flow ϕ_ε can usually only be approximated by simulation, we have to limit our investigations to the numerical approximation of Φ, i.e., the *macroscopic time stepper*. In order to construct Φ we use two operators

$$\begin{aligned} \mathcal{R} &: \mathbb{R}^n \to \mathbb{R}^N, \qquad \text{(restriction)} \\ \mathcal{L} &: \mathbb{R}^N \to \mathbb{R}^n, \qquad \text{(lifting)} \end{aligned} \tag{2.5}$$

to communicate between the microscopic ($\mathbb{R}^n$) and macroscopic ($\mathbb{R}^N$) levels. The *restriction operator* $\mathcal{R}$ maps a full state of the system to a low-dimensional reduced state; the *lifting operator* $\mathcal{L}$ initializes a high-dimensional full state from a low-dimensional state. Usually, the construction of a restriction operator is simple in the sense, that it is known from physical intuition of the system at hand; it defines the macroscopic quantities of interest, e.g., moments of a distribution or order parameters. On the other hand, the construction of a lifting operator is much more involved, since one has to compute a high-dimensional state from a low-dimensional one, e.g., construct a full distribution from only knowing the mean and variance. This is a *one-to-many* operation and the definition of the lifting is consequently not unique. In a continuation setup for numerical bifurcation analysis it is often possible to use information from previous continuation steps in the construction of $\mathcal{L}$ (see e.g., Paper I and Paper IV).

Finally, the construction of the macroscopic time-stepper proceeds in three steps: lift – evolve – restrict (see also Fig. 2.1). Precisely, the three-step scheme P is defined as

$$P(t; \cdot) = \mathcal{R}(\phi_\varepsilon(t; \mathcal{L}(\cdot))). \tag{2.6}$$

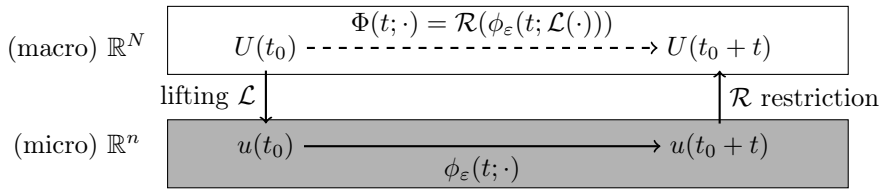

Figure 2.1: Sketch of the lift–evolve–restrict scheme (2.6) as proposed by [KGH+03] and used for the explicit macroscopic time stepper.

This is the original explicit approach by Kevrekidis and co-workers, where the macroscopic time stepper is given as $\Phi = P$ [KS09]. Note, that this is only an approximation of the flow Φ on the slow manifold, since the lifting operator is in general not initializing on the slow manifold (*lifting error*). In order to assure a good lifting operator it is often required that

$$\mathcal{R} \circ \mathcal{L} = I \tag{2.7}$$

is fulfilled and then the flow on $\mathcal{M}_\varepsilon$ is supposedly well-approximated by $\Phi = P$ [KS09, AHS14]. A closer investigation of (2.7) reveals, that it is merely a statement of consistency of the restriction and lifting step: performing a restriction immediately after a lifting without time integration in between should return the original state. However, this constraint makes no statement about the closeness of the lifted point to the slow manifold. In the implicit equation-free methods (cf. Sec. 2.2) the constraint is relaxed, which makes the choice of lifting operators more robust. Another way to circumvent (2.7) is to use the constrained-runs scheme based on the zero-derivative principle (see [ZGKK09, VKR09, ZVG+12] and Sec. 2.4.1) to initialize the system on the slow manifold and compute the dynamics from there. We will present the implicit equation-free approach in the next section.

2.2 Implicit Equation-Free Methods

A major disadvantage of classical equation-free methods (cf. Sec. 2.1) is the crucial dependence on the lifting operator. It is supposed to initialize the system close to the unknown slow manifold which justifies the approximation of the flow on the slow manifold by the explicit macroscopic time stepper, i.e., $\Phi \approx P$. Even the check $\mathcal{R} \circ \mathcal{L} = I$ is not a sufficient condition for the lifting operator to initialize the system close to the slow manifold. It is only an approximation for the correct constraint $\mathcal{R} \circ \pi_\varepsilon \circ \mathcal{L} = I$, where π_ε denotes the stable fiber projection (see the discussion in Paper I and the end of Sec. 2.1 for details).

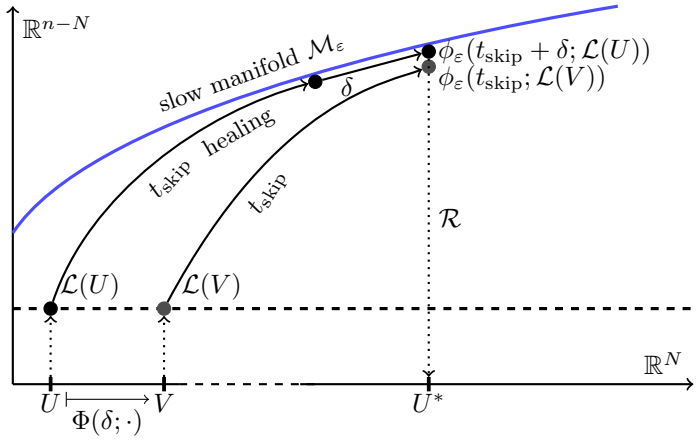

Figure 2.2: Sketch of the implicit equation-free scheme (2.8).

Different schemes have been investigated for initializing the system on the slow manifold, which can be rather complicated and numerically hard to solve in real-world applications (see e.g., Sec. 2.4.1 for the constrained runs scheme). An elegant alternative that can be easily implemented is the *implicit equation-free method*. The aim is the approximation of the flow Φ on the slow manifold based on the map P (cf. (2.6)) without the need to explicitly initialize the system close to the slow manifold. Instead, we utilize the fast attraction to the normally hyperbolic invariant manifold in order to obtain the flow on it.

The remainder of the section deals with the derivation of Φ which is sketched in Fig. 2.2. An important observation is, that Φ has to be defined implicitly. Assume, that the time-δ map on the slow manifold maps a macroscopic state U to another macroscopic state V. This V is yet unknown, since Φ is not available. We employ P in order to find V. Starting at U, we apply the lifting $\mathcal{L}$, evolve for a time $t_{\text{skip}}+\delta$ and restrict $\mathcal{R}$. The time t_{skip} is short compared to the characteristic time scale on the slow manifold and brings the system back to the slow manifold. It is called the healing time, since it "heals" the lifting error. The additional time δ is the time step on the slow manifold. Finally, the restriction $\mathcal{R}$ brings the state back to the macroscopic level. The whole path is described by $P(t_{\text{skip}}+\delta;U)=U^*$ (see (2.6) for the definition of P). Since we know by assumption, that V is the result of a time step δ of U on the slow manifold, we reach the same point U^* by applying $P(t_{\text{skip}};V)$ just for the healing time t_{skip}. Consequently, we can solve for the implicitly-defined V:

$$\begin{aligned} P(t_{\text{skip}}+\delta;U) &= P(t_{\text{skip}};V) \\ \text{and set} \qquad \Phi(\delta;U) &:= V. \end{aligned} \tag{2.8}$$

A Newton iteration is usually used to compute the implicitly-defined V. This concludes the definition of the slow flow Φ. It is shown in Paper I that this flow is exponentially close to the exact flow Φ_* on the slow manifold. The estimate

$$\|\Phi(\delta, U) - \Phi_*(\delta, U)\| \leq C \exp(-K t_{\text{skip}}), \tag{2.9}$$

with constants $C, K > 0$ makes this statement precise. Note, that a longer healing time t_{skip} gives a smaller error. By using the flow Φ on the slow manifold, it is possible to formulate an ODE in *healed variables* $U_{\text{healed}} = P(t_{\text{skip}}; U)$, i.e., an ODE describing the dynamics on the slow manifold, by

$$\frac{d}{dt}\mathcal{R}(\phi_\varepsilon(t_{\text{skip}}; \mathcal{L}(U))) = \frac{\partial}{\partial \delta}\mathcal{R}(\phi_\varepsilon(t_{\text{skip}} + \delta; \mathcal{L}(U)))\Big|_{\delta=0}. \tag{2.10}$$

The left-hand side is the time-derivative of the *healed* macroscopic quantity and the right-hand side describes the dynamics on the slow manifold projected to the macroscopic variables (see also Fig. 2.2). Note, that in contrast to previous approaches with a healing time, the healing is applied to both sides of the equation instead of just to the right-hand side (see, e.g., [GKT02]). Equation (2.10) can be used in higher-level tasks for coarse projective integration and coarse bifurcation analysis (cf. Sec. 2.3). The assumptions and proofs for the statements made above are discussed in detail in Paper I and are not repeated here. The main ideas are based on Fenichel's theory (cf. Sec. 1.3). The convergence proof makes use of the persistence of the slow manifold, the stable fiber projections and the existence of a slow flow on the manifold to obtain the exponential estimates.

To conclude this section, we note that implicit equation-free methods can be applied to the same problems as explicit equation-free methods. They put equation-free computations in an elegant and rigorous mathematical formulation and prevent the lifting errors, which are difficult to deal with otherwise. Note, that the implicit equation-free method computes the correct dynamics on the slow manifold but at points different from the user-provided points. This is due to the healing step that changes the value of the macroscopic variables. For numerical continuation and bifurcation analysis the dynamics at a user-defined point on the slow manifold is not required (see Paper I). If a point on the slow manifold with a certain value of the macroscopic quantity is needed anyway the method of "matching the restriction" can be used (see Sec. 2.4.3).

2.3 Higher-Level Tasks

After having defined a macroscopic time stepper it is possible to perform so-called higher-level tasks. These tasks perform computations known from low-

dimensional systems on the coarse level utilizing the equation-free methods and the macroscopic time stepper in particular. We are mainly interested in *coarse projective integration* and *coarse bifurcation analysis*.

2.3.1 Coarse Projective Integration

The goal of coarse projective integration is to find the macroscopic state $U(t_0 + \Delta t)$ from the initial condition $U(t_0)$ for a time Δt that is long compared to the slow time scale. This task could be done by the given macroscopic time stepper (2.4), but it would require a very long integration time, since we are interested in the slow dynamics. Instead, we can use short simulation bursts to gain information about the right-hand side F of the macroscopic dynamics. Using a Taylor approximation to linear order and the explicit (2.6) or implicit (2.10) formulation of equation-free methods, we obtain

$$\begin{aligned} &\text{expl.: } U(t+\Delta t) &&= U(t) + F(U(t))\Delta t, \\ &\text{impl.: } \mathcal{R}(\phi_\varepsilon(t_{\text{skip}}; \mathcal{L}(U(t+\Delta t)))) &&= \mathcal{R}(\phi_\varepsilon(t_{\text{skip}}; \mathcal{L}(U(t)))) + F(U(t))\Delta t. \end{aligned}$$

The macroscopic right-hand side is approximated as

$$\begin{aligned} &\text{expl.: } F(U(t)) &&= \frac{\mathcal{R}(\phi_\varepsilon(\delta; \mathcal{L}(U(t)))) - U(t)}{\delta}, \\ &\text{impl.: } F(U(t)) &&= \frac{\mathcal{R}(\phi_\varepsilon(t_{\text{skip}} + \delta; \mathcal{L}(U(t)))) - \mathcal{R}(\phi_\varepsilon(t_{\text{skip}}; \mathcal{L}(U(t))))}{\delta}. \end{aligned} \tag{2.11}$$

This method is called coarse projective integration, since it projects the coarse dynamics from a short scale (δ) into the future ($\Delta t > \delta$). Coarse projective integration is simply the well-known Euler iteration for the (unknown) macroscopic dynamics. It can be beneficially applied for saving computational time (in the case $\Delta t \gg \delta$) or for coarse backward integration, i.e., $\Delta t < 0$ (see also [GK04] and Paper I). A coarse projective integration with negative time step converges to sinks of the macroscopic dynamics and can therefore be used to gain information about otherwise inaccessible solutions. In order to save overall computation time, the computation of lifting and restriction operators has to be fast compared to the computation of a long macroscopic trajectory. Note, that the implicit formulation of equation-free methods turns for $t_{\text{skip}} = 0$ and $\mathcal{R} \circ \mathcal{L} = I$ into the explicit formulation. Therefore, implicit equation-free methods could be viewed as a generalization of the explicit equation-free framework.

2.3.2 Coarse Bifurcation Analysis

Bifurcation analysis is probably the biggest achievement in the field of dynamical systems. Despite its success bifurcation analysis is still limited to low-dimensional systems. Even for three-dimensional dynamical systems there is no complete list of generic bifurcations available yet. One of the major advantages of equation-free methods is the ability to perform bifurcation analysis on the macroscopic level of interest. Thereby, systems with high-dimensional phase space can be analyzed on the coarse level. All methods known from bifurcation theory (cf. Sec. 1.2) can be directly applied to equation-free computations by taking advantage of the macroscopic time stepper. The right-hand side F of the macroscopic system is obtained numerically (see (2.11)) and bifurcation analysis is applied to this function. Consequently, all evaluations of functions and Jacobians are performed by short simulation bursts of the microscopic model combined with the lifting and restriction operators.

In order to compare results of an implicit equation-free bifurcation analysis with experimential data or data obtained by direct numerical simulation of the system, one should use healed quantities. The Newton iterations in numerical continuation of equilibria converge to the root of (2.11) and a macroscopic value U is obtained. This state is in general not on the slow manifold. Therefore, one has to heal the state U, i.e., $U_{\text{healed}} = P(t_{\text{skip}}; U) = \mathcal{R}(\phi_\varepsilon(t_{\text{skip}}; \mathcal{L}(U)))$, in order to obtain a state on the slow manifold. Note, that in explicit equation-free computations there is no systematic way to compute healed quantities and the quality of the results depends crucially on a good choice of a lifting operator. Healed quantities and a comparison between explicit and implicit methods are discussed in detail in Paper I.

2.4 Existing Methods

Many algorithms and methods have been developed in the same spirit of equation-free methods in order to gain insight into the long-term behavior and the slow manifolds of dynamical systems. This section provides an overview about existing methods with sight on the relation to equation-free methods. The presented methods are restricted to those that have already been used in the context of equation-free methods. Other methods for multi-scale problems that solve special problems are not discussed in detail. Among those are methods for determining slow manifolds such as Quasi Steady-State Approximation (QSSA, [BH25]), Computational Singular Perturbation (CSP, [LG88, LG94]), Intrinsic Low-Dimensional Manifold (ILDM, [MP92]), Method of Invariant Manifolds

(MIM, [GK92, GK03]) and Straigthening Out Method (SO, [Mac04, KBS14]). In this section, we present the constrained runs scheme (in Sec. 2.4.1), the gap-tooth scheme (in Sec. 2.4.2) and the method of matching the restriction (in Sec. 2.4.3).

2.4.1 Constrained Runs Scheme

The *constrained runs scheme* (CRS) has been introduced and developed in [GK05, GKKZ05, ZGKK09, ZVG+12] as a method to numerically find slow manifolds. CRS has first been studied in the context of explicit slow-fast systems (cf. [GKKZ05, ZGKK09]) where the splitting into slow and fast variables is known. Afterwards, the method has been generalized to systems with mixed variables, i.e., both slow and fast, where it is known that a parametrization of the slow manifold by observables is available [ZVG+12].

The starting point for CRS is a general ODE system

$$\begin{aligned} \dot{x} &= f(x,y), \qquad x \in \mathbb{R}^{n_f}, \\ \dot{y} &= g(x,y), \qquad y \in \mathbb{R}^{n_s}, \end{aligned}$$

where $f : \mathbb{R}^{n_f} \times \mathbb{R}^{n_s} \to \mathbb{R}^{n_f}, g : \mathbb{R}^{n_f} \times \mathbb{R}^{n_s} \to \mathbb{R}^{n_s}$ are smooth functions and $\dot{}$ denotes the derivative w.r.t. time t. It is not necessary that x is fast and y is slow, but rather that the observables y parametrize the slow manifold, i.e., the slow manifold can at least locally be written as a graph $x = h(y)$.

The key insight for the constrained runs scheme is the *zero derivative principle* (ZDP) introduced by [Kre79] and independently by [Lor80]. The m-th ZDP algorithm approximates the slow manifold to increasingly higher order by solving the $m+1$-st zero derivative condition

$$\left(\frac{d^{m+1}x}{dt^{m+1}}\right)\Big|_{(x,y^*)} = 0 \tag{2.12}$$

for x keeping the observable y^* fixed. We denote the approximated graph of order m as $\bar{h}_m$. Note, that for $m = 0$ one recovers the quasi steady-state assumption (QSSA, [BH25]) $\dot{x} = 0$. Already from the QSSA it is clear that the obtained point is not exactly on the slow manifold since $\dot{x} = 0$ does not have to be fulfilled everywhere. Nevertheless, the accuracy for the approximation by ZDP is increasing with the order m as

$$\left\|\bar{h}_m(\cdot) - h(\cdot)\right\| = \mathcal{O}(\varepsilon^{m+1})$$

for an explicit slow-fast system with time scale separation ε.

The m-th constrained runs algorithm is definded by the map

$$L_m(x) = x - (-s)^{m+1} \left(\frac{d^{m+1}x}{dt^{m+1}} \right) \Bigg|_{(x,y^*)}, \tag{2.13}$$

where s is the iterative step size. It is easy to see that a fixed point $x^\#$ of the map L_m solves (2.12). It is shown in [ZVG+12], that under some conditions the functional iteration of (2.13) is stable, i.e., the eigenvalues of the linearization of L_m at $x^\#$ lie in the unit disk. In the case of an unstable fixed point, the authors of [ZVG+12] suggest the use of a Newton method instead. It is further explained in [ZGKK09], that a recursive projection method (RPM, [SK93]) or a Newton Krylov Generalized Minimal Residual Method (NK-GMRES, [Kel95, VKR09]) could be used to stabilize the algorithm or to speed up computations for only weakly stable algorithms.

In conclusion, CRS is a very useful algorithm to find points on the slow manifold while keeping an observable y^* fixed. The algorithm is reminiscent of the lifting operator in equation-free computations; given a macroscopic state y^* find a corresponding high-dimensional state (x, y^*) on the slow manifold. Therefore, CRS seems to be a good candidate to provide an otherwise hard-to-construct lifting operator. However, there are some drawbacks, which effectively prevent the use of CRS in an equation-free setup. First, the macroscopic variables in equation-free computations are not necessarily given by some of the variables in the ODE system. They are rather functions of many or all of the variables. In some cases a coordinate transformation of the ODE system could overcome this issue, but the computations can be very complicated in high-dimensional nonlinear systems. This is exactly what we wanted to avoid with the use of equation-free methods in the first place. Another limiting factor lies in the heart of the constrained runs scheme itself; the zero derivative principle. Typically, time derivatives have to be computed numerically in the equation-free framework. In particular in noisy systems this task can be difficult and becomes increasingly complicated for larger m in (2.12). The good numerical approximation of higher-order derivatives is a field in its own and the best algorithm depends on the problem at hand. These problems make the application of CRS very difficult in a real-world equation-free computation. Nevertheless, future research might find a way to beneficially apply CRS in the lifting step of equation-free computations.

2.4.2 Gap-Tooth Scheme

The *gap-tooth scheme* is the analog of coarse projective integration in the space domain. The method has been introduced in [KGH+03] and has been further developed in [SRK05, KS09]. The algorithm is briefly presented in this section.

We would like to study a microscopic model

$$\frac{du}{dt} = f(u), \qquad \text{or} \qquad \partial_t u = f(u, \partial_r u, \dots, \partial_r^d u, x), \tag{2.14}$$

where $u \in \mathbb{R}^n, n \gg 1$ is the microscopic variable, t denotes time, r denotes the space variable with highest-order derivative d, and f is the vector field. In both cases, we would like to solve the system in a large domain by running simulations only in small boxes. In the ODE case, spatial dependence is obtained by interpolation in space. We assume that a microscopic time stepper, i.e., a simulation, for (2.14) is available. We further assume, that the macroscopic model is given by a (one-dimensional) PDE for the macroscopic variable U of the form

$$\partial_t U(t, r) = F(r, U, \partial_r U, \dots, \partial_r^d U). \tag{2.15}$$

Also lifting and restriction operators are assumed to be available. In the first step, we would like to solve (2.15) for short times on a large domain. Since the interesting domain size is usually much bigger than the computationally accessible domain and the right-hand side F of (2.15) is not available, we would like to use the microscopic model (2.14) in small domains to gain information about the large domain.

The space is discretized as $r_j = jH$ with the large grid size H and we denote the macroscopic time $t = i\tau$ with macroscopic time scale τ. In a finite-difference scheme, we are interested in the gridded solution $\{U_j^i\}$ at grid nodes $U_j^i = U(i\tau, jH)$. Our goal is to simulate the model in small boxes $h \ll H$ centered at the grid points, i.e., we solve (2.14) in the *teeth* $[r_j - h/2, r_j + h/2]$. Then, we compute the solution in the *gaps* of size $H - h$ in between the teeth. The steps of the gap-tooth scheme are as follows:

1. Construct boundary conditions for the teeth using $\{U_j^i\}$.
2. Lift the coarse representation $\{U_j^i\}$ to initial data for each tooth.
3. Evolve (2.14) for time $t \in [0, \tau]$ in the teeth.
4. Restrict to find the coarse solution at $t = \tau$.

In the restriction step, the coarse variables have to be determined on the bigger boxes of size H by interpolation. This can be a linear interpolation between nodes as in coarse projective integration. But it can also be an interpolation by higher-order polynomials or splines in order to arrive at a certain smoothness that is determined by the specific problem.

This method allows one to obtain a macroscopic solution for large domains and short time using simulations for small domains and short time. Combining

the gap-tooth scheme with coarse projective integration enables one to solve for large domains and long time using simulations for small domains and short times. The combination of both is called *patch dynamics* (cf. [KS09, SRK09] for details).

2.4.3 Matching the Restriction

In equation-free computations it can be useful to find a microscopic state u on the slow manifold which has a certain macroscopic value U defined by the restriction operator $\mathcal{R}(u) = U$ (cf. [GKKZ05, ZVG+12] and Sec. 2.2). The goal of this method is reminiscent of the constrained runs scheme with the difference that U does not have to be a variable of the original dynamical system. The problem of finding u has been studied in [VSM+11, MSB+14]. Employing implicit equation-free methods (cf. Sec. 2.2 and Paper I) we solve

$$\mathcal{R}(\phi_\varepsilon(t_{\text{skip}}; \mathcal{L}(\tilde{U}))) = U \tag{2.16}$$

for $\tilde{U}$ and afterwards set $u = \phi_\varepsilon(t_{\text{skip}}; \mathcal{L}(\tilde{U}))$. The solution u is close to the slow manifold with error $\sim \exp(-Kt_{\text{skip}})$, where $K > 0$ is a constant.

2.5 Comparison to Other Methods and Critical Issues in Equation-Free Computations

The previous sections have shown that the equation-free framework is a useful tool to gain insight into otherwise inaccessible phenomena. The main advantages are 1) the computation of macroscopic solutions over macroscopic time scales (coarse projective integration); and 2) large spatial domains (gap-tooth scheme) by using microscopic simulations; and 3) the possibility for a macroscopic bifurcation analysis. Even for relatively simple systems where the computational cost is low, the conceptual advantage of a macroscopic bifurcation analysis is convincing. Nevertheless, it is worth mentioning that equation-free methods are not the only framework for performing multi-scale computations.

First, there are a number of classical approaches for obtaining coarse information of certain microscopic systems. Among the most successful approaches are the homogenization method [SP80, PBL78]; averaging and mean-field methods [Sta87]; and renormalization methods [Wil75]. These methods aim at deriving macroscopic equations from certain classes of fine-scale models in a systematic way. Due to the problems described in Chap. 2 this is not always possible

or the coarse model can only be constructed in certain cases. Therefore, it is worth studying a general framework. This general framework is provided by techniques that establish a so-called *closure-on-demand*, i.e., they provide the necessary information on the macroscopic level as it is needed by running microscopic models. The advantage is that detailed models, which are expensive to solve numerically, can be used in short time and small spatial domains in order to gain insight into the macroscopic domain. This multi-scale approach is maintained by a separation of time scales or spatial scales. The equation-free framework obtains this closure-on-demand by switching between levels using restriction and lifting operators allowing for the construction of the macroscopic time stepper (2.4). In equation-free methods, the macroscopic equations or even its properties are generally unknown. Attempts to decide on the nature of the macroscopic equations are formulated in the baby-bathwater scheme [LKGK03], which aims at finding the highest spatial order of the derivatives in a coarse PDE problem.

Another approach for multi-scale computations, that has been developed along the same ideas as the equation-free approach is the *heterogeneous multi-scale method* (HMM) [EE03, EEL+07]. The closure-on-demand is obtained by so-called *compression* and *reconstruction* operators that are the exact equivalents of the restriction and lifting operators in the equation-free context. Where equation-free methods focus on a general way to solve an unknown macroscopic equation, HMM takes a different point of view. The "heterogeneous" in HMM stems from the fact that different physical models are intended to be used on different scales. For example, the macroscopic level might be described by a PDE, which is assumed to be solvable by a numerical scheme. Nevertheless, a detailed description of a microscopic system might be needed in small domains to resolve the correct physical behavior. An example is crack formation, where the system dynamics can be described by a known coarse model but has to be defined on a fine scale close to the crack [EEH03]. HMM couples these two levels with different descriptions to an overall system. Examples are shown in [EE03] and called "dynamic homogenization".

Other methods that focus on the improvement of computation speed and stabilization of Newton iterations converging to unstable macroscopic states are the *extended multigrid method* [Bra02] and the *recursive projection method* [SK93], respectively. Both methods also map between macroscopic and microscopic levels, extrapolate microscopic computations in time and interpolate spatial scales to solve the macroscopic systems. All frameworks are developed in the same spirit of multi-scale systems and combining ideas from all methods could be very beneficial. Among other contributions, the HMM-FE method is an important application to engineering problems. It incorporates finite-element computations into the HMM framework (see [EEH03, EEL+07] for details). On the other hand, equation-free methods have been developed with a view on bifurca-

tion analysis [TQK00, RTK02], which is to some extent missing in HMM.

Due to the similarity of the described methods, there are problems that have to be solved in all the existing frameworks. The biggest problem is to construct good operators to initialize the microscopic system at a desired state. The situation has been significantly improved by the implicit equation-free methods (see Paper I) and the reduction of the lifting error. Another problem that goes along with bifurcation analysis is the determination of Jacobians needed in the corrector step of the continuation scheme. These Jacobians can be difficult to obtain for noisy systems (see Paper IV) and a lot of work has to be done to construct them reliably. It is important to notice that this problem does not only occur in stochastic systems, but also in deterministic systems that employ stochastic initialization of the microscopic state in order to compute ensemble averages, e.g., in molecular dynamics.

The ultimate goal in equation-free computations is the automatic determination of bifurcation diagrams without any choices left for the user except for adjusting parameters for the algorithm. This would push equation-free methods to a completely new level and would make them immediately applicable to realistic problems in industry. It would also allow one to develop a general purpose toolbox for equation-free computations that automatically runs bifurcation analysis for a given microscopic system on a macroscopic level. To achieve this goal, many attempts have been made in the recent past. The main missing ingredients for such an automatic algorithm are the automatic determination of lifting and restriction operators. Lifting operators can be constructed in some applications in a semi-automatic fashion by using combinations of reference states from previous microscopic simulations [SSGK10]. This is especially useful when performing pseudo-arclength continuation, where the microscopic states can be assumed to be close to the last one on the branch. A combination with implicit methods could obtain a reasonably stable algorithm to initialize a microscopic system consistent with the macroscopic scale in an automatic fashion. Nevertheless, these methods are far from being well-studied and a lot of research is needed to improve the applicability.

The other direction of defining an automatic restriction operator can be performed by manifold learning techniques that are able to determine the most relevant directions in phase space, thereby separating the directions on the slow manifold from the ones orthogonal to it. Since the slow manifold can be geometrically very complex, it is necessary to use non-linear manifold learning techniques. One very promising approach are diffusion maps [CLL+05, CL06], that approximate the distance of two points in Euclidean space by the corresponding distance determined by a "diffusion process". Diffusion maps effectively determine a low-dimensional description of the relevant dynamics in the high-dimensional phase space of the systems. In the terms of the equation-free

framework, diffusion maps describe a restriction operator. This is another brick in the puzzle to construct an automatic equation-free method. Due to their potential as restriction operators in equation-free computations, diffusion maps have been studied as part of this thesis and will be discussed in the next chapter.

Chapter 3

Diffusion Maps

"I have had my results for a long time: but I do not yet know how I am to arrive at them."
C. F. Gauss, in: The Mind and the Eye by A. Arber, 1954.

The challenge in big data sets is to extract relevant information from an overwhelming amount of data. A *data set*

$$X = \{x_i \in \mathbb{R}^n \mid i = 1, \dots, N\} \tag{3.1}$$

contains N *data points* x_i in n-dimensional space. These data points can be measurements of an experiment, e.g., N measurements of temperature and pressure of a gas ($n = 2$), or trajectories of a dynamical system (1.1) where N plays the role of time (cf. Paper V for this interpretation). For big data sets, i.e., either $N \gg 1$ or $n \gg 1$ or both $N, n \gg 1$, it is often difficult to extract the structure of the data in order to formulate and proof a scientific hypothesis. For simple data sets, e.g., $n = 2$, the data points can be visualized on a two-dimensional plot to study the structure and to fit functions to the data. In general, data can lie on a manifold that can be complicated to analyze. A standard example from manifold learning is the so-called swiss roll where N data points are sampled from the surface

$$(\theta \cos\theta,\, y,\, \theta \sin\theta) \in \mathbb{R}^3, \qquad y \in [-1, 1], \quad \theta \in [0, 4\pi], \tag{3.2}$$

embedded in three-dimensional space (see Fig. 3.1). Nevertheless, it is possible to find a two-dimensional representation of each point by using the angle θ and height y as coordinates. But, due to the non-linearity of the manifold, all linear projections to a low-dimensional space would result in a mixing of points.

The general problem of finding low-dimensional embeddings for $n > 3$ is even harder since an intuitive visualization of the manifold in three-dimensional space is lacking. One way to approach this problem is to investigate projections of the data onto suitable subspaces. Historically, the first step in this direction is formulated in Principal Component Analysis (PCA) [Pea01]. The *principal components* are the eigenvectors of a covariance matrix for the data. Hence, the first principal component points into the direction of the highest covariance of the point cloud and the second principal component in the direction of highest covariance orthogonal to the direction of the first principal component and so on. Let us be more specific and assume that the data is given as an $N \times n$ matrix X, where each row of X contains a measurement $x_i \in \mathbb{R}^n$ and the column mean is zero, i.e., without loss of generality the data is clustered around the origin. Note, that we use the same symbol X for the data set (3.1) and the data matrix, but the usage should always be clear from context. The corresponding symmetric covariance matrix $X^T X$ can be diagonalized and in the case of mutually different eigenvalues the first eigenvector w_1, i.e., the eigenvector corresponding to the largest eigenvalue, points into the direction of highest variance. Since $X^T X$ is symmetric, the eigenvectors can be chosen to be orthogonal to each other, even in the case of degeneracy. The *score*

$$t_{ik} = \langle x_i, w_k \rangle, \qquad i = 1, \dots, N, \quad k = 1, \dots, n$$

defined by the inner product $\langle \cdot, \cdot \rangle$ of the data point x_i and unit eigenvector w_k (also called weights) gives the component of x_i in the direction of w_k in the eigenbasis of $X^T X$. The transformation of the whole data set X into the new basis yields the $N \times n$ matrix $T = (t_{ik})$ that represents the data in the transformed basis. Instead of using an eigendecomposition of the covariance matrix, more efficient algorithms exist to perform a *singular value decomposition* (SVD) of X such that

$$X = U \Sigma W^T, \tag{3.3}$$

where U and W are the $N \times N$ and $n \times n$ orthogonal matrices of the left and right singular vectors, respectively. Σ is the $N \times n$ rectangular diagonal matrix of the singular values σ_i. Using (3.3), the orthogonality of U and that $\Sigma^T \Sigma = \Sigma^2 = \operatorname{diag}(\sigma_1^2, \dots, \sigma_n^2)$ is the $n \times n$ diagonal matrix with the squared singular values on the diagonal, one obtains

$$X^T X = W \Sigma^T U^T U \Sigma W^T = W \Sigma^2 W^T.$$

Therefore, the singular value decomposition yields the matrix of eigenvectors W and the eigenvalues $\lambda_i = \sigma_i^2$ of the covariance matrix. In particular for large data

matrices X, it can be computationally and numerically beneficial to use the SVD instead of constructing $X^T X$ explicitly and perform an eigendecomposition, since the covariance matrix $X^T X$ might have a bad condition number. Using (3.3) the score matrix is obtained by

$$T = XW = U\Sigma$$

where each row contains the representation of a measurement in the PCA eigenbasis. Despite the success of PCA in many applications over the last century, it is not able to extract non-linear information from the data set. In general, a k-dimensional manifold is at least locally diffeomorphic to $\mathbb{R}^k$. Therefore, in order to obtain a dimension reduction, the first k PCA components corresponding to the k largest eigenvalues of $X^T X$ should be sufficient to describe the manifold. Since PCA uses linear projections it cannot unroll the swiss roll as we will see in the example in Sec. 3.1. Here, non-linear manifold learning techniques are necessary to obtain low-dimensional non-linear embeddings and to gain information about the closeness of points, i.e., the geodesic distance of points along the unknown manifold.

Many attempts have been made recently to obtain low-dimensional embeddings of non-linear manifolds (see e.g., Isomap [TSL00, Iso], Local-linear embedding [RS00] and Laplacian Eigenmaps [BN02]). We will focus on diffusion maps [CLL+05, CL06] following the idea, that it might be advantageous in certain applications to use the so-called *diffusion distance* D_t between data points instead of the commonly used Euclidean distance. The diffusion distance is small, if the transition probability between the data points in a random walk defined by a Markov matrix is high (see Paper V for a detailed definition of D_t). The goal of the diffusion map algorithm is to find a non-linear transformation of the data into diffusion space $\Psi_1, \ldots, \Psi_n$ such that the diffusion distance D_t on the data set equals the Euclidean distance in the transformed space of the Ψ_i. In order to compute the diffusion map transformation, the $N \times N$ distance matrix d with elements

$$d_{ij} = \|x_i - x_j\|$$

is rescaled with a soft-thresholding of characteristic length ε, i.e., with a Gaussian kernel, to yield

$$A_{ij} = \exp\left(-\frac{d_{ij}^2}{\varepsilon^2}\right).$$

Note, that large distances d_{ij} are mapped to small positive values in A_{ij}. The Markov transition matrix M with elements

$$M_{ij} = \left(\sum_{j=1}^{N} A_{ij}\right)^{-1} A_{ij}$$

defines a random walk, i.e., a diffusion process, on the data set X. Here, $\sum_{j=1}^{N} A_{ij}$ is a normalization constant such that M_{ij} describes the probability to make a transition $i \to j$ in one time step. Consequently, the rows are normalized, i.e., $\sum_{j=1}^{N} M_{ij} = 1$ for all i, such that M is a stochastic matrix. It is used to compute the eigenvalues $\{\lambda_0, \ldots, \lambda_{N-1}\}$ and eigenvectors $\{\Psi_0, \ldots, \Psi_{N-1}\}$

$$M\Psi_j = \lambda_j \Psi_j.$$

Since M is a stochastic matrix, the eigenvalues λ_j are non-negative and the biggest eigenvalue is $\lambda_0 = 1$ due to the normalization of M. Without loss of generality, we assume that the eigenvalues are ordered, i.e., $\lambda_i \geq \lambda_j$ for $i < j$. The transformation of the data to the k-dimensional embedding is then given as

$$x_i \mapsto y_i = [\lambda_1^t \Psi_{1,i}, \ldots \lambda_k^t \Psi_{k,i}],$$

where t is the diffusion time. It is shown in [CLL+05] that the diffusion distance is given by the Euclidean distance

$$D_t^2(x_i, x_j) = \|y_i - y_j\|^2, \tag{3.4}$$

which is in general only an approximation if a low-dimensional embedding is used, i.e., $k < N - 1$. In comparison to PCA, which has no parameters to choose, diffusion maps has the characteristic scale ε and the diffusion time t as free parameters. A detailed description of the algorithm and possibilities to choose ε and t are given in Paper V and [MSLK14].

3.1 Examples

We now apply principal component analysis and diffusion maps to two educational test cases: 1) the initially introduced example of the two-dimensional swiss roll data set and 2) a one-dimensional spiral curve, both embedded into three-dimensional space. We compare the two algorithms with each other and show that diffusion maps are able to extract the low-dimensional data from non-linear manifolds in these examples, while PCA fails because of the linear projections.

We generate a swiss roll data set with $N = 2000$ data points using (3.2) and a spiral curve

$$(\sin\theta\cos(2\theta), \sin(2\theta), \cos\theta), \qquad \theta \in [0, 2\pi] \tag{3.5}$$

with $N = 500$ data points (see Fig. 3.1, top row). In a preparation step the data is centered, such that it has zero mean (see also the discussion about PCA above). Both manifolds are non-linear and as a consequence PCA fails to embed

the data set into low-dimensional space. In the case of the swiss roll the order of points is mixed and in the spiral curve an artificial intersection is observed in two-dimensional space (see Fig. 3.1, middle row). In contrast, diffusion maps are able to embed both data sets into low-dimensional space (see Fig. 3.1, bottom row). The swiss roll is 'unrolled' in diffusion map space and the spiral curve is transformed to a circle.

In conclusion, diffusion maps are advantageous over principal component analysis in detection of non-linear structures and extraction of relevant information from non-linear manifolds. Therefore, diffusion maps are capable of extracting relevant information from a big data set where intuitive insight about the macroscopically interesting quantities is missing. This is particularly interesting in applications for dynamical systems with time scale separation. Typically, an analysis of macroscopic quantities is necessary to obtain the relevant dynamics on the coarse level (see also the discussion on equation-free methods in Chap. 2). These low-dimensional quantities are often tailored to fulfill a specific purpose in the modeling procedure. Diffusion maps provide a more general and user-independent approach to obtain these coarse variables (see [MSLK14]). As such, diffusion maps might be used in an automatic equation-free framework to provide a canonical restriction operator (see also Chap. 6 for a discussion on future work) that is purely defined on the observed data and not on individual choices of the user. If future research provides a way to construct a lifting operator in the same user-independent spirit, it will be possible to extract coarse bifurcation diagrams from simulations and experiments without making any specific choices for the coarse variables. Before proceeding to the next section, we would like to remark, that the diffusion map algorithm is sensitive to the scaling of the variables, i.e., they should have numerical values of about the same magnitude, and to the sampling of the manifold, i.e., data should be available in the same amount from all parts of the manifold. These limitations have to be taken into account when working with diffusion maps. The problem of variables with different magnitude can usually be solved by a rescaling (see Paper V) and the problem of non-uniform distribution of data points can be tackled with methods developed in [CLL+05].

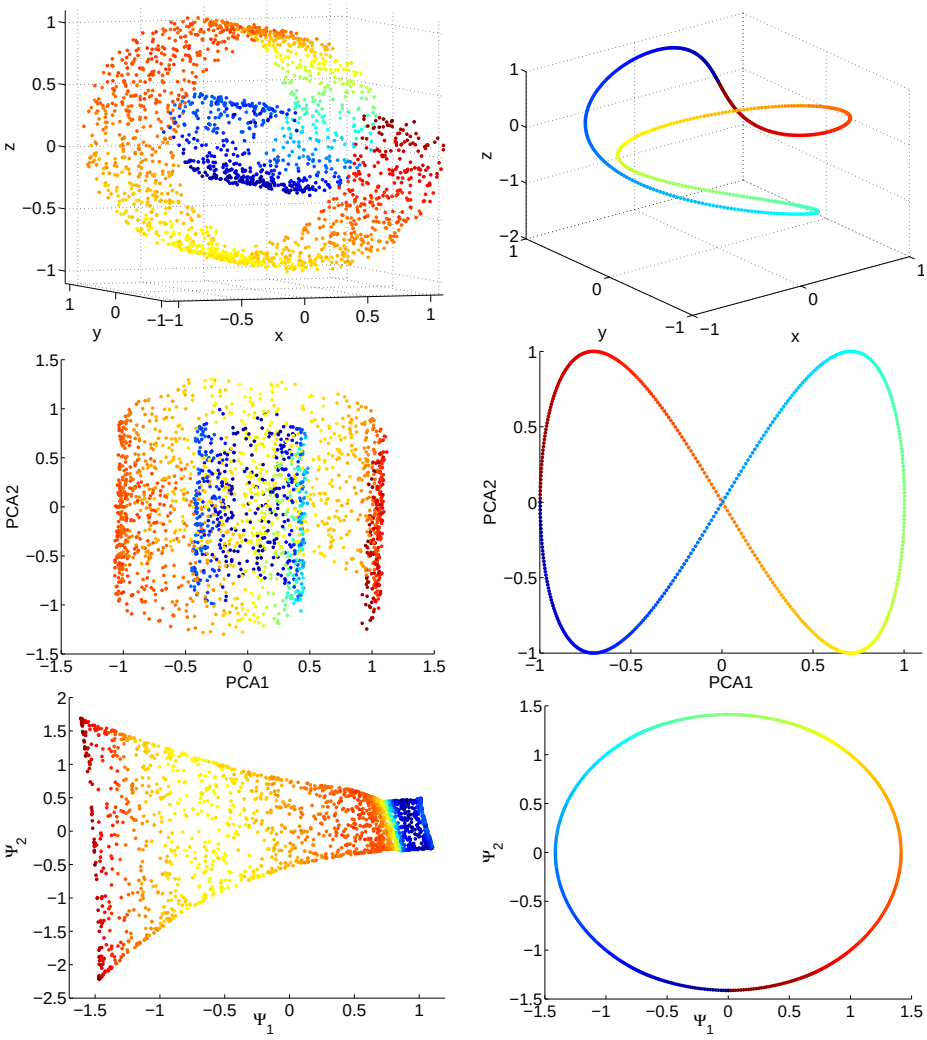

Figure 3.1: Embedding of the swiss roll data set (3.2) ($N = 2000$ data points, left column) and the spiral curve data set (3.5) ($N = 500$ data points, right column) in two-dimensional space using principal component analysis (middle row) and diffusion maps (bottom row). PCA is parameter-free and the parameters $\varepsilon = 0.17$, and $t = 3$ have been used for diffusion maps.

Chapter 4

Applications

"Practical application is found by not looking for it, and one can say that the whole progress of civilization rests on that principle."

J. Hadamard, in: Mathematical Circles Squared by H. Eves, 1972.

Equation-free methods have been developed with the idea to apply them to problems in physics and chemistry. Consequently, the first applications of the methods were lattice Boltzmann dynamics, kinetic Monte Carlo simulations and molecular dynamics (see [TQK00, KGH+03] for the first papers on equation-free methods). Since their introduction, equation-free methods have been further developed and applied to a huge variety of problems in multi-scale analysis of dynamical systems. Applications to traffic models (Paper I and Paper II), pedestrian dynamics (Paper V) and neural networks (Paper III and Paper IV) have been studied as part of this PhD thesis and the main results are discussed briefly in this section (see the corresponding papers in Appendix A for a detailed description).

4.1 Traffic Models

To understand and control traffic phenomena becomes increasingly important in our inter-connected world of the 21st century. In particular, traffic jams and safety are major topics with the goal to improve traffic for all traffic participants. Here, we focus on the discussion of traffic jams.

Traffic phenomena typically involve at least two scales. On the one hand, macroscopic descriptions are necessary in order to extract relevant information from detailed traffic models. Since traffic jams are large-scale phenomena, the positions and velocities of individual cars are less important for measuring traffic jams than densities of cars and the car flux on the road. On the other hand, the behavior of individual drivers on the microscopic scale might influence the formation and persistence of traffic jams. Numerous detailed models are available and in use to model individual car dynamics. On the other side of the scale, coarse descriptions by PDEs are used to model the dynamics of densities (not to be confused with the coarse, low-dimensional dynamics in equation-free methods). The goal of an equation-free analysis of traffic is to bridge this gap between the two scales; namely to gain insight into regimes where the derivation of macroscopic equations from detailed microscopic models is too difficult due to their complexity.

The studies in Paper I and Paper II use an optimal velocity model [OKW05, OWS10] for drivers on a ring road [BHN+95, SFK+08, TKF+13] to show how the new implicit equation-free method can be applied to traffic problems. The model is a compromise between a full-scale realistic model and an oversimplified model. It inherits several modeling assumptions: i) all drivers behave in the same way and have the same parameters, ii) there is only one-lane traffic and iii) there are no stochastic effects. These assumptions are used to provide a clear presentation of the implicit equation-free methods and to speed up simulations. All assumptions could be altered for future studies. One could for example study the influence of different preferred driving speeds or two-lane traffic.

In Paper I we present a two-parameter bifurcation analysis in the two parameters maximal velocity v_0 and headway h. Implicit equation-free methods are introduced for the first time and shown to significantly reduce the lifting error. It is argued that healed quantities, i.e., points after a transient that are close to the slow manifold, should be used for comparison with data obtained in measurements or from direct microscopic simulations. The main convergence result guarantees an exponentially small error in the difference between approximated and correct flow on the slow manifold. Furthermore, we compute relevant information for real-world applications: i) dependence of traffic jams on parameters, e.g., speed-limits, ii) unstable solution branches that act as boundaries between

basins of attraction for free flow and traffic jams and iii) coexistence of solutions, i.e., jams and free flow coexist.

4.2 Pedestrian Models

The same motivational arguments as in traffic models apply to the modeling of pedestrian behavior and pedestrian flow. Again, coarse quantities, e.g., density in crowds, indicate whether a crowd is close to a dangerous or undesired situation. Especially in emergency and evacuation scenarios, the control of pedestrian flow is of big importance for the security of people. Here, one typically wants to optimize evacuation times from certain areas and therefore maximize the pedestrian flux through exits. Another application to non-emergency situations is the pedestrian flow in canteens or shopping malls with the objective to either minimize or maximize the time a pedestrian spends in certain areas.

A widely used model for pedestrian dynamics is the social force model by Helbing and Molnár [HM95, Hel01], which models pedestrians as self-propelled particles interacting with each other via so-called social forces. The geometry of a building or room enters via repelling interactions with walls. For the situation of two pedestrian crowds in counter flow in a corridor with door in the middle the social force model has been applied in [CHS12] to study the onset of macroscopic oscillations with equation-free methods. The door width was used as the main bifurcation parameter giving rise to oscillations from a blocked state in a Hopf bifurcation. The same model as in [CHS12] is used in Paper V to study the emergent oscillations with diffusion maps (cf. Chap. 3). The paper has two main results: 1) the macroscopic bifurcation has been verified with diffusion maps showing that the main information could be extracted in an automatic, user-independent way and 2) a dimension reduction from 800 to 3 dimensions was performed using the diffusion map embedding.

4.3 Neuronal Networks

Besides particle-type models, equation-free methods can also be applied to weakly-stochastic systems that obtain a deterministic macroscopic dynamics. Neuronal networks, which are inherently stochastic, gained much attention over the past years. A widely-used class are artificial neural networks that had a huge significance as a model class for the development of learning algorithms.

We investigated a fairly well-studied biological model for learning in the neuronal

network of the barn owl's auditory system [KGvH99, KLWvH01, LKvH01] with equation-free methods in Paper III and Paper IV. The main results are 1) the coarse bifurcation analysis for the influence of the learning window using implicit equation-free methods (see also Paper I) and 2) the observation of traveling waves in the synaptic connectivity matrix. The analysis of the coarse bifurcation was made possible by equation-free methods defining a suitable periodicity measure for the connectivity matrix. This slowly-varying one-dimensional quantity was used as a macroscopic variable in a numerical continuation procedure which would be impossible to perform in the 8400-dimensional stochastic dynamical system for the synaptic strengths. The main obstacle here is the noise on the synaptic level which makes it almost impossible for classical continuation software to continue stationary solutions with direct microscopic simulation and to extract coarse bifurcation diagrams in a post-processing step. Since the dynamics behaves nearly deterministic on the macroscopic scale equation-free methods could be used to track solution branches up to the accuracy determined by the noise. The observation of traveling waves in the microscopic model was possible by long-term simulations. Their prediction is the outcome of a detailed study of the model and has to be verified by other groups in experimental studies.

Chapter 5

Conclusion

"If I have seen further it is by standing on the shoulders of giants."
I. Newton, 1676.

In Chap. 1 an introduction to dynamical systems with separation of time scales has been presented. The key results from Fenichel's theory [Fen79] have been reviewed in order to establish notation and to introduce the theoretical basis for the analysis in the following chapters. Chap. 2 presented the main topic of the thesis: the equation-free framework introduced by Kevrekidis and co-workers [KGH+03]. The fundamental ideas of equation-free computations and the state-of-the-art of existing methods have been reviewed in order to distinguish previous work from the contributions on *implicit* equation-free methods developed in this PhD thesis. Furthermore, important concepts of equation-free computations have been introduced in order to give the reader an easy entrance to the applications following in the articles about the optimal velocity model (Paper I and Paper II) and the barn owl's auditory system (Paper III and Paper IV) in Appendix A. Chap. 3 reviewed methods on dimensionality reduction and manifold learning. In particular, the linear method of principal component analysis has been compared with the non-linear manifold learning technique of diffusion maps. The presented examples on the swiss roll and spiral curve data sets demonstrated the ability of diffusion maps to extract the geometry of non-linear manifolds and prepared for the more complicated analysis of pedestrian

dynamics in Paper V. Following the general discussion about the equation-free framework and the diffusion map algorithm, the main results on the applications in the papers have been discussed in Chap. 4. This was meant to give the big picture of the application-wise research performed during the work for the PhD thesis without going into too much detail. These details are supplemented in the research papers in Appendix A, which form the main part for assessment of the research outcome of the PhD studies.

In conclusion, the equation-free framework has shown to be very versatile and furthermore, that it can be applied to many different areas to gain a qualitative and quantitative understanding of the system behavior. The work has shown that implicit equation-free methods [MSB+14] have a lot of potential in multi-scale modeling, especially in systems which are difficult to study with conventional methods. The original equation-free idea has been extended by applying the lift-evolve-restrict scheme (2.6) to both sides of the macroscopic equation, consequently making all integration methods implicit. This greatly improved the applicability to real-world problems as the lifting error was significantly reduced by estimating the dynamics on the slow manifold (cf. Figure 6.2 in Paper I). For the cases of finding equilibria and finding a lifted state on the slow manifold corresponding to a certain restricted state, implicit methods have already been used in [VSM+11] (called InitMan, see also the discussion in Paper I). The implicit methods presented in [MSB+14] extend these methods by defining the flow implicitly in general and giving convergence results. The obtained bifurcation diagrams (see Figure 6.1 in Paper I) agree perfectly with the results from direct numerical simulations and continuation of the full microscopic optimal velocity model and are to great extent independent of the lifting operator.

In many applications, the possibility to compute coarse bifurcation diagrams is of particular interest as they give information about the long-term behavior and stability regions for the underlying system. In this work, the other main advantage of equation-free computations for applications, namely the speed-up of computations using coarse projective integration, has not been discussed in detail. This was mainly because we focussed on the theoretical basis of equation-free methods and we investigated microscopic models that have been reasonably low-dimensional (8400 dimensions in the case of the barn owl's auditory system, 120 dimensions in the optimal velocity model) such that simulations could be performed on time scales, that are accessible by direct simulations. This would not be the case in large-scale simulations, e.g., industrial finite-element models, and here, coarse projective integration is a way to keep computation time short.

The study of diffusion maps has been included to make a first step into the direction of a user-independent formulation of the equation-free framework. As stated in detail in Chap. 3 and in the discussion about future research directions

in Chap. 6, diffusion maps could be used as a canonical restriction operator. Nevertheless, the missing and more complicated part in the development of a general equation-free formulation is a generic lifting operator. Ideas on how to construct such a generic lifting procedure are discussed in the next chapter.

Chapter 6

Future Research Directions

"Science is built up with facts, as a house is with stones. But a collection of facts is no more a science than a heap of stones is a house."

H. Poincaré, Hypotheses in Nature, 1913.

Before closing the thesis I would like to give an outlook on possible future research directions. This overview is definitely not exhaustive and is only meant to give an idea. As equation-free methods are still a young research field, there are many possibilities for future research.

Methods The main part of the thesis deals with equation-free methods. It is pointed out in Chap. 2 that problems arise in equation-free methods in the definition of lifting and restriction operators. These operators are not predefined in the framework and have to be supplemented by each user. Therefore, they are highly subjective and the finding of suitable operators usually takes time and makes an application as a toolbox for engineering purposes complicated. An option for providing a generic restriction operator, i.e., an automatic way to construct macroscopic variables from a microscopic state, could be provided by diffusion maps (cf. Chap. 3). Diffusion maps are certainly not the only manifold learning method and many different methods for dimension reduction (see the

discussion in Chap. 3) can be used as a generic restriction. Since basically all algorithms for non-linear manifold learning depend on parameters, e.g., the characteristic length scale ε in the diffusion map algorithm, this only consititutes a semi-automatic restriction. The combination of diffusion maps with equation-free techniques and the detailed study of diffusion maps as restriction operators would be one direction of future research.

Even more difficult is the construction of an automatic lifting as it is inherently underdetermined (one-to-many operation). Here, knowledge from previous states in a numerical continuation scheme might be used to construct physically-relevant microscopic states. Little has been done in that direction so far (see [SSGK10] for an approximation of an "inverse diffusion map") and much more research is needed in finding generic lifting operators. Another promising candidate for a generic lifting operator could be the constrained runs scheme (see Sec. 2.4.1). This would conclude all the necessary ingredients for a first study on a fully-automatic equation-free method.

Another methodological improvement is necessary in the case of stochastic systems. Here, Barkley, Kevrekidis and Stuart [BKS06] have already done some research that resulted in the formulation of moment maps. Avitabile, Hoyle and Samaey [AHS14] used this method to study an agent-based model for consumer lock-in. The idea is to choose low-order moments of a probability distribution as macroscopic variables for stochastic systems. This method could be combined with implicit equation-free methods (see Paper I) to improve the applicability to more complicated models.

Applications There is a broad spectrum of possible future applications for equation-free methods. The introduced implicit equation-free methods could be used to further investigate the already introduced models with respect to different aspects. This could be changing the behavior of cars in the optimal velocity model (see Paper I and Paper II) such that drivers have an individual preferred driving speed drawn from some probability distribution. The influence of the changes on the bifurcation diagrams and therefore the jam formation would be the main focus of these investigations.

For the pedestrians model, other room layouts and geometries could be studied. This is especially important for evacuation scenarios, where buildings have to be evacuated as quickly as possible in case of emergency. The equation-free methods can help to extract relevant macroscopic dynamics and this could be combined with optimization methods to adjust room layouts such that the evacuation time is minimized. Furthermore, pedestrian and traffic models could be coupled to improve the applicability to real-world networks and to model

realistic scenarios for cities.

There is also the possibility to further investigate neuronal networks. One further application is the olfactory system. It is shown in [Ell08] that odor discrimination is basically a macroscopic process and the corresponding bifurcation diagrams could help in designing artificial noses, that could be used for instance in the detection of drugs and explosives at airports.

Experiments Another interesting challenge is to apply equation-free methods to experiments. In [BSS+13] a beam pendulum with impacts has already been studied in an equation-free fashion. Nevertheless, much work has to be done in order to obtain reliable numerical methods that can handle the noise present in all real-world systems. Equation-free experiments are in general an interesting class to investigate. From an abstract point of view, the restriction operator plainly constitutes the measured quantity and the lifting operator is related to a certain control of the system. In order to perform an on-line equation-free bifurcation analysis in experiments, a feedback mechanism to the system is needed to be able to implement a Newton-like algorithm for finding branches. Especially the detection of unstable branches poses many challenges.

These experimental techniques could be applied to pedestrian problems, e.g., room evacuation with obstacle in front of the exit. Pre-studies have shown that a clever placement of a triangular obstacle in front of emergency exits could improve the flow. Further, hysteresis states are also observed in numerical simulations that are related to group effects (see [SSM+14, STS+14]) which have to be verified in pedestrian experiments. Furthermore, existing models could be analyzed equation-free and subsequently be compared to existing experimental data, e.g., to the geometry of an annulus and pedestrian counter-flow presented in [MGM+12, JARLP12].

Appendix A

Papers

"I have tried to avoid long numerical computations, thereby following Riemann's postulate that proofs should be given through ideas and not voluminous computations."

D. Hilbert, Report on Number Theory, 1897.

This appendix includes the scientific publications that have been written during the course of the PhD studies. They are attached to give the evaluation committee and other readers a complete overview about the scientific outcome and enable them to judge the studies. All papers are referenced in the main text and are supposed to supplement the thesis with detailed information. Where the main text is meant as an overview and introduction into the field of equation-free methods and multi-scale analysis in general, the papers provide the reader with detailed results and proofs.

With this layout of main text plus papers in the appendix, I hope to give the reader a good introduction to the field while at the same time keeping unnecessary repetition of text and results at a minimum. For the convenience of the reader, the papers are included in the style of the journal they are published in or submitted to. Each paper is preceded by a short resumé, putting it into the context of the thesis and highlighting the main results.

I Implicit Methods for Equation-Free Analysis: Convergence Results and Analysis of Emergent Waves in Microscopic Traffic Models

The paper on implicit equation-free methods [MSB+14] contains the main mathematical result of the thesis. It introduces a general implicit formulation for the macroscopic time stepper into the framework of equation-free methods and gives error estimates for the approximated flow on the slow manifold. This formulation results in a reduction of the lifting error by estimating the macroscopic dynamics on the slow manifold. The presented formalism eases the application of equation-free methods, since no additional algorithms, e.g., the zero-derivative principle, are necessary to initialize the system on the slow manifold. The article also puts the healing step, often implemented in equation-free methods as a workaround to obtain reasonable results, on a mathematically rigorous foundation.

The theoretical results are applied to circular traffic flow modeled with an optimal velocity model. A detailed coarse bifurcation analysis, first in one and than in two parameters, for the formation of traffic jams is presented and adds a macroscopic interpretation to the study of traffic problems. The research presented in the paper opens up for further developments, both theoretical and in applications (see also Chap. 6). Theoretical considerations include the construction of an automatic equation-free method (cf. the discussion in Sec. 2.5 and Chap. 6). On the application side, the extension of the algorithms to more complex traffic networks and the combination of car and pedestrian traffic pose new challenges.

At the hand-in date of the thesis the paper has been accepted for publication in the SIAM Journal on Applied Dynamical Systems.

Implicit Methods for Equation-Free Analysis: Convergence Results and Analysis of Emergent Waves in Microscopic Traffic Models

Christian Marschler*, Jan Sieber†, Rainer Berkemer‡, Atsushi Kawamoto§, and Jens Starke¶

Abstract. We introduce a general formulation for an implicit equation-free method in the setting of slow-fast systems. First, we give a rigorous convergence result for equation-free analysis showing that the implicitly defined coarse-level time stepper converges to the true dynamics on the slow manifold within an error that is exponentially small with respect to the small parameter measuring time scale separation. Second, we apply this result to the idealized traffic modeling problem of phantom jams generated by cars with uniform behavior on a circular road. The traffic jams are waves that travel slowly against the direction of traffic. Equation-free analysis enables us to investigate the behavior of the microscopic traffic model on a macroscopic level. The standard deviation of cars' headways is chosen as the macroscopic measure of the underlying dynamics such that traveling wave solutions correspond to equilibria on the macroscopic level in the equation-free setup. The collapse of the traffic jam to the free flow then corresponds to a saddle-node bifurcation of this macroscopic equilibrium. We continue this bifurcation in two parameters using equation-free analysis.

Key words. equation-free methods, implicit methods, lifting, traffic modeling, optimal velocity model, traveling waves, stability of traffic jams

AMS subject classifications. 65P30, 37M20, 37Mxx, 34E13

1. Introduction.

When one studies systems with many degrees of freedom, for example, systems with a large number of particles or interacting agents, one is often interested not so much in the trajectories at the microscopic level (that is, of individual particles), but in the behavior on the macroscopic scale (of the overall distribution of particles). The classical example is the motion of molecules of a gas, resulting in the laws of thermodynamics. In this classical case the macroscopic description is derived in statistical mechanics from knowledge about the microscopic behavior through time scale separation. Other important examples are emerging patterns in physical, chemical, and biological systems, e.g., Rayleigh-Bénard convection rolls [32], the Belousov-Zhabotinsky reaction [3, 44], and stripes on zebra skin or patterns on butterfly wings [41]. A common approach in the physics literature to deriving macroscopic descriptions are the so-called adiabatic elimination or the slaving principle [15, 16]. These concepts are related to the theorems in the mathematical literature about reductions to center manifolds or slow manifolds [7, 20, 40].

For systems where no explicit macroscopic description can be derived from microscopic models, Kevrekidis and coworkers proposed that, if the number of particles is moderate, then

*Department of Mathematics, Technical University of Denmark, Matematiktorvet 303B, DK-2800 Kgs. Lyngby, Denmark (c.marschler@mat.dtu.dk).

†College of Engineering, Mathematics and Physical Sciences, University of Exeter, North Park Road, Exeter (Devon) EX4 4QF (j.sieber@exeter.ac.uk).

‡AKAD University of Applied Sciences, Maybachstrasse 18-20, D-70469 Stuttgart, Germany (rainer.berkemer@akad.de).

§Toyota Central R&D Labs., Inc., Nagakute, Aichi 480-1192, Japan (atskwmt@mosk.tytlabs.co.jp).

¶Department of Mathematics, Technical University of Denmark, Matematiktorvet 303B, DK-2800 Kgs. Lyngby, Denmark (j.starke@mat.dtu.dk).

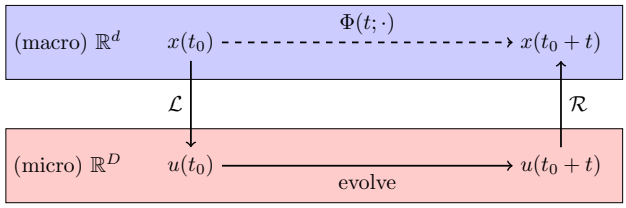

Figure 1.1. *Sketch of the macroscopic time stepper $\Phi(t;\cdot)$. The macroscopic state $x(t_0)$ is mapped to a microscopic state $u(t_0)$ by using the lifting operator $\mathcal{L}$. The available microscopic time stepper is used to evolve the system to the microscopic state $u(t_0+t)$, which is mapped to a macroscopic state $x(t_0+t)$ using the restriction operator $\mathcal{R}$. This procedure constitutes the coarse-level time stepper $\Phi(t;\cdot)$.*

it is sometimes possible to skip the derivation of a macroscopic description by performing the analysis of the dynamics in the macroscopic scale directly. This approach relies on evaluating short bursts of appropriately initialized simulations of the microscopic model (see, for example, [22, 23, 24] for recent reviews). It is called *equation-free* because it assumes that the macroscopic model exists but is not available as an explicit formula. Equation-free methods are particularly appealing if either explicit macroscopic descriptions are unavailable, or one wants to study the underlying system near the boundary of validity of its macroscopic description (for example, as one decreases the number of particles, finite size effects may start to appear as small corrections to the macroscopic model). Equation-free analysis has been applied for a large class of multiscale models that roughly fit the description of *singularly perturbed systems* [9] in a broad sense (see motivation in [24]), such as stochastic systems [28, 37], agent-based models [5, 6, 14], molecular dynamics [4] or neural dynamics [26, 33], to perform high-level tasks such as bifurcation analysis, optimization or control design [8, 36].

The basic building block of equation-free analysis is an approximate coarse-level time stepper $\Phi(t;\cdot)$ for short times t (compared to the slow time scale) in the phase space of macroscopic variables (say, $\mathbb{R}^d$). This coarse-level time stepper is typically composed of three steps: *lift* (operator $\mathcal{L}$), *evolve*, and *restrict* (operator $\mathcal{R}$), as shown in Figure 1.1. To compute the map $\Phi(t;x)$ on a given macroscopic state $x \in \mathbb{R}^d$, one has to apply a lifting operator $\mathcal{L}$ to map x to a microscopic state $u \in \mathbb{R}^D$ (typically, $D \gg d$); then one runs the microscopic simulation for the time t; and finally one maps the end state of the microscopic simulation back into $\mathbb{R}^d$ using a restriction operator $\mathcal{R}$. A proof of any claim that this would be a good approximation of the true dynamics of the macroscopic variable x for a given example will have to invoke the following sequence of arguments. Initially assume that the microscopic system is a slow-fast system with a transversally stable slow manifold, for which the macroscopic quantity x is a coordinate. The first question is then: does the approximate coarse-level time stepper Φ converge to the true dynamics on the slow manifold in the limit $\varepsilon \to 0$, where ε is the parameter measuring the time scale separation? In addition to the case discussed here, equation-free analysis is also applied to high-dimensional, stochastic (or chaotic) systems showing macroscopic behavior because the dynamics of the microscopic degrees of freedom averages out rapidly [2, 38, 34]. In these cases another question must be addressed: in which sense is the averaging process approximating a classical slow-fast system?

1.1. An implicit coarse-level time stepper. Before equation-free analysis can be performed, one must find the restriction and lifting operators $\mathcal{R}$ and $\mathcal{L}$. Figure 1.1 suggests the relation $\Phi(t;\cdot) = \mathcal{R} \circ \text{evolve} \circ \mathcal{L}$. However, this will not approximate the true macroscopic flow in general. Why? Let us assume that the microscopic system is slow-fast and the macroscopic system corresponds to the slow flow on the slow manifold in the coordinate x. Then an arbitrary choice of $\mathcal{L}$ and $\mathcal{R}$ does not lead to a coarse time-stepper Φ which approximates the slow flow in any way, even in the limit of infinite time scale separation ($\varepsilon \to 0$). The source of the error is an initialization of the microscopic system away from the slow manifold. One relies on the separation of time scales in a so-called healing step to reduce this error. However, in most reviews this healing is applied inconsistently [22, 23, 24]. That is, healing would not lead to Φ converging to the true slow flow in the limit of infinite time scale separation, even in the ideal case of a slow-fast system. A consistent way to perform healing are so-called *constrained-runs* corrections after lifting, developed in [12, 42, 43]. These papers developed schemes of increasing complexity to compensate for this error source.

An alternative, explained in Section 2, is to use an implicitly defined coarse-level time stepper Φ, where the slow flow is not measured at predetermined points in space but rather at healed points. In the special case of computation of equilibria, the use of the implicit time stepper reduces to the formula introduced as the "third method" by Vandekerckhove *et al* [39]. In Section 3, we give a detailed proof of the convergence of the implicitly defined coarse-level time stepper Φ to the flow on the slow manifold, answering the question of convergence for the implicit time stepper. The approximation error of Φ (under some transversality conditions) is exponentially small in the parameter ε measuring the time scale separation. Our theorem does not require that the time scale separation parameter ε approach zero, merely that it be sufficiently small. The precise statement is then that the error is of order $\exp(-Kt_{\text{skip}})$, where K is the rate of attraction transversal to the slow manifold and t_{skip} is the healing time. In Section 4 we discuss the assumptions and consequences of the convergence theorem and compare it to other results in the literature.

1.2. Macroscopic behavior of a microscopic traffic model. In Section 5 and Section 6 we apply the implicit coarse time stepper to a traffic modeling problem that fits into the framework of equation-free analysis: a large number of cars (the microscopic particles) on a circular road that interact with each other, resulting in so-called phantom jams moving slowly along the road against the direction of traffic, i.e., forming a traveling wave at the microscopic level.

The mathematical modeling and analysis of traffic flow dynamics has a considerable history (see, e.g., [17, 29, 31] for reviews). Macroscopic traffic models use partial differential equations, such as Burger's equation [29], for modeling the flow. They model the density of cars as a continuous quantity to directly formulate macroscopic equations for density and flux along the road. In contrast, microscopic particle models (deterministic [1] or stochastic [19, 35]) can be used to describe the behavior of individual cars or drivers. An advantage of microscopic models is that parameters can be assigned directly to the individual drivers' behavior (for example, aggressiveness, inertia, or reaction delay) such that these parameters' influence and the trajectories of individual cars can be investigated. Another use of microscopic models is to test the effects of new devices for individual cars, for example, cruise control, on the overall

traffic prior to their implementation in real traffic. In this paper we use the optimal velocity model [1] as an example of an underlying microscopic model. The optimal velocity model results in a set of coupled ordinary differential equations, but despite its simplicity it can reproduce the phenomenon of phantom traffic jams. An advantage of choosing the optimal velocity model is that we have guidance from the results of direct bifurcation analysis of the full microscopic system when only a few cars are involved [11, 30] as well as from perturbation analysis based on the discrete modified Korteweg–de Vries equation [10]. Direct bifurcation analysis of the microscopic system becomes infeasible when the number of cars gets large. Furthermore, it is difficult to analyze macroscopic quantities for which typically no equations are explicitly given such as the mean and standard deviation of headways or densities of cars. In Section 6 we show how this difficulty can be tackled by using equation-free methods for the bifurcation analysis on a macroscopic level.

In Section 7 we summarize the obtained results and give an overview of open problems.

2. Nontechnical description of general equation-free analysis with implicit lifting.

Equation-free analysis as described by [23] is motivated by ideas from the analysis of slow-fast systems: one assumes that on a long time scale the dynamics is determined by only a few state variables and the other state variables are *slaved*. Mathematically this means that the flow of a high-dimensional system under study converges rapidly onto a low-dimensional manifold on which the system is governed by an ordinary differential equation (ODE). In many practical applications convergence is achieved only in the sense of statistical mechanics (the effects of many particles averaging out; see [2, 6]). We give our description and subsequent convergence proofs of equation-free analysis using the terminology of slow-fast systems with transversally stable slow manifolds following the notation of [9]. The traffic problem discussed in Section 5 and 6 does not require the notion of weak (averaged) convergence.

2.1. The notion of a slow-fast system.

Let

$$\dot{u} = f_\varepsilon(u) \tag{2.1}$$

be a smooth dynamical system defined for $u \in \mathbb{R}^D$, where f_ε depends smoothly on the parameter ε. We assume that ε is a *singular perturbation parameter*. This means that the flow M_ε generated by (2.1),

$$M_\varepsilon : \mathbb{R} \times \mathbb{R}^D \to \mathbb{R}^D, \qquad (t; u) \mapsto M_\varepsilon(t; u)$$

has a whole smooth d-dimensional submanifold $\mathcal{C}_0$ of equilibria for $\varepsilon = 0$: if $u \in \mathcal{C}_0$, then $M_0(t; u) = u$ (and, thus, $f_0(u) = 0$) for all t. The dimension d is the number of slow variables. In the notation of singular perturbation theory, t measures the time on the *fast* time scale. We assume that this manifold $\mathcal{C}_0$ is transversally uniformly exponentially stable for $\varepsilon = 0$, which corresponds to the stable case of Fenichel's geometric singular perturbation theory [9]. For this case we know that the flow $M_\varepsilon(t; \cdot)$ has a transversally stable invariant manifold $\mathcal{C}_\varepsilon$ for small nonzero ε, too. This manifold $\mathcal{C}_\varepsilon$ is called the slow manifold, and the flow M_ε, restricted to $\mathcal{C}_\varepsilon$, is called the slow flow. For the traffic problem the time scale separation is present as demonstrated numerically later in Section 5.2.

2.2. Lifting, restriction, and time stepping. The equation-free approach to coarse graining [23] does not require direct access to the right-hand side f_ε of the microscopic system (2.1) but merely the ability to evaluate $M_\varepsilon(t;u)$ for finite positive times t (typically $t \ll 1/\varepsilon$ in the fast time scale t) and arbitrary u. It also relies on two smooth maps that have to be chosen beforehand:

$$\begin{aligned} \mathcal{R} &: \mathbb{R}^D \to \mathbb{R}^d && \text{the } \textit{restriction} \text{ operator,} \\ \mathcal{L} &: \mathbb{R}^d \to \mathbb{R}^D && \text{the } \textit{lifting} \text{ operator.} \end{aligned}$$

In the optimal velocity model discussed in Section 6, $\mathcal{R}$ is chosen as a mapping from headway profiles to the standard deviation σ and $\mathcal{L}$ constructs a headway profile by using σ (cf. (6.3) and (6.4)).

The basic idea underlying [23] is that one can analyze the dynamics of (2.1) on the slow manifold $\mathcal{C}_\varepsilon$ by studying a map in the space of restricted variables x in the domain of $\mathcal{L}$ (called $\operatorname{dom}\mathcal{L} \subset \mathbb{R}^d$) of the form (cf. Figure 1.1)

$$\textit{Lift} \quad \to \quad \textit{Evolve} \quad \to \quad \textit{Restrict},$$

or, to be precise, the map

$$P_\varepsilon(t;\cdot) : x \mapsto \mathcal{R}(M_\varepsilon(t;\mathcal{L}(x))) = [\mathcal{R} \circ M_\varepsilon(t;\cdot) \circ \mathcal{L}](x) \tag{2.2}$$

for selected times $t \ll 1/\varepsilon$. The central question is: how can one compose a macroscopic time stepper, that is, an approximate time-δ map $\Phi(\delta,\cdot) : \mathbb{R}^d \to \mathbb{R}^d$, using coordinates in the domain of $\mathcal{L}$ for the flow M_ε restricted to $\mathcal{C}_\varepsilon$? One important observation is that this map Φ must be defined implicitly. Figure 2.1 shows how one can define a good approximate time-δ map $\Phi(\delta;\cdot)$. It contains an additional parameter t_{skip}, called the *healing time* in [23]. This healing time must be applied to both the argument x and the result y of Φ. Thus, $\Phi(\delta;\cdot)$ is given implicitly by solving

$$\begin{aligned} P_\varepsilon(t_{\text{skip}};y) &= P_\varepsilon(t_{\text{skip}}+\delta;x), && \text{that is,} \\ \mathcal{R}(M_\varepsilon(t_{\text{skip}};\mathcal{L}(y))) &= \mathcal{R}(M_\varepsilon(t_{\text{skip}}+\delta;\mathcal{L}(x))) \end{aligned} \tag{2.3}$$

for y, and setting $\Phi(\delta;x) := y$. Under some genericity conditions on $\mathcal{R}$, $\mathcal{L}$, and M_ε the order of approximation for Φ is exponentially accurate for increasing t_{skip} if we assume that $\varepsilon t_{\text{skip}}$ and $\varepsilon(t_{\text{skip}}+\delta)$ are bounded:

$$\|\Phi(\delta;x) - \Phi_*(\delta;x)\| \le C\exp(-K\,t_{\text{skip}}). \tag{2.4}$$

In this estimate $K > 0$ and $C > 0$ are constants that depend only on a uniform upper bound T_{up} for $\varepsilon t_{\text{skip}}$ and $\varepsilon(t_{\text{skip}}+\delta)$. The flow Φ_* is the exact flow M_ε, restricted to the slow manifold $\mathcal{C}_\varepsilon$, in a suitable coordinate representation in $\operatorname{dom}\mathcal{L}$. The same estimate holds also for the derivatives of Φ with respect to the initial value up to a fixed order (with more restrictive conditions on ε). So,

$$\|\partial_2^j\Phi(\delta;x) - \partial_2^j\Phi_*(\delta;x)\| \le C\exp(-Kt_{\text{skip}})$$

(possibly with other constants C) for derivative orders j less than a given k (the subscript of ∂_i^j refers to the argument of Φ with respect to which the jth derivative is taken). The degree

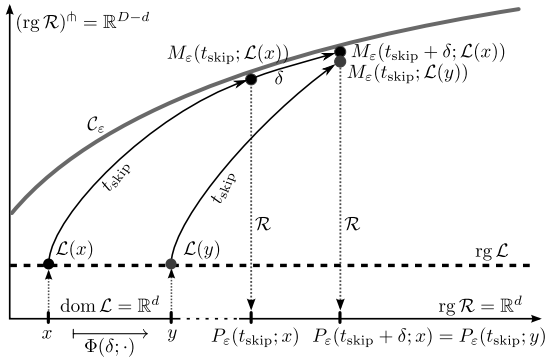

(a) implicit scheme

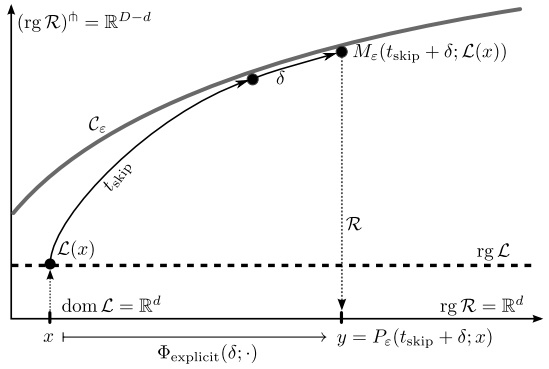

(b) explicit scheme

Figure 2.1. (*a*) *Sketch showing a typical geometry of the implicit scheme in a slow-fast system with a slow manifold* $\mathcal{C}_\varepsilon$ *and an arbitrary lifting* $\mathcal{L}$ *and restriction* $\mathcal{R}$*. The healing* $M_\varepsilon(t_{\text{skip}};\cdot)$ *is applied to all points in the domain of* $\mathcal{L}$*. Note that* $\operatorname{dom}\mathcal{L}$ *and* $\operatorname{rg}\mathcal{R}$ *can be different, but must have the same dimension.* $(\operatorname{rg}\mathcal{R})^{\pitchfork}$ *refers to an arbitrary transversal complement of* $\operatorname{rg}\mathcal{R}$*.* (*b*) *The explicit scheme is shown for comparison.*

of achievable differentiability is determined by the time scale separation: the smaller ε is, the smoother the slow manifold $\mathcal{C}_\varepsilon$ is, and, thus, the higher we can choose the maximal derivative order k.

Based on the implicitly defined approximate flow map Φ, one can now perform higher-level tasks in equation-free analysis.

2.3. Bifurcation analysis of macroscopic equilibria. Bifurcation analysis for equilibria boils down to finding fixed points and their stability and bifurcations for $\Phi(\delta;\cdot)$ with some small, arbitrary δ (that is, $\delta \ll 1/\varepsilon$ in our notation). In terms of $\mathcal{R}$ and $\mathcal{L}$, the equation $\Phi(\delta; x_0) = x_0$, defining the equilibrium x_0, reads (cf. Figure 2.1)

$$\mathcal{R}(M_\varepsilon(t_{\text{skip}} + \delta; \mathcal{L}(x_0))) = \mathcal{R}(M_\varepsilon(t_{\text{skip}}; \mathcal{L}(x_0))). \tag{2.5}$$

This equation has been proposed and studied already in [39]. In applications, (2.5) is solved using a Newton iteration (cf. (6.9) in the optimal velocity model). Since the time stepper is defined implicitly, one finds the stability and bifurcations of an equilibrium x_0 by studying the generalized eigenvalue problem

$$\left[\frac{\partial}{\partial x}\left[\mathcal{R}(M_\varepsilon(t_{\text{skip}}+\delta;\mathcal{L}(x)))\right]\Big|_{x=x_0}\right]x = \lambda\left[\frac{\partial}{\partial x}\left[\mathcal{R}(M_\varepsilon(t_{\text{skip}};\mathcal{L}(x)))\right]\Big|_{x=x_0}\right]x. \tag{2.6}$$

This eigenvalue problem will give the eigenvalues of the implicitly-known flow $\Phi(\delta;\cdot)$, linearized with respect to its second argument x in the equilibrium x_0 such that bifurcations occur when λ is on the unit circle.

2.4. Projective integration. In projective integration one approximates the ODE for the flow on the slow manifold $\mathcal{C}_\varepsilon$ in the coordinate $x \in \mathbb{R}^d$. The ODE for the true flow Φ_* on the slow manifold is an implicit ODE with the solution $x(t)$, which will be derived in detail in Section 3. Its approximation based on Φ is

$$\frac{\mathrm{d}}{\mathrm{d}t}\mathcal{R}(M_\varepsilon(t_{\text{skip}};\mathcal{L}(x))) = \frac{\partial}{\partial\delta}\mathcal{R}(M_\varepsilon(t_{\text{skip}}+\delta;\mathcal{L}(x)))\Big|_{\delta=0}. \tag{2.7}$$

For fixed t_{skip} the left-hand side is a function of $x \in \mathbb{R}^d$ such that the time-derivative of this function defines (implicitly) the time-derivative of x. The term inside the partial derivative on the right-hand side is a function of two arguments, δ and x, for which one takes the partial derivative with respect to its first argument δ in $\delta = 0$, making also the right-hand side a function of x only. Consequently, every integration scheme becomes implicit. For example, if one wants to perform an explicit Euler step of stepsize Δt starting from x_j at time t_j, this becomes an implicit scheme (defining x_{j+1} as the new value at time $t_{j+1} = t_j + \Delta t$):

$$\frac{1}{\Delta t}\left[P_\varepsilon(t_{\text{skip}};x_{j+1}) - P_\varepsilon(t_{\text{skip}};x_j)\right] = \frac{1}{\delta}\left[P_\varepsilon(t_{\text{skip}}+\delta;x_j) - P_\varepsilon(t_{\text{skip}};x_j)\right], \tag{2.8}$$

or, in terms of restricting and lifting,

$$\begin{aligned}\mathcal{R}(M_\varepsilon(t_{\text{skip}};\mathcal{L}(x_{j+1}))) - \mathcal{R}(M_\varepsilon(t_{\text{skip}};\mathcal{L}(x_j)))\\ = \frac{\Delta t}{\delta}\left[\mathcal{R}(M_\varepsilon(t_{\text{skip}}+\delta;\mathcal{L}(x_j))) - \mathcal{R}(M_\varepsilon(t_{\text{skip}};\mathcal{L}(x_j)))\right]\end{aligned}$$

Projective integration becomes attractive if either one can choose Δt much larger than t_{skip} and δ, or one can set Δt negative, enabling integration backward in time on the slow manifold (cf. (6.14) and Figure 6.1), even though the original system is very stiff in $\mathbb{R}^D$ forward in time (and thus, strongly expanding backward in time). For positive Δt the restriction on the size of Δt is given by standard consistency and stability requirements of the coarse-grained integration method restricted to the slow flow (in general the restriction is $\varepsilon\Delta t \ll 1$, which makes the maximal stepsize independent of the time-scale separation). Note that during computation of residuals and Jacobian matrices one can evaluate $P_\varepsilon(t_{\text{skip}};x)$ as a by-product of the evaluation of $P_\varepsilon(t_{\text{skip}}+\delta;x)$, assuming that the restriction $\mathcal{R}$ is of comparatively low computational cost.

2.5. Matching the restriction. Sometimes it is of interest to find a microscopic state $u \in \mathbb{R}^D$ on the slow manifold $\mathcal{C}_\varepsilon$ that has a particular $x \in \mathbb{R}^d$ as its restriction ($\mathcal{R}(u) = x$); see [12, 42, 43]. This state u is defined implicitly and can be found by solving the d-dimensional nonlinear equation

$$\mathcal{R}(M_\varepsilon(t_{\text{skip}}; \mathcal{L}(\tilde{x}))) = x \tag{2.9}$$

for $\tilde{x}$, and then setting $u = M_\varepsilon(t_{\text{skip}}; \mathcal{L}(\tilde{x}))$. This solution u is close to the true slow manifold $\mathcal{C}_\varepsilon$ with an error of order $\exp(-Kt_{\text{skip}})$, where the decay rate $K > 0$ and the possible constant in front of the exponential are independent of ε and t_{skip}. This implies that, if we choose $t_{\text{skip}} = O(\varepsilon^{-1})$ with $p \in (0, 1)$, the distance of u to $\mathcal{C}_\varepsilon$ is small beyond all orders of ε (see Section 3 for the precise conditions). Equation (2.9) was also proposed and studied in [39] (called InitMan in [39]), although without the general error estimate.

3. Convergence of equation-free analysis. This section gives a detailed discussion of the convergence results of the methods sketched in Section 2. Sections 5 and 6 study the optimal velocity model for traffic flow as an application of implicit equation-free analysis.

We formulate all assumptions on $\mathcal{R}$, $\mathcal{L}$, and M_ε for the singular perturbation parameter ε at $\varepsilon = 0$, even though it is typically difficult to vary ε in complex model simulations. However, stating the conditions at $\varepsilon = 0$ ensures that they are uniformly satisfied for all sufficiently small ε, which is the range of parameters for which the statements of this section are valid (cf. [9]). Throughout this section various constants will appear in front of exponentially growing or decaying quantities. As the concrete values of these constants do not play a role, we will use the same variable name C on all occasions without meaning them to be the same. We will state which quantities the constant C depends on whenever we use exponential estimates.

The notation ∂_k^j refers to the jth derivative with respect to the kth argument. For example, $\partial_2^j M_\varepsilon$ refers to the jth-order partial derivative of the flow M_ε with respect to its second argument (the starting point), and the zeroth derivative refers to the value of flow $M_\varepsilon(t; \cdot)$ itself.

3.1. Existence of transversally stable slow manifold. As introduced in Section 2.1, the microscopic flow $M_\varepsilon(t; u_0)$ is the solution of

$$\dot{u} = f_\varepsilon(u), \quad u(t) \in \mathbb{R}^D, \tag{3.1}$$

starting from initial condition $u_0 \in \mathbb{R}^D$, which for $\varepsilon = 0$ has a d-dimensional manifold of equilibria $\mathcal{C}_0$. That is, $f_0(u) = 0$ if $u \in \mathcal{C}_0$. In order to avoid the discussion of what happens when the flow M_ε reaches certain boundaries or becomes large while following the slow dynamics, we assume that the manifold $\mathcal{C}_0$ of equilibria of M_0 is compact. Our first assumption guarantees transversal stability of $\mathcal{C}_0$.

Assumption 1 (Separation of time scales and transversal stability). *There exists a constant $K_0 > 0$ such that for all points $u \in \mathcal{C}_0$ the Jacobian $\partial f_0(u)$ has $D - d$ eigenvalues with real part less than $-K_0$.*

This implies that the flow M_0 approaches the slow manifold $\mathcal{C}_0$ with a rate faster than K_0 from all initial conditions u in some neighborhood of $\mathcal{C}_0$. That is, for every u in an appropriate open neighborhood $\mathcal{U}$ of the slow manifold $\mathcal{C}_0$ there exists a point $p \in \mathcal{C}_0$ such that

$$\lim_{t \to \infty} M_0(t; u) = p$$

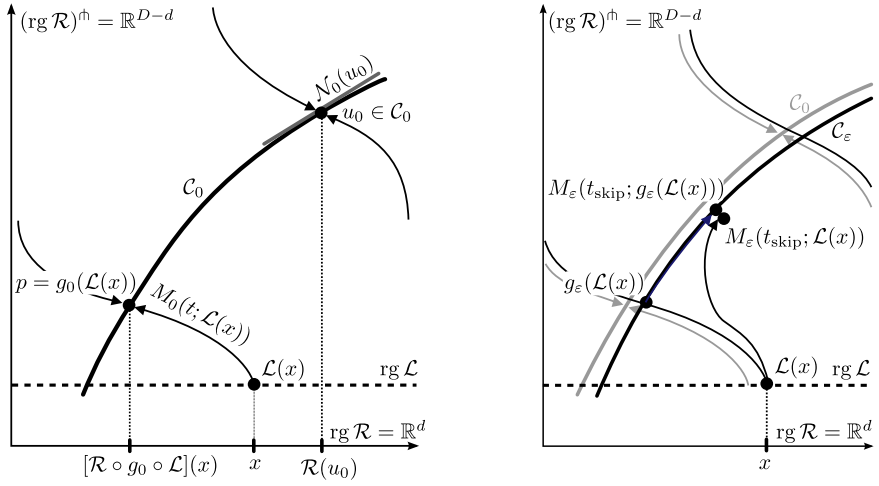

Figure 3.1. *Sketch of geometrical interpretation of transversality assumptions. Note that* $(\operatorname{rg}\mathcal{R})^{\pitchfork}$ *refers to an arbitrary transversal complement of* $\operatorname{rg}\mathcal{R}$*. Panel* (*a*) *shows the geometry at* $\varepsilon = 0$*: The trajectory starting at* $\mathcal{L}(x)$ *must converge to* $\mathcal{C}_0$*, and its limit is called* $g_0(\mathcal{L}(x))$*. The overall map* $\mathcal{R} \circ g_0 \circ \mathcal{L}$ *must be a local diffeomorphism. This entails that the Jacobian* $\partial\mathcal{R}$ *must have full rank on the tangent space* $\mathcal{N}_0(u_0)$ *in any* $u_0 \in \mathcal{C}_0$ (*also shown in* (*a*)), *and that* $\operatorname{rg}\mathcal{L}$ *intersects each fiber* (*the set of points* u *converging to the same* $u_0 \in \mathcal{C}_0$) *transversally. Shown in panel* (*b*)*:* g_ε *and* $\mathcal{C}_\varepsilon$ *are* $O(\varepsilon)$ *perturbations of* g_0 *and* $\mathcal{C}_0$*, and* $M_\varepsilon(t_{\text{skip}}; \mathcal{L}(x)) - M_\varepsilon(t_{\text{skip}}; g_\varepsilon(\mathcal{L}(x)))$ *are* $\exp(-Kt_{\text{skip}})$ *close for* $t_{\text{skip}} > 0$.

(note that for $\varepsilon = 0$ all points on the slow manifold $\mathcal{C}_0$ are equilibria), and the distance can be bounded via

$$\|M_0(t;u) - p\| \le C\exp(-K_0 t)\|u - p\|, \quad \|\partial_2^j M_0(t;u)\| \le C\exp(-K_0 t)$$

for all $t \ge 0$ and $j \ge 1$, where the constant C depends only on the derivative order j.

Since the slow manifold $\mathcal{C}_0$ is compact, one can choose a uniform constant C for all u in the neighborhood $\mathcal{U}$. The above assumption implies the existence of a smooth map (called the *stable fiber projection*),

$$g_0 : \mathcal{U} \to \mathcal{C}_0, \quad \text{defined by} \quad g_0(u) := p, \tag{3.2}$$

assigning to each u its limit $p \in \mathcal{C}_0$ under the flow M_0 (see Figure 3.1(a)).

We recall now two central persistence results of classical singular perturbation theory [9]. First, the slow manifold $\mathcal{C}_0$ persists for sufficiently small ε, deforming to a smooth nearby manifold $\mathcal{C}_\varepsilon$ (as shown in Figure 3.1(b)). This manifold $\mathcal{C}_\varepsilon$ is also compact. Restricted to $\mathcal{C}_\varepsilon$, the flow M_ε is governed by a smooth ODE (the *slow* flow) with a right-hand side for which all derivatives up to a given order k are proportional to ε (larger k requires smaller ε):

$$\|f_\varepsilon(u)\| \le \varepsilon, \qquad \left\|\partial^j f_\varepsilon(u)[v_1, \ldots, v_j]\right\| \le \varepsilon\|v_1\| \cdot \ldots \cdot \|v_j\| \tag{3.3}$$

for all $j = \{1, \dots, k\}$, $u \in \mathcal{C}_\varepsilon$ and $v_1, \dots, v_j \in \mathcal{N}_\varepsilon(u)$. (Here $\mathcal{N}_\varepsilon(u)$ is the tangent space of $\mathcal{C}_\varepsilon$; for $\varepsilon = 0$ it is the null space of the linearization of f_0 in u on the slow manifold $\mathcal{C}_0$.) Note that typically one has only $\|\partial^j f_\varepsilon(u)|_{\mathcal{C}_\varepsilon}\| \leq C\varepsilon$, but we can set the constant C equal to unity without loss of generality by rescaling time or redefining the parameter ε. Thus, the flow $M_\varepsilon(t;\cdot)$ is a global diffeomorphism on the slow manifold $\mathcal{C}_\varepsilon$ which has growth bounds of order ε forward and backward in time:

$$\|\partial_2^j M_\varepsilon(t;\cdot)|_{\mathcal{C}_\varepsilon}\| \leq C\exp(\varepsilon|t|), \qquad \|\partial_2^j M_\varepsilon^{-1}(t;\cdot)|_{\mathcal{C}_\varepsilon}\| \leq C\exp(\varepsilon|t|), \tag{3.4}$$

for some constant C independent of t and ε and all derivative orders j up to a fixed order k. Note that $M_\varepsilon^{-1}(t;\cdot) = M_\varepsilon(-t;\cdot)$ exists for all times t as long as one restricts the flow M_ε to the slow manifold $\mathcal{C}_\varepsilon$.

Second, the stable fiber projection map g_0 persists for small ε, getting perturbed smoothly to a map g_ε, defined for each u in the neighborhood $\mathcal{U}$ of the slow manifold $\mathcal{C}_0$ (and its perturbation $\mathcal{C}_\varepsilon$). The map g_ε picks for every point $u \in \mathcal{U}$ the unique point $g_\varepsilon(u)$ inside the slow manifold $\mathcal{C}_\varepsilon$ such that the trajectories starting from u and $g_\varepsilon(u)$ converge to each other forward in time with an exponential rate K of order 1 (that is, K is uniformly positive for all sufficiently small ε and all $u \in \mathcal{U}$):

$$\|\partial_2^j M_\varepsilon(t;u) - \partial_2^j M_\varepsilon(t;g_\varepsilon(u))\| \leq C\exp(-Kt)\|u - g_\varepsilon(u)\| \tag{3.5}$$

for all $t \geq 0$, $u \in \mathcal{U}$, and $0 \leq j \leq k$, where the constant C is uniform for $u \in \mathcal{U}$. In general, the decay rate K has to be smaller than the rate K_0 asserted to exist in Assumption 1 for $\varepsilon = 0$. More precisely, for every rate $K < K_0$ there exists a range $(0, \varepsilon_0)$ of ε for which (3.5) holds. Choosing ε_0 smaller permits one to choose K closer to K_0. The stable fiber projection map g_ε is an order-ε perturbation of g_0:

$$\|\partial^j g_\varepsilon(u) - \partial^j g_0(u)\| \leq C\varepsilon \tag{3.6}$$

for all $j = \{0, \dots, k\}$ and a constant C that is uniform for all $u \in \mathcal{U}$. The black curves transversal to $\mathcal{C}_\varepsilon$ in Figure 3.1(b) illustrate the fibers, that is, which points of $\mathcal{U}$ get mapped onto the same point in $\mathcal{C}_\varepsilon$ under g_ε. Note that the fibers are not trajectories for $\varepsilon > 0$; rather they are $(D-d)$-dimensional manifolds.

3.2. Transversality conditions on restriction and lifting. One assumption on the restriction $\mathcal{R}$ and the lifting $\mathcal{L}$ is that they are both smooth maps.

Furthermore, we assume that the lifting operator $\mathcal{L}$ maps some bounded open set $\operatorname{dom}\mathcal{L} \subset \mathbb{R}^d$ into the basin of attraction $\mathcal{U}$ of $\mathcal{C}_0$ for $\varepsilon = 0$. We will make all convergence statements in this section for $x \in \operatorname{dom}\mathcal{L}$.

We formulate the transversality conditions on $\mathcal{R}$ and $\mathcal{L}$ with the help of the tangent space $\mathcal{N}_0(u)$ to the slow manifold $\mathcal{C}_0$ in a point $u_0 \in \mathcal{C}_0$, which is given as

$$\mathcal{N}_0(u_0) = \ker \partial f_0(u_0). \tag{3.7}$$

Remember that the stable fiber projection g_0 maps all $u \in \mathcal{U}$ onto the slow manifold $\mathcal{C}_0$. The tangent space $\mathcal{N}_\varepsilon(u)$ to the perturbed slow manifold $\mathcal{C}_\varepsilon$ in a point $u \in \mathcal{C}_\varepsilon$ is a perturbation of $\mathcal{N}_0(u)$ of order ε.

Assumption 2 (Transversality of $\mathcal{R}$ and $\mathcal{L}$).

1. *The map* $g_0 \circ \mathcal{L}$ *is a local diffeomorphism between* $\operatorname{dom}\mathcal{L} \subset \mathbb{R}^d$ *and the slow manifold* $\mathcal{C}_0$ *for every* $x \in \operatorname{dom}\mathcal{L}$.
   Equivalently, the composition of the linearizations $\partial g_0(\mathcal{L}(x)) \in \mathbb{R}^{D\times D}$ *and* $\partial\mathcal{L}(x) \in \mathbb{R}^{D\times d}$ *has full rank for all* $x \in \operatorname{dom}\mathcal{L} \subset \mathbb{R}^d$.
2. *The map* $\mathcal{R} : \mathcal{U} \to \mathbb{R}^d$, *restricted to the slow manifold* $\mathcal{C}_0$, *is a local diffeomorphism between* $\mathcal{C}_0$ *and* $\mathbb{R}^d$ *for every* u *in some relatively open subset* $\operatorname{dom}\mathcal{R} \cap \mathcal{C}_0$.
   Equivalently, the dimension of the space $\partial\mathcal{R}(u)\mathcal{N}_0(u)$ *equals* d *for every* $u \in \operatorname{dom}\mathcal{R}\cap\mathcal{C}_0$.
3. *The set* $\operatorname{dom}\mathcal{R}\cap\mathcal{C}_0$ *contains* $g_0(\mathcal{L}(\operatorname{dom}\mathcal{L}))$ *as a subset, and the boundary of* $\operatorname{dom}\mathcal{R}\cap\mathcal{C}_0$ *has a positive distance from the boundary of* $g_0(\mathcal{L}(\operatorname{dom}\mathcal{L}))$.

Note that points 1 and 2 of Assumption 2 are generically satisfied in a given $x \in \mathbb{R}^d$ or $u_0 \in \mathcal{C}_0$. By convention we keep $\operatorname{dom}\mathcal{L}$ and $\operatorname{dom}\mathcal{R}$ such that the transversality conditions are uniformly satisfied in $\operatorname{dom}\mathcal{L}$ and $\operatorname{dom}\mathcal{R}$. The assumption that $\operatorname{dom}\mathcal{R}$ (the region where $\mathcal{R}$ satisfies Assumption 2) contains the set $g_0(\mathcal{L}(\operatorname{dom}\mathcal{L}))$ guarantees that the map $x \mapsto \mathcal{R}(g_0(\mathcal{L}(x)))$ is locally invertible for all $x \in \operatorname{dom}\mathcal{L}$ and that its linearization is uniformly regular in $\operatorname{dom}\mathcal{L}$. All points of Assumption 2 and the invertibility of the slow flow, $M_\varepsilon(t;\cdot)$ restricted to the slow manifold $\mathcal{C}_\varepsilon$, can be combined to ensure that the map

$$\mathbb{R}^d \supseteq \operatorname{dom}\mathcal{L} \ni x \mapsto \mathcal{R}(M_\varepsilon(t; g_\varepsilon(\mathcal{L}(x)))) \in \mathbb{R}^d \tag{3.8}$$

is locally invertible for all $\varepsilon \in [0, \varepsilon_0)$ and for all times t satisfying

$$|t| \le T_{\text{up}}/\varepsilon \tag{3.9}$$

for some constant T_{up}. The constant T_{up} is independent of ε, t, and $x \in \operatorname{dom}\mathcal{L}$. It is determined by the distance between the boundaries of $\operatorname{dom}\mathcal{R}$ and $g_\varepsilon(\mathcal{L}(\operatorname{dom}\mathcal{L}))$. This distance is positive because of point 3 in Assumption 2 and the fact that g_ε is a small perturbation of g_0. Then the time it takes a trajectory on $\mathcal{C}_\varepsilon$ to reach the boundary of $\operatorname{dom}\mathcal{R}$ starting from $g_\varepsilon(\mathcal{L}(\operatorname{dom}\mathcal{L}))$ is of order $1/\varepsilon$ such that we can introduce the constant T_{up}. All components of the map (3.8) are locally invertible: $g_\varepsilon \circ \mathcal{L} : \operatorname{dom}\mathcal{L} \to \mathcal{C}_\varepsilon$ by Point 1 of Assumption 2 (transversality of $\mathcal{L}$); $M_\varepsilon(t;\cdot)$ is a diffeomorphism on $\mathcal{C}_\varepsilon$; and $\mathcal{R}$, restricted to $\mathcal{C}_0$ (and, hence, to $\mathcal{C}_\varepsilon$), is also locally invertible due to Point 2 of Assumption 2. For $\varepsilon = 0$ the map (3.8) is independent of t. Moreover, the norm of the derivative of the map (3.8) and its inverse are also uniformly bounded if $|\varepsilon t| \le T_{\text{up}}$

3.3. Map of exact flow M_ε into $\mathbb{R}^d$. Next, we give a coordinate system and a constructive procedure that maps the flow M_ε, restricted to the slow manifold $\mathcal{C}_\varepsilon$, back to $\mathbb{R}^d$. This kind of map is called a "lifting" of the flow M_ε on $\mathcal{C}_\varepsilon$ to its cover $\mathbb{R}^d$ in, e.g., [9], but we do not use this term here to avoid confusion with the lifting operation $\mathcal{L}$, used in an equation-free context (cf. for example [23]). For any fixed t_{skip} the following map $X_\varepsilon : \operatorname{dom}\mathcal{L} \to \mathcal{C}_\varepsilon$ introduces coordinates of (part of) $\mathcal{C}_\varepsilon$ in $\operatorname{dom}\mathcal{L}$:

$$X_\varepsilon(x) = M_\varepsilon(t_{\text{skip}}; g_\varepsilon(\mathcal{L}(x))).$$

This map is locally invertible because $g_0 \circ \mathcal{L}$ is a local diffeomorphism between $\operatorname{dom}\mathcal{L}$ and $\mathcal{C}_0$ (and, hence, $g_\varepsilon \circ \mathcal{L}$ is a diffeomorphism between $\operatorname{dom}\mathcal{L}$ and $\mathcal{C}_\varepsilon$ for small ε), and $M_\varepsilon(t_{\text{skip}};\cdot)$ is a global diffeomorphism on $\mathcal{C}_\varepsilon$ (see (3.4)). Moreover, if $M_\varepsilon(t_{\text{skip}}; g_\varepsilon(\mathcal{L}(x)))$ is in the interior

of the domain of $\mathcal{R}$, then one can find, for a given $u = X_\varepsilon(x) \in \mathcal{C}_\varepsilon$, a preimage $\tilde{x} \approx x$ of any point $\tilde{u} \in \mathcal{C}_\varepsilon$ close to u by solving

$$\mathcal{R}(X_\varepsilon(\tilde{x})) = \mathcal{R}(\tilde{u}) \tag{3.10}$$

for $\tilde{x}$. This follows from Assumption 2 (transversality for $\mathcal{R}$). In particular, point 3 of Assumption 2 gives the bound on the range of t_{skip} for which the linearization of (3.10) is regular: the trajectory $t \mapsto M_\varepsilon(t; g_\varepsilon(\mathcal{L}(x)))$ should not leave $\operatorname{dom}\mathcal{R}$ for $t \in [0, t_{\text{skip}}]$, which is guaranteed for $t_{\text{skip}} < T_{\text{up}}/\varepsilon$. By requiring $\tilde{x} \approx x$, the preimage $\tilde{x}$ of $\tilde{u}$, defined by (3.10), becomes unique.

Let $x(\delta) \in \operatorname{dom}\mathcal{L} \subset \mathbb{R}^d$ be a trajectory of the flow M_ε on $\mathcal{C}_\varepsilon$ in the coordinates defined by X_ε. By definition, x satisfies $X_\varepsilon(x(\delta)) = M_\varepsilon(\delta; X_\varepsilon(x(0)))$. As long as $X_\varepsilon(x(\delta))$ is in the domain of $\mathcal{R}$, we can apply $\mathcal{R}$ to this identity to obtain

$$\begin{aligned} \mathcal{R}(X_\varepsilon(x(\delta))) &= \mathcal{R}(M_\varepsilon(\delta; X_\varepsilon(x(0)))), \qquad \text{that is,} \\ \mathcal{R}(M_\varepsilon(t_{\text{skip}}; g_\varepsilon(\mathcal{L}(x(\delta))))) &= \mathcal{R}(M_\varepsilon(t_{\text{skip}} + \delta; g_\varepsilon(\mathcal{L}(x(0))))) \end{aligned} \tag{3.11}$$

(inserting the definition of X_ε). Hence, the flow M_ε on $\mathcal{C}_\varepsilon$, written in the coordinates $x \in \operatorname{dom}\mathcal{L}$, satisfies the implicit ODE

$$\frac{\mathrm{d}}{\mathrm{d}t}\mathcal{R}(M_\varepsilon(t_{\text{skip}}; g_\varepsilon(\mathcal{L}(x)))) = \frac{\partial}{\partial\delta}\mathcal{R}(M_\varepsilon(t_{\text{skip}} + \delta; g_\varepsilon(\mathcal{L}(x))))\Big|_{\delta=0} \tag{3.12}$$

as long as $\varepsilon t_{\text{skip}} < T_{\text{up}}$ and $\varepsilon(t_{\text{skip}} + \delta) < T_{\text{up}}$ such that the resulting trajectory $x(\delta)$ stays in $\operatorname{dom}\mathcal{L}$ and $X_\varepsilon(x(\delta)) = M_\varepsilon(t_{\text{skip}}; g_\varepsilon(\mathcal{L}(x(\delta))))$ stays in $\operatorname{dom}\mathcal{R}$. For different values of t_{skip} we get different coordinate representations of the same flow, all related to the representation with $t_{\text{skip}} = 0$ via the global diffeomorphism $M_\varepsilon(t_{\text{skip}}; \cdot)$ on $\mathcal{C}_\varepsilon$, which is a near-identity transformation if $t_{\text{skip}} \ll 1/\varepsilon$ (see (3.4)).

Let us denote the flow corresponding to the trajectory $x(\delta)$ in (3.11) as $\Phi_*(\delta; \cdot) : \operatorname{dom}\mathcal{L} \to \operatorname{dom}\mathcal{L}$. The flow Φ_* is generated by the ODE (3.12). If $\varepsilon t_{\text{skip}} \le T_{\text{up}}$ and $\delta \ll 1/\varepsilon$, this flow map $\Phi_*(\delta; \cdot)$ is defined implicitly by solving the following system for y_*,

$$\mathcal{R}(M_\varepsilon(t_{\text{skip}}; g_\varepsilon(\mathcal{L}(y_*)))) = \mathcal{R}(M_\varepsilon(t_{\text{skip}} + \delta; g_\varepsilon(\mathcal{L}(x)))), \tag{3.13}$$

and setting $\Phi_*(\delta; x) := y_*$. The local invertibility of X_ε guarantees that there is a solution y_* close to x and that the solution y_* is unique in the vicinity of x. For larger δ, one breaks down the flow into smaller time steps such that one can apply the local solvability at every step:

$$\Phi_*(\delta; x) = \Phi_*(\delta/m; \cdot)^m[x] \tag{3.14}$$

for sufficiently large integer m. This construction of Φ_* achieves a representation of the exact flow M_ε restricted to $\mathcal{C}_\varepsilon$ that is globally unique on $\operatorname{dom}\mathcal{L}$ for all δ with $\varepsilon(t_{\text{skip}} + \delta) \le T_{\text{up}}$.

3.4. Approximate flow map and its convergence. We now define the approximate flow map $y = \Phi(\delta; x)$. Its definition is similar to (3.13), in particular, it is also implicit. To highlight where the difference between y and y_* comes from, we put the defining equation for $y_* = \Phi_*(\delta; x)$ directly below the implicit definition of y:

$$\begin{aligned} \mathcal{R}(M_\varepsilon(t_{\text{skip}}; \mathcal{L}(y))) &= \mathcal{R}(M_\varepsilon(t_{\text{skip}} + \delta; \mathcal{L}(x))), \\ \mathcal{R}(M_\varepsilon(t_{\text{skip}}; g_\varepsilon(\mathcal{L}(y_*)))) &= \mathcal{R}(M_\varepsilon(t_{\text{skip}} + \delta; g_\varepsilon(\mathcal{L}(x)))), \end{aligned} \tag{3.15}$$

where the equation at the top defines $y = \Phi(\delta; x)$. To check how the difference $y - y_*$ depends on x, t_{skip}, δ, and ε we use a regular perturbation argument by comparing solutions of the two equations in (3.15). We rely on (3.5), which guarantees that the perturbations are small, and the invertibility of the map (3.8), which guarantees that the linearization of the left-hand side with respect to y and its inverse are uniformly bounded for $\varepsilon(t_{\text{skip}} + \delta) \leq T_{\text{up}}$.

Theorem 3.1 (Convergence of approximate flow map). *Let $K \in (0, K_0)$ be a given constant. We assume that the assumptions on time scale separation (Assumption 1) and transversality (Assumption 2) hold for $\mathcal{L}$, M_ε and $\mathcal{R}$ such that*

$$x \mapsto \mathcal{R}(M_\varepsilon(t; g_\varepsilon(\mathcal{L}(x))))$$

is a local diffeomorphism if $|\varepsilon t| \leq T_{\text{up}}$ with some $T_{\text{up}} > 0$ that is uniform for all ε and all $x \in \operatorname{dom} \mathcal{L}$.

Then there exist a lower bound t_0 for t_{skip}, an upper bound ε_0 for ε, and a constant $C > 0$ such that $y = \Phi(\delta; x)$ and $y_* = \Phi_*(\delta; x)$ are well defined by (3.15), and the estimate

$$\|\partial_2^j \Phi(\delta; x) - \partial_2^j \Phi_*(\delta; x)\| \leq C \exp(-K t_{\text{skip}}) \tag{3.16}$$

holds for all orders $j \in \{0, \dots, k\}$, all $x \in \operatorname{dom} \mathcal{L}$, $\varepsilon \in (0, \varepsilon_0)$, $t_{\text{skip}} \in (t_0, T_{\text{up}}/\varepsilon]$, and $\delta \in [0, T_{\text{up}}/\varepsilon - t_{\text{skip}}]$.

(Remember that k is defined above (3.3).) Note that the assumptions of Theorem 3.1 require that $\varepsilon t_{\text{skip}}$ and $\varepsilon(t_{\text{skip}} + \delta)$ be bounded by T_{up}. Hence, the theorem ensures convergence of $\Phi(\delta; x)$ to $\Phi_*(\delta; x)$ only if $t_{\text{skip}} \to \infty$ and $\varepsilon \to 0$ simultaneously. Since ε is usually fixed in applications, this theorem is not enough to ensure convergence for $t_{\text{skip}} \to \infty$ uniform for ε.

The proof of Theorem 3.1 splits the error $\Phi(\delta; x) - \Phi_*(\delta; x)$ using the fiber projection g_ε. The projection of the error onto $\mathcal{C}_\varepsilon$ using g_ε is zero by construction, and the error transversal to the manifold decays exponentially due to (3.5), giving a perturbation of order $\exp(-K t_{\text{skip}})$. This implies that we can apply the implicit function theorem if $\varepsilon(t_{\text{skip}} + \delta) \leq T_{\text{up}}$, giving an error of order $\exp(-K t_{\text{skip}})$ for the difference $y - y_*$ and for the first- and higher-order derivatives. The details of the proof are given in Appendix A.

4. Discussion of the general convergence statement and its assumptions. Theorem 3.1 is a local statement with respect to x, claiming convergence only in a region $\operatorname{dom} \mathcal{L}$ in which the transversality conditions are uniformly satisfied. One has to restrict the times t_{skip} and δ such that the slow flow $M_\varepsilon(t; g_\varepsilon(x))$ cannot leave the region $g_\varepsilon(\operatorname{dom} \mathcal{R})$ for the times $t = t_{\text{skip}}$ and $t = t_{\text{skip}} + \delta$. This is appropriate because in many cases, during continuation or projective integration the maps $\mathcal{R}$ and $\mathcal{L}$ get adapted (for example, for the traffic problem investigated in Section 6, $\mathcal{L}$ is varied along the curve of macroscopic equilibria).

4.1. Comparison to the explicit equation-free approach. The convergence theorem, Theorem 3.1, implies that for smaller ε and a longer healing time t_{skip} the deviation from the true flow reduces as long as $\varepsilon(t_{\text{skip}} + \delta) \leq T_{\text{up}}$ and $\varepsilon t_{\text{skip}} \leq T_{\text{up}}$. This is in contrast to the approach proposed by [23], where the coarse flow map was defined in an explicit way: $\Phi_{\text{explicit}}(\delta; x) = \mathcal{R}(M_\varepsilon(\delta; \mathcal{L}(x)))$ or $\Phi_{\text{explicit}}(\delta; x) = \mathcal{R}(M_\varepsilon(\delta + t_{\text{skip}}; \mathcal{L}(x)))$ [28, 37, 5]. Following this approach, one would analyze equilibria of the slow flow and their stability by studying fixed points of the map

$$\Phi_{\text{explicit}}(t; \cdot) : x \mapsto \mathcal{R}(M_\varepsilon(t; \mathcal{L}(x))) \tag{4.1}$$

for x, where $0 < t \ll 1/\varepsilon$ is chosen such that it includes a healing time t_{skip} ($t > t_{\text{skip}}$). (Compare (4.1) with definition (3.15): $y = \Phi(\delta; x)$ if $\mathcal{R}(M_\varepsilon(t_{\text{skip}}; \mathcal{L}(y))) = \mathcal{R}(M_\varepsilon(t_{\text{skip}} + \delta; \mathcal{L}(x)))$.) For $1 \ll t \ll 1/\varepsilon$ the map $\Phi_{\text{explicit}}(t; \cdot)$ is a perturbation of order $O(\varepsilon t) \ll 1$ of the map $x \mapsto \mathcal{R}(g_0(\mathcal{L}(x)))$. Any flow map on the slow manifold must be a perturbation of the identity of order εt for small εt. Thus, the explicit map $\Phi_{\text{explicit}}(t; \cdot)$ can be a valid approximation for the flow on the slow manifold in any coordinates only if $\mathcal{R} \circ g_0 \circ \mathcal{L}$ equals the identity on $\mathbb{R}^d$. Often this requirement is approximated by $\mathcal{R} \circ \mathcal{L} = I$, because g_0 is in general unknown [21, 26, 27, 33, 36]. Note that there is no ε- or t dependence in the limiting map $\mathcal{R} \circ g_0 \circ \mathcal{L}$, resulting in the much more restrictive condition $\mathcal{R} \circ g_0 \circ \mathcal{L} = I$ than transversality Assumption 2 on $\mathcal{R}$ and $\mathcal{L}$. Moreover, $\mathcal{R} \circ g_0 \circ \mathcal{L} = I$ is only a consistency condition, making it possible for $\Phi_{\text{explicit}}(t; \cdot)$ to resemble the map of a slow flow. If this consistency condition is violated, then $\Phi_{\text{explicit}}(t; \cdot)$ will show dynamics independent of the properties of the flow on the slow manifold. For example, if the map $\mathcal{R} \circ g_0 \circ \mathcal{L}$ has a stable fixed point, then $\Phi_{\text{explicit}}(t; \cdot)$ will also have a stable fixed point independent of the slow flow M_ε on $\mathcal{C}_\varepsilon$.

One way to ensure that the operator Φ_{explicit} approximates the slow flow is to construct a lifting operator that maps onto the slow manifold $\mathcal{C}_\varepsilon$. This has been achieved up to finite order of ε through constrained-runs corrections to $\mathcal{L}$ [42, 43]. In our notation the first-order version of this scheme would correspond to defining the lifting $\mathcal{L} : \mathbb{R}^d \ni x \mapsto u \in \mathbb{R}^D$ as the (locally unique) u satisfying $\mathcal{R}(u) = x$ and $\mathrm{d}/\,\mathrm{d}t(\mathcal{R}^\dagger(u)) = 0$ (zero-derivative principle), where $\mathcal{R}^\dagger$ is an arbitrary operator satisfying $\mathbb{R}^D = \ker \mathcal{R} \oplus \ker \mathcal{R}^\dagger$. Zagaris *et al.* [42, 43] developed general mth-order versions of this scheme. Vandekerckhove *et al.* [39] compared the constrained-runs schemes from [42, 43] to the results of the implicit expression (2.9) (called InitMan in [39]) for various examples, finding (2.9) uniformly vastly superior in terms of convergence and performance. Equation (2.9) also requires only the solution of a d-dimensional, not a D-dimensional, system (usually $d \ll D$). Using (3.11) it is not necessary to find a microscopic state u on the slow manifold matching a particular restriction x ($\mathcal{R}u = x$). A usage of InitMan prefixed at each single step of an explicit equation-free scheme would do so and is an alternative. Recognizing that the slow flow is given by an implicit ODE from the beginning reduces the computational overhead, because matching the restriction is required only at user-specified points.

4.2. Testing the transversality conditions and choosing the healing time and coarse dimension. The conditions listed in Assumption 1 and Assumption 2 contain terms that are unknown in practice. For example, the fiber projection g_0 and the tangent space $\mathcal{N}_0$ to the slow manifold are both inaccessible because in many cases one cannot vary the time scale separation parameter ε. However, observing the minimal singular value of the linearization $\partial_2 P_\varepsilon(t_{\text{skip}}; x) = \partial/\partial x[\mathcal{R}(M_\varepsilon(t_{\text{skip}}; \mathcal{L}(x)))]$ with respect to x (a d-dimensional matrix) provides an indicator: in points where the transversality condition is violated, the linearization becomes singular.

Similarly, the condition number of the linearization $\partial_2 P_\varepsilon(t_{\text{skip}}; x)$, $\operatorname{cond} \partial_2 P_\varepsilon(t_{\text{skip}}; x)$, guides the choice of the optimal healing time t_{skip}. All tasks involve solving nonlinear equations with a Jacobian $\partial_2 P_\varepsilon(t_{\text{skip}}; x)$. While the error due to finite time scale separation becomes smaller, $\operatorname{cond} \partial_2 P_\varepsilon(t_{\text{skip}}; x)$ can grow with t_{skip} such that other errors may become dominant when they are amplified by $\operatorname{cond} \partial_2 P_\varepsilon(t_{\text{skip}}; x)$. In particular, when the microscopic system is a Monte

Carlo simulation, a trajectory $M_\varepsilon(t;u)$ is determined via ensemble runs, and the accuracy of the evaluation of M_ε is only of the order of $1/\sqrt{S}$, where S is the ensemble size.

The linearization $\partial_2 P_\varepsilon(t_{\text{skip}};x)$ also helps to reveal whether one has too many coarse variables, that is, whether d is too large such that the flow M_ε restricted to the assumed slow manifold $\mathcal{C}_\varepsilon$ is not sufficiently slow (still containing rapidly decaying components). Then $\partial_2 P_\varepsilon(t_{\text{skip}};x)$ becomes close to singular, too. Note that any solution found, for example, by solving the fixed point equation (2.5) is still a correctly identified fixed point with correctly identified stability. However, the linearization of (2.5) becomes close to singular.

4.3. Chaotic and stochastic systems. Barkley, Kevrekidis, and Stuart [2] analyzed how the equation-free approach can be used to analyze moment maps of stochastic systems or high-dimensional chaotic systems that converge in a statistical mechanics sense to low-dimensional stochastic differential equations (SDEs). These moment maps play then the same role as the macroscopic map $\Phi(\delta;\cdot)$ in our case. The authors of [2] observe that the choice of δ strongly influences the number and stability of fixed points. Also the inclusion of additional macroscopic variables (increasing d) changes the results of the equation-free analysis qualitatively. It is unclear how the implicit scheme (2.3) behaves in the situations studied by [2]. While [2] also invokes a separation-of-time-scales argument to study approximation quality for the stochastic systems, their setting does not fit into the assumptions underlying Fenichel's theorem but requires weaker notions of convergence based on averaging over a chaotic attractor (see [13] for a review). An adaptation of the analysis in [2], and possibly further adaptation of the implicit scheme (2.3), is the missing link between Theorem 3.1 establishing convergence for the idealized situation, given in Section 3, and applications of equation-free analysis to stochastic or chaotic systems.

5. Traffic Modeling — The Optimal Velocity Model. We now turn to the equation-free analysis of a system that fits into the framework of implicit equation-free analysis. We will perform some of the typical tasks listed in Section 2 and apply the implicit equation-free analysis introduced in Sections 2 and 3.

We consider N cars driving around a ring road of length L. The individual drivers' behavior is assumed to be uniform and deterministic, modeled by an optimal velocity model [1] of the form

$$\tau\ddot{x}_n + \dot{x}_n = V(x_{n+1} - x_n), \qquad n = 1, 2, \ldots, N \tag{5.1}$$

where x_n is the position of car n, τ is the inertia of the driver and car, and V is an optimal velocity function, prescribing the preferred speed of the driver depending on the distance to the car in front (the *headway*). The ring road implies periodic boundary conditions in space

$$x_{n+N} = x_n + L. \tag{5.2}$$

In order to do numerical bifurcation analysis, we rewrite the second-order ODE (5.1) as a system of first-order ODEs:

$$\begin{aligned} \dot{x}_n &= y_n \\ \dot{y}_n &= \tau^{-1}\left[V(x_{n+1} - x_n) - y_n\right]. \end{aligned} \tag{5.3}$$

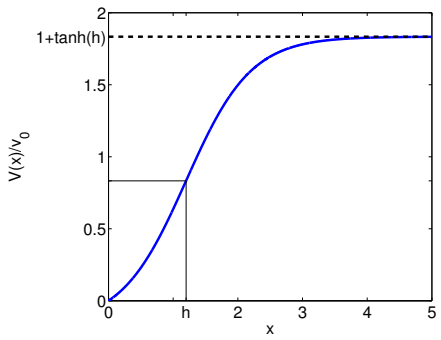

Figure 5.1. *Optimal velocity function $V(x)/v_0$ defined in (5.4) for $h = 1.2$. The maximal velocity $v_0(1 + \tanh(h))$ is obtained for $x \to \infty$. v_0 acts as a scaling parameter for V. The inflection point of the optimal velocity function V is at h.*

Similar to [1, 10] we choose the function

$$V(\Delta x_n) = v_0(\tanh(\Delta x_n - h) + \tanh(h)), \tag{5.4}$$

shown in Figure 5.1, as the optimal velocity function. In (5.4), $v_0(1+\tanh(h))$ is the maximal velocity, $\Delta x_n := x_{n+1} - x_n$ is the headway, and the inflection point h of V determines the desired safety distance between cars. The reviews [17, 29, 31] put behavioral models based on optimal velocity functions into the general context of traffic modeling and discuss possible choices of optimal velocity functions. One conclusion from [31] is that the choice of V does not affect the overall bifurcation diagram of a single jam qualitatively (some choices of V can give rise to unphysical behavior such as cars briefly moving backwards, though). Depending on parameters and initial conditions, the system either shows free-flow behavior, that is, all cars move with the same velocity and headway, or it develops traffic jams, which means that there coexist regions of uniformly small headways and low speeds, spatially alternating with regions of free flow with uniformly large headways and large speeds. We focus on the dynamics near the formation of a single jam. In equilibrium the single traffic jam moves along the ring with nearly (due to a finite number of cars) constant shape and speed as a traveling wave against the direction of traffic. In the full system (5.3) the single traffic jam is a traveling wave perturbed by small periodic oscillations; see Figure 5.3(b) below.

5.1. Direct Simulations. The uniform flow, starting from initial condition

$$\begin{aligned} x_n(0) &= (n-1)\frac{L}{N} \\ y_n(0) &= V\left(\frac{L}{N}\right), \end{aligned} \tag{5.5}$$

is a solution of (5.3), where all cars move with the same velocity $y_n(t) = V(\frac{L}{N})$ and headway $\Delta x_n(t) = \frac{L}{N}$. We focus on two types of long-time behavior, the uniform flow and traveling wave

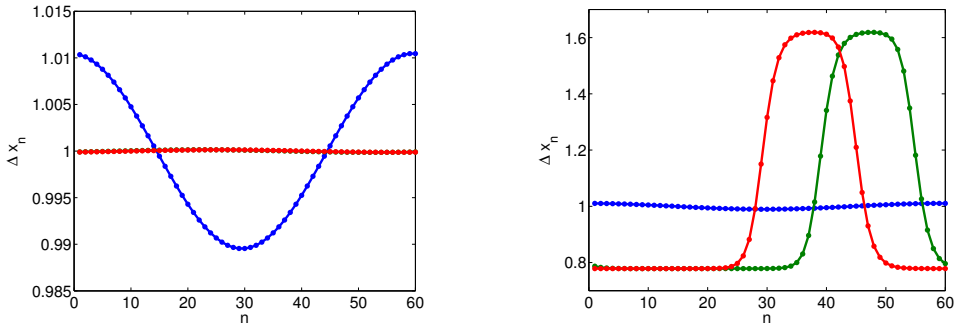

(a) $h = 1.2$, $v_0 = 0.87$ (b) $h = 1.2$, $v_0 = 0.91$

Figure 5.2. *Comparison of the two traffic flow regimes. The initial condition (blue) is compared with the final state (red $= T = 5\times10^4$, green$= T-500$). (a) Free flow regime. (b) Traffic jam regime. Note the different scales of Δx_n on the vertical axis.*

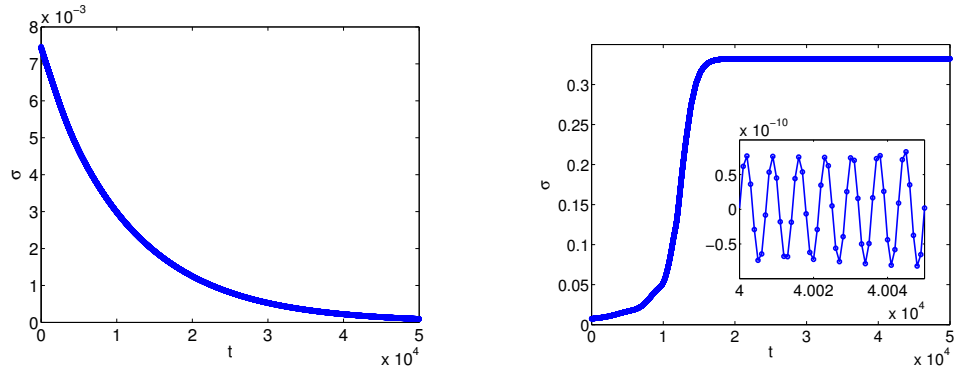

(a) $h = 1.2$, $v_0 = 0.87$ (b) $h = 1.2$, $v_0 = 0.91$

Figure 5.3. *Time evolution of the macroscopic variable σ for the same parameters as in Figure 5.2. (a) The decay to the stable free flow. (b) Using the same initial condition as in (a), the system converges to a stable traffic jam. The inset in (b) shows the difference between the macroscopic variable σ and its long-term average σ^* over the last 10000 time steps of the simulation. One expects small oscillations of σ in time due to the finite number of cars. However, these small oscillations are below the tolerance of the ODE solver.*

solutions. To give a qualitative picture of these, we run two simulations, initializing system (5.3) with initial conditions close to the uniform flow, or adding a periodic perturbation of strength μ:

$$\begin{aligned} x_n(0) &= (n-1)\frac{L}{N} + \mu \sin\left(\frac{2\pi}{N}n\right) \\ y_n(0) &= V\left(\frac{L}{N}\right). \end{aligned} \tag{5.6}$$

For all simulations, we use $N = L = 60$. The simulations were run for a time $T = 5 \cdot 10^4$ using the MATLAB `ode45`-solver [18] with absolute and relative tolerance 10^{-8}. All parameters for the simulation can be found in table B.1 in Appendix B. For our one-parameter analysis, we also fix the desired safety distance $h = 1.2$. Figures 5.2 and 5.3 show the long-time behavior of the initial condition (5.6) for the velocity parameters $v_0 = 0.87$ and $v_0 = 0.91$, respectively. In Figure 5.2, the headway is shown as a function of car number. It can be seen that the initial perturbation decays to the uniform flow for the trajectory for $v_0 = 0.87$ but converges to a traveling wave solution for $v_0 = 0.91$.

We choose the standard deviation σ for the headway as the macroscopic measure (called x in sections 2 and 3) describing the traffic flow

$$\sigma = \sqrt{\frac{1}{N-1} \sum_{n=1}^{N} (\Delta x_n - \langle \Delta x \rangle)^2}, \quad \text{where } \Delta x_n = x_{n+1} - x_n. \tag{5.7}$$

Here, $\langle \Delta x \rangle = 1$ is the mean of all headways. The free flow corresponds to $\sigma = 0$ and the decay of σ to the free flow is shown in Figure 5.3(a). If v_0 is chosen equal to 0.91, σ increases until it settles to an equilibrium, where a traveling wave of fixed shape is observed. It can be seen in the inset of Figure 5.3(b) that the macroscopic variable oscillates even in its steady state. These small-scale oscillations are expected due to the finite number of cars, because cars arrive at the rear and leave from the front of the jam at periodic intervals. However, the oscillation amplitude is orders of magnitude smaller than the macroscopic dynamics, such that the oscillations are obscured by discretization effects of the ODE solver (which shows subtolerance oscillations even for systems with stable equilibria).

5.2. Time scale separation. In order to apply the theoretical results from Sections 2 and 3, we have to check the extent to which the assumption about separation of time scales is valid. Initially, we use simulations to estimate the time scale separation, showing that the studied one-jam solution forms a one-dimensional stable submanifold, which we will then study in Section 6.

The simulation result shown in Figure 5.4 highlights that a one-dimensional slow manifold exists corresponding to a single jam. For Figure 5.4 we perturbed an initial nonequilibrium traffic jam (blue circles) by adding random numbers drawn from a uniform distribution in $[-0.5, 0.5]$. This perturbed state (red circles) is then simulated using (5.3) for 1000 time steps. The resulting state is observed to rapidly converge back to a single-jam solution (black crosses). Note that the drift of the jams has been subtracted in order to center the profiles for a better comparison. In Figure 5.4(a) the traffic jam at time $t = 1000$ is very slightly more pronounced than the initial jam (which was in nonequilibrium position, though). The time scale separation can be observed clearly in the time evolution of the macroscopic variable σ (cf. Figure 5.4(b)). For a very short time ($t \approx 10$), the macroscopic variable adjusts rapidly. This corresponds to the fast scale (see inset in Figure 5.4(b)). Observing the system for a much longer time of $t = 1000$, the slow drift in the macroscopic variable corresponds to the slow time scale. A numerical inspection yields a time-scale separation of approximately four orders of magnitude, i.e., $\varepsilon \approx 10^{-4}$, which appears to be different from $1/N$ (cf. also Figure 5.3 for visualizations of the slow dynamics).

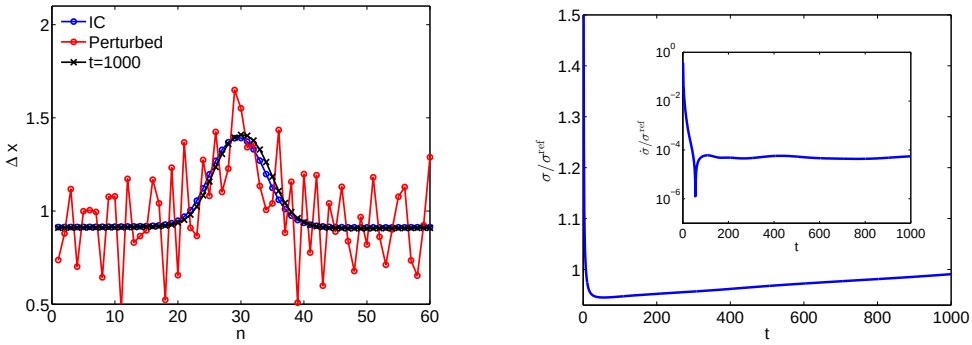

(a) (b)

Figure 5.4. *Visualization of the time scale separation for system (5.3). (a) An initial nonequilibrium traffic jam (blue circles) is perturbed with uniformly distributed noise to yield a new profile (red circles). A microscopic simulation of 1000 time steps brings the system back to a single traffic jam (black crosses), which is slightly more pronounced than the initial jam. (b) The same simulation as in (a) shown in the macroscopic variable σ (scaled with $\sigma^{ref} = 0.16$). After a short time ($t \approx 10$), the system relaxes to a one-jam solution. During this process, σ is decreased drastically and settles on the fast time scale (see inset). Afterwards, σ increases again on a four-orders-of-magnitude slower time scale.*

The next section presents an equation-free bifurcation analysis for jam formation on the macroscopic level.

6. Equation-Free Bifurcation Analysis. We choose a one-dimensional macroscopic description; that is, the standard deviation σ is the only macroscopic variable. The change of the chosen macroscopic variable σ is studied with respect to system parameters. According to the equation-free approach presented in Section 2 the macroscopic ODE has the implicit form

$$\frac{\mathrm{d}}{\mathrm{dt}}\mathcal{R}(M(t_{\mathrm{skip}}, \mathcal{L}(\sigma))) = \frac{\partial}{\partial\delta}\mathcal{R}(M(t_{\mathrm{skip}} + \delta, \mathcal{L}(\sigma)))\Big|_{\delta=0}, \tag{6.1}$$

where the derivative on the right-hand side is approximated by the finite-difference quotient with finite δ

$$F(\sigma) = \frac{\mathcal{R}M(t_{\mathrm{skip}} + \delta, \mathcal{L}(\sigma)) - \mathcal{R}M(t_{\mathrm{skip}}, \mathcal{L}(\sigma))}{\delta}, \tag{6.2}$$

and t_{skip} is the healing time, which should be chosen long enough for transients to decay (cf. the discussion in Section 5.2).

As explained in Section 2 and 3, the equation-free setup avoids an analytical derivation of a macroscopic ODE but uses (6.1) where (6.2) is evaluated by simulation bursts of length $t_{\mathrm{skip}} + \delta$. A good choice for the time δ depends on the slow dynamics. We used numerical observations to obtain a good estimate for (6.2), see also Figure 5.4. Note that the left- and right-hand sides in (6.1) depend also on the system parameters h and v_0, which are not expressly included in (6.1) and (6.2). We also drop the subscript ε of M because it enters our system only indirectly. In order to find trajectories or equilibria of (6.1)–(6.2), it is necessary to define a lifting operator $\mathcal{L}$ and a restriction operator $\mathcal{R}$. In our case, the restriction operator

$\mathcal{R}$ is given by the definition of the macroscopic measure in (5.7), i.e.,

$$\mathcal{R}(u) = \sqrt{\frac{1}{N-1}\sum_{n=1}^{N}\left(\Delta x_n - \langle \Delta x \rangle\right)^2}. \tag{6.3}$$

Our lifting operator constructs initial conditions with the help of a reference state $\tilde{u} = (\tilde{x}, \tilde{y}) \in \mathbb{R}^{2N}$, obtained during a previous microscopic simulation. We have to guaranteet hat the lifting $\mathcal{L}$ initializes the system into the vicinity of the solution of interest, which we described in Section 3 as $\mathcal{L}$ having to map into the attracting neighborhood $\mathcal{U}$ of the slow manifold.

The following description assumes that microscopic simulations start and end near a single-pulse traffic jam. The components of the reference state $\tilde{u}$ are the positions $(\tilde{x}_n)_{n=1}^N$ and the velocities $(\tilde{y}_n)_{n=1}^N$ of the cars (cf. (5.3)). Let us denote the macroscopic state corresponding to $\tilde{u}$ by $\tilde{\sigma} = \mathcal{R}(\tilde{u})$. Given a real parameter p, whose meaning we shall explain in detail below, and a reference state $\tilde{u}$, we define $\mathcal{L}_{p,\tilde{u}}(\sigma)$ to be

$$\begin{aligned}
\mathcal{L}_{p,\tilde{u}}(\sigma) = u = (x, y) &= (x_{\text{new}}, y_{\text{new}}) \in \mathbb{R}^N \times \mathbb{R}^N, \qquad \text{where} \\
\Delta x_{\text{new}} &= \frac{p\sigma}{\tilde{\sigma}}\left(\Delta\tilde{x} - \langle \Delta\tilde{x} \rangle\right) + \langle \Delta\tilde{x} \rangle, \\
x_{\text{new},1} = 0, \qquad x_{\text{new},n} &= \sum_{i=1}^{n-1} \Delta x_{\text{new},i} \qquad n = 2, \ldots, N, \\
y_{\text{new},n} &= V(\Delta x_{\text{new},n}) \qquad n = 1, \ldots, N.
\end{aligned} \tag{6.4}$$

V is the optimal velocity function (5.4), $\langle\cdot\rangle$ refers to the average of a quantity, and $\Delta\tilde{x}$ are the headways of the reference state ($\Delta\tilde{x}_n = \tilde{x}_{n+1} - \tilde{x}_n$). In (6.4) we compute the positions $x \in \mathbb{R}^N$ first and then initialize the velocities $y \in \mathbb{R}^N$ by using the optimal velocity function for these positions. The positions are initialized such that $x_1 = 0$, resulting in a unique mapping from headways to positions. The definition (6.4) of $\mathcal{L}_{p,\tilde{u}}$ contains an artificial parameter p, which we keep equal to unity throughout, except for Figure 6.2 in Section 6.1 and the error estimates in Section 6.2. A parameter value of $p \neq 1$ introduces a systematic bias into our lifting such that we can vary p gradually to investigate how our results depend on our choice of lifting. For $p \neq 1$, the lifting $\mathcal{L}_{p,\tilde{u}}$ violates the common assumption of equation-free computations, where the identity $\mathcal{R} \circ \mathcal{L} = I$ is claimed to be necessary [33, 26, 21, 27, 36]. An application of $\mathcal{L}_{p,\tilde{u}}$ and $\mathcal{R}$ without any time evolution in between, yields $\mathcal{R}(\mathcal{L}_{p,\tilde{u}}(\sigma)) = p \cdot \sigma$.

In the following, we use an equation-free pseudoarclength continuation scheme to compute bifurcation diagrams for the fixed point of (6.1)–(6.2); that is, we track a root curve (branch) of

$$F(\sigma, v_0) = 0 \tag{6.5}$$

in the (σ, v_0)-plane for the macroscopic right-hand side (6.2). The influence of speed limits on traffic jam formation motivates the choice of the velocity parameter v_0 as a bifurcation parameter. In (6.5) we include the bifurcation parameter v_0 explicitly as an argument of F. The pseudoarclength continuation contains two steps. The first step is a predictor step, where we use a secant predictor, assuming that we know two points on the branch already. Let

(σ^0, v_0^0) and (σ^1, v_0^1) be those two points. We define the secant direction by

$$w = (\sigma^1 - \sigma^0, v_0^1 - v_0^0). \tag{6.6}$$

The prediction $(\hat{\sigma}, \hat{v}_0)$ for the next point on the branch is then determined by the secant predictor

$$(\hat{\sigma}, \hat{v}_0) = (\sigma^1, v_0^1) + s\frac{w}{\|w\|}, \tag{6.7}$$

where we keep the stepsize of the predictor uniformly at $s = 10^{-3}$. The prediction is not exactly on the branch and must be corrected in the following corrector step, which is chosen to be perpendicular to the predictor direction (6.6). The corrector step solves the system

$$\begin{aligned} F(\sigma, v_0) &= 0 \\ w^{(\sigma)}(\sigma - \hat{\sigma}) + w^{(v_0)}(v_0 - \hat{v}_0) &= 0, \end{aligned} \tag{6.8}$$

where $w^{(\sigma)}$ and $w^{(v_0)}$ are the components of w in the σ and v_0 direction, respectively. System (6.8) can be solved with respect to σ and v_0 by Newton's method using

$$(\sigma^{k+1}, v_0^{k+1})^T = (\sigma^k, v_0^k) + \nu J^{-1} F(\sigma^k, v_0^k), \tag{6.9}$$

where J is the Jacobian of the left-hand side of (6.8), given by

$$J = \begin{pmatrix} F_\sigma & F_{v_0} \\ w^{(\sigma)} & w^{(v_0)} \end{pmatrix}, \tag{6.10}$$

and ν is a relaxation parameter adjusting the length of a Newton step. For all computations we used a full Newton step, that is, $\nu = 1$. If the information on the Jacobian of the system is poor, for example, in noisy or stochastic systems, it might be useful to use a damped Newton method ($\nu < 1$). The iteration is initialized with the predictor (6.7)

$$(\sigma^0, v_0^0) = (\hat{\sigma}, \hat{v}_0). \tag{6.11}$$

During the iteration the function F has to be evaluated according to its definition (6.2). This means that we lift, run the simulation of the microscopic system and then restrict with $t_{\text{skip}} = 300$ and $\delta = 2000$.

The Jacobian J is approximated via finite differences. Since $w^{(\sigma)}$ and $w^{(v_0)}$ are known from the predictor step, we only have to determine F_σ and F_{v_0}. We evaluated F at the points

$$(\sigma, v_0), \quad (\sigma + \Delta\sigma, v_0), \quad (\sigma, v_0 + \Delta v_0) \tag{6.12}$$

and computed the one-sided derivatives

$$F_\sigma = \frac{F(\sigma + \Delta\sigma, v_0) - F(\sigma, v_0)}{\Delta\sigma}, \qquad F_{v_0} = \frac{F(\sigma, v_0 + \Delta v_0) - F(\sigma, v_0)}{\Delta v_0}. \tag{6.13}$$

We started the one-parameter continuation of the traffic jam in the direction of decreasing v_0 from two profiles obtained by direct simulations at $v_0 = 0.91$ and $v_0 = 0.9$. The resulting bifurcation diagram is shown in Figure 6.1.

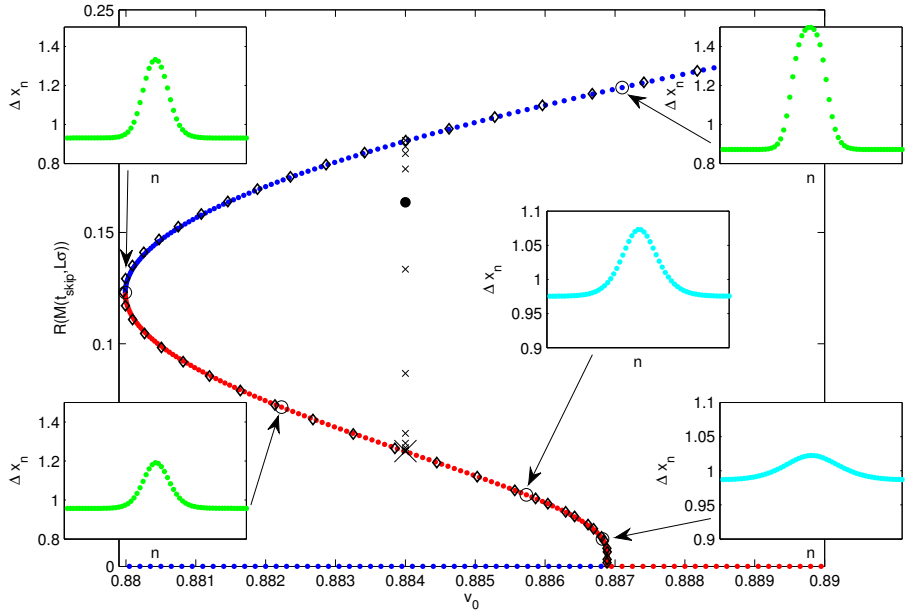

Figure 6.1. *Bifurcation diagram obtained by equation-free pseudoarclength continuation for $h = 1.2$. The traffic jam profiles are shown for selected points in the bifurcation diagram, marked with black circles. Note the change in scale on the vertical axes on the profiles for better visibility (horizontal axes show the car number n, vertical axes show headways). A fold point has been detected at $(v_0, \mathcal{R}(M(t_{\text{skip}}, \mathcal{L}\sigma))) \approx (0.88, 0.125)$, where a change in stability is observed. The blue dots mark stable states, while the red dots mark unstable states. It is due to the equation-free continuation that unstable branches can be observed. For the lifting we use (5.6) and (6.4) for continuation of the uniform flow and the traveling wave solution, respectively. Additionally, the black crosses mark a backward trajectory computed by using (6.14). Starting from the stable branch, the backward integration converges to the unstable branch (big cross). The black dot is the base point used for an error estimate in Figure 6.4. Black diamonds denote the results of a direct continuation of the full microscopic system on the macroscopic level. The data is in perfect agreement with results from implicit equation-free methods.*

The traffic jam, i.e., traveling wave, is stable for large values of v_0. When following the branch, a saddle-node bifurcation is detected at $(\mathcal{R}(M(t_{\text{skip}}, \mathcal{L}\sigma))^*, v_0^*) \approx (0.88, 0.125)$, where the traffic jam changes stability. A further decrease of v_0 at that point would make the traffic jam dissolve. But due to the equation-free pseudoarclength continuation of the continuous branch, it is possible to follow the branch around the fold point and continue the unstable branch for increasing v_0. The traffic jam stays unstable until it reaches the uniform flow at $\sigma = 0$ at a Hopf bifurcation point (cf. Section 6.3 and (6.24)). The microscopic states corresponding to selected points along the branch are shown as insets in Figure 6.1. The shape has sharp layers and a flat plateau on the stable branch, and becomes harmonic close to the equilibrium value $\sigma = 0$. Additionally, the time steps of a backward integration are shown for $v_0 = 0.884$, showing the heteroclinic connection between stable and unstable jams.

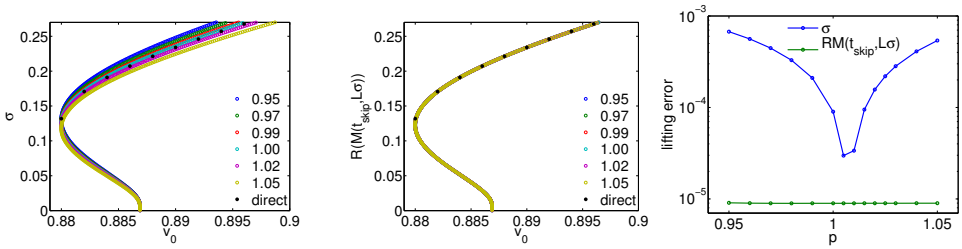

(a) (b) (c)

Figure 6.2. (*a*) *Bifurcation diagram obtained from running the implicit equation-free continuation scheme described in Section 6 for* $p = 0.95, 0.97, 0.99, 1.0, 1.02, 1.05$. *The black dots show the results from a direct downsweep of the stable branch. Depending on the value of p, the results differ visibly from the direct simulation data, which is usually used as an argument for finding a 'good' lifting operator.* (*b*) *The healed version of the bifurcation diagram; i.e.,* $\sigma_{\text{healed}} = \mathcal{R}M(t_{\text{skip}}, \mathcal{L}_{p,\tilde{u}}\sigma)$ *for different p all collapse to the same curve, fitting the direct numerical results perfectly. See also the main text in Section 2.* (*c*) *Analysis of the lifting error. The blue data points show the distances between the equation-free solution* $v_0(\sigma)$ *and the restriction of the simulation data using eq. (6.16) as a measure for the error. The results from a direct simulation of the stable branch are used as a reference curve (cf. Figure 6.2(a)). For the 'normal' equation-free data, i.e., using the unhealed macroscopic quantities, it is observed that the error is minimal at* $p = 1.005$, *corresponding to a 'good' lifting operator. The green data points show the behavior of the healed version of the bifurcation branches (cf. Figure 6.2(b)). The error is uniformly small when using the healed data.* $h = 1.2$ *for all images.*

The trajectory starts for $t_0 = 0$ at the stable branch. The Euler scheme (2.8) is used for computing the backward trajectory; that is,

$$\mathcal{R}M(t_{\text{skip}}, \mathcal{L}(\sigma_{j+1})) = \mathcal{R}M(t_{\text{skip}}, \mathcal{L}(\sigma_j)) + F(\sigma_j)\Delta t, \tag{6.14}$$

where σ_j is the solution at $t_j = j\Delta t$, and $\Delta t = -5000$ is chosen. The size of Δt is determined by the desired accuracy of the coarse projective integration.For the computation of $F(\sigma)$ the parameters from Table B.1 in Appendix B are chosen in (6.2). The backward integration converges to the unstable branch.

6.1. The influence of the choice of lifting operator. Figure 6.2 shows how the results depend on the artificial parameter p, which we introduced into the lifting operator $\mathcal{L}_{p,\tilde{u}}$. In both panels, the same bifurcation diagram is shown for several values of p and compared to the restrictions of the stable fixed points of direct long-time simulations ($T = 3 \cdot 10^5$, black dots). The case where the usual equation-free identity $\mathcal{R} \circ \mathcal{L}_{p,\tilde{u}} = I$ is fulfilled corresponds to $p = 1$. We observe that the preimages σ of the equilibria under the combination of lifting operator and healing $M(t_{\text{skip}}; \mathcal{L}_{p,\tilde{u}}(\cdot))$ depend visibly on p (panel (a) of Figure 6.2). Therefore, we compare Figure 6.2(a) with the corresponding Figure 6.2(b) for the healed macroscopic quantity

$$\sigma_{\text{healed}} = \mathcal{R}(M(t_{\text{skip}}, \mathcal{L}_{p,\tilde{u}}\sigma)) \tag{6.15}$$

for each macroscopic equilibrium σ along the branch of the bifurcation diagram. According to Section 3 the map $\mathcal{R}(M(t_{\text{skip}}, \mathcal{L}_{p,\tilde{u}}\sigma))$ is a local diffeomorphism from $\mathbb{R}^d$ into $\mathbb{R}^d$ with

$d = 1$. Plotting the bifurcation diagram in the $(v_0, \sigma_{\text{healed}})$-plane in Figure 6.2(b), we obtain a solution branch that is independent of the choice of the lifting operator, as one would expect from Theorem 3.1.

For a more detailed analysis of the error, we compute the $\mathbb{L}_2$ norm between the interpolated data sets $v_0(\sigma)$ (expressing the parameter as a function of the equilibrium location near the fold) for the direct simulation data and the data for the stable branch of the equation-free bifurcation diagram. For interpolation, the MATLAB `interp1` function [18] with the "`spline`" option is used. We use the error measure

$$\|f - g\|^2 = \int_a^b [f(\sigma) - g(\sigma)]^2 d\sigma \tag{6.16}$$

to analyze the deviation between the restriction of the direct simulation data and equation-free continuation data. Here, f and g are the interpolated data sets $v_0(\sigma)$ for the simulated data and the equation-free data, respectively, in the range of σ between $a = 0.125$ and $b = 0.25$. The unstable branches cannot be compared with direct integration of the system. The deviation E using eq. (6.16)) with lifting parameter p is shown in Figure 6.2(c). The blue data points correspond to the distance between the restriction of the simulation data and the equation-free solutions (that is, the preimages of the equation-free microscopic solutions under $M(t_{\text{skip}}; \mathcal{L}_{p,\tilde{u}}(\cdot))$ in the domain of $\mathcal{L}_{p,\tilde{u}}$) . The distance is small for values of p close to 1, where the usual identity $\mathcal{R} \circ \mathcal{L} = I$ is fulfilled. However, the distance for σ_{healed} (green data) is uniformly small, independent of the choice of p. Therefore, healed quantities should be used when comparing equation-free results to restrictions of the direct simulation data. The uniformly small errors in Figure 6.2(c) (in green) suggest that with implicit time steppers the results are not sensitive to the choice of the lifting operator. This is in contrast to most equation-free applications [23, 5, 21], which use explicit time steppers of the form $\Phi(\delta; x) = \mathcal{R}(M(\delta; \mathcal{L}(x)))$.

6.2. Influence of the healing time t_{skip} and comparison to explicit scheme. In this section, we investigate the influence of t_{skip} on the equation-free results, e.g., bifurcation diagrams and stability analysis. First, we show that the bifurcation diagrams are rather insensitive to the choice of t_{skip}, while the information of the Jacobian depends more noticeably on the value of t_{skip}.

The bifurcation diagrams obtained for $h = 1.2$ and $t_{\text{skip}} = 10, 100, 300, 1000, 2000$ are shown in Figure 6.3. In Figure 6.3(a) it can be observed that the bifurcation diagrams are similar for all choices of t_{skip}; i.e., they show the same qualitative features. Although the bifurcation diagrams are quantitatively close to each other, the information about the derivatives, i.e., the Jacobian $\partial F/\partial \sigma$, does not appear to converge to a particular value for increasing t_{skip}. Note that the scale of the y-axis is 10^{-4} in this region of the bifurcation diagram, which suggests that the slow time scale is of this order.

For all values of t_{skip}, the fold point near $\sigma = 0.12$ is detected by a sign change in the Jacobian (cf. Figure 6.3(b)). Close to the Hopf point (which would appear as a pitchfork bifurcation in the macroscopic system (6.1)) the derivative $\partial F/\partial \sigma$ is not sufficiently accurate to resolve the criticality of the Hopf (pitchfork) bifurcation, which appears to be close to being degenerate. The Hopf bifurcation point cannot be studied using the operator $\mathcal{R}$ because expression (6.3), defining $\mathcal{R}$, is singular in the uniform flow.

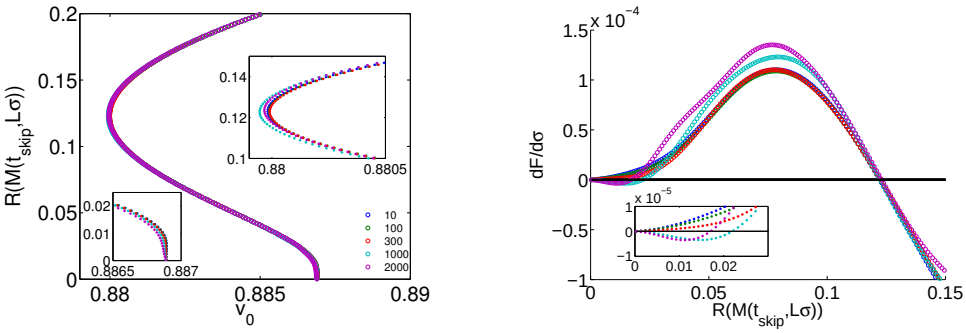

(a) (b)

Figure 6.3. (*a*) *Bifurcation diagrams for* $h = 1.2$ *and* $t_{\text{skip}} = 10, 100, 300, 1000, 2000$ *in the healed quantities of* σ*. The difference between the curves is very small. Insets show a zoom for the fold and the Hopf point.* (*b*) *Comparison of the Jacobians for the different values of* t_{skip} *along the curve. Close to the Hopf point the value of the Jacobian does not converge for increasing* t_{skip} *within the plotted range.*

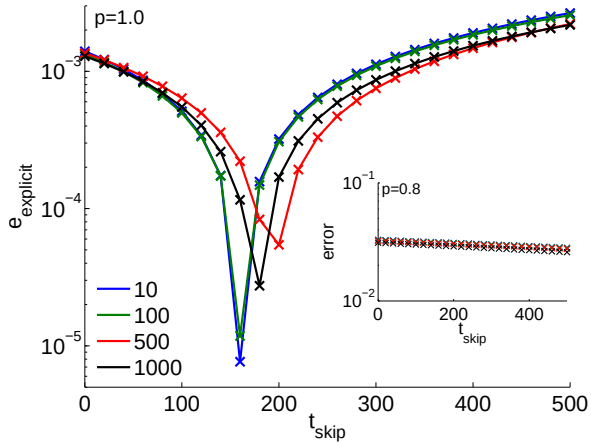

Figure 6.4. *Error analysis for the healing time* t_{skip} *in the explicit scheme, showing the error* $e_{\text{explicit}} = |\Phi_{\text{explicit}} - \Phi_*|$ *defined in* (6.17)*. Colors indicate different values for* δ*. The inset shows the same computation for a scaled lifting operator* $\mathcal{L}_{p,\tilde{u}}$ *with* $p = 0.8$*. Here, the explicit method has an error which is about two orders of magnitude larger than that for a good lifting operator* $p = 1.0$*. Note that explicit equation-free computations usually require* $\mathcal{R} \circ \mathcal{L} = I$*, and the choice of* $p = 0.8$ *violates this assumption.*

To study the influence of t_{skip} on the explicit scheme Φ_{explicit} and the implicit scheme Φ in more detail, we compare the results generated by the approximate macroscopic flow directly to a pregenerated trajectory of the microscopic flow. To this end we perform a long-term microscopic simulation of the traffic model from a reference point (Figure 6.1, black dot). After a sufficiently long transient, the dynamics settle to the slow manifold. We denote the

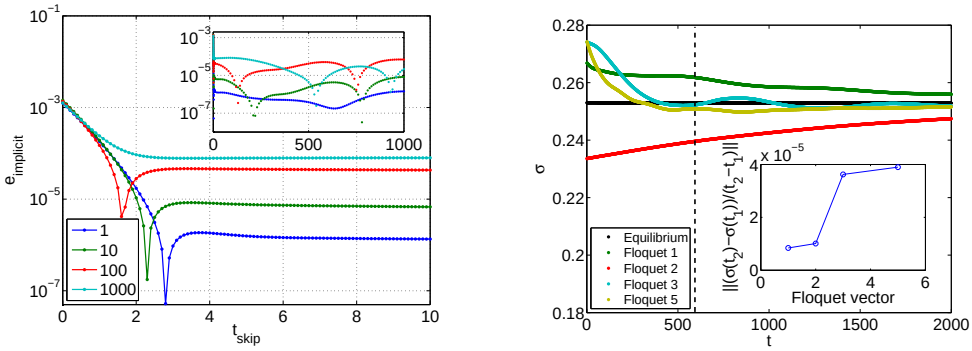

(a) (b)

Figure 6.5. (*a*) *Dependence of the error* e_{implicit} *given by* (6.18). *The error is shown in dependence on* t_{skip} *for* $\delta = 1, 10, 100, 1000$ *(see color code in the legend);* $h = 1.2, v_0 = 0.884, p = 0.8$. (*b*) *Evolution of the system for perturbations in the directions of the leading Floquet vectors (cf. also Figure 6.6 for leading Floquet exponents). These perturbations lead to oscillations in the macroscopic description. The inset shows the decay rate over a time* $t_2 - t_1 = 600$. *While the perturbations in the first two Floquet eigenvectors decay with almost the same rate, there is a gap to the next Floquet vector number* 3.

point at the end of this transient as $u(0) = \tilde{u}$. The microscopic trajectory $u(t)$ starting from $\tilde{u}$ is always close to the slow manifold. The macroscopic state corresponding to $\tilde{u}$ is denoted by $\tilde{\sigma} = \mathcal{R}(\tilde{u})$. The error of the explicit equation-free approach (scheme (4.1)) is then

$$\begin{aligned} e_{\text{explicit}}(t_{\text{skip}}, \delta; \mathcal{R}(\tilde{u})) &= |\Phi_{\text{explicit}}(\delta; \mathcal{R}(\tilde{u})) - \mathcal{R}(u(\delta))| \\ &= |\mathcal{R}(M(t_{\text{skip}} + \delta; \mathcal{L}_{p,\tilde{u}}\mathcal{R}(\tilde{u}))) - \mathcal{R}u(\delta)|. \end{aligned} \tag{6.17}$$

Figure 6.4 shows this error for several fixed δ and varying t_{skip}.

The error e_{explicit} is of order 10^{-3} to 10^{-5} for a good lifting operator, i.e., $p = 1.0$. The downward peak around $t_{\text{skip}} \approx 150$ in Figure 6.4 in logarithmic scale corresponds to a sign change of the scalar quantity $\mathcal{R}(M(t_{\text{skip}} + \delta; \mathcal{L}_{p,\tilde{u}}\mathcal{R}(\tilde{u}))) - \mathcal{R}u(\delta)$ in (6.17). For this healing time $t_{\text{skip}} \approx 150$ the lifted state is mapped into the stable fiber corresponding to $\tilde{u}$; that is, $\tilde{u} = g_\varepsilon(M(t_{\text{skip}}; \mathcal{L}_{p,\tilde{u}}(\mathcal{R}(\tilde{u}))))$. Note that for a one-dimensional slow manifold the stable fibers are codimension-one surfaces (called isochrones if the slow manifold is a periodic orbit) such that we can expect to find the fiber for which the error goes to zero for $\delta \to \infty$ by varying the healing time t_{skip}. However, this appropriate healing time may depend on the point $\tilde{u}$ on the slow manifold and is in general not known. The inset in Figure 6.4 shows the error e_{explicit} for a nonoptimal lifting operator $\mathcal{L}_{p,\tilde{u}}$, namely for $p = 0.8$. The error for the explicit method is of order 10^{-1} to 10^{-2} uniformly for t_{skip} and δ. Hence, for the explicit scheme varying t_{skip} can in general not compensate for errors introduced by the lifting operator.

When estimating the error e_{implicit} of the implicit scheme we have to first find the point σ corresponding to $\tilde{\sigma}$ after healing. Hence, the error e_{implicit} is given as

$$\begin{aligned} e_{\text{implicit}}(t_{\text{skip}}, \delta; \mathcal{R}(\tilde{u})) =& |\mathcal{R}(M(t_{\text{skip}} + \delta; \mathcal{L}_{p,\tilde{u}}(\sigma))) - \mathcal{R}(u(\delta))| \quad \text{where } \sigma \text{ solves} \\ \mathcal{R}(\tilde{u}) =& \mathcal{R}(M(t_{\text{skip}}; \mathcal{L}_{p,\tilde{u}}(\sigma))). \end{aligned} \tag{6.18}$$

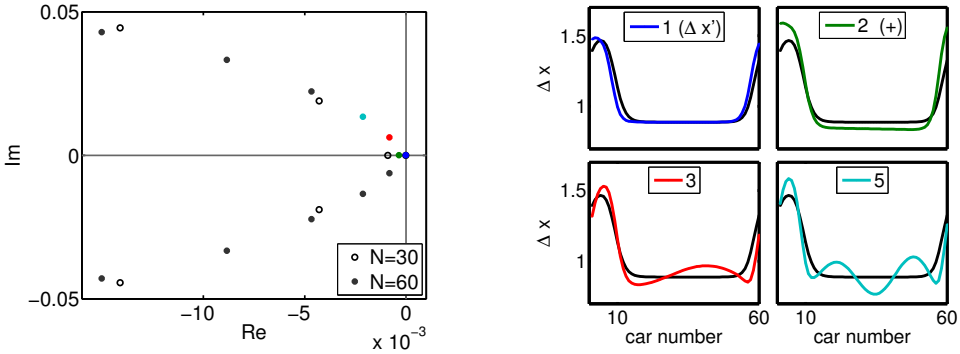

(a) Floquet exponents (b) Perturbations

Figure 6.6. *Floquet exponents (a) and leading Floquet vectors (b) of a single traffic jam (viewed as a periodic orbit of the full system (5.3)). The orbit (shown in (b)) is also highlighted in Figure 6.1 ($v_0 = 0.884$ on stable branch). In (a), we have included the spectrum of a comparable orbit for $N = 30$, $L = 30$. In (b) we have added the Floquet vectors for the dominant Floquet exponents as a perturbation to the periodic orbit. Vectors 3 and 5 are complex. (+): Vector 2 has been orthonormalized with respect to vector 1.*

Figure 6.5(a) shows e_{implicit} for $p = 0.8$ (such that the lifting operator is expected to be at some distance from the slow manifold initially), the same fixed integration times δ as in Figure 6.4, and a range of t_{skip} from 0 to 1000 (see inset in Figure 6.5(a)).

After an initial decay over a few orders of magnitude (see Figure 6.5(a) main graph) the error starts to oscillate (see inset in Figure 6.5(a)) on a small scale compared to the value of the macroscopic variable. These small-scale oscillations suggest that the assumptions of Theorem 3.1 on large time scale separation are not satisfied for the traffic flow M. To confirm this we compute the Floquet exponents for the stable stationary single-traffic-jam solution (diamond at $v_0 = 0.884$ at the end of the heteroclinic connection marked by crosses in Figure 6.1). This is a periodic orbit of the microscopic system (5.3). Figure 6.6(a) shows the leading Floquet exponents for this periodic orbit. It shows a dominant real Floquet exponent very close to the origin next to the trivial Floquet exponent 0 (which corresponds to the flow direction). This dominant real Floquet exponent corresponds to the slow time scale that the equation-free analysis attempts to capture.

Figure 6.6(a) also shows that this dominant Floquet exponent is part of a band of complex Floquet exponents that is parabola-shaped and bending toward the half-plane with negative real part (see, for example, the band of full dots in Figure 6.6(a)). The spectra for the two system sizes plotted in Figure 6.6(a) indicate that the spacing of the Floquet exponents' frequency decreases with increasing N. The parabolic shape of the band then gives a gradually increasing spectral gap for the low-frequency Floquet exponents until finite-size effects become visible (to the right of the part of the complex plane shown in Figure 6.6(a)). The spectral gap between the dominant and the following Floquet exponents gives an upper bound on the time scale separation that is much more restrictive than the initial assessment in Figure 5.4 suggested.

An explanation for the apparent discrepancy is the mode shape of the eigenvectors corresponding to the low-frequency (slow-decay) Floquet exponents shown in Figure 6.6(b). Figure 6.6(b) illustrates how perturbations into the directions of the eigenvectors for the first five Floquet exponents look (ordered by descending real parts of the exponent). The first Floquet vector corresponds to the time derivative (the linearization of the time shift). The second Floquet vector corresponds to the dominant real exponent, tangent to the slow manifold that the equation-free approach tries to capture. Floquet vector 2 is shown orthonormalized with respect to Floquet vector 1, because both Floquet vectors 1 and 2 are nearly linearly dependent. While Floquet vector 2 corresponds to a change of amplitude of the shape of the jam, the complex Floquet vectors correspond to spatial perturbations of the jam of low frequency (the spatial frequency is increasing with increasing time frequency and decay rate). When decomposing the perturbation given in Figure 5.4(a) into the eigenbasis, the contribution of the space corresponding to the low-frequency, slow-decay Floquet vectors was small such that one can observe only small-amplitude low-frequency oscillations after the initial rapid decay of all high-frequency strong-decay directions (see inset in Figure 5.4(b)).

These results explain the oscillations observed in Figure 6.5(a). A perturbation of an equilibrium traffic jam in the directions of the leading Floquet vectors is shown in Figure 6.5(b). Small-scale oscillations are visible in the macroscopic trajectories. These oscillations lead to additional oscillations in Figure 6.5(a) after an initial rapid exponential decay of the error. Consequently, Theorem 3.1 is, strictly-speaking, valid only up to a small residual, which in our system is much smaller than the overall dynamics. Thus, the equation-free approach is applicable (and implicit schemes have smaller error than explicit ones) even if the conditions of Theorem 3.1 are not met.

6.3. Continuation of the fold in two parameters. A two-parameter scan, showing one-parameter bifurcation diagrams in the velocity parameter v_0 for different values of the safety distance h, is presented in Figure 6.7(a). The curve of folds as a result of two-parameter continuation in Figure 6.7(a) shows how the fold merges with another saddle-node point in a cusp. The system of equations for continuation of the fold is [25]

$$\begin{aligned} F(\sigma, v_0, h) &= 0 \\ F_\sigma(\sigma, v_0, h) &= 0 \\ w^{(\sigma)}(\sigma - \hat{\sigma}) + w^{(v_0)}(v_0 - \hat{v}_0) + w^{(h)}(h - \hat{h}) &= 0 \end{aligned} \tag{6.19}$$

with the Jacobian

$$J = \begin{pmatrix} F_\sigma & F_{v_0} & F_h \\ F_{\sigma\sigma} & F_{v_0\sigma} & F_{h\sigma} \\ w^{(\sigma)} & w^{(v_0)} & w^{(h)} \end{pmatrix}. \tag{6.20}$$

Since derivatives of second order are needed, we apply an approximation of second-order accuracy for the derivatives, i.e., centered differences for the parameter derivatives in v_0 and h and one-sided second-order schemes for derivatives in σ. We use the one-sided second-order approximation for F_σ, because σ is nonnegative by definition. Details for the numerical evaluation of the derivatives can be found in Appendix C.

During the two-parameter continuation the Newton iteration used full Newton steps ($\nu = 1$ in (6.9)). Panel (b) of Figure 6.7 shows the results; they are in perfect agreement with the

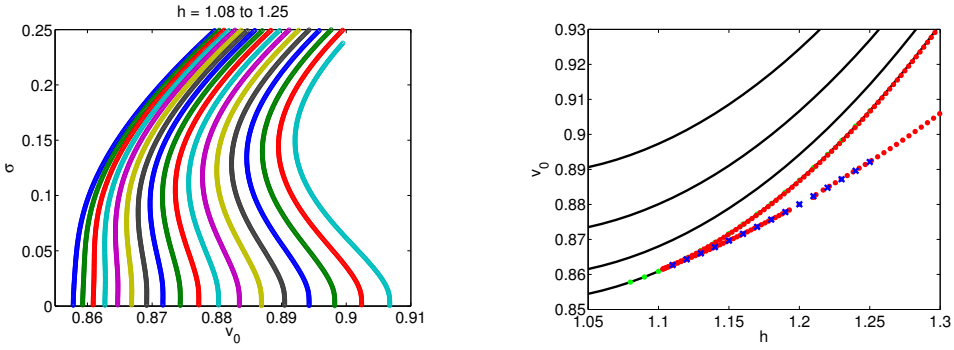

(a) (b)

Figure 6.7. (*a*) *Bifurcation diagrams for* $h \in [1.08, 1.25]$*, where* h *increases from the left curve to the right curve.* (*b*) *Two-parameter continuation of the fold point in the parameters* v_0 *and* h*. The blue crosses mark the points determined from the bifurcation diagrams of the one-parameter continuation, and the red circles are the results from a two-parameter continuation. The black lines show analytical results for the Hopf bifurcation at* $\sigma = 0$ *(cf.* (6.24)*). The numerical results for the Hopf bifurcation (zeros from bifurcation diagrams in the left panel) are denoted as green dots; they are in perfect agreement with the analytical results. Note that in the parameter plane projection, the difference between the Hopf and the fold point is barely visible, and the first Hopf curve and the numerical data are obscured by the numerical data for the fold continuation.*

data obtained by a one-parameter continuation. For comparison we have included the Hopf bifurcation point of the full microscopic system at $\sigma = 0$. The Hopf bifurcation is a pitchfork bifurcation at the macroscopic level. However, since the standard deviation as macroscopic measure is nonnegative by definition, it shows only the nonnegative branches. The analytic expression for the Hopf bifurcation parameter can be found by linearizing system (5.3) around the uniform flow and using the ansatz $(x_n(t), y_n(t)) = (x_n(0)\exp(i\omega t), y_n(0)\exp(i\omega t))$. This results in the system

$$i\omega x_n = y_n \tag{6.21}$$

$$i\omega y_n = \tau^{-1}\left[V'\left(\frac{L}{N}\right)(x_{n+1} - x_n) - y_n\right], \tag{6.22}$$

where ω is the frequency and $V'(\frac{L}{N})$ the first derivative of the optimal velocity function at equilibrium. Eliminating x_n and using the periodic boundary conditions results in

$$\left(1 - \frac{\omega^2\tau}{V'\left(\frac{L}{N}\right)} + \frac{i\omega}{V'\left(\frac{L}{N}\right)}\right)^N = 1. \tag{6.23}$$

This implicitly defines v_0 as a function of h (through V) and can be solved for our specific choice of V (see (5.4)) to yield

$$v_0 = \frac{1 - \cos(2\pi j/N)}{\tau \sin^2(2\pi j/N)\left(1 - \tanh^2\left(h - \frac{L}{N}\right)\right)}, \tag{6.24}$$

where $j = \{1, 2, \ldots N-1\}$. The Hopf curves for the first four spatial frequencies ($j = 1, 2, 3, 4$) are shown in Figure 6.7(b). The analytical results for the first Hopf curve are in perfect agreement with the numerical data. Note that the curves for the Hopf bifurcation point and the fold point are close to each other in the parameter plane shown in Figure 6.7(b).

7. Conclusion and Outlook. In this paper we have derived an implicit method for equation-free analysis and proved its convergence for slow-fast systems with transversally stable slow manifolds. We gave a demonstration by performing an equation-free bifurcation analysis on a one-dimensional macroscopic description emerging from a microscopic traffic model based on a deterministic optimal velocity model for individual drivers. We demonstrated that the obtained bifurcation diagrams are independent of the lifting operator and the healing time in a suitable region. The bifurcation diagram shows a saddle-node bifurcation, which is continued in a two-parameter equation-free pseudoarclength continuation. Since the Hopf bifurcation, i.e., the macroscopic pitch fork, is known analytically, this traffic model is an ideal test case for comparison with new numerical methods. The stability in Figure 6.1 changes at $(v_0, \sigma) = (0.887, 0)$, i.e., sign change of the eigenvalue, indicating a bifurcation. In general, a sufficient characterization would require checking higher-order derivatives of the macroscopic right-hand-side F, which can be numerically demanding in an equation-free computation. A detailed study of the application of the presented implicit equation-free methods to study pitch-fork bifurcations is a possible research direction for future work.

The proof of convergence for the implicit coarse-level time stepper assumes that the slow manifold is transversally stable. The review [13] lists the senses in which a fast high-dimensional chaotic or stochastic system converging in the mean can be viewed as a slow-fast system converging to its slow manifold. In practical applications the result from Section 3.1 may be used as a plausibility check: the equation-free methodology of Kevrekidis *et al* appeals to the notions of singular perturbation theory (cf. the illustrative example in [24]). For any particular system under study, one can check whether this intuition is indeed justified by testing whether the results for the implicit time stepper given by (2.3) are indeed independent of the lifting $\mathcal{L}$ and the healing time t_{skip} if one varies both gradually. For example, Barkley, Kevrekidis and Stuart [2] show that moment maps for simple stochastic or chaotic systems violate this principle in certain regions of their phase space.

For the traffic problems studied in our paper, one long-standing problem is the motion of several phantom jams, i.e., multipulse solutions, relative to each other. For a large number of cars (including the $N = 60$ cars we used) this motion is very slow and therefore near impossible to observe in direct numerical simulations (a phenomenon that is called meta-stability). An open question is whether one can derive a computable criterion that predicts, for a given configuration of several jams and given driver parameters, which of those will collapse or merge and when. This criterion might be based on the shape of the traveling wave. One particularly appealing feature of equation-free analysis is that one can continue macroscopic equilibria in N, the number of cars, using the microscopic model. The complexity of the implicit scheme is independent of N. The increase of computational time is determined by the cost of the microscopic simulation with increasing N, since each function evaluation will be more costly (in our case, proportional to N). Hence, the computational complexity of the overall scheme is proportional to N.

Models closer to situations of practical interest, say with more realistic optimal velocity functions, randomly assigned driver behavior parameters, an element of randomness in the driver behavior, or multiple lanes, as discussed in the literature [17, 29, 31], are also amenable to equation-free analysis. This should provide additional information to help match parameters of macroscopic models to microscopic driver and road parameters.

Acknowledgments. J. Starke and R. Berkemer thank Toyota CRDL for financial support. J. Starke would also like to thank the Danish Research Council FTP under the project number 09-065890/FTP and the Villum Fonden under the VKR-Centre of Excellence 'Ocean Life' for financial support. The research of J. Sieber is supported by EPSRC grant EP/J010820/1.

Appendix A. Proof of Theorem 3.1. For the proof of Theorem 3.1 we have to analyze the two equations (for y and y_*, respectively)

$$\mathcal{R}(M_\varepsilon(t_{\text{skip}};\mathcal{L}(y))) = \mathcal{R}(M_\varepsilon(t_{\text{skip}}+\delta;\mathcal{L}(x))), \tag{A.1}$$

$$\mathcal{R}(M_\varepsilon(t_{\text{skip}};g_\varepsilon(\mathcal{L}(y_*)))) = \mathcal{R}(M_\varepsilon(t_{\text{skip}}+\delta;g_\varepsilon(\mathcal{L}(x)))). \tag{A.2}$$

In both equations $x \in \mathbb{R}^d$ enters as a parameter. For (A.2) we have established already in Section 3 that there exists a solution y_*, and that it is locally unique. Equations (3.13) and (3.14) gave a procedure for picking y_* in a globally unique way by starting with $y_* = x$ for $\delta = 0$ and then extending the solution for varying δ until one reaches the desired value of δ. This procedure achieves unique solvability for y_* for all $x \in \operatorname{dom}\mathcal{L}$ and for $t_{\text{skip}} \in [t_0, T_{\text{up}}/\varepsilon)$ and $\delta \geq 0$ satisfying $t_{\text{skip}} + \delta < T_{\text{up}}/\varepsilon$. For equation (A.1) we have to prove the existence of a solution y, and prove that it is close to y_* (including all derivatives with respect to x up to order k).

In order to do this, we need to make the consequences of Fenichel's Theorem more explicit. The Fenichel result (3.4) implies that the map ($\mathcal{U}$ is the neighborhood of $\mathcal{C}_0$, which also contains $\mathcal{C}_\varepsilon$)

$$\mathcal{F}_\varepsilon : \mathbb{R}\times\mathcal{U} \ni (\tau,u) \mapsto M_\varepsilon(\tau/\varepsilon; g_\varepsilon(u))$$

is well defined and k times differentiable for all $u \in \mathcal{U}$ and all $\tau \in \mathbb{R}$. This map $\mathcal{F}_\varepsilon$ is the flow map when restricted to the slow manifold $\mathcal{C}_\varepsilon$, and projects all points in the neighborhood of the slow manifold $\mathcal{C}_\varepsilon$ along the stable fibers using g_ε. Note that τ is the time on the *slow* time scale as we divide by ε in the evaluation of the map. The derivatives of $\mathcal{F}_\varepsilon$ with respect to its second argument u are uniformly bounded for all $u \in \mathcal{U}$ as long as as $\tau \in [0, T_{\text{up}}]$:

$$\|\partial_2^j \mathcal{F}_\varepsilon(\tau;\cdot)\| \leq C, \quad (j = 0\ldots, k, \text{ and } \tau \in [0, T_{\text{up}}]). \tag{A.3}$$

Correspondingly, the map

$$A_\varepsilon(\tau;\cdot) = \mathcal{R}(\mathcal{F}_\varepsilon(\tau;\mathcal{L}(\cdot))) : \operatorname{dom}\mathcal{L} \ni x \mapsto \mathcal{R}(M_\varepsilon(\tau/\varepsilon; g_\varepsilon(\mathcal{L}(x)))) \tag{A.4}$$

is well defined for all $\tau \in \mathbb{R}$ and locally invertible for all $\varepsilon \in [0, \varepsilon_0)$ and τ satisfying $|\tau| < T_{\text{up}}$. Note that the range of admissible ε includes $\varepsilon = 0$, because the limit of the right-hand side of (A.4) for $\varepsilon = 0$ is well defined as the solution of a differential-algebraic equation on $\mathcal{C}_0$ on

the slow time scale. The norms of the derivatives of A_ε and its (locally unique) inverse can be bounded by a uniform constant C independent of $\varepsilon \in [0, \varepsilon_0)$ and τ as long as $|\tau| \leq T_{\mathrm{up}}$:

$$\|\partial_2^j A_\varepsilon(\tau;\cdot)\| \leq C, \qquad \|\partial_2^j A_\varepsilon^{-1}(\tau;\cdot)\| \leq C. \tag{A.5}$$

Similarly, the motion transversal to the slow manifold $\mathcal{C}_\varepsilon$ consists of a fast decay and a slow tracking of the dynamics on $\mathcal{C}_\varepsilon$. Let $K < K_0$ be a given contraction rate, and choose the upper bound ε_0 such that the contraction property (3.5) of the stable fiber projection g_ε holds for all $\varepsilon < \varepsilon_0$ and all $u \in \mathcal{U}$. Then we can express the transversal component of the flow starting from an arbitrary $u \in \mathcal{U}$ and $t \geq 0$ in the form

$$M_\varepsilon(t;u) = M_\varepsilon(t; g_\varepsilon(u)) + \exp(-Kt) M_\varepsilon^\perp(t;u) \tag{A.6}$$

(this defines $M_\varepsilon^\perp$). In the right-hand side of (A.6) the map $M_\varepsilon^\perp$ is k times differentiable with respect to its argument u for all $\varepsilon \in [0, \varepsilon_0)$ (including $\varepsilon = 0$), and the norms of $M_\varepsilon^\perp(t;u)$ and its partial derivatives $\partial^j M_\varepsilon^\perp(t;u)$ are uniformly bounded for all $t \in [0,\infty)$, $\varepsilon \in [0,\varepsilon_0)$ and $u \in \mathcal{U}$:

$$\|M_\varepsilon^\perp(t;x)\| \leq C, \qquad \|\partial_2^j M_\varepsilon^\perp(t;x)\| \leq C. \tag{A.7}$$

The prefactor $\exp(-Kt)$ can also be extracted if the smooth restriction map $\mathcal{R}$ is applied to both terms on the left-hand side of (A.6), and if we insert $\mathcal{L}(x)$ for u. Thus,

$$\mathcal{R}(M_\varepsilon(t;\mathcal{L}(x))) - \mathcal{R}(M_\varepsilon(t; g_\varepsilon(\mathcal{L}(x)))) \tag{A.8}$$

$$= \int_0^1 \partial\mathcal{R}\Big(M_\varepsilon(t; g_\varepsilon(\mathcal{L}(x))) + \rho[M_\varepsilon(t;\mathcal{L}(x)) - M_\varepsilon(t; g_\varepsilon(\mathcal{L}(x)))]\Big)\,\mathrm{d}\rho \times [M_\varepsilon(t;\mathcal{L}(x)) - M_\varepsilon(t; g_\varepsilon(\mathcal{L}(x)))] \tag{A.9}$$

$$= \int_0^1 \partial\mathcal{R}\Big(\mathcal{F}_\varepsilon(\varepsilon t;\mathcal{L}(x)) + \rho\exp(-Kt) M_\varepsilon^\perp(t;\mathcal{L}(x))\Big)\,\mathrm{d}\rho \exp(-Kt) M_\varepsilon^\perp(t;\mathcal{L}(x)). \tag{A.10}$$

We applied the mean-value theorem to equate (A.8) and (A.9). To get to the right-hand side of (A.10), we inserted the representation (A.6) and used the definition of the map $\mathcal{F}_\varepsilon$. This right-hand side in (A.10) has the form

$$\text{right-hand side of (A.10)} = \exp(-Kt) r_\varepsilon(\varepsilon t, t; x), \tag{A.11}$$

where the first argument of r_ε refers to the time dependence of A_ε in the argument of $\partial\mathcal{R}$. Note that we have introduced the slow time scale as an additional argument into r_ε. We will consider $r_\varepsilon(\tau, t; x)$ for arbitrary $\tau \in [0, T_{\mathrm{up}}]$ and $t \in [0,\infty)$ below, and later insert $\tau = \varepsilon t$ as a particular case. The map $r_\varepsilon(\tau, t; x)$ is k times continuously differentiable with respect to x. The norm of r_ε and the norm of its derivatives with respect to x are uniformly bounded for $x \in \operatorname{dom}\mathcal{L}$, $\varepsilon \in [0,\varepsilon_0)$, $\tau \in [0, T_{\mathrm{up}}]$, and $t \in [0,\infty)$ because all of its ingredients have bounded derivatives (listed in (A.3), (A.7)):

$$\|r_\varepsilon(\tau, t; x)\| \leq C, \qquad \|\partial_3^j r_\varepsilon(\tau, t; x)\| \leq C \tag{A.12}$$

for $j \in \{1, \dots, k\}$. Let us define the times corresponding to t_{skip} and δ on the slow time scale as:

$$\tau_{\text{skip}} = \varepsilon t_{\text{skip}}, \qquad \Delta = \varepsilon\delta. \tag{A.13}$$

If τ_{skip} and $\tau_{\text{skip}} + \Delta$ are in $[0, T_{\text{up}}]$, then the solution y_* of the exact flow satisfies (using the locally invertible map A_ε defined in (A.4))

$$A_\varepsilon(\tau_{\text{skip}}; y_*) = A_\varepsilon(\tau_{\text{skip}} + \Delta; x). \tag{A.14}$$

Using r_ε and A_ε, equation (A.1) can be rewritten as

$$A_\varepsilon(\tau_{\text{skip}}; y) + s_1 r_\varepsilon(\tau_{\text{skip}}, t_1; y) = A_\varepsilon(\tau_{\text{skip}} + \Delta; x) + s_2 r_\varepsilon(\tau_{\text{skip}} + \Delta, t_2; x), \tag{A.15}$$

where

$$\begin{aligned} s_1 &= \exp(-K t_{\text{skip}}), \quad & s_2 &= \exp(-K(t_{\text{skip}} + \delta)), \\ t_1 &= t_{\text{skip}} \geq 0, & t_2 &= t_{\text{skip}} + \delta \geq 0. \end{aligned} \tag{A.16}$$

We will first consider solvability of (A.15) with respect to y for general s_1 and s_2 close to 0, and t_1, $t_2 \in [0, \infty)$. This solution y will depend on the parameters s_1, s_2, t_1, and t_2 (among others). Whenever we subsequently insert the particular values from (A.13) and (A.16) for τ_{skip}, Δ, s_1, s_2, t_1, and t_2, the solution y of (A.15) becomes also a solution of (A.1). For each of the terms, A_ε, A_ε^{-1}, and r_ε, we have uniform upper bounds ((A.5) and(A.12)) for their norms and all derivatives up to order k for the entire range of arguments: x, $y \in \operatorname{dom} \mathcal{L}$, $\tau_{\text{skip}} \in [0, T_{\text{up}}]$, $\tau_{\text{skip}} + \Delta \in [0, T_{\text{up}}]$, t_1, $t_2 \in [0, \infty)$, and $\varepsilon \in [0, \varepsilon_0)$ (where ε_0 is determined by the choice of decay rate K as given by Fenichel's Theorem). Thus, we can use (A.14) and (A.15) to establish the existence of y and its distance to y_* using the implicit function theorem at the point $s_1 = s_2 = 0$.

The exact solution y_* is a uniformly regular solution of (A.15) for $s_1 = s_2 = 0$, all $x \in \operatorname{dom} \mathcal{L}$, $\varepsilon \in [0, \varepsilon_0)$, $\tau_{\text{skip}} \in [0, T_{\text{up}}]$, and $\Delta \in [-\tau_{\text{skip}}, T_{\text{up}} - \tau_{\text{skip}}]$. Thus, for small s_1 and s_2, equation (A.15) has a locally unique solution $y \in \operatorname{dom} \mathcal{L}$ which depends smoothly on all parameters (we write $y(x, s_1, s_2)$ to emphasize the dependence on $(s_1, s_2) \in \mathbb{R}^2$) such that

$$\|\partial_1^j y(x, s_1, s_2) - \partial^j y_*(x)\|_\infty \leq C \|(s_1, s_2)\|_\infty$$

($j \in \{1, \dots, k\}$) for some constant C and all s_1, $s_2 \in (-\rho, \rho)$ for some $\rho > 0$. Consequently, if we choose t_0 such that $\exp(-K t_0) < \rho$ and decrease ε_0 such that $t_0 < T_{\text{up}}/\varepsilon_0$, then we have for all $\varepsilon \in (0, \varepsilon_0)$, $t_{\text{skip}} \in [t_0, T_{\text{up}}/\varepsilon]$, $\delta \in [0, T_{\text{up}}/\varepsilon - t_{\text{skip}}]$, and $x \in \operatorname{dom} \mathcal{L}$ that

$$\begin{aligned} &\Big\| \partial_1^j y\big(x, \exp(-K t_{\text{skip}}), \exp(-K(t_{\text{skip}} + \delta))\big) - \partial^j y_*(x) \Big\|_\infty \\ &\qquad \leq C \|(\exp(-K t_{\text{skip}}), \exp(-K(t_{\text{skip}} + \delta)))\|_\infty \\ &\qquad \leq C \exp(-K t_{\text{skip}}) \end{aligned}$$

for all $j \in \{1, \dots, k\}$. This establishes the convergence claim of Theorem 3.1 since y is the solution of (A.1) if $s_1 = \exp(-K\tau_{\text{skip}}/\varepsilon) = \exp(-K t_{\text{skip}})$, $s_2 = \exp(-K(\tau_{\text{skip}} + \Delta)/\varepsilon) = \exp(-K(t_{\text{skip}} + \delta))$, $t_1 = t_{\text{skip}}$, $t_2 = t_{\text{skip}} + \delta$, $\tau_{\text{skip}} = \varepsilon t_{\text{skip}}$, and $\Delta = \varepsilon\delta$.

Parameter	Value/range
τ^{-1}	1.7
L	60
N	60
μ	0.1
s	0.001
δ	2000
Δt	-5000
t_{skip}	300
v_0^*	0.8, ... ,1.0
h^*	1.0, ... ,1.7

Table B.1

Parameters for numerical studies. The quantities marked with an asterisk (*) are bifurcation parameters, where the range used is noted

Appendix B. Parameters. The parameters used for the simulations are listed in Table B.1.

Appendix C. Finite Differences. For the scheme (6.19), F is evaluated at the 17 points

$$
\begin{aligned}
&1 : (\sigma, v_0, h), \\
&2 : (\sigma + \Delta\sigma, v_0, h), && 3 : (\sigma + 2\Delta\sigma, v_0, h), \\
&4 : (\sigma + 3\Delta\sigma, v_0, h), && 5 : (\sigma + 4\Delta\sigma, v_0, h), \\
&6 : (\sigma, v_0 - \Delta v_0, h), && 7 : (\sigma, v_0 + \Delta v_0, h), \\
&8 : (\sigma + \Delta\sigma, v_0 - \Delta v_0, h), && 9 : (\sigma + \Delta\sigma, v_0 + \Delta v_0, h), \\
&10 : (\sigma + 2\Delta\sigma, v_0 - \Delta v_0, h), && 11 : (\sigma + 2\Delta\sigma, v_0 + \Delta v_0, h), \\
&12 : (\sigma, v_0, h - \Delta h), && 13 : (\sigma, v_0, h + \Delta h), \\
&14 : (\sigma + \Delta\sigma, v_0, h - \Delta h), && 15 : (\sigma + \Delta\sigma, v_0, h + \Delta h), \\
&16 : (\sigma + 2\Delta\sigma, v_0, h - \Delta h), && 17 : (\sigma + 2\Delta\sigma, v_0, h + \Delta h).
\end{aligned}
\tag{C.1}
$$

where $\Delta\sigma = \Delta v_0 = \Delta h = 0.001$ are offsets for the approximation. One can use the following second-order accuracy scheme to compute the derivatives (for better readability, the points

are just referred to by their number, e.g., $F_7 = F(\sigma, v_0 + \Delta v_0, h)$):

$$
\begin{aligned}
F_\sigma &= \frac{-3F_1 + 4F_2 - F_3}{2\Delta\sigma} \\
F_{v_0} &= \frac{F_7 - F_6}{2\Delta v_0} \\
F_h &= \frac{F_{13} - F_{12}}{2\Delta h} \\
F_{\sigma\sigma} &= \frac{-3(-3F_1 + 4F_2 - F_3) + 4(-3F_2 + 4F_3 - F_4) - (-3F_3 + 4F_4 - F_5)}{4(\Delta\sigma)^2} \\
F_{v_0\sigma} &= \frac{(-3F_7 + 4F_9 - F_11) - (-3F_6 + 4F_8 - F_{10})}{4\Delta\sigma\Delta v_0} \\
F_{h\sigma} &= \frac{(-3F_{13} + 4F_{15} - F_{17}) - (-3F_{12} + 4F_{14} - F_{16})}{4\Delta\sigma\Delta h}
\end{aligned}
$$

REFERENCES

[1] M. Bando, K. Hasebe, A. Nakayama, A. Shibata, and Y. Sugiyama, *Dynamical model of traffic congestion and numerical simulation*, Phys. Rev. E, 51 (1995), pp. 1035–1042.

[2] D. Barkley, I. G. Kevrekidis, and A. M. Stuart, *The moment map: nonlinear dynamics of density evolution via a few moments*, SIAM Journal on Applied Dynamical Systems, 5 (2006), pp. 403–434.

[3] B. P. Belousov, *A periodic reaction and its mechanism*, Collection of short papers on radiation medicine for 1958, (1959).

[4] L Chen, P.G Debenedetti, C.W Gear, and I.G Kevrekidis, *From molecular dynamics to coarse self-similar solutions: a simple example using equation-free computation*, Journal of Non-Newtonian Fluid Mechanics, 120 (2004), pp. 215 – 223.

[5] Jaime Cisternas, C. William Gear, Simon Levin, and Ioannis G. Kevrekidis, *Equation-free modelling of evolving diseases: coarse-grained computations with individual-based models*, Proceedings of the Royal Society of London. Series A: Mathematical, Physical and Engineering Sciences, 460 (2004), pp. 2761–2779.

[6] O. Corradi, P. Hjorth, and J. Starke, *Equation-free detection and continuation of a Hopf bifurcation point in a particle model of pedestrian flow*, SIAM Journal on Applied Dynamical Systems, 11 (2012), pp. 1007–1032.

[7] W. E and B. Engquist, *Multiscale modeling and computation*, Notices of the AMS, 50 (2003), pp. 1062–1070.

[8] Michael Elmegaard, Jan Rubel, Mizuho Inagaki, Atsushi Kawamoto, and Jens Starke, *Equation-free continuation of maximal vibration amplitudes in a nonlinear rotor-bearing model of a turbocharger*, ASME Conference Proceedings, 2009 (2009), pp. 369–378.

[9] N. Fenichel, *Geometric singular perturbation theory for ordinary differential equations*, Journal of Differential Equations, 31 (1979), pp. 53–98.

[10] Yu B. Gaididei, R. Berkemer, J. G. Caputo, P. L. Christiansen, A. Kawamoto, T. Shiga, M. P. Sorensen, and J. Starke, *Analytical solutions of jam pattern formation on a ring for a class of optimal velocity traffic models*, New J. Phys., 11 (2009), p. 073012.

[11] I. Gasser, G. Sirito, and B. Werner, *Bifurcation analysis of a class of 'car following' traffic models*, Physica D: Nonlinear Phenomena, 197 (2004), pp. 222 – 241.

[12] C. W. Gear, T. J. Kaper, I. G. Kevrekidis, and A. Zagaris, *Projecting to a slow manifold: Singularly perturbed systems and legacy codes*, SIAM Journal on Applied Dynamical Systems, 4 (2005), pp. 711–732.

[13] Dror Givon, Raz Kupferman, and Andrew Stuart, *Extracting macroscopic dynamics: model problems and algorithms*, Nonlinearity, 17 (2004), pp. 55–127.

[14] T. Gross and I. G. Kevrekidis, *Robust oscillations in SIS epidemics on adaptive networks: Coarse graining by automated moment closure*, Europhysics Letters, 82 (2008), p. 38004.
[15] H. Haken, *Advanced synergetics. Instability hierarchies of self-organizing systems and devices / Springer series in synergetics 20*, Springer, Berlin, 1983.
[16] ———, *Synergetics. An introduction. Nonequilibrium phase transitions and self organization in physics, chemistry and biology. 3.ed / Springer series in synergetics 1*, Springer, Berlin, 1983.
[17] Dirk Helbing, *Traffic and related self-driven many-particle systems*, Rev. Mod. Phys., 73 (2001), pp. 1067–1141.
[18] http://www.mathworks.com, Matlab R2011b, *64-bit (glnxa64)*.
[19] Masahiro Kanai, Katsuhiro Nishinari, and Tetsuji Tokihiro, *A stochastic optimal velocity model and its long-lived metastability*, Physical Review E, 72 (2009), p. 035102.
[20] Al Kelley, *The stable, center-stable, center, center-unstable, unstable manifolds*, Journal of Differential Equations, 3 (1967), pp. 546 – 570.
[21] Ioannis G. Kevrekidis, C. William Gear, and Gerhard Hummer, *Equation-free: The computer-aided analysis of complex multiscale systems*, AIChE Journal, 50 (2004), pp. 1346–1355.
[22] Ioannis G. Kevrekidis, C. William Gear, James M. Hyman, Panagiotis G. Kevrekidis, Olof Runborg, and Constantinos Theodoropoulos, *Equation-free, coarse-grained multiscale computation: enabling microscopic simulators to perform system-level analysis*, Communications in Mathematical Sciences, 1 (2003), pp. 715 – 762.
[23] Ioannis G. Kevrekidis and Giovanni Samaey, *Equation-free multiscale computation: Algorithms and applications*, Annual Review of Physical Chemistry, 60 (2009), pp. 321–344.
[24] Y. Kevrekidis and G. Samaey, *Equation-free modeling*, Scholarpedia, 5 (2010), p. 4847.
[25] Yuri A. Kuznetsov, *Elements of Applied Bifurcation Theory*, vol. 112 of Applied Mathematical Sciences, Springer, New York, third ed., 2004.
[26] Carlo Laing, *On the application of 'equation-free modelling' to neural systems*, Journal of Computational Neuroscience, 20 (2006), pp. 5–23.
[27] Ju Li, Panayotis G. Kevrekidis, C. William Gear, and Ioannis G. Kevrekidis, *Deciding the nature of the coarse equation through microscopic simulations: The baby-bathwater scheme*, Multiscale Modeling & Simulation, 1 (2003), pp. 391–407.
[28] Alexei G. Makeev, Dimitrios Maroudas, Athanassios Z. Panagiotopoulos, and Ioannis G. Kevrekidis, *Coarse bifurcation analysis of kinetic Monte Carlo simulations: A lattice-gas model with lateral interactions*, The Journal of Chemical Physics, 117 (2002), pp. 8229–8240.
[29] Takashi Nagatani, *The physics of traffic jams*, Reports on Progress in Physics, 65 (2002), p. 1331.
[30] Gabor Orosz, Bernd Krauskopf, and R.Eddie Wilson, *Bifurcations and multiple traffic jams in a car-following model with reaction-time delay*, Physica D: Nonlinear Phenomena, 211 (2005), pp. 277 – 293.
[31] Gabor Orosz, R. Eddie Wilson, and Gabor Stepan, *Traffic jams: dynamics and control*, Philosophical Transactions of the Royal Society A: Mathematical, Physical and Engineering Sciences, 368 (2010), pp. 4455–4479.
[32] Lord Rayleigh, *On convection currents in a horizontal layer of fluid, when the higher temperature is on the under side*, Phil. Mag., Ser.6, 32 (1916), pp. 529 – 546.
[33] Andreas I. Reppas, Andreas C. Tsoumanis, and Constantinos I. Siettos, *Coarse-grained bifurcation analysis and detection of criticalities of an individual-based epidemiological network model with infection control*, Applied Mathematical Modelling, 34 (2010), pp. 552 – 560.
[34] E. Sanchez-Palencia, *Homogenization method for the study of composite media*, in Asymptotic Analysis II, F. Verhulst, ed., vol. 985 of Lecture Notes in Mathematics, Springer Berlin Heidelberg, 1983, pp. 192–214.
[35] Keizo Shigaki, Jun Tanimoto, and Aya Hagishima, *A revised stochastic optimal velocity model considering the velocity gap with a preceding vehicle*, Int. J. Mod. Phys. C, 22 (2011), pp. 1005–1014.
[36] C. I. Siettos, A. Armaou, A. G. Makeev, and I. G. Kevrekidis, *Microscopic/stochastic timesteppers and 'coarse' control: A KMC example*, AIChE Journal, 49 (2003), pp. 1922–1926.
[37] C. I. Siettos, M. D. Graham, and I. G. Kevrekidis, *Coarse Brownian dynamics for nematic liquid crystals: Bifurcation, projective integration, and control via stochastic simulation*, The Journal of Chemical Physics, 118 (2003), pp. 10149–10156.

[38] Herbert Spohn, *Large scale dynamics of interacting particles*, Texts and Monographs in Physics, Springer-Verlag, 1991.

[39] Christophe Vandekerckhove, Benjamin Sonday, Alexei Makeev, Dirk Roose, and Ioannis G. Kevrekidis, *A common approach to the computation of coarse-scale steady states and to consistent initialization on a slow manifold*, Computers & Chemical Engineering, 35 (2011), pp. 1949 – 1958.

[40] A. Vanderbauwhede, *Center manifolds, normal forms and elementary bifurcations*, Dynamics Reported, 2 (1989).

[41] David A. Young, *A local activator-inhibitor model of vertebrate skin patterns*, Mathematical Biosciences, 72 (1984), pp. 51 – 58.

[42] Antonios Zagaris, C. William Gear, Tasso J. Kaper, and Yannis G. Kevrekidis, *Analysis of the accuracy and convergence of equation-free projection to a slow manifold*, ESAIM: Mathematical Modelling and Numerical Analysis, 43 (2009), pp. 757–784.

[43] A. Zagaris, C. Vandekerckhove, C. W. Gear, T. J. Kaper, and I. G. Kevrekidis, *Stability and stabilization of the constrained runs schemes for equation-free projection to a slow manifold*, Discrete and Continuous Dynamical Systems - Series A, 32 (2012), pp. 2759 – 2803.

[44] A. M. Zhabotinsky, *Periodical oxidation of malonic acid in solution (a study of the Belousov reaction kinetics)*, Biofizika, 9 (1964), pp. 306–11.

II Equation-Free Analysis of Macroscopic Behavior in Traffic and Pedestrian Flow

This paper is a proceedings article following up on the "Conference on Traffic and Granular Flow 2013" held at the Forschungszentrum Jülich in Germany [MSHS14]. The main results from Paper I have been presented from the point of view of applications and highlight the benefits for the traffic community. At the same conference, Jens Starke presented the results from [CHS12] about equation-free modeling in pedestrian problems. Together with our collaborators Jan Sieber (University of Exeter) and Poul G. Hjorth (Technical University of Denmark), we wrote this proceedings article on equation-free modeling in traffic and pedestrian flow.

The paper gives an overview about applications of implicit equation-free methods in the traffic community and demonstrates parallels in the analysis of traffic and pedestrian problems. The presentation aims at an audience familiar with modeling of car and pedestrian traffic, but not so familiar with multi-scale analysis. Further, the article focusses on a clear presentation of the topic, where many mathematical details, e.g., proofs, are omitted. Thus, the article fills a gap between the mathematics and traffic community and hopefully helps to enhance communication between these communities in order to combine knowledge across the borders of the separate fields.

At the hand-in date of the thesis the paper has been accepted for publication in "Traffic and Granular Flow'13" (Springer) with an expected publication in November 2014.

Equation-Free Analysis of Macroscopic Behavior in Traffic and Pedestrian Flow

Christian Marschler, Jan Sieber, Poul G. Hjorth and Jens Starke

Abstract Equation-free methods make possible an analysis of the evolution of a few coarse-grained or macroscopic quantities for a detailed and realistic model with a large number of fine-grained or microscopic variables, even though no equations are explicitly given on the macroscopic level. This will facilitate a study of how the model behavior depends on parameter values including an understanding of transitions between different types of qualitative behavior. These methods are introduced and explained for traffic jam formation and emergence of oscillatory pedestrian counter flow in a corridor with a narrow door.

1 Introduction

The study of pedestrian and traffic dynamics leads naturally to a description by a few macroscopic, e.g., averaged, quantities of the systems at hand. On the other hand, so-called microscopic models, e.g., multiagent systems, inherit individual properties of the agents and can therefore be made very realistic. Among more successful microscopic models are social force models for pedestrian dynamics [1, 2, 3] and optimal velocity models in traffic dynamics [4, 5, 6, 7, 8]. Although computer simulations of microscopic models for specific scenarios are straightforward to perform it is often more relevant and useful to look at the systems on a coarse scale, e.g., to investigate a few macroscopic quantities like first-order moments of distributions or other macroscopic descriptions which are motivated by the application.

Christian Marschler (e-mail: chrms@dtu.dk), Poul G. Hjorth (e-mail: pghj@dtu.dk), Jens Starke (e-mail: jsta@dtu.dk)
Department of Applied Mathematics and Computer Science, Technical University of Denmark, DK-2800 Kongens Lyngby, Denmark,

Jan Sieber (e-mail: j.sieber@exeter.ac.uk)
College of Engineering, Mathematics and Physical Sciences, University of Exeter, EX4 4QF Exeter, United Kingdom

The analysis of the macroscopic behavior of microscopically defined models is possible by the so-called *equation-free* or *coarse analysis*. This approach is motivated and justified by the observation, that multi-scale systems, e.g., many-particle systems, often exhibit low-dimensional behavior. This concept is well known in physics as slaving of many degrees of freedom by a few slow variables, sometimes refered to as "order parameters" (see e.g. [9, 10]) and is formalized mathematically for slow-fast systems by Fenichel's theory [11]. These methods aim for a description of the system in terms of a small number of variables, which describe the interesting dynamics. This results in a dimension reduction from many degrees of freedom to a few degrees of freedom. For example, in pedestrian flows, we reduce the full system of equations of motion with equations of motion for each single pedestrian to a low-dimensional system for weighted mean position and velocity of the crowd.

A difficulty for such a macroscopic analysis is that governing equations for the coarse variables, i.e., the order parameters, are often not known. Those equations are often very hard or sometimes even impossible to derive from first principles especially in models with a very complicated microscopic dynamics. To extract information about the macroscopic behavior from the microscopic models equation-free methods [12, 13, 14, 15] can be used. This is done by using a special scheme for switching between microscopic and macroscopic levels by restriction and lifting operators and suitably initialized short microscopic simulation bursts in between. Problems with the initialization of the microscopic dynamics, i.e., the so-called lifting error, have been studied in [8]. An *implicit equation-free method* for simplifying the lifting procedure has been introduced, allowing for avoiding lifting errors up to an error which can be estimated for reliable results [8]. The equation-free methodology is most suitable in cases where governing equations for coarse variables are either not known, or when one wants to study finite-size effects if the number of particles is too large for investigation of the full system, but not large enough for a continuum limit. It is even possible to apply equation-free and related techniques in experiments, where the microscopic simulation is replaced by observations of an experiment [16, 17, 18].

For pedestrian and for traffic problems, a particularly interesting case is a systematic study of the influence of parameters on solutions of the system. This leads to equation-free bifurcation analysis. One obtains qualitative as well as quantitative information about the solutions and their stability. Furthermore, it saves computational time and is therefore advantageous over a brute-force analysis or computation. The knowledge of parameter dependence and the basin of attraction of solutions is crucial for controling systems and ensuring their robustness. Changes of solutions are summarized in bifurcation diagrams and solution branches are usually obtained by means of numerical continuation. These techniques from numerical bifurcation analysis can be combined with equation-free methods to gain insight into the macroscopic behavior in a semi-automatic fashion.

In the following, we apply *equation-free bifurcation analysis* to two selected problems in traffic and pedestrian dynamics. Section 2 gives a short overview about equation-free methods. The methods introduced in Section 2 are then applied to study traffic jams in the optimal velocity model (cf. [4, 8]) in Section 3. Section 4

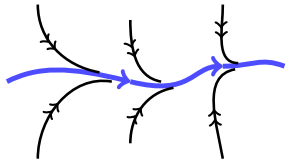

Fig. 1 Fast convergence to a slow manifold (thick blue curve). Trajectories in many dynamical systems converge very quickly to a slow manifold, along which the long-time macroscopic behavior takes place.

describes the macroscopic analysis of two pedestrian groups in counterflow through a bottleneck (cf. [3]) and Section 5 concludes the paper with a brief discussion and an outlook on future research directions.

2 Equation-Free Methods

Equation-free methods have been introduced (cf. [14, 15] for reviews) to study the dynamics of multi-scale systems on a macroscopic level without the need for an explicit derivation of macroscopic equations from the microscopic model. The necessary information is obtained by suitably initialized short simulation bursts of the microscopic system at hand. Equation-free methods assume that the system under investigation can be usefully described on a coarse scale. Evolution equations on the macroscopic level are not given explicitly. A big class of suitable systems are slow-fast systems, which have a separation of time scales. Under quite general assumptions (cf. [11]) these systems quickly converge to a low-dimensional object in phase space, the so-called *slow manifold* (cf. Fig. 1). The long-term dynamics (i.e., the macroscopic behavior) happens on this slow manifold, which is usually of much lower dimension than the overall phase space (of the microscopic system). The goal of equation-free methods is to gain insight into the dynamics on this slow manifold.

In the following we discuss the equation-free methodology in detail. The construction of a so-called macroscopic time stepper requires three ingredients to be provided by the user: the lifting $\mathscr{L}$ and restriction $\mathscr{R}$ operators to communicate between the microscopic and macroscopic levels and vice versa, and the microscopic time stepper M. Due to a separation of time scales, it is possible to construct the macroscopic time stepper by a *lift-evolve-restrict-scheme*. This scheme is subsequently used to perform bifurcation analysis and numerical continuation.

Microscopic time stepper M

To be specific, let us consider a microscopic model in the form of a high-dimensional system of N differential equations

$$\dot{u} = f(u). \tag{1}$$

This can be any model of traffic or pedestrian dynamics, possibly depending on a set of parameters. We generally assume that the number of degrees of freedom and thereby the dimension N of u is large. Note that a second-order model, e.g., the social force model with forces $f_{\text{force}}(x)$, can be written as a first-order model of the type (1) by including the velocities $\dot{x} = v$ into the equation. Then u has the form $u = (x, v)$, and the right-hand side is $f(u) = f((x, v)) = [v, f_{\text{force}}(x)]$. We assume that a microscopic time stepper M for model (1) is available. That is, we have a routine M (usually a simulation or software package) with two inputs: the time $t \in \mathbb{R}$ by which we want to evolve and the initial state $u_0 \in \mathbb{R}^N$ from which we start. The output $M(t, u_0) \in \mathbb{R}^N$ is defined by the relation

$$u(t_0 + t) = M(t, u(t_0)). \tag{2}$$

That is $M(t, u_0)$ is the state u of (1) after time t, starting from u_0 at time t_0.

Separation of time scales

We also assume that the dynamics on the macroscopic scale can be described by a few macroscopic variables $x \in \mathbb{R}^n$, where n is much smaller than the phase space dimension N of the microscopic model. This assumption is typically true in many-particle systems, e.g., pedestrian flow and traffic problems. The goal of equation-free methods is then to construct a time stepper for x on the macroscopic level,

$$x(t_0 + t) = \Phi(t, x(t_0)), \tag{3}$$

based on repeated and appropriately initialized runs, i.e., simulation bursts, of the microscopic time stepper M for u. In practice, a user of equation-free methods begins with the identification of a map, the so-called restriction operator

$$\mathscr{R} : \mathbb{R}^N \to \mathbb{R}^n,$$

which reduces a given microscopic state $u \in \mathbb{R}^N$ to a value of the desired macroscopic variable $x \in \mathbb{R}^n$. The assumption about the variables x describing the dynamics at the macroscopic scale has to be made more precise. We require that for all relevant initial conditions u and a sufficiently long transient time t_{skip} the result of the microscopic time stepper (2) is (at least locally and up to a small error) uniquely determined by its restriction, i.e., its macroscopic behavior. That is, if for two initial

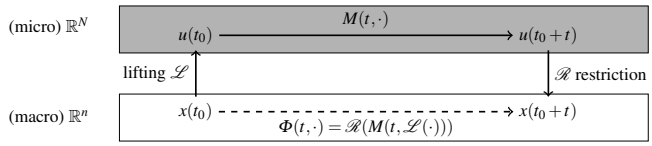

Fig. 2 Scheme for construction of the macroscopic time stepper Φ using the lifting $\mathscr{L}$ and restriction operator $\mathscr{R}$ for switching between microscopic and macroscopic levels. M denotes the microscopic time stepper.

conditions u_0 and u_1 the relation

$$\begin{aligned} &\mathscr{R}M(t_{\text{skip}};u_0) = \mathscr{R}M(t_{\text{skip}};u_1) \quad \text{holds, then} \\ &|\mathscr{R}M(t_{\text{skip}}+t;u_0) - \mathscr{R}M(t_{\text{skip}}+t;u_1)| < C\exp(\varepsilon t - \gamma t_{\text{skip}}) \end{aligned} \tag{4}$$

for all $t \geq 0$. In (4) the pre-factor C should be of order unity and independent of the choice of t, u_0 and u_1. The growth rate ε is also assumed to be smaller than the decay rate γ. This is what we refer to as *separation of time scales* between macroscopic and microscopic dynamics. Requirement (4) makes the statement "the dynamics of u on long time scales can be described by the macroscopic variable $x = \mathscr{R}u$" more precise. We also see that the error in this description can be made as small as desired by increasing the *healing time* t_{skip}. In fact, requirement (4) determines what a good choice of t_{skip} is for a given problem.

In order to complete the construction of the macroscopic time stepper Φ, the user has to provide a lifting operator

$$\mathscr{L} : \mathbb{R}^n \to \mathbb{R}^N,$$

which reconstructs a microscopic state u from a given macroscopic state x. See [19, 20, 21] for proposals how to construct good lifting operators for explicit equation-free methods (see Eq. (6) below). In the case of implicit equation-free methods the choice of a lifting operator is not as delicate [8]. Also note that the choice of lifting operator is not unique.

Macroscopic time stepper Φ

We can now assemble the approximate macroscopic time stepper Φ for x by applying the steps *Lift-Evolve-Restrict*, as illustrated in Fig. 2 in a judicious manner (cf. Fig. 3 for a detailed construction): the time-t image $y = \Phi(t;x)$ of an initial condition $x \in \mathbb{R}^n$ is defined as the solution y of the implicit equation

$$\mathscr{R}M(t_{\text{skip}};\mathscr{L}y) = \mathscr{R}M(t_{\text{skip}}+t;\mathscr{L}x). \tag{5}$$

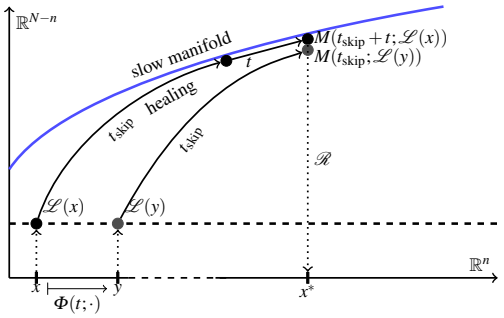

Fig. 3 Visualization of the implicit scheme (5). The macroscopic time stepper Φ maps the macroscopic state x to the yet unknown macroscopic state y. The scheme *lift-evolve-restrict* is applied to both states. Additionally to the healing step t_{skip} the dynamics on the slow manifold are observed for state x for an additional (long) time t. Both "paths" are compared at the macroscopic end point x^*. Note, that this scheme defines y implicitly.

Note, that the macroscopic time stepper has originally been introduced as the explicit definition (cf. also Fig. 2)

$$\tilde{\Phi}(t;x) = \mathscr{R}M(t;\mathscr{L}x). \tag{6}$$

The explicit method (6) requires that the lifting operator maps onto (or very close to) the slow manifold for every macroscopic point x. The implicit method (5) does not have this requirement and should be the method of choice (cf. the discussion in Section 3). The implementation of the explicit and implicit time stepper is further illustrated in Table 1 using pseudocode. Equation (5) is a nonlinear but in general regular system of n equations for the n-dimensional variable y. Note that the construction (5) does not require an explicit derivation of the right-hand side $F : \mathbb{R}^n \to \mathbb{R}^n$ of the assumed-to-exist macroscopic dynamical system

$$\dot{x} = F(x). \tag{7}$$

However, it can be used to evaluate (approximately) the right-hand side F in desired arguments x (see below). The convergence of the time stepper Φ to the correct time-t map Φ_* of the assumed-to-exist macroscopic equation (7) is proven in detail in [8]. The error $|\Phi(t;x) - \Phi_*(t;x)|$ is of order $\exp(\varepsilon t - \gamma t_{\text{skip}})$.

required functions: lift, evolve, restrict (cf. main text)
solution at time t0: x

```
function res = Phi(t,x)
u1 = lift(x); u2 = evolve(t,u1); res = restrict(u2);
end
```

explicit scheme	implicit scheme

`y = Phi(t,x);`	`choose dy, tol, y[0] = x, n = 0, err = 2*tol`
	
	`function res = F(y)`
	`  res = Phi(tskip,y) - Phi(tskip+t,x);`
	`end`
	
	`while err > tol`
	`  Fy  = F(y[n]);`
	`  dF  = Jacobian(F,y[n],dy);`
	`  y[n+1]  = y[n] - (dF)^(-1)*(Fy);`
	`  err  = abs(y[n+1] - y[n]);`
	`  n  = n+1;`
	`end`
	`y  = y[n];`

Table 1 Pseudocode algorithm for computing the macroscopic solution y after time t using the macroscopic time stepper for the solution x using the explicit (6) and implicit (5) scheme, respectively. The implicit scheme uses a Newton iteration with a given tolerance `tol` to find y. For one-dimensional y the Jacobian `dF` is given by `(F(y[n]+dy)-F(y[n]))/dy`. Note, that the complexity of the implicit scheme stems mainly from the Newton iteration, which is not specific for equation-free computations.

Advantages of equation-free methods

What additional benefits can the macroscopic time stepper Φ have beyond simulation of the low-dimensional dynamics (which could have been accomplished by running long-time simulations using M directly)?

- *Finding locations of macroscopic equilibria* regardless of their dynamical stability: macroscopic equilibria x are given by solutions to the n-dimensional implicit equation $\Phi(t_0;x) = x$, or, in terms of lifting and restriction:

$$\mathscr{R}M(t_{\text{skip}} + t_0; \mathscr{L}x) = \mathscr{R}M(t_{\text{skip}}; \mathscr{L}x) \tag{8}$$

  for a suitably chosen time t_0 (a good choice is of the same order of magnitude as t_{skip}). The stability of an equilibrium x, found by solving (8), is determined by solving the generalized eigenvalue problem $Ax = \lambda Bx$ with the Jacobian matrices

$$A = \frac{\partial}{\partial x}\mathscr{R}M(t_{\text{skip}} + t_0; \mathscr{L}x), \quad B = \frac{\partial}{\partial x}\mathscr{R}M(t_{\text{skip}}; \mathscr{L}x).$$

Stability is determined by the modulus of the eigenvalues λ (where $|\lambda| < 1$ corresponds to stability).

- *Projective integration* of (7): one can integrate the macroscopic system (7) by point-wise approximation of the right-hand side F and a standard numerical integrator. For example, the explicit Euler scheme for (7) would determine the value $x_{k+1} \approx x((k+1)\Delta t)$ from $x_k \approx x(k\Delta t)$ implicitly by approximating

$$F(x_k) = \frac{1}{\delta}\left[\mathscr{R}M(t_{\text{skip}}+\delta;\mathscr{L}x_k) - \mathscr{R}M(t_{\text{skip}};\mathscr{L}x_k)\right]$$

with a small time δ, and then solving the implicit equation

$$\mathscr{R}M(t_{\text{skip}};\mathscr{L}x_{k+1}) - \mathscr{R}M(t_{\text{skip}};\mathscr{L}x_k) = F(x_k)$$

with respect to x_{k+1}. Projective integration is useful if the macroscopic time step Δt can be chosen such that $\Delta t \gg \delta$, or for negative Δt, enabling integration backward in time for the macroscopic system (7).

- *Matching the restriction*: Sometimes it is useful to find a "realistic" microscopic state u, corresponding to a given macroscopic value x. "Realistic" corresponds in this context to "after rapid transients have settled". This can be accomplished by solving the nonlinear equation

$$\mathscr{R}M(t_{\text{skip}};\mathscr{L}y) = x \tag{9}$$

for y and then setting $u = M(t_{\text{skip}};\mathscr{L}y)$.

The formulas (8) and (9) have already been presented and tested in [22], where they were found to have vastly superior performance compared to alternative proposals for consistent lifting (such as presented in [19, 20, 21]).

Bifurcation analysis and numerical continuation

Building on top of the basic uses of the macroscopic time stepper Φ, one can also use advanced tools for the study of parameter-dependent systems. Suppose that the microscopic time stepper M (and, thus, the macroscopic time stepper Φ) depends on a system parameter p. We are interested in how macroscopic equilibria and their stability change as we vary p. In the examples in Sections 3 and 4 the primary system parameter is the target velocity (traffic) and door width (pedestrians), respectively.

When tracking equilibria in a parameter-dependent problem one may start at a parameter value p_0, where the desired equilibrium x_0 (given by $\Phi(t_0;x_0,p_0) = x_0$) is stable so that it can be found by direct simulations. This achieves a good initial guess, which is required to solve the nonlinear equations (8) reliably with a Newton iteration for near-by p close to p_0. In the traffic system studied in Section 3 the equilibrium corresponding to a single phantom jam undergoes a saddle-node bifurcation (also called fold, that is, the equilibrium turns back in the parameter changing

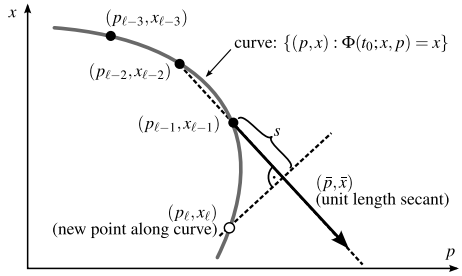

Fig. 4 Pseudo-arclength continuation of a curve of fixed points $\{(p,x) : \Phi(t_0;x,p) = x\}$ of the macroscopic time stepper Φ. A new point $(\bar{p},\bar{x})$ is computed along the secant through $(p_{\ell-2},x_{\ell-2})$ and $(p_{\ell-1},x_{\ell-1})$ in a so-called predictor step. The following corrector step solves the equilibrium condition (cf. (10)) in the perpendicular direction to find the next equilibrium (p_ℓ,x_ℓ) on the curve.

its stability, see Fig. 5(a) for an illustration). In order to track equilibria near folds one needs to extend the nonlinear equation for the macroscopic equilibrium with a so-called pseudo-arclength condition, and solve for the equilibrium x and the parameter p simultaneously [23, 24]. That is, suppose we have already found a sequence (p_k,x_k), $k = 1,\ldots,\ell-1$, of equilibria and parameter values. We then determine the next pair (p_ℓ,x_ℓ) by solving the extended system for (p_ℓ,x_ℓ):

$$\begin{aligned} 0 &= \Phi(t_0;x_\ell,p_\ell) - x_\ell && \text{equilibrium condition} \\ s &= \bar{p}_\ell(p_\ell - p_{\ell-1}) + \bar{x}_\ell^T(x_\ell - x_{\ell-1}) && \text{pseudo-arclength condition.} \end{aligned} \tag{10}$$

The vector

$$(\bar{p}_\ell,\bar{x}_\ell^T) = \frac{(p_{\ell-1}-p_{\ell-2},x_{\ell-1}^T - x_{\ell-2}^T)}{|(p_{\ell-1}-p_{\ell-2},x_{\ell-1}^T - x_{\ell-2}^T)|} \tag{11}$$

is the secant through the previous two points, scaled to unit length, and s is the approximate desired distance of the newly found point (p_ℓ,x_ℓ) from its predecessor $(p_{\ell-1},x_{\ell-1})$. The continuation method (10) permits one to track equilibria through folds such as shown in Fig. 5(a) or Hopf bifurcations such as shown in Fig. 6(b) (where the equilibrium becomes unstable and small-amplitude oscillations emerge). For a more detailed review on methods for bifurcation analysis the reader is referred to standard references, e.g., [23, 24].

3 Traffic Models

We apply the methods introduced in Section 2 to the optimal velocity (OV) model [4] as an example of microscopic traffic models. The model captures the main features of experiments of cars on a ring road [6]. We exploit equation-free numerical bifur-

cation analysis to answer the following questions; 1) for which parameter values in the OV model do we expect traffic jams and 2) how severe are they?

The equations of motion for car n in the OV model are

$$\tau\ddot{x}_n + \dot{x}_n = V(x_{n+1} - x_n), \qquad V(\Delta x_n) = v_0(\tanh(\Delta x_n - h) + \tanh(h)), \tag{12}$$

where $\tau = 0.588$ is the reaction time and V is the optimal velocity function depending on the velocity parameter v_0 and inflection point h. Periodic boundary conditions $x_{n+N} = x_n + L$ are used for $N = 60$ cars on a ring road of length $L = 60$. Depending on the choice of v_0 and h one observes uniform flow, i.e., all cars have *headway* $\Delta x_n = 1$, or a traffic jam, i.e., a region of high density of cars. It is worth noting, that bistable parameter regimes can exist, i.e., a stable uniform flow and a stable traffic jam coexist and one or the other emerges, depending on initial conditions.

First, we fix $h = 1.2$ and study the bifurcation diagram in dependence of v_0. Before we are able to apply the algorithms presented in Section 2, we have to define the lifting and restriction operators.

The restriction and lifting operators

The restriction operator $\mathscr{R}$, used to compute the macroscopic variable to describe phenomena of interest (here the deviation of the density profile from a uniform flow) of the microscopic model on a coarse level, is chosen as the standard deviation of the distribution of headway values

$$\mathscr{R}(u) = \sigma = \sqrt{\frac{1}{N-1}\sum_{n=1}^{N}(\Delta x_n - \langle \Delta x \rangle)^2}, \tag{13}$$

where $\langle \Delta x \rangle$ is the mean headway.

As the numerical continuation operates in a local neighborhood of the states, the lifting operator can be based on a previously computed microscopic reference state $\tilde{u} = (\tilde{x}, \tilde{y})$ for positions $\tilde{x}$ and velocities $\tilde{y}$ and its macroscopic image under $\mathscr{R}$, $\tilde{\sigma} = \mathscr{R}\tilde{u}$. We use $\tilde{u}$ and $\tilde{\sigma}$ to obtain a microscopic profile u for every $\sigma \approx \tilde{\sigma}$:

$$\mathscr{L}_\mu(\tilde{u}, \sigma) = u = (x, y) = (x_{\text{new}}, V(x_{\text{new}})), \quad x_{\text{new}} = \frac{\mu\sigma}{\tilde{\sigma}}(\Delta\tilde{x} - \langle \Delta\tilde{x} \rangle) + \langle \Delta\tilde{x} \rangle. \tag{14}$$

We let the lifting $\mathscr{L}_\mu$ depend on an artificial parameter μ. We will vary μ later to demonstrate that the resulting bifurcation diagram is independent of the particular choice of $\mathscr{L}$.

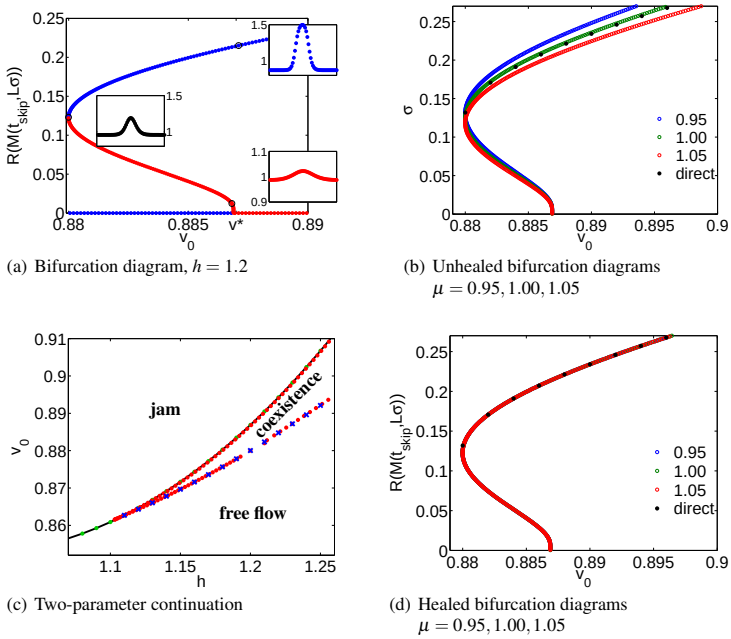

(a) Bifurcation diagram, $h = 1.2$

(b) Unhealed bifurcation diagrams $\mu = 0.95, 1.00, 1.05$

(c) Two-parameter continuation

(d) Healed bifurcation diagrams $\mu = 0.95, 1.00, 1.05$

Fig. 5 Equation-free bifurcation analysis for the optimal velocity model (12). (a) Bifurcation diagram in healed quantities for $h = 1.2$. Headway profiles are shown for selected points (black circles) along the branch. Blue and red dots denote stable and unstable solutions, respectively. (b) and (d) show bifurcation diagrams for different lifting operators. Healed values in (d) lie exactly on the same branch and recover the results from direct simulation (black dots). Thus, the choice of lifting operator $\mathscr{L}$ does not affect the results if one reports the healed values (in contrast to (b), reporting the solutions σ of (8)). (c) Two-parameter bifurcation diagram for continuation of the fold point. Saddle-node (blue crosses) and Hopf points (green dots) from measurements in one-dimensional diagrams are in perfect agreement with the continuation in two parameters h and v_0 and the analytical curve (black line).

Numerical results

The results of the equation-free bifurcation analysis are shown in Fig. 5. The bifurcation diagram for fixed $h = 1.2$ (cf. Fig. 5(a)) shows a stable traffic jam for parameter values $v_0 > v^* = 0.887$. By continuation of the solution from a stable traffic jam towards smaller values of v_0 a saddle-node bifurcation is found at $v_0 = 0.88$. The traffic jam loses stability and an unstable solution exists for $v_0 \in [0.88, 0.887]$. Continuing further along the branch, a Hopf bifurcation, i.e., a macroscopic pitchfork bifurcation, where traffic jams are born as small-amplitude time-periodic patterns,

is found at $v_0 = 0.887$. At this point, stable uniform flow solutions ($\sigma = 0$) change their stability to unstable uniform flow solutions. For $v_0 \in [0.88, 0.887]$ two stable solutions coexist. In this one-dimensional system, the unstable solution separates the stable and the unstable fixed point, acting as a barrier. Thus, the bifurcation diagram also informs us about the magnitude of the disturbance necessary to change the behavior of the system from a stable traffic jam to a stable free flow. Headway profiles are shown for selected points along the branch to illustrate the microscopic solutions. In Fig. 5(b) and Fig. 5(d) the comparison of different lifting operators is shown. While the unhealed values σ (cf. Fig. 5(b)) of the equilibrium depends on the choice of μ, the healed values $\mathscr{R}M(t_{\text{skip}};\mathscr{L}\sigma)$, used in the implicit equation-free methods (cf. Fig. 5(d) and [8]) are in perfect agreement with results from direct simulations (black dots).

In order to study the dependence on both parameters v_0 and h simultaneously, we use an extended set of equations to continue the saddle-node bifurcation point in Fig. 5(c). Blue crosses and green dots denote measurements of the saddle-node and Hopf points from one-parameter continuations, respectively. The two-parameters continuation (red dots) is in perfect agreement with the measurements. As a check of validity, the Hopf curve (black line below red dots) can be computed analytically (cf. e.g., [8]) and is shown for comparison.

In conclusion, the analysis pinpoints the parameter values for the onset and collapse of traffic jams. This information is of potential use to understand the role of speed limits. The two-parameter bifurcation diagram in Fig. 5(c) shows a free flow regime for small v_0 and large h (bottom right part of the diagram). On the other hand, a large velocity parameter v_0 and a small safety distance h lead to traffic jams (top left part). In between, a coexistence between free flow and traffic jams is found. The final state depends on the initial condition. A speed limit lower than the saddle-node values is necessary to assure a global convergence to the uniform free flow.

4 Pedestrian Models

For further demonstration of the equation-free bifurcation analysis, we also apply it to a social force model describing pedestrian flow [1, 25]. A particular setup with two crowds passing a corridor with bottleneck [26] from opposite sites (the crowd marked blue moving to the right, the crowd marked red moving to the left) is analyzed with respect to qualitative changes of the system behavior [3, 27]. To this end, a coarse bifurcation analysis is used to determine which bifurcations occur and thereby to understand which solutions are expected to exist. Details about the model and the analysis of the bottleneck problem can be found in [3]. Here, we focus on the coarse analysis of the problem.

Two parameters have been chosen as the main bifurcations parameters; the ratio of desired velocities of the two crowds $r_{v_0} = v_0^r / v_0^b$ and the width of the door w acting as a bottleneck. Microscopic simulations of the model for two crowds of size $N = 100$ reveal two fundamentally different regimes of the dynamics. One finds a

blocked state and a state that is oscillating at the macroscopic level (cf. Fig. 6(a)) for small and large door widths, respectively. The question we would like to answer is: how and where does the transition from a blocked to an oscillating state happen? In mathematical terms the question is, where is the bifurcation point and what type of bifurcation is observed at the transition?

The restriction and lifting operators

We define the macroscopic quantity m as

$$m = \frac{m_r + m_b}{2}, \qquad m_{(r,b)} = \frac{\sum_{i\in(r,b)} \kappa(x_i) x_i}{\sum_{i\in(r,b)} \kappa(x_i)}, \tag{15}$$

where $m_{(r,b)}$ is a weighted average of the longitudinal component for the blue and red pedestrian crowd, respectively. κ gives more weight to pedestrians close to the door (see [3] for details). Since we expect oscillations from microscopic observations the pair of variables $(m,\dot{m})$ is used as the macroscopic variable for the equation-free methods. The transient from the initial condition to a limit cycle in the macroscopic description is shown for $w = 0.7$ in Fig. 6(c). The restriction operator $\mathscr{R} = (m,\dot{m})$ is therefore defined by the macroscopic description (15) and its derivative.

The lifting operator $\mathscr{L}$ uses information about the distribution of the pedestrians in front of the door to initialize a sensible microscopic state. The distribution of positions of pedestrians along the corridor is known from numerical studies and is observed to be well-approximated by a linear density distribution, i.e., the distribution is of the form $p(|x|) = a|x| + b$, where $|x|$ is the distance from the door along the corridor axis. The slope a and interception b are determined by simulations for all parameter values of interest. The lifting uses these distributions to map, i.e., lift $(m,\dot{m})$ to a "physically correct" microscopic state. All velocities are initially set to 0, such that we lift to a microscopic state with $\dot{m} = 0$ (see [3] for details).

Numerical results

Using equation-free bifurcation analysis, the bifurcation diagram is computed for the fixed ratio $r_{v_0} = 1$. Fig. 6(d) shows the maximum and minimum of $m(t)$ as a function of w. The transition from a blocked state to an oscillating state is clearly observed and the bifurcation point is found to be at $w = 0.56$. The transition is analyzed in detail in [3] and the bifurcation point is identified as a Hopf bifurcation point using Poincaré sections, i.e., a discretization of the recurrent dynamics in time. This method is also implicit with a healing time t_{skip} determined by the first crossing of the Poincaré section. The Hopf bifurcation gives rise to macroscopic oscillations for large door width w emerging from a stable blocked state for w small enough.

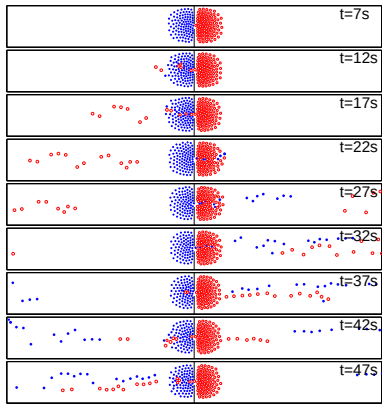

(a) Snapshots

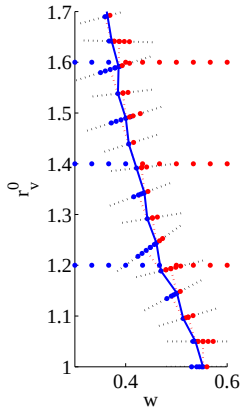

(b) Two-parameter space

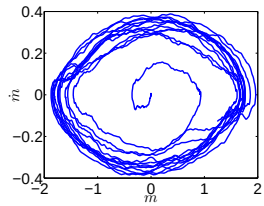

(c) Transient and limit cycle

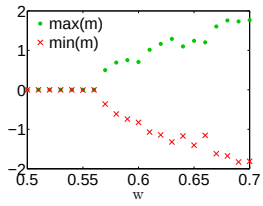

(d) Bifurcation diagram

Fig. 6 Coarse analysis of the pedestrian dynamics in a corridor with bottleneck. (a) Snapshots of a microscopic simulation show oscillating behavior for large enough door width $w = 0.6$. (b) Two-parameter plane explains the dynamics of the system and the point for the Hopf bifurcation. (c) Transient and limit cycle in the macroscopic description for $w = 0.7$. (d) The coarse bifurcation diagram reveals a Hopf bifurcation at a critical door width $w = 0.56$.

Let us now study the influence of r_{v_0} on the location of the bifurcation point. The system for macroscopic continuation is analyzed by a predictor-corrector method using a linear prediction and a subspace search for the correction in order to study the two-parameter problem and to continue the Hopf point. The results are shown in Fig. 6(b). Keeping the other model parameters fixed, this gives an overview of the behavior of the system on a macroscopic level in two parameters.

The application of equation-free analysis is not limited to pedestrians in a bottleneck scenario. One could also think of applications in evacuation scenarios (see, e.g., [28, 29]), where parameter regimes with blocked states have to be avoided at all cost. It is also possible to apply equation-free analysis to discrete models, e.g., cellular automaton models [30, 31]. This motivates further studies using equation-

free methods in traffic and pedestrian flow in order to systematically investigate and finally optimize the parameter dependencies of the macroscopic behavior of such microscopic models.

5 Discussion and Conclusion

We have demonstrated, that equation-free methods can be useful to analyze the parameter dependent behavior in traffic and pedestrian problems. Implicit methods allow us to improve the results further by reducing the lifting error. The comparison between traffic and pedestrian dynamics shows that both problem classes can be studied with the same mathematical tools. In particular, the use of coarse bifurcation analysis reveals some information about the system that could not be obtained by simpler means, e.g., direct simulations of a microscopic model, since they cannot investigate unstable solutions. Nevertheless, unstable solutions are important in order to understand the phase space and parameter dependence of the dynamics. In particular, in the case of a one-dimensional macroscopic dynamics the unstable solutions act as barriers between separate stable regimes defining reliable operating ranges. The knowledge of their locations can be used to systematically push the system over the barrier to switch to another more desirable solution, e.g., leading to a transition from traffic jams to uniform flow. In the application to two-dimensional macroscopic dynamics, we find the precise dividing line between oscillations and blocking in two parameters.

Finally, let us constrast equation-free analysis to the most obvious alternative. A common approach to determining the precise parameter value at which the onset of oscillations occurs, is to run the simulation for sufficiently long time and observe if the transient behavior vanishes. This approach suffers from two problems. First, close to the loss of linear stability in the equilibrium (i.e. close to the bifurcation point) the rate of approach to the stable orbit or fixed point is close to zero as the Jacobi matrix becomes singular. This makes the transients extremely long, resulting in unreliable numerics. Second, even eventually decaying transients may grow intermittently (the effect of *non-normality*) such that the criteria for the choice of the transient time to observe are non-trivial. Equation-free computations working on the macroscopic level in a neighborhood of the slow manifold do not suffer from these long transients, as they are based on direct root-finding methods.

In conclusion coarse bifurcation analysis can be used in future research to improve safety in traffic problems and evacuation scenarios of large buildings in case of emergency. The main advantage is, that realistic models can be used and a qualitative analysis of the macroscopic behavior is still possible. The method works almost independent of the underlying microscopic model and has a significant potential for helping traffic modellers to gain insight into previously inaccessible scenarios.

Acknowledgements The authors thank their collaborators R. Berkemer, A. Kawamoto and O. Corradi. The research of J. Sieber is supported by EPSRC grant

EP/J010820/1. J. Starke was partially funded by the Danish Research Council under 09-065890/FTP and the Villum Fonden (VKR-Centre of Excellence “Ocean Life”).

References

1. D. Helbing, P. Molnár, Phys. Rev. E **51**, 4282 (1995)
2. D. Helbing, Rev. Mod. Phys. **73**, 1067 (2001)
3. O. Corradi, P. Hjorth, J. Starke, SIAM Journal on Applied Dynamical Systems **11**(3), 1007 (2012)
4. M. Bando, K. Hasebe, A. Nakayama, A. Shibata, Y. Sugiyama, Phys. Rev. E **51**(2), 1035 (1995)
5. I. Gasser, G. Sirito, B. Werner, Physica D: Nonlinear Phenomena **197**, 222 (2004)
6. Y. Sugiyama, M. Fukui, M. Kikuchi, K. Hasebe, A. Nakayama, K. Nishinari, S.i. Tadaki, S. Yukawa, New J. Phys. **10**(3) (2008)
7. G. Orosz, B. Krauskopf, R. Wilson, Physica D: Nonlinear Phenomena **211**, 277 (2005)
8. C. Marschler, J. Sieber, R. Berkemer, A. Kawamoto, J. Starke, ArXiv e-prints (2013)
9. H. Haken, *Synergetics. An introduction.* (Springer, Berlin, 1983)
10. H. Haken, *Advanced synergetics.* (Springer, Berlin, 1983)
11. N. Fenichel, Journal of Differential Equations **31**, 53 (1979)
12. I.G. Kevrekidis, C.W. Gear, J.M. Hyman, P.G. Kevrekidis, O. Runborg, C. Theodoropoulos, Communications in Mathematical Sciences **1**, 715 (2003)
13. I.G. Kevrekidis, C.W. Gear, G. Hummer, AIChE Journal **50**(7), 1346 (2004)
14. I.G. Kevrekidis, G. Samaey, Annual Review of Physical Chemistry **60**(1), 321 (2009)
15. Y. Kevrekidis, G. Samaey, Scholarpedia **5**(9), 4847 (2010)
16. J. Sieber, B. Krauskopf, Nonlinear Dynamics **51**(3), 365 (2008)
17. E. Bureau, F. Schilder, I.F. Santos, J.J. Thomsen, J. Starke, Journal of Sound and Vibration **332**(22), 5883 (2013)
18. D.A.W. Barton, J. Sieber, Phys. Rev. E **87**, 052916 (2013)
19. C.W. Gear, T.J. Kaper, I.G. Kevrekidis, A. Zagaris, SIAM Journal on Applied Dynamical Systems **4**, 711 (2005)
20. A. Zagaris, C.W. Gear, T.J. Kaper, Y.G. Kevrekidis, ESAIM: Mathematical Modelling and Numerical Analysis **43**(04), 757 (2009)
21. A. Zagaris, C. Vandekerckhove, C.W. Gear, T.J. Kaper, I.G. Kevrekidis, Discrete and Continuous Dynamical Systems - Series A **32**(8), 2759 (2012)
22. C. Vandekerckhove, B. Sonday, A. Makeev, D. Roose, I.G. Kevrekidis, Computers & Chemical Engineering **35**(10), 1949 (2011)
23. W.J. Beyn, A. Champneys, E. Doedel, W. Govaerts, Y.A. Kuznetsov, B. Sandstede, in *Handbook of Dynamical Systems*, *Handbook of Dynamical Systems*, vol. 2, ed. by B. Fiedler (Elsevier Science, 2002), pp. 149 – 219
24. Y.A. Kuznetsov, *Elements of Applied Bifurcation Theory*, *Applied Mathematical Sciences*, vol. 112, 3rd edn. (Springer, New York, 2004)
25. A. Seyfried, B. Steffen, T. Lippert, Physica A: Statistical Mechanics and its Applications **368**(1), 232 (2006)
26. J. Zhang, W. Klingsch, A. Schadschneider, A. Seyfried, Journal of Statistical Mechanics: Theory and Experiment **2012**(02), P02002 (2012)
27. C. Marschler, J. Starke, P. Liu, I.G. Kevrekidis, Phys. Rev. E **89**, 013304 (2014)
28. D. Helbing, I.J. Farkas, P. Molnar, T. Vicsek, Pedestrian and evacuation dynamics **21**, 21 (2002)
29. A.U.K. Wagoum, M. Chraibi, J. Mehlich, A. Seyfried, A. Schadschneider, Computer Animation and Virtual Worlds **23**(1), 3 (2012)
30. C. Burstedde, K. Klauck, A. Schadschneider, J. Zittartz, Physica A: Statistical Mechanics and its Applications **295**(34), 507 (2001)
31. S. Nowak, A. Schadschneider, Phys. Rev. E **85**, 066128 (2012)

III Bifurcation of Learning and Structure Formation in Neuronal Maps

This letter discusses the application of equation-free methods to the neuronal network of the barn owl's auditory system [MFESvH14]. The two main results are the macroscopic bifurcation analysis of neuronal networks using equation-free methods and the observation and investigation of slowly traveling waves in the connectivity matrix of the neuronal network. Furthermore, the noisy microscopic system is studied on a macroscopic level, which behaves almost deterministically. As typical for a letter the highlights are described less-detailed which complicates following all derivations. Therefore, a follow-up article has been written to give all derivations for a full understanding of the system and the coarse analysis (see Paper IV).

The letter describes the application of equation-free methods to a realistic neuronal network model of the barn owl's auditory system. It is meant to present equation-free methods for a biophysics community and to point out new research directions in these fields. The macroscopic, coarse-grained analysis of realistic high-dimensional systems is still at its infancy and needs more detailed studies of real-world applications in these areas. This article points out the benefit of a coarse analysis and hopefully triggers new research in that direction.

At the hand-in date of the thesis the paper has been sent to Europhysics Letters for review.

Bifurcation of Learning and Structure Formation in Neuronal Maps

Christian Marschler[1], Carmen Faust-Ellsässer[2], Jens Starke[1] and J. Leo van Hemmen[3]

[1] *Department of Applied Mathematics and Computer Science, Technical University of Denmark, 2800 Kongens Lyngby, Denmark*
[2] *Interdisciplinary Center for Scientific Computing, University of Heidelberg, 69120 Heidelberg, Germany*
[3] *Physik Department & BCCN – Munich, Technische Universität München, 85747 Garching bei München, Germany*

PACS 87.18.Sn – Neural networks and synaptic communication
PACS 87.18.Hf – Spatiotemporal pattern formation in cellular populations
PACS 02.30.Oz – Bifurcation theory

Abstract – Most learning processes in neuronal networks happen on a much longer time scale than that of the underlying neuronal dynamics. To explore a network's learning ability, it is therefore useful to analyze slowly-varying, macroscopic, order parameters. We study the synaptic learning process giving rise to map formation in the laminar nucleus of the barn owl's auditory system. Using equation-free methods, we perform a bifurcation analysis of spatio-temporal structure formation in the associated synaptic-weight matrix. In so doing, we analyze learning as a bifurcation process and follow the unstable states as well. A simple time translation of the learning window function shifts the bifurcation point of structure formation and goes along with traveling waves in the map, without changing the animal's sound-localization performance.

Introduction. – If conceived cleverly and combined with its gigantic dimension reduction, the notion of order parameter has turned out to be extremely useful. One of the oldest examples is the "magnetization" m of an Ising ferromagnet, $m \equiv N^{-1}\sum_{i=1}^{N} S_i$ with $S_i = \pm 1$ corresponding to spin up or down. It tells us whether the system is in an up ($m > 0$) or down ($m < 0$) state below the critical temperature [1]. An order parameter such as m is a macroscopic characterization of a microscopic state the system is in, and varies slowly in time as compared to its (very many) microscopic constituents. Here we focus on an important additional advantage of a well-conceived order parameter in that we can now pursue dynamically *un*stable macroscopic states by employing recently developed multiscale methods (equation-free analysis, see *e.g.,* [2]). One can therefore perform a complete bifurcation analysis.

Biological physics has meanwhile provided a plethora of systems that possess at least two different time scales, a fast one and a slow one, but the accompanying order-parameter choice has attracted hardly any attention and its bifurcation analysis even less. As a generic example, we analyze structure formation in the auditory system of the barn owl [4] and the way in which a map of azimuthal sound localization arises in the laminar nucleus. This is the first station where phase-locked signals from left and right ear come together so as to form a map as a consequence of synaptic learning [3–7].

In the present context a map is a neuronal representation of the outside sensory world. What is actually mapped here is the interaural time difference (ITD) corresponding to horizontal direction. Until now, all maps were static. As we will see, under the high-dimensional microscopic neuronal and synaptic dynamics a sound-localization map arises that can be reduced to a bifurcation of the corresponding low-dimensional order parameter. The bifurcation analysis of the macroscopic dynamics is made possible by equation-free methods [2, 10, 14, 19]. The surprise is in both the bifurcation and the ensuing map that behaves as a slowly traveling wave.

In the auditory system of the barn owl, feeder axons come from left and right ear (through the cochlear and magnocellular nucleus) and pass along to the laminar nucleus (NL), making a sharp turn when they enter it [8]. There they all have a practically uniform signal velocity of about 4 m/s and touch the laminar neurons in an intertwining manner. For our purpose, the latter can be imagined as a row of neurons; cf. Fig. 1. The approxi-

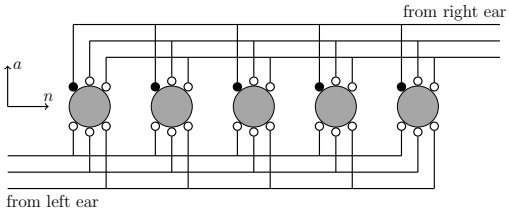

Fig. 1: Sketch of the structural setup of the barn owl's laminar nucleus (NL), an essential part of the auditory system. The $1 \leq n \leq N$ neurons in a row (5 gray circles, in reality and in computations $N = 30$) are connected to $1 \leq a \leq A$ axonal fibers (3 from right and 3 from left). Axons from left and right ear are connected to laminar neurons through synapses (small circles). Map formation needs a tuning of both the synapses on each neuron through the firing of the neuron they are on [5] and of the synapses on different neurons, which should "know" what the others do so that a topographically ordered map can emerge [6]. The latter tuning is performed by means of axon-mediated spike-based learning (AMSL), here indicated by solid circles connected to *the same* axon; cf. Eq. (6) below.

mately uniform velocity is essential to map formation, the precise speed in the feeder axons is not.

Model of the barn owl's auditory system. – We adapt the NL model of Kempter et al. [6] with $N = 30$ neurons in a row connected to $A = 280$ axons, so that the neurons receive input from 140 axons from each ear. For each synapse there are two indices, the neurons $1 \leq n \leq N$ and the axons $1 \leq a \leq A$ it is connected to. The distance between neurons is given by $d = 27\,\mu$m and the propagation speed of the signals is taken [8] to be $c = 4\,$m/s. According to the finite propagation speed c of the signals, the time delay between neighboring neurons connected to the same axon is $\tilde{\Delta} = d/c = 6.75\,\mu$s. For all numerical simulations, time has been discretized in steps of $\Delta t = 5\mu$s, with time delays given in units of Δt. Due to a pre-processing in the brain [8], input signals along different axons arrive at the NL border at different times. Accordingly, a uniform distribution of delays $\Delta_a \in [0, 2T]$ has been chosen with

$$\Delta_a = \begin{cases} \left(\frac{2T}{A/2}\right) a & , 1 \leq a \leq \frac{A}{2} \quad \text{(left ear)} \\ \left(\frac{2T}{A/2}\right)\left(a - \frac{A}{2}\right) & , \frac{A}{2} + 1 \leq a \leq A \quad \text{(right ear)} \end{cases} \tag{1}$$

and $T = A/4$ is the period of the input cochlear signal, a cochlear best frequency [8], covering two periods each ear. Combining both delay types, Eq. (1) gives for synapse (a, n) connected to left and right ear the total delay

$$\Delta_{an} = \begin{cases} \Delta_a + n\tilde{\Delta} + t_{\mathrm{ITD}} & , 1 \leq a \leq A/2 \\ \Delta_a + (N + 1 - n)\tilde{\Delta} & , A/2 + 1 \leq a \leq A \end{cases} \tag{2}$$

with t_{ITD} as interaural time difference in units of Δt.

The process of learning is modeled as spike-timing dependent synaptic plasticity (STDP) [5, 7] and described by the change of synaptic weights with time. Hence, in order to study the learning behavior, we assign to each synapse (a, n) a time-dependent synaptic weight $J_{an}(t) \in [J_{\min}, J_{\max}] = [0, 2]$. The local synaptic weight J_{an}^{loc} changes on a slow time scale $\xi = 10^{-3} \ll 1$ in dependence upon the arrival times t_a of presynaptic spikes and the firing times t_n of the postsynaptic neuron n it is on [5,6,9], while $\eta \in [0, 1]$ is the important learning parameter accompanying the learning window $\mathcal{W}$,

$$\frac{\mathrm{d}}{\mathrm{d}t} J_{an}^{\mathrm{loc}}(t) = \xi \quad \Big[w^{\mathrm{in}} \delta(t - t_a) + w^{\mathrm{out}} \delta(t - t_n) + w^{\mathrm{unlearn}} + p(t)\,(J^{\max} - J_{an}) + \eta\,\mathcal{W}(t) \Big] . \tag{3}$$

Here δ is a Dirac δ-function, $w^{\mathrm{in}} = 0.02$ takes care of a synaptic change on arrival of a spike at t_a and so does $w^{\mathrm{out}} = -0.25$ for t_n, when the postsynaptic neuron fires, while $w^{\mathrm{unlearn}} = -3 \cdot 10^{-4}$ describes a slow "forgetting". The $p(t)$ term incorporates intrinsic noise uniformly distributed in $[0, 10^{-4}]$ to model fluctuations on the level of the synaptic strength. Finally, the learning window

$$\mathcal{W}(t) = \sum_{t_n} W_{\hat{u}}(t - t_n)\delta(t - t_a) + \sum_{t_a} W_{\hat{u}}(t_a - t)\delta(t - t_n) \tag{4}$$

describes STDP with $W_{\hat{u}}$ as learning window shifted by $\hat{u} = -1$. Later on, $\hat{u}$ is used as additional parameter in the study of traveling waves; see Fig. 5. With hindsight [5], the underlying philosophy is simple. If we have an excitatory synapse and $t_a - t_n < 0$ so that the arriving spike instructs the neuron to fire and shortly thereafter it does so, the synapse performs a good job. Accordingly, it ought to be strengthened and hence $W_{\hat{u}}(t_a - t_n) > 0$. If on the other hand $t_a - t_n > 0$, the spike comes too late and the synapse should be weakened: $W_{\hat{u}}(t_a - t_n) < 0$. The function $W_{\hat{u}}$ has already been specified in [6] as

$$W_{\hat{u}}(s) = \begin{cases} 2\exp\left(\frac{s-\hat{u}}{\tau_2}\right) - \exp\left(\frac{s-\hat{u}}{\tau_0}\right) & , s < \hat{u} \\ \exp\left(-\frac{s-\hat{u}}{\tau_1}\right)\left[2\left(1 + (s - \hat{u})\frac{\tau_1+\tau_2}{\tau_1\tau_2}\right)\right. & \\ \left. - \left(1 + (s - \hat{u})\frac{\tau_0+\tau_1}{\tau_0\tau_1}\right)\right] & , s \geq \hat{u}. \end{cases} \tag{5}$$

The time constants are $\tau_0 = 5$, $\tau_1 = 30$ and $\tau_2 = 50$ (in units of Δt). Before proceeding, we need to give map formation the finishing touch through axon-mediated spike-based learning (AMSL); cf. Kempter et al. [6]. Let $\rho = 0.1$ be a small parameter accounting for contributions from neighboring neurons in (6) and define for axon a at neuron n the quantity $S_{an} = \sum_k j_{ak}^{\mathrm{loc}}$. The sum over k can be over nearest neighbors, or next nearest neighbors, or here over all synapses connected to the *same* axon. Then, with (3), the full synaptic dynamics is given by the differential equation

$$\frac{\mathrm{d}}{\mathrm{d}t} J_{an} \equiv \dot{J}_{an} = \dot{j}_{an}^{\mathrm{loc}}(t) + \rho S_{an}. \tag{6}$$

Hebbian learning is in the style of "practice makes perfect" and accordingly η is the important parameter. Once the

barn owl's head is full-grown, it takes two more weeks before the animal can perform azimuthal sound localization or, equivalently, before the laminar map has been completed. Hence we can choose a time much longer than the neuronal time scale (ms) and much shorter than the time of map completion, say 10 minutes, so as to segregate the two time scales of neuronal activity and map formation.

Equations (4) and (6) describe learning, i.e., map formation processes in terms of developing synaptic strengths and hence contain the neuronal dynamics explicitly through spike times t_a and t_n, which are generated by a neuronal dynamics, orders of magnitude faster [4] than the synaptic one. The neuronal dynamics may well be taken to be simple, viz., the integrate-and-fire model [12, 13], governed by a membrane potential of the form

$$h_n(t) = \sum_{a=1}^{A} \sum_{j:t_n^f < t_{an,j} \le t} J_{an}(t)\epsilon(t - t_{an,j}) \qquad (7)$$

where t_n^f is the most recent firing time of neuron n, $t_{an,j}$ is the j-th arrival spike at synapse (a, n), and

$$\epsilon(t) = \begin{cases} (t/\tau^2)\exp(-t/\tau) & t \ge 0 \\ 0 & t < 0 \end{cases} \qquad (8)$$

describes the excitatory postsynaptic response at the soma with time constant $\tau = 20\Delta t$. Despite its simplicity, the model is nonlinear as h_n is reset to 0, once h_n passes a threshold $\theta = 4.2$ from below. The synaptic weights J_{an} in (7) steer the dynamics of the neurons and, conversely, in the long run the latter shape the way in which the former develop.

Macroscopic bifurcation analysis. – To investigate the map dynamics, we would like to average out the neuronal dynamics and focus on the bifurcation behavior of map formation in dependence upon the learning window's amplitude η and the AMSL coupling strength ρ. In fact, we expect the details of the neuronal dynamics to be immaterial. It is here that equation-free bifurcation analysis proves to be quite helpful [2, 10, 14]. For the analysis, we need to define a suitable macroscopic order parameter X that should measure for the problem at hand how well the map represents the sound-source direction. To get an impression of what we can expect, we turn to Fig. 2. If a map is random or awkward, we require $X \approx 0$. On the other hand, $X \approx 1$ should signal a clearly organized map representing the relative periodicity (cf. Fig. 2) of the synaptic matrix $J = (J_{an})$. In view of these requirements the choice below is quite natural,

$$X = \frac{1}{(A-2T)N} \sum_n \left[\sum_{a=1}^{A/2-T} \mathcal{J}_{an} + \sum_{a=A/2+1}^{A-T} \mathcal{J}_{an} \right] \qquad (9)$$

$$\mathcal{J}_{an} = (J_{an} - J_{a+T/2,n})\ \delta(J_{an}, J_{(a+T)n})\ \Theta(J_{an} - \tilde{J})$$

where X depends on the time t, $\tilde{J} = 1.3$ is a significance level for the synaptic weights (see below), and Θ is the Heaviside step function. The Kronecker $\delta(J_{an}, J_{(a+T)n})$ assures a correct period across the axons and the prefactor $1/(A-2T)N$ normalizes the sum. The Kronecker δ is implemented with tolerance 0.01. If the period is T, a synapse is weighted with the difference to the synapse half a period in front. For a fully developed matrix J, this is usually $J_{a+T/2,n} - J_{an} = J_{\max} - J_{\min} = 2$ with $J_{\min} = 0$.

Accordingly, a uniform matrix without stripe structure results in a small positive value of X. Furthermore, the Θ function in (9) takes only synaptic weights $J_{an} > \tilde{J}$

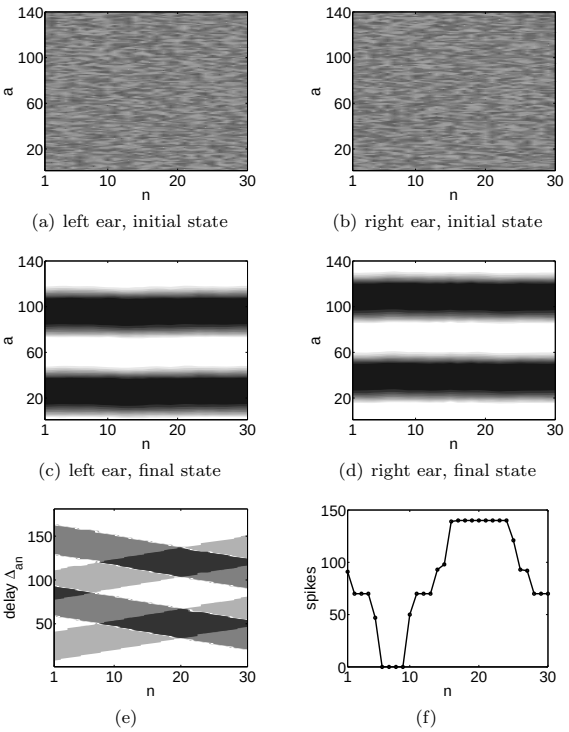

(a) left ear, initial state (b) right ear, initial state (c) left ear, final state (d) right ear, final state (e) (f)

Fig. 2: (a,b) Initial condition $J_{an}(0)$ for synaptic strengths connected to axons from left and right ear. (c,d) After a successful learning session employing model Eq. (1) – Eq. (7), a striped structure emerges in the synaptic weight matrix J, *i.e.,* a map, enabling the barn owl to azimuthally localize its prey. A gray scale indicates the strength of the synapse from the minimum weight (white) to the maximum weight (black). Synapses are spatially arranged on *parallel* axons connected to left and right ear (see Fig. 1). (e) According to (2) the delay for an incoming signal depends not only on the axon a but also on the neuron n. Plotting the delay Δ_{an} for strong synapses (black stripes in (c,d)) results in an overlap where signals arrive at the same time (here at $n = 20$). A neuron being a threshold element, the overlap of left and right white stripes in a delay plot practically defines the map width. (f) During a simulation of 10000 time steps with the fully-developed connectivity matrix the spiking activity shows a maximum at neuron 20 encoding the angle of prey.

into account. The point is that a synaptic weight matrix with stripe structure but too small $|J_{an}|$ values is not able to let the neurons fire so that prey detection would be impossible. We note that, due to the rectangularly shaped spatial patterns across the axons, a Fourier representation to check the periodicity is not useful [11].

We like to gain insight in the way in which the macroscopic order parameter X evolves in time in dependence upon η. Hence we need a bifurcation analysis on a coarse level and disregarding details of the underlying microscopic dynamics of the neurons. Exactly here equation-free analysis [2,10] comes in and allows to investigate the macroscopic behavior of the neuronal network as it leads to a map. The number of synapses is 2 to 3 orders of magnitude larger than that of the neurons and the dynamics of the former is adiabatic w.r.t. the latter, i.e., at least 6 order of magnitude slower.

Equation-free methods. – In equation-free computations (see [2] for a review), a microscopic dynamical system

$$\dot{x}(t) = f(x(t), \eta), \quad x \in \mathbb{R}^m, \quad f : \mathbb{R}^m \times \mathbb{R} \to \mathbb{R}^m \quad (10)$$

is described by a model function f depending on a parameter $\eta \in \mathbb{R}$. Here the microscopic model (10) summarizes the learning of the neuronal network defined in Eqs. (1) – (7). By choosing a suitable order parameter X such as the one in (9), the high-, i.e., m-dimensional dynamics in (10) can be reduced to a coarse, say M-dimensional scale,

$$\dot{X}(t) = F(X(t), \eta), \quad X \in \mathbb{R}^M, \; F : \mathbb{R}^M \times \mathbb{R} \to \mathbb{R}^M \quad (11)$$

where F describes the not explicitly but only implicitly given macroscopic dynamics and $M \ll m$; here $M = 1$. We can obtain the macroscopic dynamical properties of F by running suitably chosen short simulation bursts, *i.e.,* short simulations, of the microscopic system f and using (see [2,14])

$$X(t + \delta t) = \mathcal{R}[s^k(\mathcal{L}(X(t)), dt)] \quad (12)$$

where s solves (10) numerically with time step dt where $\delta t = kdt, k \in \mathbb{N}$. To be able to perform the continuation of the macroscopic quantity depending on the parameter η, *i.e.,* the amplitude of the learning window in (3), the lifting operator $\mathcal{L} : \mathbb{R}^M \to \mathbb{R}^m$ and restriction operator $\mathcal{R} : \mathbb{R}^m \to \mathbb{R}^M$ are used repeatedly to switch between microscopic and macroscopic level. This procedure is shown in Fig. 3. In order to perform a macroscopic time step, a macroscopic state $X(t)$ is lifted with $\mathcal{L}$ (see also (15)) to a microscopic state $x(t)$, which is then evolved in time by the underlying model (Eq. (1) – Eq. (7)) with the time stepper s. The resulting state $x(t + \delta t)$ is subsequently used to compute the macroscopic state $X(t + \delta t)$ at time $t + \delta t$ by applying the restriction operator $\mathcal{R}$ (defined by (9)).

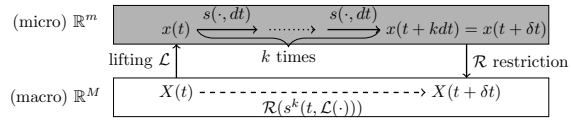

Fig. 3: Sketch of the macroscopic time stepper used in the equation-free method. A macroscopic state $X(t)$ is mapped onto a microscopic state $x(t)$ by using the lifting operator (15). The available microscopic model represented by Eqs. (1) – (7) constitutes the microscopic time stepper s that is applied for k steps of size dt to yield a microscopic state $x(t + kdt)$ at time $t + kdt$. Finally, the microscopic state is mapped onto a macroscopic state $X(t + \delta t)$ through the restriction operator (9). This procedure defines the macroscopic time stepper (12).

The unknown macroscopic right-hand side F is usually approximated as

$$F(X) = \frac{X(t + \delta t) - X(t)}{\delta t}. \quad (13)$$

This explicit scheme makes it difficult to determine the correct dynamics, since the lifting operator usually initializes the microscopic state away from the slow manifold where the macroscopic dynamics takes place (lifting error). Recently introduced implicit equation-free methods [14] allow to determine the not explicitly given right-hand side of Eq. (11) as

$$F(X) = \frac{\mathcal{R}[s^{k+k_{\text{skip}}}(\mathcal{L}(X(t)), dt)] - \mathcal{R}[s^{k_{\text{skip}}}(\mathcal{L}(X(t)), dt)]}{\delta t} \quad (14)$$

where $t_{\text{skip}} = k_{\text{skip}} dt$ is the "healing" time. The implicit scheme (14) circumvents these lifting errors [14].

To numerically compute bifurcation diagrams, the stationary states of the order parameter X defined by $F(X, \eta) = 0$ are continued with respect to the parameter η using a predictor-corrector method [15,16]. A linear secant prediction and a Newton method as corrector are used. The Jacobian is computed by means of a finite-difference scheme.

The restriction operator $\mathcal{R}$ is determined by the definition of the macroscopic variable (9) and the lifting operator $\mathcal{L}(X) = J$ is chosen as

$$J^{\text{new}} = J^{\text{old}} + \text{rand}(-\epsilon, \epsilon) + \alpha \, \text{bin}(J^{\text{old}} > 1). \quad (15)$$

The above computation adapts the previous state J^{old} of the continuation using noise with amplitude $\epsilon = 0.005$. $\text{rand}(-\epsilon, \epsilon)$ is a $A \times N$ uniformly distributed random matrix in $[-\epsilon, \epsilon]$ and $\text{bin}(J^{\text{old}} > 1)$ is a binarization of the connectivity matrix J. The binarization modifies strong synapses that are relevant to the restriction operator $\mathcal{R}$. The random matrix with small elements is added to obtain a small perturbation to the known state J^{old}. Note that the definition of the lifting operator $\mathcal{L}$ is not unique. The choice to modify known solutions through (15) on a branch is a convenient way to utilize knowledge from previous solutions in order to construct such a lifting close

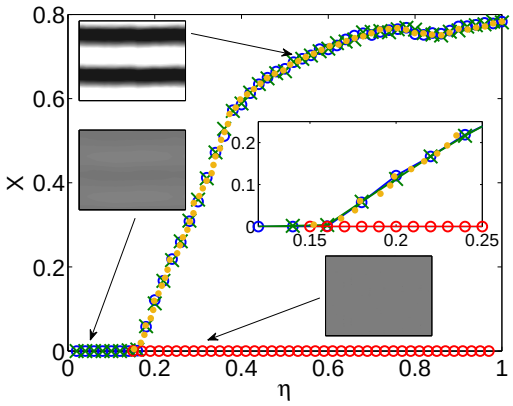

Fig. 4: Macroscopic bifurcation diagram of order parameter X as function of the learning window amplitude η. Using equation-free bifurcation analysis, it is possible to continue branches and to detect bifurcation points of the network learning. A stable branch is found for $X > 0$ using different methods, down-sweep (circles) and up-sweep (crosses) in direct simulations and implicit equation-free continuation (dots). The bifurcation diagram shows a bifurcation reminiscent of a transcritical bifurcation at $\eta^* = 0.16$. The branch at $X = 0$ changes stability and the unstable branch after the bifurcation is continued using one-sided Newton corrections (circles). The inset shows a magnification of the bifurcation region. The three small insets show microscopic states for comparison. See [17] for a video of the learning process.

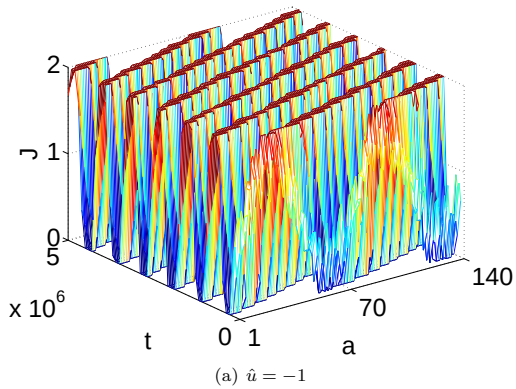

(a) $\hat{u} = -1$

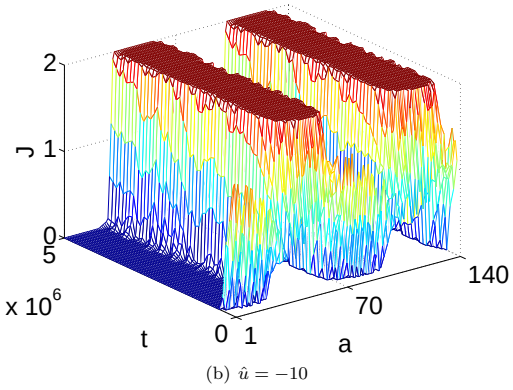

(b) $\hat{u} = -10$

Fig. 5: Traveling waves in the synaptic weight matrix for different values of the shift $\hat{u}$ in the learning window; cf. (5). (a) For $\hat{u} = -1$, the stripes travel through the network at a nonzero but slow speed. (b) The traveling waves turn into a standing wave for $\hat{u} = -10$. The temporal multiplication factor of 10^6 clearly indicates that synaptic dynamics leading to map formation is adiabatic w.r.t. the neuronal one.

to the low-dimensional slow manifold (see e.g. [10] for a description of different lifting operators). To initialize J close to a desired macroscopic value $\hat{X}$, the coefficient α is adjusted so that $\mathcal{R}(J^{\text{new}}) = \hat{X}$.

We start the continuation of the macroscopic stable branch with the fully developed connectivity matrix for $\eta = 1$ (cf. Fig. 2) corresponding to a macroscopic fixed point of the system with $X(\eta) = 0.8$; see Fig. 4 where the stable branch for $\eta = 1$ is found at the macroscopic value of $X = 0.8$. Continuing this fixed point in η yields a stable branch of solutions. In Fig. 4, the branch obtained by implicit equation-free continuation (dots) coincides with the results from direct simulations in an up- (crosses) and down-sweep (circles), respectively. Here the macroscopic solution $X > 0$ encodes the stripe structure, *i.e.,* the correct connectivity matrix for sound localization. By investigating the eigenvalue of the (1×1) Jacobian of the linearized system along the branch, a bifurcation point is found at $\eta^* \approx 0.16$. For $\eta < \eta^*$, the solution $X = 0$ corresponds to a non-structured connectivity matrix, leading to a system that is not able to perform sound localization. Choosing a microscopic state with $X = 0$ as initial condition for an arbitrary $\eta < \eta^*$, it is possible with the equation-free continuation techniques presented here to find an unstable macroscopic solution at $X = 0$ even for $\eta > \eta^*$. The detection of an unstable branch gives information about the underlying dynamics and is never possible by direct simulations. By visual inspection of the bifurcation diagram in Fig. 4, the bifurcation is reminiscent of a transcritical one, and not the usual pitchfork.

Strict detection of the bifurcation type is, however, complicated by two factors. First, because of the very nature of X, only the non-negative part of the bifurcation ($X \geq 0$) can be observed, thereby obscuring the branch in the strictly negative domain. Second, inherent noise in the macroscopic dynamics because of stochasticity in the underlying microscopic model complicates determining higher-order derivatives and thereby the bifurcation type. Additional analysis has shown that even though a variation of the AMSL coupling strength ρ induces spatial inhomogeneities, the periodicity measure X hardly changes.

Traveling waves in the synaptic connectivity matrix. – Besides the dependence upon η, the position of

the bifurcation point also depends on the learning-window shift $\hat{u}$ (see Eq. (4)) and corresponds to *traveling waves* in the map. The maps found until now in previous work were always stationary. It turns out that the striped structure, although a fixed point of the macroscopic order parameter X, is not a stationary state of the connectivity matrix J. Instead, very slowly traveling waves are observed; see Fig. 5. The traveling waves have the same speed on axons from left and right ear, which is the reason why the function of the network does not change and prey detection remains possible as the maximum activity of the network stays at the same neuron; cf. Fig. 2. The speed of the traveling waves depends on the shift $\hat{u}$ in the learning window. By using a certain value (here $\hat{u} = -10$) it is possible to obtain standing waves, corresponding to a stationary state also on a microscopic level. Surprising as they are, the present findings are purely numerical but invite biological interpretation and experimental verification, e.g., through periodic waxing and waning of dendritic spines [18].

Conclusion. – In conclusion, the application of equation-free methods in conjunction with a bifurcation analysis to learning in neuronal networks opens up the way to new insight into previously inaccessible phenomena such as: 1) study of unstable solutions; 2) detection and classification of macroscopic bifurcation points. Here we exhibit a transcritical bifurcation replacing the well-known pitchfork and identify the onset of structure formation in, e.g., maps of synaptic connectivities; 3) significant reduction of computation time. A striking example is provided by our finding traveling waves instead of a time-invariant pattern in the sound-localization map of the barn owl, as shown in Fig. 5.

* * *

Thanks are due to Ioannis G. Kevrekidis for fruitful discussions. This work was funded by the German Research Council DFG (FOR 643) and the Villum Fonden under the VKR-Centre of Excellence 'Ocean Life'.

REFERENCES

[1] K. Huang, *Statistical Mechanics*, 2nd ed. (Wiley, New York, 1987) Chapters 14–16.
[2] I. G. Kevrekidis and G. Samaey, Annu. Rev. Phys. Chem. **60**, 321–344 (2009).
[3] W. E. Sullivan and M. Konishi, Proc. Natl. Acad. Sci. USA **84**, 8400–8404 (1986), Fig. 3A
[4] M. Konishi, Sci. Am. **268**/4, 66–73 (1993)
[5] W. Gerstner, R. Kempter, J.L. van Hemmen, H. Wagner, Nature **383**, 76–78 (1996).
[6] R. Kempter, C. Leibold, H. Wagner, J.L. van Hemmen, Proc. Natl. Acad. Sci. USA **98**, 4166–4171 (2001).
[7] G.-Q. Bi and M.-M. Poo, Annu. Rev.. Neurosci. **24**, 139–166 (2001).
[8] C. E. Carr and M. Konishi, Proc. Natl. Acad. Sci. USA **85**, 8311–8315 (1988).
[9] R. Kempter, W. Gerstner, J.L. van Hemmen, Phys. Rev. E **59**, 4498–4514 (1999).
[10] I. G. Kevrekidis, C. W. Gear, J. M. Hyman, P. G. Kevrekidis, O. Runborg, and C. Theodoropoulos, Comm. Math. Sci. **1**, 715–762 (2003).
[11] J. L. van Hemmen, A. Longtin, A. N. Vollmayr, Chaos **21**, 047508 (2011).
[12] A. N. Burkitt, Biol. Cybern. **95**, 1–19 & 97–112 (2006).
[13] S. Scarpetta and A. de Candia, PLoS ONE **8**, e64162 (2013).
[14] C. Marschler, J. Sieber, R. Berkemer, A. Kawamoto, and J. Starke, SIAM J. Appl. Dyn. Sys., accepted for publication. ArXiv e-print 1301.6044 (2013).
[15] E. Doedel, H. B. Keller, and J. P. Kernevez, Int. J. Bifurc. Chaos **1**, 493–520 & 745–772 (1991).
[16] W.-J. Beyn, A. Champneys, E. Doedel, W. Govaerts, Y. A. Kuznetsov, and B. Sandstede, in: B. Fiedler, Ed., *Handbook of Dynamical Systems*, Vol. 2, Elsevier (2002).
[17] Suppl. material at [URL].
[18] U. V. Nägerl, K.I. Willig, B. Hein, S.W. Hell, and T. Bonhoeffer, Proc. Natl. Acad. Sci. USA **105**, 18982–18987 (2008).
[19] C. Marschler, J. Sieber, P.G. Hjorth, and J. Starke, in: *Traffic and Granular Flow '13*, Springer (2014). Accepted for publication.

IV Equation-Free Bifurcation Analysis of a Learning Process in a Neuronal Network

This paper [MFEvHS14] is the follow-up of Paper III and gives all necessary details to follow each step in the derivations. Therefore, it gives a self-contained presentation of the application of equation-free methods to a coarse modeling of neuronal networks. Furthermore, the paper studies not only a periodicity measure for the connectivity matrix but also another macroscopic quantitiy, the so-called vector strength. Both coarse quantities are shown to capture the same qualitative results, showing the robustness of the analysis. Additionally, the traveling waves that have been observed in Paper III are studied in more detail, e.g., the wave speed with respect to the dependence on system parameters.

The detailed presentation of the paper is tailored for biologists and therefore also presents algorithms, e.g., Newton's root-finding algorithm, which would be known to mathematicians. We hope to encourage discussions across borders of research fields which could help to understand the complicated models of neuronal networks and could open up for new ways, e.g., by equation-free methods, to analyze the complicated dynamics on scales that are relevant for experiments.

At the hand-in date of the thesis the paper is a manuscript that will be submitted to the Journal of Mathematical Biology.

Journal of Mathematical Biology manuscript No.
(will be inserted by the editor)

Christian Marschler · Carmen Faust-Ellsässer · J. Leo van Hemmen · Jens Starke

Equation-Free Bifurcation Analysis of a Learning Process in a Neuronal Network

the date of receipt and acceptance should be inserted later

Abstract. Usually, learning processes of neuronal networks happen on a much longer time scale than the neuron dynamics. Therefore, it seems natural to take macroscopic, slowly-varying, quantities, i.e., order parameters, into account in order to investigate the learning functionality of a neuronal network. We apply equation-free methods to study pattern formation of stripe structures in the synaptic weight matrix in a learning process modeling the nucleus laminaris in the barn owl's auditory system. Learning is efficient only after a bifurcation to this stripe structure and goes along with traveling waves in the patterns on a much slower time scale. The dependence of wave speed and detailed bifurcation structure on system parameters is investigated.

1. Introduction

The analysis of biological phenomena by means of mathematical methods got much attention in recent years. In particular, the modeling of neuronal networks using multiscale techniques from dynamical systems theory is in the focus of concurrent research [Buckley and Nowotny (2011), Laing (2006)]. The choice of the right mathematical tool depends on the size of the system under investigation. Great progress has been made in studying and understanding small systems with a few degrees of freedom. The advantage is that many results from non-linear dynamical systems theory can be applied [Meiss (2007), Arnold et al (1997)]. On the other hand, large systems with many degrees of freedom can often be understood on a

Christian Marschler: Department of Applied Mathematics and Computer Science, Technical University of Denmark, Matematiktorvet 322, 2800 Kgs. Lyngby, Denmark

Carmen Faust-Ellsässer: Interdisciplinary Center for Scientific Computing, University of Heidelberg, 69120 Heidelberg, Germany

J. Leo van Hemmen: Physik Department T35, Technische Universität München, 85747 Garching bei München, Germany

Jens Starke: Department of Applied Mathematics and Computer Science, Technical University of Denmark, Matematiktorvet 322, 2800 Kgs. Lyngby, Denmark

Key words: neuronal networks – equation-free analysis – learning window – pattern formation

coarse level with methods from statistical physics, see e.g., the statistical description of turbulence in fluid dynamics by the approach of Kolmogorov [Frisch (1995)] or the slaving principle [Haken (1983)]. Several difficulties arise when studying meso-scale systems, i.e., systems with an intermediate number of degrees of freedom. If these systems have dynamics on different time scales, it is often possible to gain insight using ideas from slow-fast systems [Fenichel (1979)]: after a short transient, the dynamics of these systems happen on a normally-attracting low-dimensional slow manifold. The resulting dimension reduction is often so significant that these systems can be analyzed in the same way as low-dimensional systems on this slow manifold.

Here, we apply so-called equation-free methods [Kevrekidis et al (2003), Kevrekidis and Samaey (2009)] for analyzing systems with multiple time scales to the well-studied biological problem of the learning process in the auditory system of the barn owl (see e.g., [Carr and Konishi (1988), Gerstner et al (1993), Kempter et al (2001), van Hemmen (2002)]).

The barn owl's auditory system is a suprisingly simple but nevertheless very efficient part of its brain (cf. Section 2 for the mathematical model). It is responsible for prey detection with an azimuthal accuracy of 2° [Leibold et al (2001)] by using the time delay of an incoming signal between the two ears, i.e., the inter-aural time difference (ITD). This enables the barn owl to hunt even in complete darkness just by using sound cues. The input is processed in the nucleus laminaris (NL), a linearly-ordered array of neurons, which evaluates the ITD by coincidence detection [Kempter et al (1998), Leibold and van Hemmen(2002), van Hemmen (2002)]. Signals from the two ears arrive at the NL border from opposite sides and travel in opposite directions along the NL, yielding a maximal neuronal activity at the overlap. The idea goes back to Jeffress [Jeffress (1948)], who proposed this model of coincidence detection already in 1948.

Although the mature barn owl is a deadly predator, a newly-hatched owl is not capable of this accurate prey detection. It has to go through a learning process in which the connections, i.e., synapses, in the NL are adjusted. This process can be described by spike-time dependent plasticity (STDP) [Gerstner et al (1996)], an enhancement of the classical Hebbian learning [Hebb (1949)], and leads to a map formation, i.e., a representation of the outside world on a neuronal level [van Hemmen (2002)]. By the formation of the map, ITDs are effectively mapped to neuron activity and a prey detection becomes possible.

The dynamics of this learning process is well-known on the neuronal level with many degress of freedom [Kempter et al (2001)], i.e., one degree of freedom for each synapse. Nevertheless, the interesting dynamics happens on a coarse scale, i.e., the detection of prey by the one dimensional angle. This macroscopic level is of interest for systematically studying the influence of parameters on the learning outcome. Usually, the equations of motion on this level are unknown and cannot easily be derived in closed

form from the underlying microscopic model. So-called equation-free methods [Kevrekidis and Samaey (2009)] bridge the gap between microscopic and macroscopic levels and allow to analyze systems with different time scales, e.g., the learning behavior. By using two operators for communicating between different levels, called restriction and lifting in the equation-free framework, it is possible to obtain information on the macroscopic level by using short simulations of the microscopic model (cf. Section 3 for details).

In this article, we apply the equation-free methods to a model of the NL of the barn owl in order to study map formation. In particular, we investigate the influence of the learning window, introduced in Section 2, on the learning outcome. This is achieved by computing bifurcation diagrams both by direct simulations and by the use of equation-free methods. We further use the equation-free methods to compute unstable branches, which would otherwise be impossible to detect by direct simulations.

The paper is organized as follows. In Section 2, the NL model is reviewed. The input model and neuron dynamics, i.e., high-dimensional dynamics, are introduced and the learning process is described in terms of the learning window. Section 3 shortly reviews the ideas of equation-free computations and introduces the restriction and lifting operators in particular. We also introduce equation-free versions of Newton's algorithm and the false position (regula falsi) method. Numerical results on the map formation, represented by stripe pattern in the connectivity matrix, and the numerical bifurcation analysis are presented in Section 4. The numerical investigations are further extended by the analysis of traveling wave solutions of the stripe pattern in Section 5. Finally, we discuss the results and give an outlook on open questions in Section 6.

2. The Model of the Neuronal Learning Process

In this section, the model for the NL of the barn owl is introduced. After defining the structure of the NL, the input model and the neuron dynamics are presented in Sections 2.1 and 2.2, respectively. The model for the learning process in Section 2.3 is based on the model presented in [Kempter et al (2001)] and extended with a global unlearning process and noise on the synaptic strengths.

The idea for the NL model of the barn owl is inspired by Jeffress' model [Jeffress (1948)], which is the simplest way to map a time difference to a place code. This mapping is achieved by a linearly-ordered array of coincidence detectors which are connected to signal lines from two sides(cf. Figure 1). The coincidence detectors emit a signal (to a post-processing unit), if two input signals arrive at the same time. A time delay, i.e., the ITD in the case of the NL, between the two input lines shifts the maximal activity to one side, since the signals overlap away from the central coincidence detector. Consequently, the time delay is mapped to a place. This method is also frequently used in electronical applications, e.g., robots [Huang et al (1997)], to determine the position of sound sources. The same

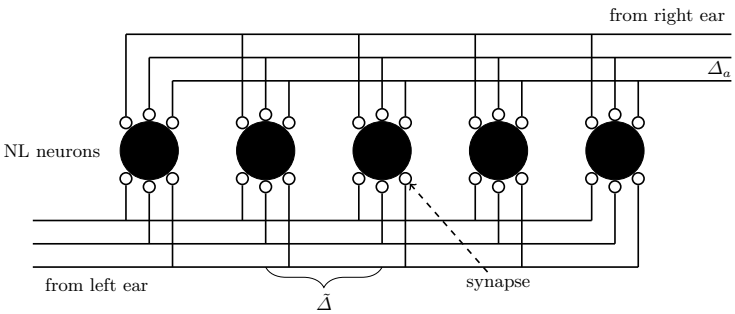

Fig. 1. Scheme of the nucleus laminaris (NL) of the barn owl's auditory system. N neurons (5 black circles in the sketch) are connected to A axonal fibres (6 lines in the sketch). The axonal fibers from the left and right ear are connected to the neurons by synapses (small circles).

linearly-ordered array of neurons has been found in the barn owl's auditory system [Carr and Konishi (1988)] and is called nucleus laminaris (cf. Figure 1).

We adapt the model of [Kempter et al (2001)] of the NL with $N = 30$ neurons connected to $A = 280$ axons, i.e., 140 axons from each ear. Throughout the paper, we will index neurons with $n \in \{1, \ldots, N\}$ and axons with $a \in \{1, \ldots, A\}$. Hence, a synapse is uniquely identified by the tupe (a, n). The distance between neurons is $d = 27\mu$m and the propagation speed of the signals is $c = 4$m/s. For all numerical simulations we discretize time in steps of $\Delta t = 5\mu$s, i.e., time delays are given in units of Δt. According to the finite propagation speed c of the signals, the time delay between neighboring neurons connected to the same axon is $\tilde{\Delta} = d/c = 1.35$. Due to a pre-processing in the brain the input signal arrives at different times on each axon at the NL border. Therefore, a uniform distribution of axonal delays $\Delta_a \in [0, 2T]$ is chosen, where

$$\Delta_a = \begin{cases} \left(\frac{2T}{A/2}\right) a & ,1 \le a \le A/2 \quad \text{(left ear)} \\ \left(\frac{2T}{A/2}\right) (a - A/2) & ,A/2+1 \le a \le A \quad \text{(right ear)} \end{cases} \tag{1}$$

and T is the period of the input signal (cf. Section 2.1). Combining both delay types, we can compute the total delay of synapse (a, n) to be

$$\Delta_{an} = \begin{cases} \Delta_a + n\tilde{\Delta} + t_{\mathrm{ITD}} & ,1 \le a \le A/2 \quad \text{(left ear)} \\ \Delta_a + (N+1-n)\tilde{\Delta} & ,A/2+1 \le a \le A \quad \text{(right ear)} \end{cases} \tag{2}$$

where t_{ITD} is the inter-aural time difference in units of Δt.

2.1. Input Model

The learning process in the auditory system of the barn owl is influenced by sounds received from prey. Input signals, e.g., sounds from mice, have

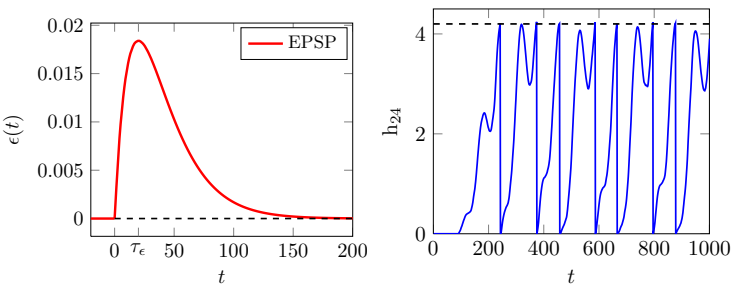

Fig. 2. Left. Excitatory post-synaptic potential (EPSP) for $\tau_\epsilon = 20$. **Right**. Neuron potential h of neuron 24 for $t = 10^3$ timesteps. After the neuron potential has reached the firing threshold $\theta = 4.2$, it is reset to zero.

a natural frequency of $\nu = 3$kHz, corresponding to a period of $T = 70$ (in units of Δt). Therefore, signals from the ears to the NL are emitted every T timesteps. In order to model inaccuracies in the signal conduction process a noise σ is introduced to the input signal. The noise σ is drawn uniformly from $[-\Delta t, \Delta t]$ for every incoming signal and is allowed to have different values on different axonal lines a and neurons n. Hence, the jth arrival time at synapse (a, n) is given by

$$t_{an,j} = jT + \sigma + \Delta_{an} + t_{\text{ITD,left ear}} \ . \tag{3}$$

Here, t_{ITD} is added to the arrival times of the left ear by convention. To mimick a natural learning process in which sound sources change position a new t_{ITD} is uniformly chosen from the interval $[-T/2, T/2]$ every 10^4 timesteps.

The arriving signal at the NL border is not solely determined by the arrival time $t_{an,j}$. It has a temporal structure modeled as an excitatory post-synaptic potential (EPSP) with charateristic time τ_ϵ given by

$$\epsilon(t) = \begin{cases} \frac{t}{\tau_\epsilon^2} \exp(-\frac{t}{\tau_\epsilon}) & , t \geq 0, \\ 0 & , t < 0. \end{cases} \tag{4}$$

The EPSP is modeled with $\tau_\epsilon = 20$ (in units of Δt) and shown in Figure 2, left panel.

2.2. Neuron Dynamics

The NL neurons are modeled as integrate-and-fire units [Burkitt (2006)]. They receive input signals from the A axons in the form of EPSPs and integrate over all incoming input signals. After the neuron potential h_n of neuron n reaches the firing threshold θ from below, the neuron emits a signal, i.e., it spikes, and the neuron potential is reset to zero. The post-processing of the emitted signal does not influence the learning process and

is therefore not modeled in this paper. Precisely, the neuron potential $h_n(t)$ of neuron n at time t is given as the sum over all incoming signals since the last emmited spike

$$h_n(t) = \sum_{a=1}^{A} \sum_{j:t_n^f < t_{an,j} \leq t} J_{an}(t)\epsilon(t - t_{an,j}), \tag{5}$$

where t_n^f is the most recent firing time of neuron n and J_{an} is the time-dependent synaptic weight matrix (see Section 2.3 for details about the time dependence). The history of the firing times is important for the learning process (cf. Section 2.3). It is indexed with $i \in \mathbb{N}$ such that $t_{n,i}^f$ is the i-th firing time of neuron n with

$$h_n\left(t_{n,i}^f\right) > \theta, \tag{6}$$

where $\theta = 4.2$ is the firing threshold. A typical spiking behavior of a neuron in a fully-developed network can be seen in Figure 2, right panel. Note, that the neuron potential h_n is not a state variable in the dynamics but an auxiliary quantitiy to compute firing times. At each time t it can be computed from the state variables J_{an}, the most recent spiking time t_n^f, and input signals $t_{an,j}$.

2.3. Learning Dynamics

The process of learning is modeled as synaptic plasticity (see the discussion in e.g., [van Hemmen (2001),Kempter et al (1999)]) and described by the change of synaptic weights with time. Hence, in order to study the learning behavior, each synapse (a, n) is assigned a time-dependent synaptic weight $J_{an}(t) \in [J_{\min}, J_{\max}]$. According to [Hebb (1949)], synapses attached to neurons that (immediately) fire after receiving an incoming spike will be strenghtened. This classical Hebbian learning has been extended by [Gerstner et al (1996)] to incorporate a decrease in synaptic weights if the timing is wrong, i.e., if a neuron fires before an input spike arrives. This learning model is called *spike-time dependent plasticity* (STDP) and is a prototype for a self-organized formation of a functioning network.

The process of STDP is modeled by the learning window $W(s)$, that adjusts the synaptic weights J_{an} according to the time difference s of incoming and outgoing spikes [Gerstner et al (1996)]. Here, we use the definition of a learning window introduced in [Kempter et al (2001)] (cf. Figure 3)

$$W(s) = \begin{cases} 2\exp(\frac{s-\hat{u}}{\tau_2}) - \exp(\frac{s-\hat{u}}{\tau_0}) & , s < \hat{u}, \\ \exp(-\frac{s-\hat{u}}{\tau_1})\left[2\left(1 + (s-\hat{u})\frac{\tau_1+\tau_2}{\tau_1\tau_2}\right) - \left(1 + (s-\hat{u})\frac{\tau_0+\tau_1}{\tau_0\tau_1}\right)\right] & , s \geq \hat{u}. \end{cases} \tag{7}$$

The time constants are $\tau_0 = 5$, $\tau_1 = 30$ and $\tau_2 = 50$ (in units of Δt). For the analysis of map formation in Section 4 we fix $\hat{u} = -1$. In Section 5 we vary $\hat{u}$ which results in different wave speeds of the emergent traveling waves.

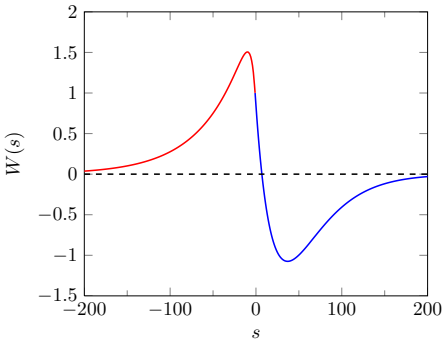

Fig. 3. Learning window $W(s)$ depending on time difference s for $\hat{u} = -1$, see also (7).

In addition to the learning window W which models STDP, further contributions to the learning dynamics are introduced. Each time a spike arrives at the synapse (a, n), its strength $J_{an}(t)$ is increased by $w^{\text{in}} = 0.02$, while each outgoing spike weakens the synapse by $w^{\text{out}} = -0.25$. In a quiescent network where no input signals or outgoing spikes appear, the synaptic weight decays constantly with $w^{\text{unlearn}} = -3 \cdot 10^{-4}$. Finally, the last contribution to the change in synaptic strength is a small noise $p(t) \in [0, 10^{-4}]$ proportional to $J^{\max} - J_{an}$ such that fully developed synapses experience less noise. Here, $p(t)$ is a random variable drawn from a uniform distribution at each time step. Since the synaptic weight can not increase without bound due to biological constraints, we choose $J^{\max} = 2$ as the maximal weight for a synapse. Similarly, the minimum synaptic weight is chosen to be $J^{\min} = 0$. Collecting all these contributions results in the local learning dynamics for J^{loc}_{an} which are later used to compute the global learning dynamics for J_{an}.

$$\begin{aligned} \dot{J}^{\text{loc}}_{an}(t) = \xi \Big[& \sum_j w^{\text{in}} \delta(t - t_{an,j}) + \sum_i w^{\text{out}} \delta(t - t^f_{n,i}) \\ & + w^{\text{unlearn}} + p(t) \cdot (J^{\max} - J_{an}) \\ & + \eta \Big\{ \sum_j \sum_i W(t - t^f_{n,i}) \delta(t - t_{an,j}) \\ & + \sum_{j: t_{an,j} \le t} \sum_i W(t_{an,j} - t) \delta(t - t^f_{n,i}) \Big\} \Big]. \end{aligned} \tag{8}$$

The constant $\xi = 10^{-3} \ll 1$ is the time scale for the learning process taking into account that learning is a slow process and η is the amplitude of the learning window W. The influence of the learning window is investigated in Section 4 for $\eta \in [0, 1]$.

It is shown in [Leibold et al (2001), Kempter et al (2001)] that map formation, i.e., a correct prey detection, is obtained by an additional mech-

anism. This process is the so-called *axon-mediated spike-based learning* (AMSL). It allows changes in synaptic strength at synapse (a, n) to propagate along the same axon a and therefore to influence the weights on other synapses connected to the same axon. To model AMSL, we introduce the total axonal change matrix

$$S_{an} = \sum_{k=1}^{N} j_{ak}^{loc}, \tag{9}$$

which sums all synaptic changes of all neurons connected to axon a. Hence, the complete learning rule is given as

$$\dot{J}_{an} = j_{an}^{\mathrm{loc}} + \rho S_{an}, \tag{10}$$

where $\rho = 0.1$ is a coupling parameter for AMSL.

3. Equation-Free Analysis

Equation-free methods are designed for analyzing systems with a separation of (time) scales [Kevrekidis et al (2003)]. Often, system dynamics are given on a more detailed level than relevant for applications. An example is molecular dynamics, where the system is given on a molecular level, while the interesting quantities are statistical moments, e.g., the temperature and pressure of a gas. In many applications, the microscopic, high-dimensional dynamics is fast, while the macroscopic, low-dimensional dynamics happens on a slow time scale. Those slow-fast systems, also studied as *singular perturbed systems* [Fenichel (1979)], show a gap in their eigenvalue spectrum (of the linearized flow around the slow manifold), denoting the directions with eigenvalues $|\mathrm{Re}\lambda| \gg 0$ as fast, while the others are slow. In the case of an attracting slow manifold the fast dynamics converges quickly to that manifold, such that after an initial transient, the system shows dynamics on the slow manifold. The dynamics on this manifold often have orders of magnitude fewer degrees-of-freedom than the full phase space. Although equations of motion exist on this manifold, the explicit derivation of these low-dimensional equations from the full dynamics is often complicated or impossible. Equation-free techniques avoid the derivation of macroscopic equations and obtain a so-called closure-on-demand, i.e., the necessary macroscopic information is obtained by short simulation bursts. A review on equation-free methods can be found in [Kevrekidis and Samaey (2009)]. Here, we briefly repeat the basic ideas to introduce notation for later reference.

We assume, that the microscopic, high-dimensional dynamical system is given as a system of first-order differential equations

$$\dot{x}(t) = f(x(t)), \qquad x \in \mathbb{R}^m, \quad f : \mathbb{R}^m \to \mathbb{R}^m. \tag{11}$$

Instead of assuming f to be smooth we allow for a stochastic right-hand side of (11) as long as the macroscopic behavior can be approximated by

deterministic dynamics. Further, we assume that the microscopic time stepper s solves (11) as the numerical equivalent of the flow. Given an initial condition $x(t)$ and a finite time step dt, the microscopic time stepper s can be used to compute the state $x(t + dt)$ of the system at time $t + dt$:

$$x(t + dt) = s(x(t), dt). \tag{12}$$

The equation-free analysis is independent of the specific implementation of s. It is one of the major advantages, that equation-free methods can be formulated as a wrapper, i.e., a super structure, around already existing code. For a system with a normally-attracting slow manifold, the evolution equations for the macroscopic quantities X can formally be denoted as

$$\dot{X}(t) = F(X(t)), \qquad X \in \mathbb{R}^M, \quad F : \mathbb{R}^M \to \mathbb{R}^M, \tag{13}$$

where F is *a priori* unknown. Usually $M \ll m$, yielding a large reduction of dimensionality for the macroscopic system (13). Note, that typically both f and F depend on parameters, e.g., η in the NL model. The dependence is suppressed to ease notation.

The goal is to construct a macroscopic time stepper S for the macroscopic dynamics (13) with not explicitly given right-hand side F in order to obtain numerical information of the low-dimensional dynamics. In the equation-free setup, the microscopic time stepper s is used together with so-called restriction $\mathcal{R}$ and lifting $\mathcal{L}$ operators to construct S. Here, $\mathcal{R}$ and $\mathcal{L}$ map between the high- and low-dimensional spaces, respectively. Thus, microscopic time steppers can perform system level tasks (cf. [Kevrekidis et al (2003)]).

The restriction operator

$$\mathcal{R} : \mathbb{R}^m \to \mathbb{R}^M \tag{14}$$

maps a state in the high-dimensional space to the interesting low-dimensional quantity. In physical problems, the concrete definition of $\mathcal{R}$ is often known from experience and intuition. It is inspired by the choice of interesting quantities, e.g., first moments of a distribution in statistical mechanics or the center of mass in classical mechanics. The construction of the lifting operator

$$\mathcal{L} : \mathbb{R}^M \to \mathbb{R}^m \tag{15}$$

is usually much more involved. It constructs a microscopic state corresponding to the low-dimensional quantities and is therefore a one-to-many operator. The choice of the correct lifting operator is left to the user and requires some experience. Special care has to be taken for the definition of $\mathcal{L}$ to initialize a state close to the slow manifold. A bad choice can result in large excursions in the high-dimensional phase space or even change the basin of attraction. The error caused by mapping to a state off the slow manifold in this lifting operation is called *lifting error*. The difficulties in finding a good lifting operator with a small lifting error can be relaxed when using

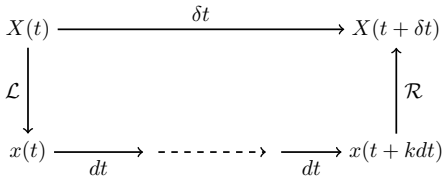

Fig. 4. Graphical representation of the macroscopic time stepper S. A macroscopic state $X(t)$ is lifted to a microscopic state $x(t)$ using the lifting operator $\mathcal{L}$. Then, the microsopic time stepper s is applied k times to compute a macroscopic time step $\delta t = kdt$. Last, the macroscopic state $X(t+\delta t)$ is constructed by applying the restriction operator $\mathcal{R}$ to the resulting microscopic state $x(t+kdt)$.

implicit equation-free methods [Marschler et al (2013)]. The specific choice of $\mathcal{R}$ and $\mathcal{L}$ for analyzing the learning process in the barn owl's auditory system is presented in Section 4.

If the lifting and restriction operators are available, a macroscopic time stepper can be constructed by

$$X(t+\delta t) = S(X(t), \delta t) = \mathcal{R}[s^k(\mathcal{L}(X(t)), dt)], \tag{16}$$

where $\delta t = kdt$ (cf. Figure 4) is a macroscopic time step. Note, that other choices for the macroscopic time stepper S are possible (see e.g., [Vandekerckhove et al (2011), Marschler et al (2013)]). For our analysis, we use (16) as the most common choice for a macroscopic time stepper (see e.g., [Kevrekidis et al (2003), Kevrekidis and Samaey (2009)]).

The macroscopic time stepper S can be used to compute the macroscopic evolution $X(t)$ without the knowledge of the underlying macroscopic equations of motion (13). Further higher-level tasks can be performed, e.g., a numerical bifurcation analysis (cf. Section 4). It is also possible to use the macroscopic time stepper for coarse projective integration, i.e., an Euler step in the macroscopic dynamics. Under some circumstances the time step in the coarse projective integration method can be chosen much larger than the integration time δt. Therefore, a coarse projective integration can reduce the computing time for macroscopic trajectories [Kevrekidis and Samaey (2009)].

In this paper, we will focus on the coarse numerical bifurcation analysis. In Sections 3.1 and 3.2, we introduce equation-free versions of 1) Newton's method and the 2) false position method (regula falsi) as root finding algorithms. Section 3.3 introduces recently developed 3) implicit equation-free methods [Marschler et al (2014)]. These three methods can be used in the corrector step of a pseudo-arclength continuation to correct a pre-liminary prediction to the macroscopic stationary branch (cf. [Kuznetsov (2004)] for an introduction to pseudo-arclength continuation).

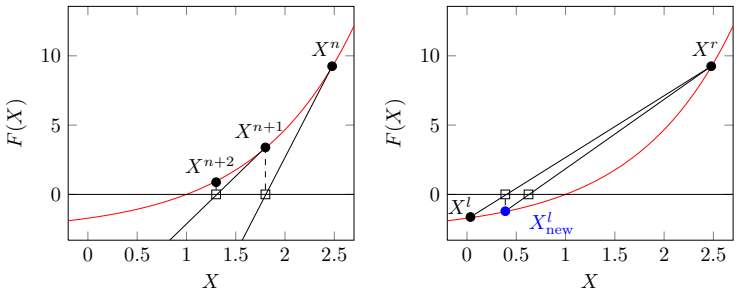

Fig. 5. Left. Newton's algorithm to determine the root of a function F (red line). A better approximation X^{n+1} for the root of F is computed by (18) using an initial guess X^n, the function value $F(X^n)$ and the slope $F_X(X^n)$. This method is iterated until a desired accuracy is achieved. **Right**. The false position method finds an embraced root between two initial guesses X^l and X^r left and right from the root, respectively. By a linear approximation through these two points, a new root is obtained. For a next iteration step, one of the previous roots (cf. X^l_{new} in the figure) is replaced according to the algorithm presented in Section 3.2. In contrast to Newton's method, no information about the first derivative is needed.

3.1. Newton Algorithm

In the following, we describe how the macroscopic time stepper can be used to compute bifurcation diagrams. The analysis of the learning process in the barn owl's auditory system in Section 4 only requires a one-dimensional coarse variable. Therefore, we focus on the one-dimensional case and the computation of macroscopic fixed points of (13), which are defined as

$$\dot{X} = 0 = F(X). \tag{17}$$

Since F is not available in closed form and only accessible through the macroscopic time stepper, numerical methods have to be used to find its roots. The most common method for this task is Newton's algorithm for finding an approximate root close to an initial guess (see e.g., [Press et al (2007)]). First, an initial guess X^0 for the root of F is chosen, which is preferably close to the true root. Subsequent iterations are computed by

$$X^{n+1} = X^n - F_X^{-1}\big|_{X^n} F(X^n), \tag{18}$$

where $n \in \mathbb{N}_0$ and F_X^{-1} is the inverse of the Jacobian of F (cf. Figure 5, left panel). In the one-dimensional case, F_X is simply $\partial F/\partial X$, i.e., the first derivative of F. Note, that it can be computationally very expensive to compute the inverse of the Jacobian in higher dimensions. Hence, a variant of the Newton's algorithm called Newton-Krylov method has been developed, which substitutes the computation of the inverse of the Jacobian by the computation of matrix-vector products (for details, see [Vandekerckhove et al (2009),Knoll et al (2005)]).

The unknown functions F and its Jacobian F_X in equation (18) can be approximated by using the macroscopic time stepper (16) as

$$F(X) = \frac{X(t+\delta t) - X(t)}{\delta t}, \qquad F_X(X) = \frac{F(X+\Delta X) - F(X)}{\Delta X}. \tag{19}$$

The values of δt and ΔX are problem-specific and have to be chosen such that the derivative approximation is reasonable, i.e., a behavior compatible with the assumption of being in the linear regime. Note, that it is also possible to use symmetric derivatives, e.g., the central difference approximation

$$F(X) = \frac{X(t+\delta t) - X(t-\delta t)}{2\delta t} \tag{20}$$

or any other higher-order approximations, if the numerical determination of the derivatives by a first order approximation is too inaccurate.

3.2. False Position Method

The application of Newton's algorithm yields unreliable results for problems with noisy data: noise complicates the numerical determination of F and F_X and the noise is amplified in higher-order derivatives [McDevitt (2012), Kruttiventi et al (2010)]. To avoid this problem, it is convenient in one-dimensional systems to use the false position method [Press et al (2007)]; a combination of the secant and the bisection method.

The method works as follows (cf. Figure 5, right panel). Initially, two points X^l and X^r are chosen, such that a root is embraced by them, i.e., $F^l := F(X^l) < 0$ and $F^r := F(X^r) > 0$ or vice versa. A better guess X^{new} is computed as the root of the line through these two points.

$$X^{\text{new}} = X^r \frac{F^r(X^r - X^l)}{F^r - F^l}, \qquad F^{\text{new}} = F(X^{\text{new}}). \tag{21}$$

If $F^{\text{new}} \cdot F^l > 0$, i.e., X^{new} is on the same side of the root as X^l, replace (X^l, F^l) with $(X^{\text{new}}, F^{\text{new}})$. Otherwise, replace (X^r, F^r) instead. This process is iterated until a desired error tolerance, i.e., either $|F(X^l)|$ or $|F(X^r)|$ are small, or the maximum number of iterations is reached.

The function F^{new} in (21) is approximated with (19) as in the Newton algorithm. Since the Jacobian is not needed for the false position method, it is more robust against noise. The trade-off is, that it can only be used in one-dimensional problems due to the embracing of the root between two points. An advantage is, that the false position method is guarenteed to converge to the root, if it is between the two initial guesses and if it is the only root in between them.

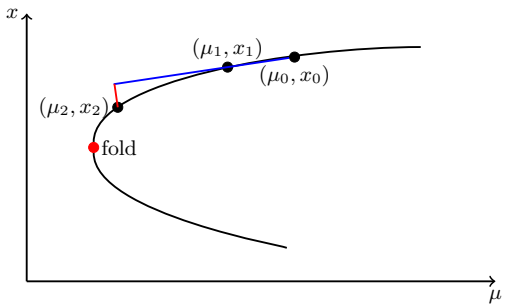

Fig. 6. Scheme of the pseudo-arclength continuation. In the predictor step (blue line), a new guess is computed from the two previous stationary points (μ_0, x_0) and (μ_1, x_1) (black dots to the right) by linear interpolation. The corrector step (red line) finds a root (μ_2, x_2) (black dot) in an orthogonal subspace to the predictor. Due to the correction in an orthogonal subspace, pseudo-arclength continuation is able to continue branches around fold points (red dot).

3.3. Implicit Equation-Free Method

Another recently introduced method to obtain the dynamics on the slow manifold is the implicit equation-free method that uses a healing time t_{skip}. The flow is applied to a lifted state $\mathcal{L}(X)$ over a time t_{skip} in order to follow the fast dynamics to the slow manifold. Therefore, one initializes the system at a different microscopic state, i.e., the healed state on the slow manifold, than intended. Consequently, all numerical iteration and continuation methods become implicit. A detailed derivation and discussion of the method can be found in [Marschler et al (2013)] (see also [Marschler et al (2014)] for an overview). For finding macroscopic fixed points, the function $F(X)$ in (19) is replaced by

$$F(X) = \frac{\mathcal{R}[s^{k+k_{\text{skip}}}(\mathcal{L}(X(t)), dt)] - \mathcal{R}[s^{k_{\text{skip}}}(\mathcal{L}(X(t)), dt)]}{\delta t}, \qquad (22)$$

where $\delta t = k dt$ and $t_{\text{skip}} = k_{\text{skip}} dt$. Like in (19), the values δt and t_{skip} have to be chosen problem-specific.

3.4. Pseudo-Arclength Continuation of Fixed Points

All methods presented in Sections 3.1, 3.2 and 3.3 can be used in the corrector step of a pseudo-arclength continuation to continue stationary branches in variable-parameter space (cf. Figure 6 for the scheme). A secant predictor in pseudo-arclength continuation computes a new point on a secant through two previous points on the branch.In the following corrector step, a root finding algorithm, e.g., Newton's method or false position method, is used to find a root of F in the orthogonal subspace of the predictor. This step is iterated until the root is found with a given pre-defined error tolerance

defined by $|F|$. The result of the corrector step is accepted as a new point on the branch and can be used in the next iteration of the pseudo-arclength continuation.

One advantage of pseudo-arclength continuation is, that it can continue branches around fold points, which is not possible with natural continuation, i.e., a correction step with fixed parameter values. Hence, pseudo-arclength continuation is typically chosen over natural continuation.

4. Map Formation and Coarse Bifurcation Analysis

We now show the numerical results for the model presented in Section 2. In Section 4.1 the map formation and the correct function of the neuronal network is presented. These results have already been discussed in [Kempter et al (2001)] and are reproduced here as a basis for the new results in Section 4.2. Section 4.2 shows the coarse bifurcation analysis of the learning process based on the equation-free methods introduced in Section 3. The influence of the amplitude η of the learning window is studied and further discussed in Section 6.

4.1. Stripe Formation and Coincidence Detection

In order to study the learning process, i.e., the map formation, a random synaptic weight matrix $J(0)$ is initialized at the beginning of a simulation, where the synaptic weights are drawn from a uniform distribution in $[0.7, 1.3]$ (remember, that $J^{\min} = 0$ and $J^{\max} = 2$). An initial matrix $J(0)$ is shown for the left and the right ear in Figure 7, top row. The history of incoming and outgoing spikes is always initialized with an empty history, such that the neurons first obtain a non-vanishing potential h_n after the first incoming signal. In order to test the correct behavior of the neuronal network, $\eta = 1.0$ is chosen as the initial amplitude of the learning window. After $T = 5 \cdot 10^5$ time steps the learning rule (10) has formed a stripe structure in the matrix $J(T)$ (cf. Figure 7, bottom row). It is worth mentioning, that these stripe structures are not stationary states of the microscopic system. Although the stripes are conserved as a pattern, they move through the weight matrix J as a traveling wave on a slow time scale (cf. Section 5). The spike activity pattern is unchanged by the traveling wave. Hence, prey detection is possible independent of the phase of the traveling wave.

Another interesting observation is, that the formation of a stripe structure after the learning process is independent of the initial condition, but the shift between the left and right ear can be different. The shift is determined by the different initial conditions and the random ITDs, which change every 10^4 time steps. Since the shift is fixed after the initial learning process prey detection is not influenced.

For the correct function of the auditory system it is also important, that the maximal neuronal activity is at the neuron, where the overlap of the signals is highest. We investigate this behavior by plotting the absolute delay Δ_{an} for synapses with synaptic strength $J^{\max}$ separately for left (red) and

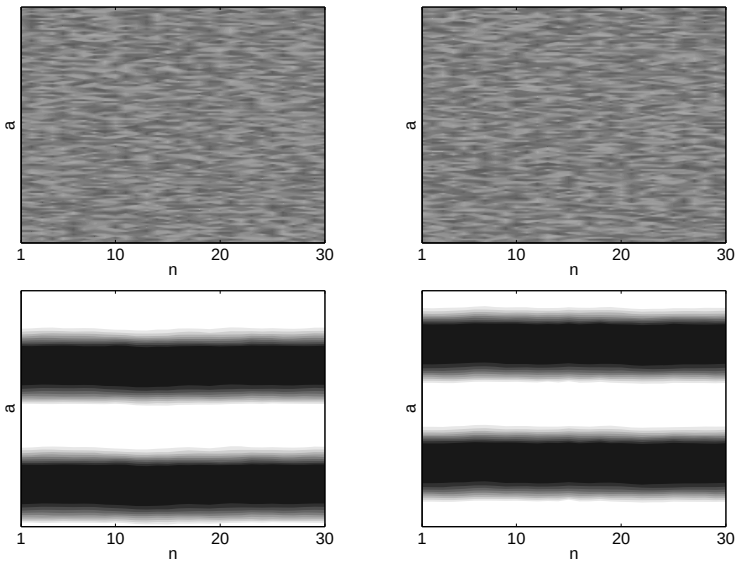

Fig. 7. Top. Initial synaptic weight matrix $J(0)$. Weights are uniformly distributed in $[0.7, 1.3]$. The left (right) panel corresponds to the left (right) ear. **Bottom**. After a learning session of 10^6 time steps, a map is formed and a stripe structure is observed. The black stripes have the maximal weight $J^{\max}$, while the white regions have minimum weight $J^{\min}$.

right (orange) ear for $t_{\mathrm{ITD}} = 0$ (cf. Figure 8, left panel). A maximal overlap is observed at neuron 20 (yellow region) meaning that signals arrive here at the same time. This coincidence of the signal should lead to a maximum in the neuron activity. The number of spikes for each neuron in a simulation of 10^4 time steps of a fully developed synaptic weight matrix J for $t_{\mathrm{ITD}} = 0$ can be seen in Figure 8, right panel. The maximum of the neuron activity is exactly at the neuron with the maximal overlap of the stripes of the weight matrix J. This is the verification of Jeffress' model of coincidence detection in the NL model.

Although the overlap position can be different for different initial conditions $J(0)$, it is important to note, that this different shift is not influencing the ability to detect angles by ITD. Once a structure is built up in the learning process, the shift between the stripes is fixed and the network can be used to determine angles by ITDs. By running simulations for a fully developed synaptic weight matrix J for fixed ITDs in $[-35, 35]$, it is observed that the maximum of the activity shifts linearly with the ITD, yielding a unique map from an ITD, i.e., an angle, to neuron activity (see Figure 9).

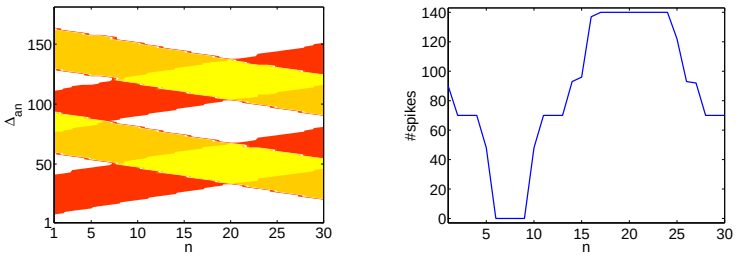

Fig. 8. Left. Absolute delay against the neuron number for synapses with maximal weight $J^{\max}$. The overlapping region (bright yellow) denotes the neurons, where input signals with $t_{\mathrm{ITD}} = 0$ arrive at the same time. **Right**. Number of emitted spikes of NL neurons during a simulation of a fully developed synaptic weight matrix J over 10^4 time steps. The maximal activity is at the neuron, where the overlap of the left and right ear is maximal (cf. left panel). This verifies the correct function of the NL as a linearly-ordered array of coincidence detectors as described by Jeffress' model.

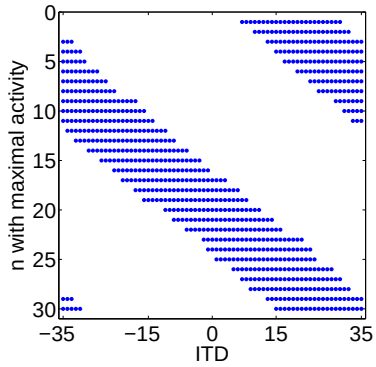

Fig. 9. Location of the maximal neuronal activity as in Figure 8, right panel, during a 10^4 time step simulation of a fully developed synaptic weight matrix. It is shown, that the maximal activity shifts linearly with the ITD. Therefore, a neuronal activity is uniquely mapped to an ITD, i.e., an angle.

4.2. Bifurcation Analysis of the Learning Process

The results presented in Section 4.1 showed a pattern formation in the synaptic weight matrix enabling the barn owl to detect its prey. With the model at hand, it is possible to study the influence of parameters on the learning process. Since the learning window W is mainly responsible for a successful learning (cf. [Kempter et al (2001)]), we study the influence of the amplitude η on the map formation. In order to investigate this macroscopic phenomenon, we define a one-dimensional macroscopic variable V, also called order parameter, to distinguish between a synaptic weight ma-

trix with stripe structure (see Figure 7, bottom row) and a random matrix (see Figure 7, top row). To capture the salient features of J, we choose

$$V = \frac{1}{(A-2T)N} \sum_n \left[\sum_{a=1}^{A/2-T} (J_{an} - J_{a+T/2,n}) \delta(J_{an}, J_{(a+T)n}) \Theta(J_{an} - \tilde{J}) + \sum_{a=A/2+1}^{A-T} (J_{an} - J_{a+T/2,n}) \delta(J_{an}, J_{(a+T)n}) \Theta(J_{an} - \tilde{J}) \right] \tag{23}$$

where $\tilde{J} = 1.3$ is a lower bound for the synaptic weights, δ is the Kronecker-δ and Θ is the Heaviside step function. T is the input period, which is also the spatial period of the stripe structure (see Figure 7 and the discussion at the end of this section). V measures the relative periodicity of the matrix J: the Kronecker-δ assures a correct period across the axons. In the computations, it is implemented with a tolerance, i.e., $\delta(J_{an}, J_{(a+T)n}) = 1$ if $|J_{an} - J_{(a+T)n}| < 0.01$ and 0 otherwise, to take numerical inaccuracies and noise into account. If the period is correct, the synapse is weighted with the difference to the synapse half a period ahead. For a fully developed matrix J this usually amounts to $J_{an} - J_{a+T/2,n} = J^{\max} - J^{\min} = 2$. By that choice it is avoided, that a uniform matrix without stripe structure gets assigned a large positive value V. Further, the Θ-function takes only synaptic weights $J_{an} > \tilde{J}$ into account. Since a synaptic weight matrix with stripe structure but too small values in strength is not able to let the neurons fire and therefore a prey detection would not be possible. Note, that a Fourier representation of the spatial periodicity is not useful, since the hard limit $J^{\max}$ of the maximal synaptic weight leads to a rectangular-shaped spatial pattern across axons.

In terms of equation-free nomenclature V defines the restriction operator $\mathcal{R}$. It maps the high-dimensional weight matrix J to a one-dimensional variable $V = \mathcal{R}(J)$. Before the equation-free tools (cf. Section 3) can be used, a lifting operator $\mathcal{L}$ has to be defined. Generally, it is difficult to find $\mathcal{L}$ for the high-dimensional microscopic dynamics. A possible workaround for equation-free bifurcation analysis is to use the results from previous solutions, e.g., from long term simulations converging to a stable state. Assuming, that a microscopic state J^{old} is known, a new synaptic weight matrix can be initialized as

$$J^{\text{new}} = J^{\text{old}} + \text{rand}(-\epsilon, \epsilon) + \alpha \text{bin}(J^{\text{old}} > 1), \tag{24}$$

where the old state J^{old} is perturbed by a small noise $\epsilon = 0.005$. $\text{rand}(-\epsilon, \epsilon)$ denotes a $A \times N$ random matrix with entries uniformly distributed between $-\epsilon$ and ϵ and $\text{bin}(J^{\text{old}} > 1)$ is a binary representation of all matrix entries over the certain threshold of 1, i.e., $(\text{bin}(J^{\text{old}} > 1))_{an} = 1$ if $J^{\text{old}}_{an} > 0$ and 0 otherwise. Here, only large synaptic weights are used for the scaling, since small values are not taken into account in the computation of V. To initialize the microscopic system close to a desired macroscopic value $\hat{V}$,

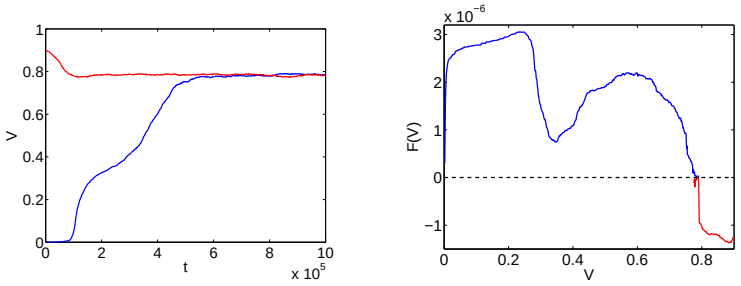

Fig. 10. Left. Evolution of the macroscopic variable V during a learning session of 10^6 time steps and $\eta = 1$. The initial simulation reaches a stationary state $V^* = 0.78$ after about $6 \cdot 10^5$ time steps (blue curve). The resulting synaptic weight matrix is used to lift V^* to a larger value $V = 0.9$. This new initial condition is simulated again for 10^6 timesteps, yielding a convergence to the same macroscopic stationary state V^* (red curve). **Right**. The macroscopic right-hand side $F(V)$ of (13) is computed from the direct simulation in the left panel. The function F is zero at the unstable and stable macroscopic fixed point $V = 0$ and $V^* = 0.78$, respectively. Note, that the order-of-magnitude of F resembles the slow time scale.

the coefficient α is adjusted such that $\mathcal{R}(J^{\text{new}}) = \hat{V}$. By this choice of $\mathcal{L}$ microscopic states are initialized close to the known state J^{old}, i.e., close to the slow manifold. Hence, the lifting operator is successfully defined in a neighborhood of known solutions and is therefore good enough for equation-free pseudo-arclength continuation. Furthermore, the so-called lifting error is reduced (cf. Section 3), which is usually introduced into the system by applying the lifting operator.

With the definition of the macroscopic variable V in (23) it is possible to investigate its evolution during a learning session. The results are shown in Figure 10. Starting with a random synaptic weight matrix $J(0)$, corresponding to $V(J(0)) = 0$, and $\eta = 1$ as in Figure 7, an increase of V is observed (blue line). After about $6 \cdot 10^5$ time steps, V reaches a stationary state at $V^* \approx 0.78$. Using the final microscopic state of this simulation in the lifting process to construct a starting configuration with $V = 0.9$ (red line), V decreases and converges back to the same macroscopic stationary state. Note that this macroscopic stationary state is not necessarily a fixed point of the microscopic dynamics. In fact, traveling waves in the synaptic weight matrix J can be observed, which leave the macroscopic variable V unchanged (cf. also Section 5). It is worth mentioning, that the stationary state is not exact in the sense that $\dot{V} = 0$. Due to the noise on the synapses and the noise in the input, V is fluctuating around a deterministic stationary state. The equilibrium is stationary in the sense that the long-term average

$$\langle V \rangle = \lim_{t \to \infty} \frac{1}{j^{\max}} \sum_{j=1}^{j^{\max}} V(t+j) \tag{25}$$

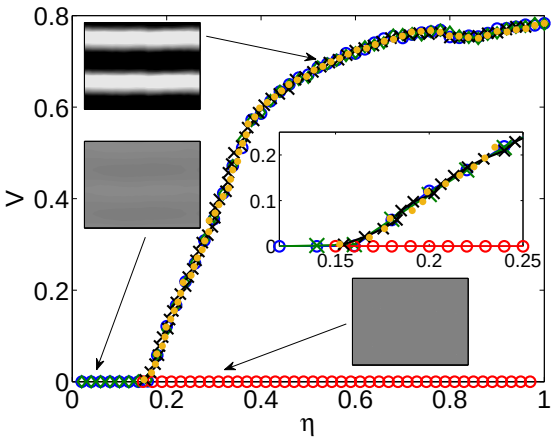

Fig. 11. Bifurcation diagram for the macroscopic variable V. Blue circles and green diamonds denote direct simulations of an up and downsweep, respectively. The red circles correspond to an unstable stationary branch obtained by the equation-free method. Black crosses follow the stable branch with the false position method and yellow dots are used for the pseudo-arclength continuation using implicit equation-free methods. All used methods show the same qualitative results but the noise leads to different quantitative results on the scale of the noise. An enlargement of the bifurcation region at $\eta = 0.16$ is shown in the inset. Furthermore, corresponding microscopic states are shown for comparison.

is constant, where $j^{\max}$ is a suitable upper limit, large compared to the characteristic time scale of the noise.

The macroscopic vector field $F(V)$ can be computed numerically from the trajectories $V(t)$ in Figure 10, left panel, using (19) with $\delta t = 5 \cdot 10^4$. A vanishing $F(V)$ shows, that $V = 0$ and $V = V^*$ are two stationary points (cf. Figure 10, right panel). Close to V^* the function F is noisy due to the noise in the model (cf. Section 2), which is amplified in the derivative. Without computing the first derivative $F_V = \partial F / \partial V$ numerically, a visual inspection of Figure 10, right panel, shows, that $F_V(0) > 0$ and $F_V(V^*) < 0$. Therefore, $V = 0$ is an unstable and V^* is a stable fixed point.

In order to investigate the change of system behavior with parameters, the final state of the simulation for $\eta = 1$ is used as a starting point for a downsweep to follow the stable stationary branch directly. $\Delta\eta = -0.02$ is chosen as a step size in the parameter direction and the respective last synaptic weight matrix is used as an initial condition for the next step. Each initial condition is simulated for an additional learning period of 10^6 time steps. The direct simulations show (cf. Figure 11, blue circles), that $V = 0$ is obtained for $\eta < \eta^* \approx 0.16$, indicating a qualitative change in system behavior. This bifurcation from a pattern structure to some other microscopic configuration destroys the ability of the barn owl to detect prey.

Therefore, if the amplitude η of the learning window is too small, the barn owl is unable to survive.

Before investigating the region around the bifurcation point in more detail, we use the final microscopic state of the downsweep at $\eta = 0.02$ as a starting point for an upsweep with $\Delta\eta = 0.02$. The same procedure as in the downsweep is used. The simulation results show (cf. Figure 11, green diamonds), that the upsweep exactly follows the downsweep. The only visible difference stems from the noise of each specific simulation. Since upsweep and downsweep follow the same stable branch, hysteresis behavior can be ruled out.

In order to test the applicability of equation-free methods, pseudo-arclength continuation (cf. Section 3.4) together with the false position method (cf. Section 3.2) in the corrector step is used to continue the stable branch from $\eta = 1$ downwards (cf. Figure 11, black crosses). The two final states at $\eta = 1.00$ and $\eta = 0.98$ from the previous downsweep are chosen to initialize the secant predictor. The length of the predictor step is chosen as 0.02 and the macroscopic right-hand side F is approximated with (19) and $\delta t = 2 \cdot 10^5$. The left and right values V^l and V^r in (21) are chosen orthogonal to the predictor step and $ds = 0.1$ away from the prediction point. The number of iterations in the correction step is fixed to $k^{\max} = 12$ iterations, independent of the actual error. A comparison with the downsweep data in Figure 11 shows, that the equation-free false position method continuation follows the stable branch exactly (up to noise-induced fluctuactions) until the bifurcation point is reached. The equation-free approach gives the same quantitative and qualitative results as the direct simulation. Hence, we are assured that equation-free methods can be used to study the pattern formation behavior of the neuronal network. Unfortunately, the noise-robust false position method fails after the bifurcation point, i.e., for $\eta < \eta^*$. The algorithm relies on the fact, that a root is in between two initial guesses. Since $V = 0$ for $\eta < \eta^*$, one would have to obtain a negative guess. This is not possible, since V is non-negative by definition.

In order to check whether implicit methods can be used for equation-free pseudo-arclength continuation, we applied (22) in the corrector step to continue the same stable branch as with the false-position method. A healing time $t_{\text{skip}} = 10^4$ and a time step $\delta t = 10^5$ is used together with an error tolerence $5 \cdot 10^{-4}$ of the residual as a convergence criterion for the Newton iteration (18). Microscopic states from the previous downsweep were used in the lifting process to obtain states close to the slow manifold. To deal with the noise in the derivatives, the dynamics on the slow manifold is assumed to be in a linear regime. Therefore, macroscopic trajectories can be fitted with a function of the form $V(t) = a + b\exp(-ct)$, where $a, c > 0$ and $b \in [-1, 1]$. By using this monotone function, the noise is removed and a reasonable estimate for F and F_V is possible. However, if the fit fails or the confidence interval is too large, i.e., more than 100% deviation from the predicted mean, the finite difference approximation (19) is used as a backup

method. The implicit Newton method shows the same qualitative results as the false position method (cf. Figure 11, yellow dots).

Since the false position method can not be applied for $V = 0$, we can not use it to continue the unstable branch at $V = 0$ for $\eta > \eta^*$. Instead, we use a one-sided Newton's method (cf. Section 3.1) to continue the unstable branch. Instead of using (19) like in the false position method, the central-difference approximation (20) is used to approximate F. A long simulation of $3 \cdot 10^6$ time steps has been run and F is approximated along this trajectory with $\delta t = 5 \cdot 10^4$. Note, that such a long integration time was necessary since the divergence from the unstable stationary state is very slow close to the bifurcation point η^*. $\Delta V = 0.01$ has been chosen to approximate F_V along the trajectory. By using a long simulation for estimating F and F_V instead of many short ones, one can reduce the influence of the lifting error. With the approximated functions F and F_V, the root of F is determined by Newton's method(18). If the relative error tolerance is smaller than 10^{-3}, the iteration is aborted and the actual value is accepted as a root. If an iteration in the algorithm yields an unphysical state $V \lesssim 0$, the algorithm is aborted and $V = 0$ is accepted as the stationary point. The advantage of the Newton method is, that the stability information is obtained along with the algorithm, since F_V has to be computed anyway. By using Newton's method, the unstable branch at $V = 0$ is continued for $\eta > \eta^*$. At $\eta^* = 0.16$, Newton's method converges to the stable branch, indicating the closeness to the bifurcation point. Note, that it is not possible to determine the bifurcation point with a higher accuracy than the noise level. Therefore, the value for the bifurcation point can be determined only with an uncertainty.

Nevertheless, it is possible to compute the derivatives of F in a neighborhood of the expected bifurcation point, but one has to keep in mind, that the results have to be interpreted together with the errors. For an explanation of the used algorithm, two sample trajectories for $\eta = 0.20$ and $\eta = 0.24$ are shown in Figure 12, left panel. Both simulations where initialized with the same initial condition and the learning process was performed for $5 \cdot 10^6$ time steps. The corresponding vector fields approximated by a central-difference (20) and $\delta t = 5 \cdot 10^4$ are shown in Figure 12, right panel (blue and green curves). It is observed, that F is very noisy close to the respective macroscopic stationary states. To smoothen the functions, we discretize the function in V for $\delta V = 0.01$. The function value $F(\tilde{V})$ at a discrete point $\tilde{V}$ is then computed as the mean over all function values in $[\tilde{V} - \delta V, \tilde{V}]$. The error bars are the standard deviation in the same interval. Computing these discrete representations of F (cf. red and black error bars in Figure 12, right panel) around the bifurcation point for the stable and unstable branch, the functions F and F_V can be evaluated at the stationary branches for a range in η. The results with error bars are shown in Figure 13. It is verified within the error bars, that F is zero along the stationary branches, verifying the existence of a stable and unstable stationary state. Also, F_V crosses zero as one approaches η^* at $V = 0$. Since the Jacobian

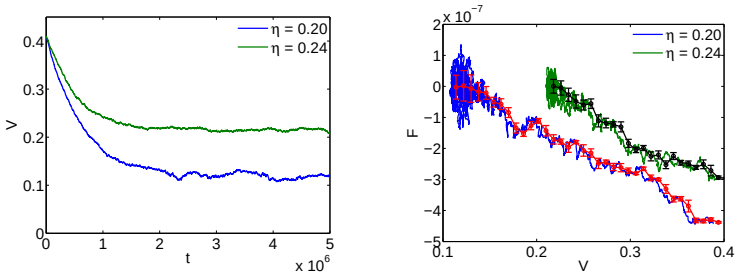

Fig. 12. Left. Direct simulation of two macroscopic trajectories for different values of η. **Right**. Central difference approximation of the first derivative for the two trajectories in the left panel (blue and green curves). Noise in the data is amplified and leads to unreliable estimates of the function, especially close to the stationary states. For further computations, F is replaced by discretized and averaged version (bin size $\delta V = 0.01$, red and black curves with error bars).

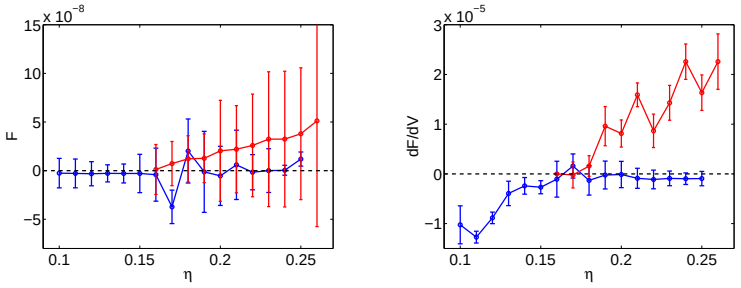

Fig. 13. Left. Vector field F evaluated at the stable (blue) and unstable branch (red) using the discretized and averaged function shown in Figure 12 (red and black curves). Within the error margins, the macroscopic right-hand side is zero, confirming the existence of two stationary branches. **Right**. First macroscopic derivative along the two branches. A transition from a stable to an unstable branch is determined at $\eta^* \approx 0.16$.

is singular at η^*, it is shown, that a bifurcation occurs. To determine the type of bifurcation in the sense of deterministic bifurcation theory, it would be necessary to check higher-order derivatives. Since the data is too noisy in the stochastic system, a useful determination of higher-order derivatives is prohibited. A further analysis would require to analyze the system with methods from random dynamical systems and bifurcation theory, which is still at its infancy [Arnold et al (1997), Crauel and Flandoli (1994)].

In order to verify the bifurcation point, we show that the chosen macroscopic measure (23) can also be replaced by another measure and the bifurcation diagram still has the same characteristics. To that end, we choose the vector strength [Goldberg and Brown (1969), Gerstner et al (1996)] as another periodicity measure. First, we apply a binarization of the connec-

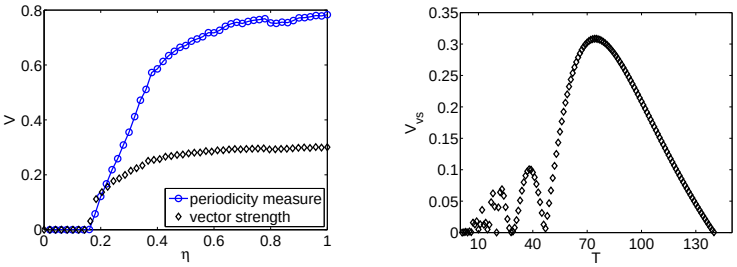

Fig. 14. Left. Comparison between periodicity measure (23) (blue circles) and the vector strength (26) (black diamonds). **Right**. Dependence of the vector strength on the period T. A peak is observed close to the input period $T = 70$, showing that the spatial period of the stripe structure correlates with the period of the input signal.

tivity matrix: $J_{an}^{\text{bin}} = 1$ for $J_{an} > \tilde{J}$ and 0 otherwise. Further, we assign a vector $\mathbf{x} = (a, n)$ to all $J_{an}^{\text{bin}} = 1$ and define the wave vector $\mathbf{k}_T = (0, 2\pi/T)$ for the input period T. After normalization of the synaptic weight matrix $\hat{J}_{an} = J_{an}/J^{\max} \in [0, 1]$ we define the vector strength

$$V_{\text{vs}} = \left| \frac{1}{AN} \sum \hat{J}_{an} \exp(i\mathbf{x} \cdot \mathbf{k}_T) \right| \tag{26}$$

as a convex sum over all non-zero elements of J^{bin}. Using the same microscopic states as in the downsweep in Figure 11, we apply (26) instead of (23). A comparison is shown in Figure 14. Obviously, the values of the vector strength are different from the other macroscopic variable but the same bifurcation point is found and the branches show the same qualitative behavior, i.e., they can be smoothly transformed into one another.

An additional check for the periodicity of the stripe structure can be performed using the wave vector $\mathbf{k}_T$. Detuning the wave vector to another period different from the input period $T = 70$, it is observed, that the vector strength drops for detuned periods. Thus, the spatial period of the stripes is indeed well-described by the input period.

5. Traveling Waves in Connectivity Matrix

As mentioned in Section 4, the synaptic weight matrix J does not converge to a stationary state on the microscopic level. Instead, after the initial map formation process, the resulting stripes travel through the synaptic weight matrix (cf. Figure 15) along the axonal direction. The slowly traveling waves are the verification for another separation of time scales. The formation of the stripe structure happens on a much shorter time scale than the characteristic time scale of the traveling waves, measured by the speed of the stripe movement. As already noted in Section 4, the function of the network is independent of this motion. Since the stripes move in parallel, the

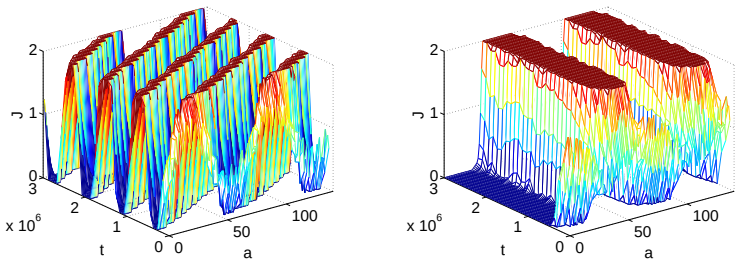

Fig. 15. Traveling wave solutions of the synaptic weight matrix shown for one neuron connected to the left ear. **Left**. For $\hat{u} = -1$ traveling waves with a finite speed are observed. The wave speed and the width of the plateau depend on $\hat{u}$. **Right**. For $\hat{u} = -10$, the speed of the traveling wave vanishes.

overlap position is invariant, i.e., the neuron with maximal activity is invariant. The process corresponds to a continuous learning/unlearning of the synapses. A possible interpretation of this process is, that a static network would be to vulnerable to external errors. Permanent learning keeps the network functional and corrects errors.

A long simulation of the microscopic synaptic weight matrix J shows, that the stripes travel through the matrix with a constant speed and shape. Therefore, they can be described as traveling waves. In this Section, we fix $\eta = 1$ and investigate the dependence of the wave speed on the shift $\hat{u}$ of the learning window.

5.1. Dependence on $\hat{u}$

Since the learning window is asymmetric, it can lead to an effective drift of the structures through the matrix. The degree of asymmetry with respect to the origin is described by the shift parameter $\hat{u}$. In [Kempter et al (2001)], it is chosen to be $\hat{u} = -1$. The influence of $\hat{u}$ in the learning window on the speed of the traveling waves is investigated in this section. Since the macroscopic measure V is constant for this kind of traveling wave, the microscopic level has to be used to analyze the behavior. By varying $\hat{u}$ in $[-15, 10]$ it is observed, that the speed of the traveling waves goes to zero for $\hat{u} \approx -10$ (cf. Figure 16, right panel). The wave speed has a big influence on the bifurcation diagrams. Numerical downsweeps have been performed for different values of $\hat{u}$ starting from $\eta = 1$. The shape of the stable branch changes significantly with $\hat{u}$ and the bifurcation point shifts drastically (cf. Figure 16, left panel).

For positive values of $\hat{u}$ the pattern formation breaks down even for reasonable large values of η. In particular, for $\hat{u} = 10$, the bifurcation point is shifted to $\eta \approx 0.82$ and the synaptic weights in J are very small (cf. blue circles in Figure 16, left panel). Another interesting behavior can be observed for negative values of $\hat{u}$. Although the shape of the stable branch is different for all values, the bifurcation point (V^*, η^*) is the same for all

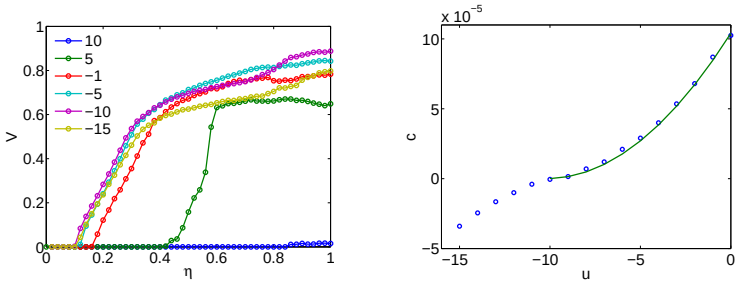

Fig. 16. Left. Comparison of the bifurcation diagrams for different values of $\hat{u}$. The bifurcation point decreases with $\hat{u}$ and approaches a constant for $\hat{u} < -5$. **Right**. Speed of the traveling wave in dependence on the shift $\hat{u}$ of the learning window. At a critical value $\hat{u}^*$ the wave speed goes to zero, leading to a standing wave. For $\hat{u} > \hat{u}^*$, the speed is well-described by the quadratic scaling $c(\hat{u}) = \alpha(\hat{u} - \hat{u}^*)^2$, where $\alpha = 10^{-6}$ (green line).

$\hat{u} < -5$. The shape close to the bifurcation point is very similar and might hint to a universal behavior.

6. Conclusion and Outlook

In this paper, we applied equation-free methods to analyze the learning behavior of the auditory system of the barn owl on a macroscopic level. Numerical investigations showed a strong influence of the learning window on the pattern formation and hence prey detection. This preliminary study motivated the choice of η as a bifurcation parameter. The learning window suggested by [Kempter et al (2001)], i.e., $\eta = 1$ in this paper, leads to a correct map formation. By using equation-free methods (cf. Sections 3 and Section 4), macroscopic bifurcation diagrams have been obtained. The bifurcation diagram in Figure 11 shows a bifurcation at η^*. This bifurcation has a big effect on the survival of the barn owl. Since the map formation is prohibited for $\eta < \eta^*$, the barn owl would not be able to detect prey.

By continuing the stable branch with an equation-free pseudo-arclength continuation using the false position method in the corrector step it is shown, that equation-free methods can be successfully applied to analyze neuronal networks. The biggest disadvantage of the false position method is its limitation to one-dimensional macroscopic variables. A generalization to higher-dimensional coarse variables could help to determine high-dimensional stationary branches, where reliable information about the macroscopic right-hand side F_V is unavailable. These methods can be especially useful in equation-free continuation of experiments, where accurate data on derivatives can be hard to obtain. In order to construct the unstable branch, a one-sided Newton method has been applied in the corrector step to find macroscopic fixed points. Another advantage of Newton's method is that it can be applied to higher-dimensional problems without any changes

to the algorithm.The use of implicit equation-free methods yielded the same results as the normal Newton and false position method. This shows, that these implicit methods can be applied as well to analyze noisy neuronal systems.

Although the existence of a macroscopic bifurcation at (V^*, η^*) could be shown by a root of the macroscopic right-hand side $F(V^*, \eta^*) = 0$, the type of the bifurcation remains unclear, due to the amplified noise in higher-order derivatives. This problem has to be tackled in general in future work in order to get reliable information about higher-order derivatives in equation-free computations. Nevertheless, the shape of the bifurcation diagram hints at a transcritical bifurcation, where the lower part is hidden due to the non-negativity of V.

Motivated by numerical investigations of the barn owl model, another time scale has been found. Very long direct simulations revealed traveling waves in the synaptic connectivity matrix. The wave speed depends on the choice of the shift $\hat{u}$ in the learning window. A detailed analysis of this effect and a rigorous (equation-free) bifurcation analysis is an interesting direction for further research.

Acknowledgements. The authors would like to thank Christian Leibold from LMU Munich for useful discussions about the implementation of the model. J. Starke would also like to thank the Danish Research Council FTP under the project number 09-065890/FTP and the Villum Fonden under the VKR-Centre of Excellence 'Ocean Life' for financial support.

References

Arnold et al (1997). Arnold VI, Kozlov VV, Neishtadt AI (1997) Mathematical aspects of classical and celestial mechanics. Springer Verlag, Berlin

Buckley and Nowotny (2011). Buckley CL, Nowotny T (2011) Multiscale model of an inhibitory network shows optimal properties near bifurcation. Phys Rev Lett 106:238,109, DOI 10.1103/PhysRevLett.106.238109

Burkitt (2006). Burkitt AN, Biol. Cybern. **95**, 1–19 & 97–112 (2006).

Carr and Konishi (1988). Carr CE, Konishi M (1988) Axonal delay lines for time measurement in the owl's brainstem. Proceedings of the National Academy of Sciences 85(21):8311–8315

Crauel and Flandoli (1994). Crauel H, Flandoli F (1994) Attractors for random dynamical systems. Probability Theory and Related Fields 100(3):365–393, DOI 10.1007/BF01193705

Fenichel (1979). Fenichel N (1979) Geometric singular perturbation theory for ordinary differential equations. Journal of Differential Equations 31:53–98

Frisch (1995). Frisch U (1995) Turbulence. The Legacy of A. N. Kolmogorov. Cambridge University Press

Gerstner et al (1993). Gerstner W, Ritz R, van Hemmen JL (1993) Why spikes? Hebbian learning and retrieval of time-resolved excitation patterns. Biological Cybernetics 69(5-6):503–515, DOI 10.1007/BF00199450

Gerstner et al (1996). Gerstner W, Kempter R, van Hemmen JL, Wagner H (1996) A neuronal learning rule for sub-millisecond temporal coding. Nature 383(6595):76–78

Haken (1983). Haken H (1983) Synergetics. An introduction. Nonequilibrium phase transitions and self organization in physics, chemistry and biology. 3.ed / Springer series in synergetics 1. Springer, Berlin

Hebb (1949). Hebb D (1949) The organization of behavior. New York: Wiley & Sons

van Hemmen (2001). van Hemmen JL (2001) Theory of synaptic plasticity. In: Moss F, Gielen S (eds) Neuro-Informatics and Neural Modeling, Handbook of Biological Physics, vol 4, North-Holland, pp 771 – 823

van Hemmen (2002). van Hemmen JL (2002) The map in your head: How does the brain represent the outside world? ChemPhysChem 3(3):291–298

Huang et al (1997). Huang J, Ohnishi N, Sugie N (1997) Building ears for robots: Sound localization and separation. Artificial Life and Robotics 1(4):157–163, DOI 10.1007/BF02471133

Jeffress (1948). Jeffress LA (1948) A place theory of sound localization. J Comp Physiol Psychol 41:35–39

Kempter et al (1998). Kempter R, Gerstner W, van Hemmen JL, Wagner H (1998) Extracting oscillations: Neuronal coincidence detection with noisy periodic spike input. Neural Computation 10:1987–2017

Kempter et al (1999). Kempter R, Gerstner W, van Hemmen JL (1999) Hebbian learning and spiking neurons. Phys Rev E 59:4498–4514, DOI 10.1103/PhysRevE.59.4498

Kempter et al (2001). Kempter R, Leibold C, Wagner H, van Hemmen JL (2001) Formation of temporal-feature maps by axonal propagation of synaptic learning. Proceedings of the National Academy of Sciences 98(7):4166–4171

Kevrekidis and Samaey (2009). Kevrekidis IG, Samaey G (2009) Equation-free multiscale computation: Algorithms and applications. Annual Review of Physical Chemistry 60(1):321–344

Kevrekidis et al (2003). Kevrekidis IG, Gear CW, Hyman JM, Kevrekidis PG, Runborg O, Theodoropoulos C (2003) Equation-free, coarse-grained multiscale computation: enabling microscopic simulators to perform system-level analysis. Communications in Mathematical Sciences 1:715 – 762

Knoll et al (2005). Knoll D, Mousseau V, Chacn L, Reisner J (2005) Jacobian-free Newton-Krylov methods for the accurate time integration of stiff wave systems. Journal of Scientific Computing 25:213–230

Kruttiventi et al (2010). Kruttiventi J, Wu J, Frankel J (2010) Obtaining time derivative of low-frequency signals with improved signal-to-noise ratio. Instrumentation and Measurement, IEEE Transactions on 59(3):596 –603, DOI 10.1109/TIM.2009.2025069

Kuznetsov (2004). Kuznetsov YA (2004) Elements of Applied Bifurcation Theory, Applied Mathematical Sciences, vol 112, 3rd edn. Springer, New York

Laing (2006). Laing C (2006) On the application of equation-free modeling to neural systems. Journal of Computational Neuroscience 20:5–23

Leibold and van Hemmen(2002). Leibold C, van Hemmen JL (2002) Mapping time. Biological Cybernetics 87:428–439

Leibold et al (2001). Leibold C, Kempter R, van Hemmen JL (2001) Temporal map formation in the barn owl's brain. Phys Rev Lett 87(24):248,101, DOI 10.1103/PhysRevLett.87.248101

Marschler et al (2013). Marschler C, Sieber J, Berkemer R, Kawamoto A, Starke J (2013) Implicit Methods for Equation-Free Analysis: Convergence Results and Analysis of Emergent Waves in Microscopic Traffic Models. ArXiv e-prints 1301.6044

Marschler et al (2014). Marschler C, Sieber J, Hjorth PG, Starke J (2014) Equation-Free Analysis of Macroscopic Behavior in Traffic and Pedestrian Flow. ArXiv e-prints 1402.0314

McDevitt (2012). McDevitt TJ (2012) Discrete Lanczos derivatives of noisy data. International Journal of Computer Mathematics 89(7):916–931, DOI 10.1080/00207160.2012.666348

Meiss (2007). Meiss J (2007) Differential dynamical systems. Society for Industrial and Applied Mathematics, Philadelphia

Press et al (2007). Press WH, Teukolsky SA, Vetterling WT, Flannery BR (2007) Numerical recipes / the art of scientific computing. Cambridge University Press, Cambridge, NY

Vandekerckhove et al (2009). Vandekerckhove C, Kevrekidis IG, Roose D (2009) An efficient Newton-Krylov implementation oftheconstrained runs scheme for initializing onaslowmanifold. Journal of Scientific Computing 39:167–188

Vandekerckhove et al (2011). Vandekerckhove C, Sonday B, Makeev A, Roose D, Kevrekidis IG (2011) A common approach to the computation of coarse-scale steady states and to consistent initialization on a slow manifold. Computers & Chemical Engineering 35(10):1949 – 1958, DOI 10.1016/j.compchemeng.2010.12.002

Goldberg and Brown (1969). Goldberg JM, Brown PB (1969) Response of binaural neurons of dog superior olivary complex to dichotic tonal stimuli: some physiological mechanisms of sound localization. Journal of Neurophysiology 32(4):613-636.

V Coarse-grained particle model for pedestrian flow using diffusion maps

This paper [MSLK14] (C. Marschler, J. Starke, P. Liu and I. G. Kevrekidis, Physical Review E, **89**, 013304, 2014. "Copyright (2014) by the American Physical Society.") is a step into the direction of a fully automatic equation-free approach. The goal of an automatic macroscopic bifurcation analysis is discussed in Chap. 6. Diffusion maps could be used as a restriction operator to construct the relevant macroscopic variables. This is one major ingredient to make equation-free analysis more user-independent and thereby more applicable in real-world problems, e.g., in engineering.

The main result of the paper is the automatic reduction of a model for pedestrian flow (see [CHS12] for the model) from 800 dimensions to 3 dimensions. This substantial dimension reduction is done automatically without choosing a good coordinate system by hand. It is shown, that the same results as in [CHS12] are obtained in an automatic fashion. Once algorithms for an automatic construction of lifting operators are available, diffusion maps can be combined with these algorithms to study the possibility of an automatic coarse bifurcation analysis.

At the hand-in date of the thesis the paper has been published in Physical Review E, **89**, 013304 (2014).

PHYSICAL REVIEW E **89**, 013304 (2014)

Coarse-grained particle model for pedestrian flow using diffusion maps

Christian Marschler[*] and Jens Starke[†]
Department of Applied Mathematics and Computer Science, Technical University of Denmark, Matematiktorvet 303B, DK-2800 Kongens Lyngby, Denmark

Ping Liu[‡] and Ioannis G. Kevrekidis[§]
Department for Chemical and Biological Engineering, Princeton University, Princeton, New Jersey 08544, USA
(Received 7 August 2013; published 14 January 2014)

Interacting particle systems constitute the dynamic model of choice in a variety of application areas. A prominent example is pedestrian dynamics, where good design of escape routes for large buildings and public areas can improve evacuation in emergency situations, avoiding exit blocking and the ensuing panic. Here we employ diffusion maps to study the coarse-grained dynamics of two pedestrian crowds trying to pass through a door from opposite sides. These macroscopic variables and the associated smooth embeddings lead to a better description and a clearer understanding of the nature of the transition to oscillatory dynamics. We also compare the results to those obtained through intuitively chosen macroscopic variables.

DOI: 10.1103/PhysRevE.89.013304 PACS number(s): 07.05.Kf, 89.20.−a, 02.70.−c

I. INTRODUCTION

Understanding the dynamics of interacting particle models is desirable in many contexts, including the modeling of pedestrian crowds, a subject of high social relevance. This type of knowledge can be used for the design of emergency exits and evacuation strategies, and to improve the flow of large crowds of pedestrians in nonemergency situations, e.g., at airport security, large conferences, or shopping malls. Pedestrians can be usefully described as particles, interacting with each other via so-called social forces as well as with the environment (see Refs. [1,2] and [3–6] for further references on pedestrian and many-particle models). This description naturally leads to the study of systems of ordinary differential equations with a large number of dimensions, i.e., four per particle (two positions and two velocities on the plane). In Ref. [7], a typical scenario where two pedestrian crowds try to pass through a door from opposite sides [1] is studied: Using the door width as a bifurcation parameter, a critical door width can be found, at which the system undergoes an apparent macroscopic Hopf bifurcation: the system transitions from a blocked state to an oscillating state with pedestrians from the two sides alternating in crossing through the door. One can simulate this system at the level of interacting individuals, yet the dynamics exhibit an inherent separation of time scales, suggesting the possibility to successfully describe the system by coarse-graining methods. The derivation of a successful collective motion model in terms of good macroscopic variables has, however, proven to be difficult [7].

In general, many dynamical systems (including interacting particles, like our pedestrian model) are characterized by a separation of scales. In such cases, it is sometimes possible to describe and understand the motion of large ensembles of particles in a collective sense through the derivation of explicit equations for the relevant leading statistics (e.g., moments). At intermediate system sizes, the infinite particle limit assumptions that underpin such collective equations become inaccurate, yet separation of time scales and the associated convergence of the high-dimensional dynamics to a low-dimensional, slow manifold (cf. Fenichel's theory [8], see also the slaving principle [9,10]) are still present. It then becomes crucial to determine good sets of macroscopic observables that parametrize this manifold; these are the variables in terms of which collective equations can now be formulated (closed). The same issue arises in equation-free methods [11,12], where a so-called restriction operator maps the high-dimensional variables to a useful low-dimensional representation. Macroscopic observables that are good candidates for low-dimensional descriptions may be known from experience, e.g., low-order moments of a particle distribution, yet for many new systems it is desirable to find such variables in a systematic and algorithmic fashion based on simulation or experimental data.

This links our particle modeling with machine learning (and, in particular, with manifold learning techniques): given observations of trajectories of our model we must determine how many, and then which slow variables are sufficient to describe the collective dynamics of pedestrian flow.

Classical linear approaches for gaining insight into large-scale, complicated data structures include principal component analysis (PCA) [13] and multidimensional scaling (MDS) [14,15]. These methods have been successfully applied to numerous problems in physics and chemistry (see, e.g., the monograph [16] and references therein). PCA and MDS, being linear methods by construction, since they employ linear combinations of the data set, are not able to economically recover complicated nonlinear structures in a data set. This has led to the invention and development of nonlinear data-mining techniques such as isomap [17], local linear embedding (LLE) [18], and spectral methods [19,20].

[*]chrms@dtu.dk
[†]jsta@dtu.dk
[‡]Present address: Department of Molecular, Cellular, and Developmental Biology, Yale University, New Haven, Connecticut 06520, USA; ping.liu@yale.edu
[§]yannis@princeton.edu; also Program in Applied and Computational Mathematics.

TABLE I. Model parameters.

Number of pedestrians N_p	200
Terminal velocity v^0	1.5 m s^{-1}
Reaction time τ	0.22 s
Pedestrian-pedestrian repulsion V	15 m^2 s^{-2}
Pedestrian-wall repulsion V_B	10 m^2 s^{-2}
Pedestrian-pedestrian length scale σ	1 m
Pedestrian-wall length scale R	2 m
Corridor width C_w	5 m
Corridor length C_l	45 m

In this paper, the recently developed nonlinear manifold learning method of diffusion maps [21,22] is used to analyze pedestrian model data, focusing on the oscillatory regime, at a macroscopic level. Systematically selecting a few leading diffusion map components naturally leads to user-independent, data-based dimension reduction; this is particularly helpful in problems for which experience and empirical insight in appropriate variable selection is lacking.

The remainder of the paper is structured as follows. The pedestrian model and the diffusion map algorithm are introduced in Secs. II and III, respectively. In Sec. IV the diffusion map representation of the pedestrian model is computed and the results are compared with those in Ref. [7]. Section V contains a brief discussion and an outlook for future applications.

II. PEDESTRIAN MODEL

The particle model from Ref. [7] is used to study the behavior of pedestrians in a long, narrow corridor, trying to pass through a door, modeled as an opening in the middle of the corridor, from opposite sides. The observed behavior drastically depends on the door width w. A small door blocks the corridor, while a larger door gives rise to oscillatory behavior, with crossings from alternate sides, in an apparent Hopf bifurcation. The model is a variation of the model of Helbing and Molnár [1,2], who studied the behavior of pedestrians affected by social forces, extended by noise in order to avoid deadlock situations.

According to the social force model, the equations of motion for a particle (a pedestrian) is given as

$$\ddot{\mathbf{z}}_i = \mathbf{F}_i^0 + \sum_j \mathbf{f}_{ij} + \sum_B \mathbf{f}_{iB} + \mathbf{n}_i, \tag{1}$$

where $\mathbf{z}_i \in \mathbb{R}^2$ is the ith particle position $i = \{1, \ldots, N_p\}$, and N_p is the total number of particles. The four different contributions in (1) are the direction force $\mathbf{F}_i^0$, the pedestrian-pedestrian interaction $\mathbf{f}_{ij}$, the pedestrian-wall interaction $\mathbf{f}_{iB}$, and the noise $\mathbf{n}_i$. They are described in more detail in Appendix A. All model parameters can be found in Table I. Throughout the paper, numerical values are given in units of the characteristic length scale for the pedestrian interaction σ [(A2)].

Since pedestrians interact with the environment via the wall force $\mathbf{f}_{iB}$, the geometry of the corridor plays an important role. In Ref. [7] a corridor of length C_l and width C_w with a door of width w in the middle of the corridor is studied (Fig. 1). Two

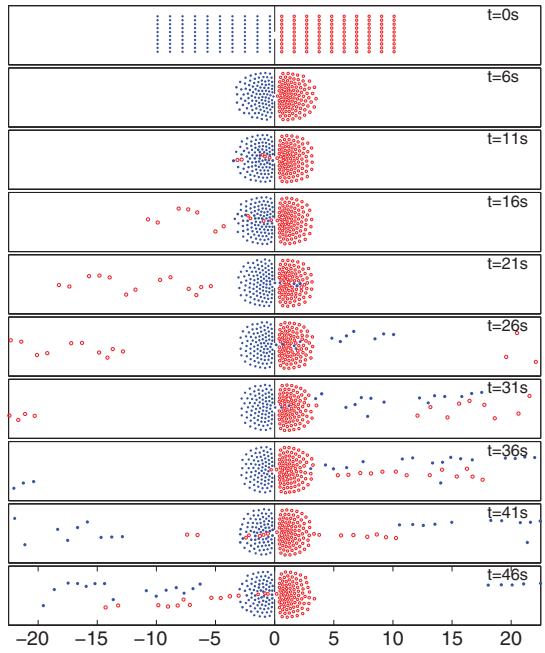

FIG. 1. (Color online) Snapshots showing the oscillatory dynamics of the pedestrian motion for $w = 0.6 > w^* = 0.55$. After initialization, the pedestrians form two milling crowds one on each side of the door ($t = 6$ s). At $t = 11$ s, the (red circle) crowd on the right begins moving through the door, leading to a net flux to the left. After some time, pressure from the right-hand side of the door has decreased enough so that the (blue dot) crowd on the left can break through ($t = 21$ s). At $t = 36$ s, the situation is reversed, and now the red circle crowd can start moving through the door again. This behavior repeats in a periodic fashion, analyzed in Ref. [7].

crowds of pedestrians try to pass the door from opposite sides and the two crowds have the same population size $N_p/2$. For pedestrians starting on one side of the door, the target direction $\mathbf{e}_i^0$ is the center of the door. At the moment pedestrian i passes the door, $\mathbf{e}_i^0$ is updated to point to the end of the corridor, i.e., $\mathbf{e}_i^0$ is chosen parallel to the corridor longitudinal axis. The number of pedestrians is conserved by applying periodic boundary conditions.

In Ref. [7], a coarse equation-free bifurcation analysis was presented using the macroscopic variables

$$m = \frac{1}{2}(m_{\text{red}} + m_{\text{blue}}) \quad \text{and} \quad \dot{m} = \frac{dm}{dt}, \tag{2}$$

where

$$m_\alpha = \frac{\sum_{i\in\alpha} \kappa(x_i) x_i}{\sum_{i\in\alpha} \kappa(x_i)} \tag{3}$$

is a weighted average for pedestrian group α (red, blue) using the weighting function $\kappa(x)$, which gives more weight to pedestrians close to the door. The particular choice of

macroscopic variables was a compromise between filtering for noise reduction and clarity of the ensuing macroscopic description. The more natural choice $m = (m_{\text{red}} - m_{\text{blue}})/2$ and $\dot{m}$ as macroscopic variables gave rise to a noisy macroscopic signal. Further analysis by tools from dynamical systems theory, e.g., bifurcation analysis, was hindered by this noise. Therefore, (2) has been chosen to study the pedestrian behavior (see Ref. [7] for a detailed discussion). An apparent Hopf bifurcation is detected at a door width w^*. For $w < w^*$, the door is too small for pedestrians to pass. They gather in front of the door in what (neglecting small fluctuations of $\mathbf{n}_i$) corresponds to a macroscopic equilibrium. For $w > w^*$, the door is large enough to let pedestrians pass through, leading to macroscopic oscillations (Fig. 1). Moreover, the fast time scale is observed during the early stages of the transient after initialization ($t = 0$). These transients decay over a time scale of $\approx$3 s, while the oscillations have a longer time scale of 40 s. For systems with a smaller gap between time scales, transients take longer. Those systems can still be analyzed by means of diffusion maps using longer simulations.

The selection of variables in Ref. [7] was intuitive and may well depend on the authors. The purpose of the following is to find macroscopic variables intrinsic to the problem data; we also expect these variables to result in good noise filtering.

III. DIMENSION REDUCTION BY DIFFUSION MAPS

Diffusion maps were recently proposed (see Refs. [21–23]) as a nonlinear manifold learning/dimension reduction technique. The goal is to find a (nonlinear) coordinate transformation (i.e., a diffusion map), between the data space and a (low-dimensional) embedding space; the Euclidean distance in the embedding space approximates the *diffusion distance* (defined in Appendix B). Briefly, and qualitatively, the diffusion distance between two data points is small if it is easy to transition between them in a well-defined diffusion process on a graph determined by the data (see Appendix B for details).

If the high-dimensional data happen to lie on (close to) a low-dimensional curved manifold, diffusion maps have been used to extract a parametrization of this manifold and gain insight into the geometric structure underlying the data (see, e.g., Refs. [24–30]). Details of the procedure for diffusion map computation, highlighting the dimension reduction aspect, are presented in Appendix B; they are intended mainly to introduce notation, and are not an extensive review on diffusion maps.

We focus on data resulting from dynamic simulations/observations (possibly multiple ones) of dynamical systems (here, our particle-based pedestrian model); the diffusion maps computation is a purely postprocessing step. We ignore the temporal structure of the data (which also allows us to merge different trajectories); for the exploitation of time information in the form of delay reconstructions in a diffusion map context see Ref. [31]. The ordering in time of data points $x_i = x(t_i)$, taken from a trajectory $x(t)$ at discrete times $t_i = i\Delta t, i \in \{1, \ldots, N\}$, will thus not influence the diffusion map construction. The only quantities of interest are the pairwise distances of the points in data space; it is thus possible to analyze the structure of data when the underlying equations of motion are unknown.

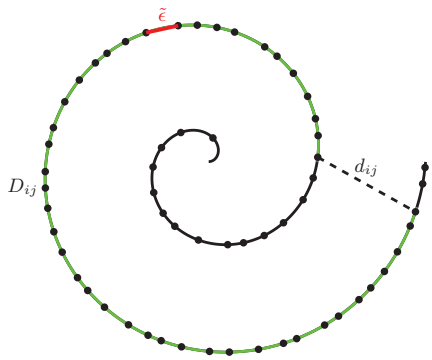

FIG. 2. (Color online) One-dimensional manifold embedded in $\mathbb{R}^2$. The data points are created using (4). $\tilde{\epsilon}$ is representative of a characteristic distance between data points on the manifold [red (dark gray) segment]. d_{ij} denotes the Euclidean distance between two points i and j (dashed line). Although the Euclidean distance is small between these points, the geodesic distance along the manifold, denoted by D_{ij}, is much larger [green (light gray) segment], making it a much better measure of the actual closeness of the two points.

A standard toy illustration example is the swiss roll data set in Fig. 2 (cf. [32]). An embedding into $\mathbb{R}^2$ is given by

$$(x_1, x_2) = (\theta \cos\theta, \theta \sin\theta), \tag{4}$$

where $\theta \in [0, 4\pi]$. Assume that the two-dimensional data points on this sampled manifold (black dots in Fig. 2) are the result of experimental observations or of a dynamical simulation. Although this manifold lies in two dimensions, it is only one-dimensional, i.e., both coordinates are functions of a single variable, θ, that parameterizes the curve. Clearly, any linear dimension reduction method, e.g., PCA and MDS, would fail to detect the one-dimensional structure of the manifold: projection of the data in Fig. 2 on any line would mix the order of data points on the manifold. Techniques such as diffusion maps, as we briefly outline below, can successfully perform this reduction.

To determine the intrinsic data geometry from such a data set X, diffusion maps use Markov chains to describe a diffusion process *on the data set*. Pairwise Euclidean distances d_{ij} are computed for all data points, and weighted (soft-thresholded, using the scaling parameter ϵ) through the diffusion kernel A_{ij} [(B3) in the Appendix B] to give pairwise affinities between the points. The rows of the resulting affinity matrix A are normalized to yield a Markov transition matrix M between points in the data set [(B4)]. The time-t diffusion distance D_t is defined in terms of this Markov matrix; it is small, if the t-step transition probability in the Markov chain is high [(B5)]. The transformation [(B10)] ensures that the Euclidean distance in diffusion map space is (an approximation of) the diffusion distance between the data points [(B7)].

For the procedure to yield informative results several (often problem-dependent) considerations apply; if, for example, in Fig. 2 the scaling parameter ϵ in (B3) is not comparable to some characteristic distance $\tilde{\epsilon}$ between the data, but even larger than the d_{ij} shown, points will be identified as close neighbors that

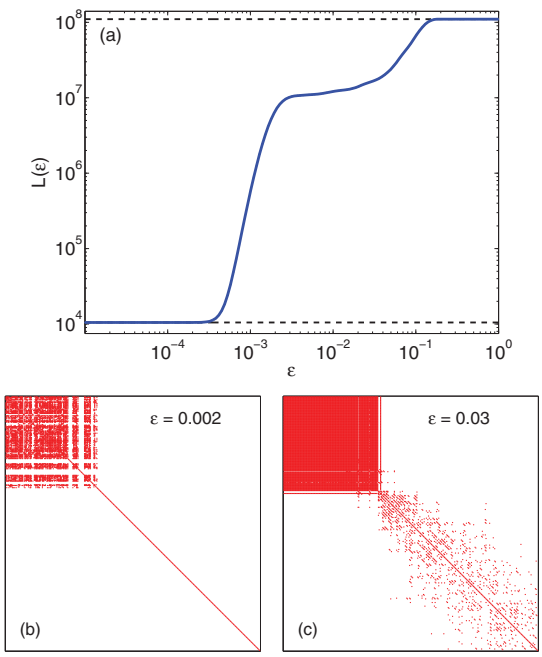

FIG. 3. (Color online) Determining appropriate ϵ values for observations over a range of door widths ($w \in [0.5,0.7]$ with $\Delta w = 0.01$ and 500 observations for each w). (a) The number L of elements in the distance matrix d smaller than ϵ is plotted as a function of ϵ. The limiting behavior (5) is shown as the dashed black lines. In between these limits, $L(\epsilon)$ shows two scaling regimes, namely $[4 \times 10^{-4}, 2 \times 10^{-3}]$ and $[2 \times 10^{-2}, 2 \times 10^{-1}]$. To clarify this, the sparsity pattern of the distance matrix d is inspected for two values of ϵ, $\epsilon = 2 \times 10^{-3}$ representing the blocked regime ($w < w^*$) and $\epsilon = 0.03$ representing the oscillating regime ($w > w^*$). (b) and (c) show the parameter-ordered matrix elements (small w: top left, large w: bottom right), which are smaller than ϵ (dots). For $\epsilon = 0.002$ [(b)], the dots are all located in the upper left corner, denoting blocked states. The oscillating regime is visible at $\epsilon = 0.03$ [(c)]. Oscillating state distances do not register in the left panel, since they are larger than $\epsilon = 0.002$.

intuitively should not be. Selection of an appropriate value for ϵ in the kernel (B3) is also problem/data dependent; one can arrive at such a value through investigation of the scaling behavior of the pairwise distances d_{ij}. Let $L(\epsilon)$ be the number of d_{ij} smaller than ϵ. For large ϵ all d_{ij} are smaller, while for small enough ϵ only the diagonal d_{ii} is smaller (actually, zero):

$$\lim_{\epsilon \to \infty} L(\epsilon) = N^2, \quad \lim_{\epsilon \to 0} L(\epsilon) = N; \tag{5}$$

clearly, ϵ should be chosen between those limits. This behavior is illustrated for the pedestrian flow example in Fig. 3, and will be discussed in more detail below. From scaling arguments, the dimension of the manifold can be estimated from the slope of $L(\epsilon)$ on a logarithmic plot [33].

Another important consideration is the relative scaling of the data coordinates so that the (weighted) Euclidean distance in the numerator of the diffusion kernel is informative for the problem considered; this would arise for example in chemical composition data where different components are present at proportions differing by orders of magnitude.

Diffusion map computation for large data sets can be computationally expensive. Naive, nonsparse storage of the Markov matrix grows like $\mathcal{O}(N^2)$. The computation of the $k+1$ largest eigenvectors can be performed taking advantage of the sparsity of the matrix d (cf. [31]). When the diffusion map coordinates for a new data point $\mathbf{x}_{N+1}$ are needed, adding the point to the data set and repeating all diffusion map computations from scratch is not necessary. Indeed, one can estimate the diffusion map coordinates of this $N+1$st out-of-sample point using the Nyström extension [25,34]: Using (B10), the $N+1$st coordinate of eigenvector $\boldsymbol{\Psi}_i$ is approximated as

$$\boldsymbol{\Psi}_{i,N+1} = \frac{1}{\lambda_i} \sum_{l=1}^{N} M_{N+1,l} \boldsymbol{\Psi}_{i,l}, \tag{6}$$

for $i = 1, \ldots, k$. It is only necessary to compute a single new row of M, thus saving computation time.

IV. RESULTS

We now turn to the application of the diffusion map algorithm (Sec. III) to specific scenarios of pedestrian flow (Sec. II). The section is structured as follows: First a metric on the high-dimensional data space is introduced, in order to construct the distance matrix in (B2). Then we use diffusion maps to obtain a two-dimensional embedding of the dynamics for fixed door width, $w = 0.7 > w^*$, and compare to the results in Ref. [7]. Finally, a diffusion map embedding for data points assembled for different values of w is computed. This allows us to characterize the bifurcation and compare the Hopf bifurcation points obtained from the two approaches.

A. Pedestrian model data

A data point $\mathbf{x}_j$, taken from a trajectory of (1), contains the positions and velocities of all pedestrians

$$\mathbf{x}_j = [\mathbf{Z}_1, \ldots, \mathbf{Z}_{N_p}] \in \mathbb{R}^n, \tag{7}$$

where $\mathbf{Z}_k = [z_{x,k}, z_{y,k}, \dot{z}_{x,k}, \dot{z}_{y,k}]$ for pedestrian k, and $n = 4N_p$. In a preprocessing step, the data points are transformed componentwise to the interval $[0,1]$ to make them comparable. More precisely, let $G = \{x, y, v_x, v_y\}$ denote the set of positions and velocities and $C = \{\text{red}, \text{blue}\}$ denote the color (grayscale), i.e., crowd, of the pedestrian, respectively. We choose the pedestrian labels such that $I_{\text{red}} = \{1, \ldots, N_p/2\}$ and $I_{\text{blue}} = \{N_p/2 + 1, \ldots, N_p\}$ denote the two index sets for the red (circles) and blue (dots) pedestrians, respectively. In a first transformation step, we shift the minimum to zero by

$$\tilde{z}_{g,i} = z_{g,i} - \min_{g,c} \quad \forall i \in I_c, \quad g \in G, \quad c \in C, \tag{8}$$

where $\min_{g,c} = \min_{i \in I_c} z_{g,i}$ for $g \in G, c \in C$. Afterwards, the data is scaled with

$$\tilde{\tilde{z}}_{g,i} = \frac{\tilde{z}_{g,i}}{\max_{g,c}} \quad \forall i \in I_c, \quad g \in G, \quad c \in C, \tag{9}$$

where $\max_{g,c} = \max_{i \in I_c} \tilde{z}_{g,i} \neq 0$ for $g \in G, c \in C$, onto the interval $[0,1]$. We drop the tilde in the following for notational convenience.

In the new data set X, the pedestrians are still labeled. Our selection of a pairwise distance between configurations should be invariant to particle label permutations. One could use, for example, an earth-mover's distance [35] for this purpose; we choose instead a metric easier to compute, employing the mean and centered moments of four features of the data set: red circle/blue dot x, y positions and red circle/blue dot velocities. A new data vector

$$\tilde{\mathbf{x}}_i = [\langle Z \rangle_{g,c}, m_2(Z)_{g,c}, \ldots, m_{100}(Z)_{g,c}] \quad \forall g \in G, \quad c \in C, \tag{10}$$

is constructed, where $\langle \cdot \rangle_{g,c}$ and $m_i(Z)_{g,c}$ is shorthand notation for the mean and ith centered moment in a list of all feature-color combinations, respectively. The resulting data set is defined as in (B1)

$$X = \{\tilde{\mathbf{x}}_i \in \mathbb{R}^n | i = 1, \ldots, N\}, \tag{11}$$

where $n = 800$. Note, that the dimension of the data points is conserved. This pre-processing step is *only* applied to compute the distance between snapshots without labels of the pedestrians. The distance between two observations $\tilde{\mathbf{x}}_i, \tilde{\mathbf{x}}_j \in X$ can then be defined as

$$d_{ij} = \|\tilde{\mathbf{x}}_i - \tilde{\mathbf{x}}_j\|. \tag{12}$$

Diffusion maps will allow us to reduce this 800-dimensional data set to a two-dimensional representation of the dynamics.

B. Length scale selection

Before the algorithm from Sec. III can be applied, an estimate for the length scale ϵ is required. The function $L(\epsilon)$ [(5)] is investigated for data points obtained over a range of w values (Fig. 3). In this figure, the limiting behavior for $\epsilon \to \infty$ and $\epsilon \to 0$ is clearly visible. Between the two limiting plateaus, a third one exists for $\epsilon \in [2 \times 10^{-3}, 3 \times 10^{-2}]$. It separates two scaling regimes. The scaling regime for smaller ϵ is representative of blocked state dynamics, when the particles simply jiggle on each side of the door, and their configurations do not change appreciably. The larger ϵ regime is representative of the oscillatory dynamics, where appreciable variations between successive data snapshots arise. This is echoed in the size of the elements d_{ij} plotted in matrix format (bottom panel in Fig. 3). In order to rationalize the different regimes, the matrix elements of d are ordered by the door width parameter, i.e., small w observations are found to the top left and large w observations towards the bottom right of Fig. 3 (bottom panel), respectively. The small distances [smaller than ϵ, marked in red (dark gray)] between blocked state configurations originate from model noise. Note that distances between blocked and oscillating states are typically large [empty regions at the top right and bottom left corner in Fig. 3 (bottom panel), respectively]. After inspection of this figure, we chose the fixed value $\epsilon = 0.03$ for all subsequent computations.

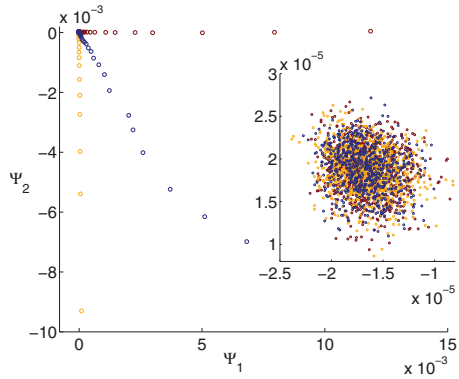

FIG. 4. (Color online) diffusion map embeddings for three trajectories in the blocked regime ($w = 0.4 < w^*$), including transients. The inset magnifies the region of the (noisy) final state. Color (grayscale) indicates the different trajectories of the system.

C. Diffusion map embedding

We first analyze, using diffusion maps [and, in particular, the one-step diffusion, i.e., $t = 1$ in (B5) and (B10) from Appendix B], the blocked regime for small door widths $w < w^*$. Here, the pedestrians congregate on both sides of the door without being able to pass through it. Initial transients in diffusion map coordinates for this regime are shown in Fig. 4 for 100 s and $\Delta t = 0.1$ s. Figure 4 shows the two-dimensional embedding from the blocked regime ($w < w^*$). The axis labels follow the naming in previous literature, where Ψ_j on the axes denotes the jth component of $\hat{\mathbf{y}}$ [(B10)], i.e., the component in the direction corresponding to the jth largest eigenvalue (after the trivial one at 1). It is clear in Fig. 4 that, after an initial transient, the data points become randomly distributed in diffusion map space; the spread of the ball in the inset is indicative of the noise in the simulation.

The picture changes drastically when analyzing a trajectory for, say, $w = 0.7 > w^*$, all other simulation parameters being kept constant. Now, a particle simulation over 500 s with $\Delta t = 0.1$ s is used, resulting in 5000 observations. Initial transients are ignored in the remainder by using the last 3500 data points only. The resulting two- and three-dimensional diffusion map embeddings are shown in Fig. 5.

The third component can be written as a function $\Psi_3(\Psi_1, \Psi_2)$, and therefore a two-dimensional embedding is sufficient to describe the long-term dynamics. These results will later be compared to the original ones in Ref. [7] in Sec. IV D.

Finally, the diffusion map embedding for data points taken from trajectories over a range of door widths $w \in [0.5, 0.7]$ (sampled with $\Delta w = 0.01$) is computed. Each trajectory was now computed for 5000 time steps and subsampled: every third data point of the last 1500 time steps was used for the embedding. Since the periodic orbits have a period of about 40 s, this covers approximately four periods and therefore yields enough data for a good embedding. The resulting matrix size (10500×10500) is close to the limit of what can be routinely handled by MATLAB on a workstation [36] without using

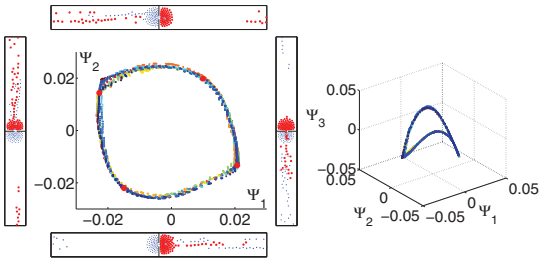

FIG. 5. (Color online) diffusion map embedding of data in the oscillating regime ($w = 0.7 > w^*$). The last 3500 data points of a trajectory (sampled with $\Delta t = 0.1$) are shown. A periodic orbit is clearly visible in the $\Psi_1-\Psi_2$ plane. Big red (dark gray) dots denote points in diffusion map space for which characteristic microscopic states are included as surrounding insets in the figure. Ψ_3 in the three-dimensional embedding can be written as a function of Ψ_1 and Ψ_2.

special algorithms for memory optimization. The resulting embeddings are shown in Fig. 6. All possible two-dimensional projections as well as the full three-dimensional embedding for the first three eigenvectors are shown.

The color (grayscale) here encodes the corresponding door width of the data points [blue (black and light gray): $w = 0.5$, red (dark gray): $w = 0.7$]. It is clearly visible in the (Ψ_2,Ψ_3) plane, that a transition from a blocked state [blue (black) points at (0,0)] to an oscillating state occurs. The amplitude of the oscillations increases with door width, in accordance with

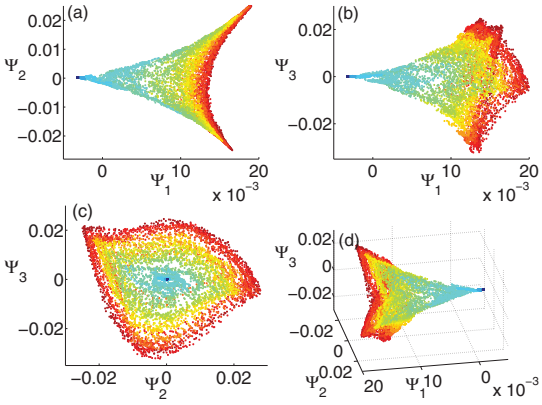

FIG. 6. (Color online) Diffusion map embeddings computed from a data set containing points for different parameter values w. The parameter range for the door width is 0.5 to 0.7 with $\Delta w = 0.01$. Every third data point from the last 1500 iterations for each parameter value has been used, resulting in a data set with 10500 data points. Various projections of the data set are shown in (a)–(d) in diffusion map space. The color (grayscale) encodes the door width from $w = 0.5$ [dark blue (black and light gray)] to $w = 0.7$ [red (dark gray)]. The Ψ_1 coordinate roughly encodes the w regime. The increase in oscillation amplitude is best visible in the (Ψ_2,Ψ_3) projection [(c)], showing periodic solutions for several door widths. As in Ref. [7], the amplitude of the oscillations grows with increasing w. The full three-dimensional representation is shown in (d).

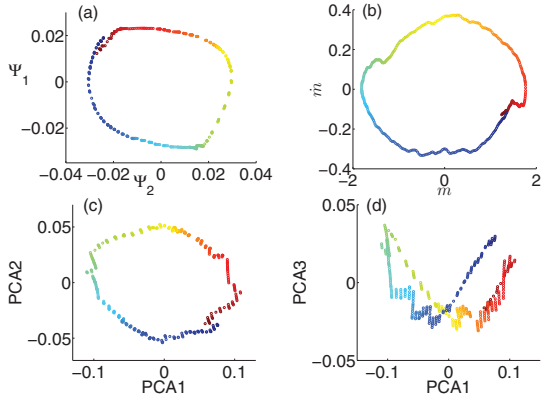

FIG. 7. (Color online) Coarse phase portraits using (a) diffusion maps, (b) the intuitive variables of Ref. [7] and (c), (d) principal components. Data points along a limit cycle are shown for the last 400 time steps of a 5000 time step simulation. Color (grayscale) indicates time (see text). There is a clear one-to-one correspondence between $(m,\dot{m})$ and (Ψ_1,Ψ_2). The diffusion map embedding appears to remove the corners in (b) [red (dark gray) and green (light gray) dots]. Two-dimensional projections of phase portraits in terms of leading PCA coefficients (c) and (d) are also included for comparison. The two-dimensional diffusion map embedding has the smoothest appearance.

the findings in Ref. [7]. One can argue, from inspection of the different projections, that Ψ_1 encodes the parameter w, distinguishing small door widths (small values of Ψ_1) from large ones (large values of Ψ_1).

D. Comparison with other macroscopic representations

We now compare the macroscopic representation of Ref. [7], which they denoted $(m,\dot{m})$, with the diffusion map representation (Ψ_1,Ψ_2). The last 400 time steps of a 5000 time step simulation, covering one oscillation period for a door width $w = 0.7$ are used for this comparison in Fig. 7. Diffusion maps do not consider time labeling of the data points, yet to assist the interpretation of these results (and since, here, the data come from a single long trajectory, so that the time labels are actually available) we use color (grayscale) in these embeddings to encode time. Blue (black) data points lie at the beginning of the trajectory, and the color (grayscale) progresses over green (light gray) to red (dark gray).

There is a clear one-to-one correspondence between $(m,\dot{m})$ (arrived at by the authors of Ref. [7] through a combination of intuition and experience) and the diffusion map coordinates (Ψ_1,Ψ_2) (which were arrived at automatically based on the intrinsic geometry of the data). It is also interesting that the diffusion map representation appears to give well-filtered phase portraits, less sensitive to noise than the $(m,\dot{m})$ but also the principal component-based ones; this actually enhances the computational quantification of the underlying Hopf bifurcation through Poincaré map sections.

One might consider as a shortcoming of the diffusion map approach the fact that, as new particle simulation data become available, one does not have explicit formulas for

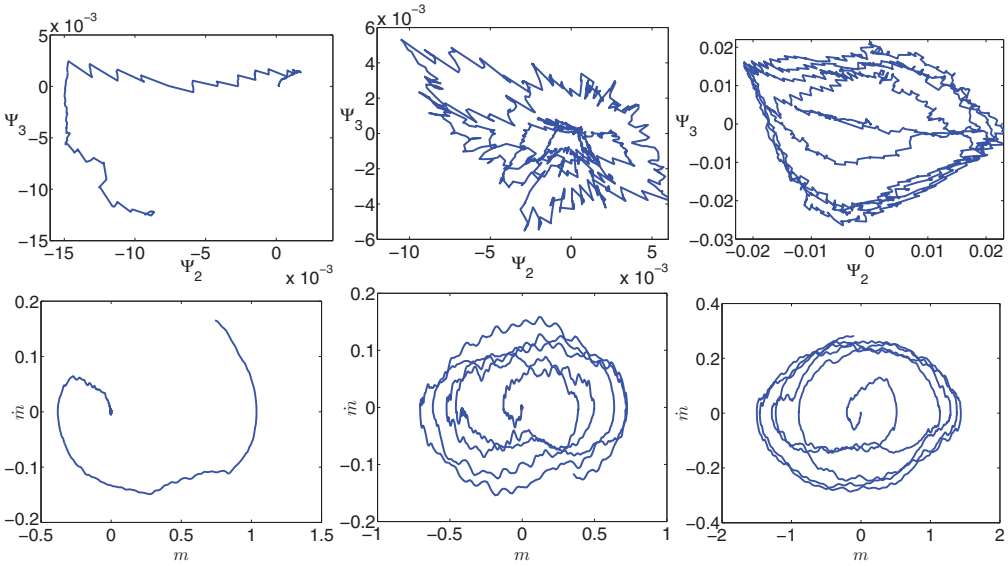

FIG. 8. (Color online) Phase space trajectories in diffusion map space (top), reconstructed through the Nyström extension [(6)] from new data points, compared to those in terms of the variables in Ref. [7] (bottom); transients are shown for the blocked regime $w = 0.53$ (left), just after the onset of oscillations for $w = 0.58$ (middle), and for $w = 0.65$ (right). For $w = 0.53$, the stationary state is stable and the trajectories approach this stable equilibrium; for $w = 0.58$ and $w = 0.65$ the trajectories spiral away from the unstable equilibrium towards the coarse limit cycle. Both embeddings exhibit the same qualitative behavior.

their embedding; in PCA, by contrast, new data on the same low-dimensional linear subspace can be expressed in PCA coordinates through a projection with a few simple inner products. This can be overcome through the use of the Nyström extension, as long as the new data points remain close to (have a sufficient number of close neighbors on) the regions of the low-dimensional manifold already sampled. Figure 8 illustrates this by presenting newly computed transients in Nyström-reconstructed diffusion map space (top) [and their counterparts in $(m,\dot{m})$ space, bottom] for $w = 0.53 < w^*$, $w = 0.58 > w^*$ and $w = 0.65 > w^*$. All trajectories were computed for 2000 time steps. The reference data set for the Nyström extensions through (6) consists of the data collected in the previous section over a range of door widths w. The plots in the variables m and $\dot{m}$ as well as the plots in Ψ_2 and Ψ_3 are clearly noisy; it appears that the Nyström extension, while allowing us to embed the data in diffusion map space, gives rise to trajectories comparably noisy to the m and $\dot{m}$ ones. Smoother trajectories could be obtained by using reference embeddings computed for a fixed door width. Nevertheless, both embeddings show the same qualitative behavior, namely a convergence to a fixed point for $w < w^*$ and oscillatory behavior for $w > w^*$.

E. Transition to oscillatory regime

In order to establish the Hopf nature of the bifurcation at $w^* = 0.55$ proposed in Ref. [7], the amplitude of Ψ_2 in Fig. 9 is plotted against the bifurcation parameter w. The figure clearly shows the gradual growth and subsequent saturation of the oscillation amplitude as a function of the door width; there is relatively little variation in the oscillation period (not shown). A comparison with the results from a direct simulation in the variables $(m,\dot{m})$ shows the same bifurcation point $w^* = 0.55$. A detailed bifurcation analysis is found in Ref. [7] and is not the focus of this paper.

Careful inspection of the snapshots of the oscillatory dynamics shows that the period of the oscillations is influenced by the return, through the periodic boundary conditions, of particles that passed through the door in the previous crossing surge. Small amplitude oscillations (close to the onset of the instability) correspond to fewer particles crossing in such a single surge event. If the particles did not have the opportunity to reenter, the problem would not be a stationary one—the density of particles congregating at each side of the door would gradually diminish after every surge, and this would

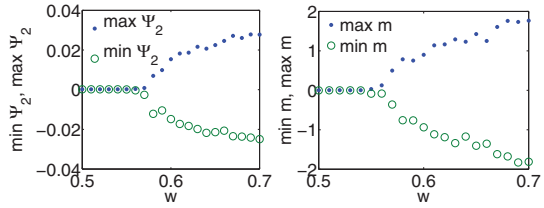

FIG. 9. (Color online) Bifurcation diagrams in diffusion map space ($\max \Psi_2$, $\min \Psi_2$) (left) and in the ($\max m$, $\min m$) variables of Ref. [7] (right). Both diagrams are consistent with an apparent Hopf bifurcation at a critical door width of $w^* = 0.55$. The panel in diffusion map space on the left appears slightly smoother.

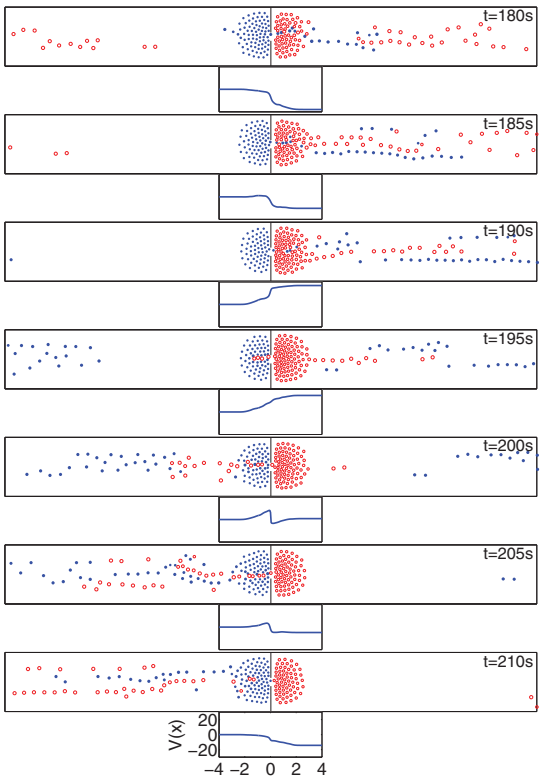

FIG. 10. (Color online) Potential $V(x)$ over x below the corresponding microscopic configuration for different times of the simulation with door width $w = 0.7$.

of course affect the switching times between crossings from alternate sides of the door. To provide an intuitive physical explanation of the mechanism underlying these switches, we show, in Fig. 10, a number of snapshots distributed along the oscillation; for each one of them we have calculated the force exerted on a colorless test pedestrian positioned on the corridor centerline by all the surrounding pedestrians. We then plot the integral of this force as a function of the position along the centerline, obtaining a sense of a pressure potential felt by the particle; the gradient of this computed quantity influences the particle motion. This potential is computed as follows: for any given fixed snapshot, the test pedestrian is located in a sequence of positions along the corridor axis, i.e., $y = 0$ and $x \in [-4,4]$ with $\Delta x = 0.05$; the force in corridor direction [(A2)] applied by the other pedestrians, $F_x(x)$, is computed, and the potential is then obtained as

$$V(x) = -\int_{-4}^{x} F_x(x')dx' \tag{13}$$

using the gauge $V(-4) = 0$. Figure 10 interleaves the evolution of the detailed state and the evolution of the potential over one oscillation period. We clearly see this pressure potential building up on the blue left-hand side of the door during the first couple of snapshots, and then reversing (as now the density of red circle particles on the red right-hand side of the door is larger). When, eventually, the blue dot particles that crossed return through the periodic boundary conditions, the blue dot particle density on the blue left-hand side of the door is roughly restored, and the pressure potential repeats.

The interactions of the pedestrians in front of the door clearly lead to surges through the door from alternate sides; the occurrence of these surges depends (as we tried to argue above) on the density of pedestrians in the neighborhood of the door. The periodic boundary conditions and the return of pedestrians through them back to the door is important in replenishing the particle density close to the door, making the behavior not just alternating, but regularly periodic and making the instability appear like a Hopf bifurcation. Other mechanisms of replenishing particle density, without periodic boundary conditions, such as the random injection of particles at some average rate, can also lead to regular periodic behavior by balancing overall particle inflow and outflow. On the other hand, keeping the densities close to the door effectively constant (through idealized particle reservoirs) would make the problem take a bistable switching aspect, with a noise-induced distribution of switching times.

In all computations in this paper, the number of red circle and blue dot particles, as well as their intrinsic properties, were taken to be identical. This makes the oscillation have a symmetric nature in time: evolving forward for half a period (coarsely) commutes with reflecting the corridor around the door ($x = 0$) and flipping particle colors (grayscales). Such a symmetry (picturesquely called ponies on a merry-go-round (POMs) [37,38]) has implications for the bifurcation scenarios possible [39]. Breaking any of these symmetries would destroy the POM nature of the limit cycles we observe.

V. CONCLUSION AND OUTLOOK

We have shown in this article that diffusion maps can be successfully applied to assist the study of pedestrian dynamics. The pedestrian model is used as a representative example of a particle system with time-scale separation. Not only does the use of diffusion maps avoid the need for user-specific selection of good coarse variables, it also appears here to lead to filtered, smoother coarse trajectories, which can be helpful in coarse-grained bifurcation analysis. Our study confirms that the use of diffusion maps is well suited for studying systems where intuition about good coarse variables is lacking.

On the other side of the coin, the lack of physical interpretation of the diffusion map embedding is a nontrivial drawback. There is clearly an upfront cost in the computation of diffusion maps, involving the computation of (many) pairwise distances and some large-scale linear algebra eigencomputations. As we already mentioned, careful data structuring, fast nearest-neighbor detection algorithms, and matrix sparsity can help make this task easier, so that the methods become applicable to very large data sets.

The automated discovery of good coarse variables is a crucial enabling technology for multiscale computations, and, in particular, for the application of equation-free techniques to new problems. In such computations, the ability to routinely transform from fine-scale (for us here, particle position and

velocity) space to coarse-grained (here diffusion map) space is an important component of the algorithms. And while, as we discussed, tools like the Nyström extension help in one direction of this transformation (the restriction to diffusion map space), the converse transformation (the lifting) is nontrivial and can involve sophisticated multiscale interpolation and extrapolation techniques (see for example the discussion in Ref. [40] and the techniques proposed there).

In our work we implicitly assumed that the appropriate macroscopic description would be in terms of deterministic, ordinary differential equations; indeed Figs. 4, 5, and 6 and our discussion of the Hopf nature of the underlying bifurcation support this assumption: our system is well modeled by a set of ODEs (modulo a little noise).

In other problems, however, stochastic effects may well be more pronounced, and the appropriate coarse description might be in terms of effective SDEs or the associated effective Fokker-Planck equations [41]; and while the estimation of coarse right-hand sides would now include both effective drifts and effective diffusivities, the role of diffusion maps remains the same: detect the coarse variables in terms of which the effective SDEs can be formulated.

It is worth noting that we have already mentioned a version of our pedestrian problem where such an effective stochastic reduction might be called for: the constant density case, where one might expect noise-induced bistable switching to lead to a distribution of surge times from alternate sides of the door.

While in this paper we reexamined, through a different approach, phenomena whose existence we already knew, our pedestrian model still possesses in its parameter space a wealth of possible behaviors that will pose their own challenges to data mining and coarse bifurcation computations. We know, for example, that for large enough door widths lane formation (the formation of striations in the pedestrian traffic pattern) will take place. The spatiotemporal nature of this instability will clearly need more and different coarse variables than the ones that were sufficient here, and the nature of the underlying coarse instability is yet to be explored.

Finally, as another interesting avenue of research, we mention the possibility of using coarse graining in the study of *heterogeneous* crowds. Here, we had blue dot and red circle pedestrians, that were otherwise identical. If the intrinsic properties of these particles (in the form of preferred target velocities, different interactions with the walls, different reaction times and/or perception distances, etc.) are not fixed, but sampled from a distribution, the problem acquires a new dimension. Recent developments involving mathematical tools from uncertainty quantification hold promise towards effective coarse graining in such heterogeneous problems [42,43].

ACKNOWLEDGMENTS

C.M. and J.S. would like to acknowledge the hospitality of Princeton University during research visits. C.M. would like to thank Otto Mønsted Fonden for financial support of the research stay in Princeton. J.S. would also like to thank the Danish Research Council FTP (09-065890/FTP) and the Villum Fonden (VKR-Centre of Excellence Ocean Life) for financial support. The work of I.G.K. and P.L. was partially supported by the US Department of Energy (DE-SC0005176 and DE-SC0002097).

APPENDIX A: SOCIAL FORCES AND MODEL PARAMETERS

The *inherent driving force* of a pedestrian i is given by its target direction $\mathbf{e}_i^0$ and velocity v^0. The force $\mathbf{F}_i^0$ tries to align the trajectory of the pedestrian to its target direction with

$$\mathbf{F}_i^0 = \tau^{-1}\left[v^0\mathbf{e}_i^0 - \dot{\mathbf{z}}_i(t)\right], \tag{A1}$$

where $\dot{\mathbf{z}}_i(t)$ is the velocity of pedestrian i at time t and τ is the reaction time.

The *pedestrian interaction* is modeled by the term

$$\mathbf{f}_{ij} = \mathbf{f}(V,\sigma,\mathbf{r}_{ij}) = \begin{cases} -V\left[\tan\left(g(\|\mathbf{r}_{ij}\|)\right) - g(\|\mathbf{r}_{ij}\|)\right]\frac{\mathbf{r}_{ij}}{\|\mathbf{r}_{ij}\|}, & \|\mathbf{r}_{ij}\| \leqslant \sigma \\ 0, & \|\mathbf{r}_{ij}\| > \sigma. \end{cases} \tag{A2}$$

Here, $\mathbf{r}_{ij}$ is the vector from pedestrian i to j, $\|\mathbf{r}_{ij}\|$ is the distance between pedestrians i and j, and V is the repulsion strength. The cutoff length σ reflects the fact that largely separated pedestrians do not influence each other. $g(\|\cdot\|) = \frac{\pi}{2}(\frac{\|\cdot\|}{\sigma} - 1)$ is introduced as a shorthand notation.

The third term describes the *interaction of pedestrians with walls*. Since pedestrians try to avoid collisions with walls, a repulsion force

$$\mathbf{f}_{iB} = \mathbf{f}(V_B,R,\mathbf{r}_{iB}) \tag{A3}$$

is introduced. It has the same functional dependence as (A2), but a different repulsion strength V_B and different range $R > \sigma$. The vector $\mathbf{r}_{iB}$ is the distance vector between pedestrian i and the closest point on boundary B.

The last term in (1) is the *additive noise*, which is introduced to avoid deadlock situations. It also reflects that people tend to avoid collisions with other persons by moving to one preferred side (assuming the pedestrian live in the same country). Here, we assume that the pedestrians tend to move to the right, leading to a noise term as

$$\mathbf{n}_i = n_i^{\parallel}\mathbf{e}_i + n_i^{\perp}\mathbf{e}_i^{\perp} = n_i^{\parallel}\mathbf{e}_i + n_i^{\perp}\begin{pmatrix} 0 & -1 \\ 1 & 0 \end{pmatrix}\mathbf{e}_i, \tag{A4}$$

where $n_i^{\parallel}$ and $n_i^{\perp}$ are the noise components parallel and perpendicular to the target direction $\mathbf{e}_i$, respectively. Both components are normally distributed with

$$n_i^{\parallel} \sim \mathcal{N}(0,(s^{\parallel})^2) \quad \text{and} \quad n_i^{\perp} \sim \mathcal{N}(0.1s^{\perp},(s^{\perp})^2) \tag{A5}$$

where $s^{\parallel} = 0.00158$ and $s^{\perp} = 0.0632$. $\mathcal{N}(\mu,s^2)$ is a normal distribution with mean μ and variance s^2.

APPENDIX B: DIFFUSION MAP ALGORITHM

For convenience of the reader and definition of notation, the diffusion map algorithm is summarized in the following, see Refs. [21,22] for details. It has been successfully applied to physical problems, e.g., the description of a driven interface in an Ising variant model [26] or the study of the dynamics of animal groups [28].

Given a set of properly scaled observations

$$X = \{\mathbf{x}_i \in \mathbb{R}^n | i = 1, \ldots, N\}, \tag{B1}$$

where N is the number of observations and n is the dimension of the data, we compute all pairwise distances and arrange them in the distance matrix d:

$$d_{ij} = \|\mathbf{x}_i - \mathbf{x}_j\|, \quad i,j = 1, \ldots, N. \tag{B2}$$

Usually, $\|\cdot\|$ is the Euclidean norm in $\mathbb{R}^n$, but it can also be chosen to be problem specific [cf. (12), where we use a norm on moments]. The scaling parameter ϵ is used to compute the affinity matrix A as

$$A_{ij} = \exp\left(-\frac{d_{ij}^2}{\epsilon^2}\right). \tag{B3}$$

Note that large distances in d are being mapped to small pairwise affinities in A. The rows of A are normalized to obtain a Markov transition matrix

$$M_{ij} = \left(\sum_{j=1}^{N} A_{ij}\right)^{-1} A_{ij}, \tag{B4}$$

where M_{ij} is the one-step probability of transitioning from $\mathbf{x}_i$ to $\mathbf{x}_j$. M therefore defines a diffusion process, i.e., a Markov chain, on X.

Using M, the time-t diffusion distance D_t between two points $\mathbf{x}_i, \mathbf{x}_j \in X$ is defined as

$$D_t(\mathbf{x}_i, \mathbf{x}_j)^2 = \sum_k \frac{\left|M_{ik}^t - M_{jk}^t\right|^2}{\phi_0(k)}, \tag{B5}$$

where

$$\phi_0(k) = \frac{\sum_{j=1}^{N} A_{kj}}{\sum_{i=1}^{N}\sum_{j=1}^{N} A_{ij}} \tag{B6}$$

is the stationary distribution (cf. [44]). The diffusion distance D_t measures the difference in probability for transitioning from state i and j to state k, respectively. If the probabilities are the same, state k is equally well connected to states i and j by a diffusion process. (In a continuous analog, D_t measures the overlap of the two distributions after time t resulting from initializing with δ distributions centered at x_i and x_j, respectively.) The terms are normalized by the stationary distribution $\phi_0(k)$, which represents the probability to find the diffusion process in state k for $t \to \infty$. We then define a transformation from points $\mathbf{x}_i \in X$ to points $\mathbf{y}_i \in Y$ such that the Euclidean distance in Y equals the diffusion distance in X, i.e.,

$$\|\mathbf{y}_i - \mathbf{y}_j\|^2 = D_t(\mathbf{x}_i, \mathbf{x}_j)^2. \tag{B7}$$

A termwise comparison with (B5) using $p_t(\mathbf{x}_i, \mathbf{x}_k) = M_{ik}^t / \sqrt{\phi_0(k)}$ yields the transformed coordinates $\mathbf{y}$:

$$\mathbf{y}_i = [p_t(\mathbf{x}_i, \mathbf{x}_1), \ldots, p_t(\mathbf{x}_i, \mathbf{x}_N)]^T, \tag{B8}$$

where $p_t(\mathbf{x}_i, \mathbf{x}_j)$ is the probability of transitioning from point $\mathbf{x}_i$ to $\mathbf{x}_j$ in t steps. A useful approximation of this embedding can be formulated in terms of the eigenvalues and eigenvectors of M; if the data indeed lie on (or reasonably close to) a low-dimensional manifold, only a few (say, the first $k+1$) leading eigenvalues/eigenvectors need to be computed

$$M\boldsymbol{\Psi}_i = \lambda_i \boldsymbol{\Psi}_i, \quad i = 0, \ldots, k, \tag{B9}$$

where $\lambda_i > \lambda_j$ for $i < j$, assuming nondegeneracy of the eigenvalues. Since M is a Markov matrix, $\lambda_0 = 1$ and Ψ_0 is a vector containing only entries of 1. The transformation from data space to diffusion map space, with $\hat{\mathbf{y}}_i \in \mathbb{R}^k$, is given by

$$\mathbf{x}_i \mapsto \left[\lambda_1^t \boldsymbol{\Psi}_{1,i}, \ldots, \lambda_k^t \boldsymbol{\Psi}_{k,i}\right]^T = \hat{\mathbf{y}}_i, \tag{B10}$$

where $\boldsymbol{\Psi}_{u,v}$ is the vth component of eigenvector $\boldsymbol{\Psi}_u$. For $k \ll N$ this transformation constitutes a dimension reduction scheme.

Note that for larger t (i.e., when using longer times in the diffusion process) higher eigenvalues become increasingly damped as we take their powers; fewer leading (slower) components of $\hat{\mathbf{y}}_i$ will then suffice to approximate the data to a given accuracy. This allows the structure of the data manifold to be investigated at different scales [45]. This approach, through its ability to parametrize curved, nonlinear, manifolds can be more economical in the representation of data possessing such structure than linear methods (such as PCA or MDS).

[1] D. Helbing and P. Molnár, Phys. Rev. E **51**, 4282 (1995).
[2] D. Helbing, Rev. Mod. Phys. **73**, 1067 (2001).
[3] D. Helbing, I. Farkas, and T. Vicsek, Nature (London) **407**, 487 (2000).
[4] D. Helbing, R. Jiang, and M. Treiber, Phys. Rev. E **72**, 046130 (2005).
[5] N. Bellomo and C. Dogbe, SIAM Rev. **53**, 409 (2011).
[6] A. J. Bernoff and C. M. Topaz, SIAM J. Appl. Dyn. Syst. **10**, 212 (2011).
[7] O. Corradi, P. Hjorth, and J. Starke, SIAM J. Appl. Dyn. Syst. **11**, 1007 (2012).
[8] N. Fenichel, J. Differ. Eqn. **31**, 53 (1979).
[9] H. Haken, in *Advanced Synergetics: Instability Hierarchies of Self-Organizing Systems and Devices*, Springer Series in Synergetics 20 (Springer, Berlin, 1983), pp. 1–356.
[10] H. Haken, in *Synergetics: An Introduction. Nonequilibrium Phase Transitions and Self Organization in Physics, Chemistry and Biology*, 3rd ed., Springer Series in Synergetics 1 (Springer, Berlin, 1983), pp. 1–371.
[11] I. G. Kevrekidis, C. W. Gear, J. M. Hyman, P. G. Kevrekidis, O. Runborg, and C. Theodoropoulos, Comm. Math. Sci. **1**, 715 (2003).
[12] I. G. Kevrekidis and G. Samaey, Annu. Rev. Phys. Chem. **60**, 321 (2009).
[13] K. Pearson, Philosophical Magazine Series **6**, 559 (1901).
[14] W. S. Torgerson, Psychometrika **17**, 401 (1952).
[15] T. Cox and M. Cox, *Multidimensional Scaling* (Chapman & Hall, London, 1994).
[16] P. Holmes, J. Lumley, and G. Berkooz, in *Turbulence, Coherent Structures, Dynamical Systems and Symmetry* (Cambridge University Press, Cambridge, 1998), pp. 1–420.

[17] A. Talwalkar, S. Kumar, and H. Rowley, in *IEEE Conference on Computer Vision and Pattern Recognition (CVPR), Anchorage, AK, 2008* (IEEE, Piscataway, NJ, 2008), pp. 1–8.
[18] S. T. Roweis and L. K. Saul, Science **290**, 2323 (2000).
[19] D. Yan, L. Huang, and M. I. Jordan, in *KDD '09: Proceedings of the 15th ACM SIGKDD International Conference on Knowledge, Discovery, and Data Mining* (ACM, New York, 2009), pp. 907–916.
[20] M. Belkin and P. Niyogi, in *Advances in Neural Information Processing Systems 14* (MIT Press, Cambridge, 2002), pp. 585–591.
[21] R. R. Coifman, S. Lafon, A. B. Lee, M. Maggioni, B. Nadler, F. Warner, and S. W. Zucker, Proc. Natl. Acad. Sci. USA **102**, 7426 (2005).
[22] R. R. Coifman and S. Lafon, Applied and Computational Harmonic Analysis **21**, 5 (2006).
[23] M. Belkin and P. Niyogi, Neural Comput. **15**, 1373 (2003).
[24] A. Kolpas, J. Moehlis, T. A. Frewen, and I. G. Kevrekidis, Math. Biosci. **214**, 49 (2008).
[25] R. R. Coifman, I. G. Kevrekidis, S. Lafon, M. Maggioni, and B. Nadler, Multiscale Modeling and Simulation **7**, 842 (2008).
[26] B. E. Sonday, M. Haataja, and I. G. Kevrekidis, Phys. Rev. E **80**, 031102 (2009).
[27] C. Laing, T. Frewen, and I. Kevrekidis, J. Comput. Neurosci. **28**, 459 (2010).
[28] T. A. Frewen, I. D. Couzin, A. Kolpas, J. Moehlis, R. Coifman, and I. G. Kevrekidis, in *Coping with Complexity: Model Reduction and Data Analysis*, Lecture Notes in Computational Science and Engineering, edited by A. N. Gorban, D. Roose, T. J. Barth, M. Griebel, D. E. Keyes, R. M. Nieminen, D. Roose, and T. Schlick, Vol. 75 (Springer, Berlin, 2011), pp. 299–309.
[29] M. A. Rohrdanz, W. Zheng, M. Maggioni, and C. Clementi, J. Chem. Phys. **134**, 124116 (2011).
[30] A. L. Ferguson, A. Z. Panagiotopoulos, I. G. Kevrekidis, and P. G. Debenedetti, Chem. Phys. Lett. **509**, 1 (2011).
[31] T. Berry, J. Cressman, Z. Gregurić-Ferenček, and T. Sauer, SIAM J. Appl. Dyn. Syst. **12**, 618 (2013).
[32] Isomap, http://isomap.stanford.edu/
[33] P. Grassberger and I. Procaccia, Phys. Nonlinear Phenom. **9**, 189 (1983).
[34] S. Kumar, M. Mohri, and A. Talwalkar, J. Mach. Learn. Res. **13**, 981 (2012).
[35] Y. Rubner, C. Tomasi, and L. Guibas, Int. J. Comput. Vis. **40**, 99 (2000).
[36] CPU: Intel Xeon W3690 3.47GHz ×6, Memory: 6GB.
[37] D. G. Aronson, M. Golubitsky, and J. Mallet-Paret, Nonlinearity **4**, 903 (1991).
[38] D. G. Aronson, M. Golubitsky, and M. Krupa, Nonlinearity **4**, 861 (1991).
[39] J. W. Swift and K. Wiesenfeld, Phys. Rev. Lett. **52**, 705 (1984).
[40] E. Chiavazzo, C. W. Gear, C. J. Dsilva, N. Rabin, and I. G. Kevrekidis, arXiv:1307.6849 [math.DS] (2013).
[41] B. Nadler, S. Lafon, R. R. Coifman, and I. G. Kevrekidis, Applied and Computational Harmonic Analysis **21**, 113 (2006).
[42] S. J. Moon, R. Ghanem, and I. G. Kevrekidis, Phys. Rev. Lett. **96**, 144101 (2006).
[43] C. Laing, Y. Zou, B. Smith, and I. Kevrekidis, J. Math. Neurosci. **2**, 1 (2012).
[44] S. Lafon and A. Lee, IEEE Trans. Pattern Anal. Mach. Intell. **28**, 1393 (2006).
[45] J. de la Porte, B. Herbst, W. Hereman, and S. van der Walt, *Nineteenth Annual Symposium of the Pattern Recognition Association of South Africa (PRASA)* (Pattern Recognition Association of South Africa, Johannesburg, 2008).

Bibliography

[AHS14] D. Avitabile, R. Hoyle, and G. Samaey. Noise reduction in coarse bifurcation analysis of stochastic agent-based models: an example of consumer lock-in. *ArXiv e-prints*, 2014. http://arxiv.org/abs/1403.5959.

[AL88] V. I. Arnol'd and M. Levi. *Geometrical methods in the theory of ordinary differential equations*, volume 372. Springer-Verlag New York, 1988.

[AW59] B. J. Alder and T. E. Wainwright. Studies in molecular dynamics. I. General method. *The Journal of Chemical Physics*, 31(2):459–466, 1959.

[Bel59] B. P. Belousov. A periodic reaction and its mechanism. *Collection of short papers on radiation medicine for 1958*, 1959.

[BH25] G. E. Briggs and J. B. S. Haldane. A note on the kinetics of enzyme action. *Biochemical Journal*, 19(2):338, 1925.

[BHN+95] M. Bando, K. Hasebe, A. Nakayama, A. Shibata, and Y. Sugiyama. Dynamical model of traffic congestion and numerical simulation. *Phys. Rev. E*, 51(2):1035–1042, 1995.

[BKS06] D. Barkley, I. G. Kevrikidis, and A. M. Stuart. The moment map: nonlinear dynamics of density evolution via a few moments. *SIAM Journal on Applied Dynamical Systems*, 5(3):403–434, 2006.

[BN02] M. Belkin and P. Niyogi. Laplacian eigenmaps and spectral techniques for embedding and clustering. In *Advances in Neural Information Processing Systems 14*, pages 585–591. MIT Press, 2002.

[Boh49] N. Bohr. *Discussion with Einstein on epistemological problems in atomic physics*. University of Copenhagen, 1949.

[Bol71] L. E. Boltzmann. *Einige allgemeine Sätze über Wärmegleichgewicht*. K. Akad. der Wissensch., 1871.

[Bra02] A. Brandt. Multiscale scientific computation: Review 2001. *Lecture Notes in Computational Science and Engineering*, 20:3–96, 2002.

[BSS+13] E. Bureau, F. Schilder, I. Santos, J. J. Thomsen, and J. Starke. Experimental bifurcation analysis of an impact oscillator—tuning a non-invasive control scheme. *Journal of Sound and Vibration*, 332(22):5883 – 5897, 2013.

[CHS12] O. Corradi, P. Hjorth, and J. Starke. Equation-free detection and continuation of a Hopf bifurcation point in a particle model of pedestrian flow. *SIAM Journal on Applied Dynamical Systems*, 11(3):1007–1032, 2012.

[CL06] R. R. Coifman and S. Lafon. Diffusion maps. *Applied and Computational Harmonic Analysis*, 21(1):5 – 30, 2006.

[CLL+05] R. R. Coifman, S. Lafon, A. B. Lee, M. Maggioni, B. Nadler, F. Warner, and S. W. Zucker. Geometric diffusions as a tool for harmonic analysis and structure definition of data: Diffusion maps. *Proceedings of the National Academy of Sciences of the United States of America*, 102(21):7426–7431, 2005.

[DCF+98] E. J. Doedel, A. R. Champneys, T. F. Fairgrieve, Y. A. Kuznetsov, B. Sandstede, and X. J. Wang. Continuation and bifurcation software for ordinary differential equations (with HomCont). *AUTO97*, 1998.

[DGK03] A. Dhooge, W. Govaerts, and Y. A. Kuznetsov. MatCont: a Matlab package for numerical bifurcation analysis of ODEs. *ACM Transactions on Mathematical Software (TOMS)*, 29(2):141–164, 2003.

[DK86] E. Doedel and J. P. Kernevez. *AUTO, software for continuation and bifurcation problems in ordinary differential equations*. California Institute of Technology, 1986.

[DS13] H. Dankowicz and F. Schilder. *Recipes for Continuation*. SIAM, 2013.

[Duf18] G. Duffing. Erzwungene Schwingungen bei veränderlicher Eigenfrequenz und ihre technische Bedeutung, 1918.

[EE03] W. E and B. Engquist. The heterogeneous multiscale methods. *Communications in Mathematical Sciences*, 1(1):87–132, 2003.

[EEH03] W. E, B. Engquist, and Z. Huang. Heterogeneous multiscale method: A general methodology for multiscale modeling. *Phys. Rev. B*, 67:092101, 2003.

[EEL+07] W. E, B. Engquist, X. Li, W. Ren, and E. Vanden-Eijnden. Heterogeneous multiscale methods: a review. *Commun. Comput. Phys.*, 2(3):367–450, 2007.

[Ell08] C. R. Ellsässer. *Simulations of a Neuron Network Model in the Olfactory System.* PhD thesis, Ruprecht-Karls-Universität Heidelberg, 2008.

[ELS01] K. Engelborghs, T. Luzyanina, and G. Samaey. DDE-BIFTOOL v. 2.00: a Matlab package for bifurcation analysis of delay differential equations. *TW Reports*, page 61, 2001.

[Eul56] L. Euler. Principia motus fluidorum. *Novi commentarii academiae swcientiarum Petropolitanae*, 6:1761, 1756.

[Fei78] M. J. Feigenbaum. Quantitative universality for a class of nonlinear transformations. *Journal of Statistical Physics*, 19(1):25–52, 1978.

[Fen79] N. Fenichel. Geometric singular perturbation theory for ordinary differential equations. *Journal of Differential Equations*, 31:53–98, 1979.

[FN74] R. J. Field and R. M. Noyes. Oscillations in chemical systems. IV. Limit cycle behavior in a model of a real chemical reaction. *The Journal of Chemical Physics*, 60(5):1877–1884, 1974.

[Gau30] C. F. Gauß. Principia generalia theoriae figurae fluidorum in statu aequilibrii: Societati regiae tradita, 1830.

[Gau67] C. F. Gauß. Allgemeine Theorie des Erdmagnetismus. *Werke*, 5:127–193, 1867.

[GH83] J. Guckenheimer and P. Holmes. *Nonlinear oscillations, dynamical systems, and bifurcations of vector fields.* New York Springer Verlag, 1983.

[GK92] A.N. Gorban and I.V. Karlin. The constructing of invariant manifolds for the Boltzmann equation. *Advances in Modelling and Analysis -C-*, 33:39–39, 1992.

[GK03] A. N. Gorban and I. V. Karlin. Method of invariant manifold for chemical kinetics. *Chemical Engineering Science*, 58(21):4751 – 4768, 2003. International Symposium on Mathematics in Chemical Kinetics and Engineering.

[GK04] C.W. Gear and I. G. Kevrekidis. Computing in the past with forward integration. *Physics Letters A*, 321:335 – 343, 2004.

[GK05] C. W. Gear and I. G. Kevrekidis. Constraint-defined manifolds: a legacy code approach to low-dimensional computation. *Journal of Scientific Computing*, 25(1):17–28, 2005.

[GKKZ05] C. W. Gear, T. J. Kaper, I. G. Kevrekidis, and A. Zagaris. Projecting to a slow manifold: Singularly perturbed systems and legacy codes. *SIAM Journal on Applied Dynamical Systems*, 4:711–732, 2005.

[GKT02] C.W. Gear, I. G. Kevrekidis, and C. Theodoropoulos. Coarse integration/bifurcation analysis via microscopic simulators: micro-Galerkin methods. *Computers & Chemical Engineering*, 26:941 – 963, 2002.

[GSS88] M. Golubitsky, I. Stewart, and D. G. Schaeffer. *Singularities and groups in bifurcation theory.* Springer, 1988.

[Hak83] H. Haken. *Synergetics. An introduction. Nonequilibrium phase transitions and self organization in physics, chemistry and biology. 3.ed / Springer series in synergetics 1.* Springer, Berlin, 1983.

[Ham34] W. R. Hamilton. On a general method in dynamics; by which the study of the motions of all free systems of attracting or repelling points is reduced to the search and differentiation of one central relation, or characteristic function. *Philosophical Transactions of the Royal Society of London*, 124:247–308, 1834.

[HDS74] M.W. Hirsch, R. L. Devaney, and S. Smale. *Differential Equations, Dynamical Systems, and Linear Algebra.* Pure and Applied Mathematics. Elsevier Science, 1974.

[Hei25] W. Heisenberg. Quantum-theoretical re-interpretation of kinematic and mechanical relations. *Z. Phys.*, 33:879–893, 1925.

[Hel01] D. Helbing. Traffic and related self-driven many-particle systems. *Rev. Mod. Phys.*, 73:1067–1141, 2001.

[HK91] J. K. Hale and H. Koçak. *Dynamics and bifurcations.* Springer, 1991.

[HM95] D. Helbing and P. Molnár. Social force model for pedestrian dynamics. *Phys. Rev. E*, 51:4282–4286, 1995.

[Hol90] P. Holmes. Poincaré, celestial mechanics, dynamical-systems theory and "chaos". *Physics Reports*, 193(3):137 – 163, 1990.

[Iso] Isomap. http://isomap.stanford.edu/.

[JARLP12] A. Jelić, C. Appert-Rolland, S. Lemercier, and J. Pettré. Properties of pedestrians walking in line: Fundamental diagrams. *Phys. Rev. E*, 85:036111, 2012.

[JG11] K. A. Johnson and R. S. Goody. The original Michaelis constant: Translation of the 1913 Michaelis-Menten paper. *Biochemistry*, 50(39):8264–8269, 2011.

[Jon95] C. K. R. T. Jones. Geometric singular perturbation theory. In *Dynamical systems*, pages 44–118. Springer, 1995.

[KBS14] K. Kristiansen, M. Brøns, and J. Starke. An iterative method for the approximation of fibers in slow-fast systems. *SIAM Journal on Applied Dynamical Systems*, 13(2):861–900, 2014.

[Kel95] C.T. Kelley. *Iterative Methods for Linear and Nonlinear Equations*. Frontiers in Applied Mathematics. SIAM, 1995.

[KGH+03] I. G. Kevrekidis, C. W. Gear, J. M. Hyman, P. G. Kevrekidis, O. Runborg, and C. Theodoropoulos. Equation-free, coarse-grained multiscale computation: enabling microscopic simulators to perform system-level analysis. *Communications in Mathematical Sciences*, 1:715 – 762, 2003.

[KGH04] I. G. Kevrekidis, C. W. Gear, and G. Hummer. Equation-free: The computer-aided analysis of complex multiscale systems. *AIChE Journal*, 50(7):1346–1355, 2004.

[KGvH99] R. Kempter, W. Gerstner, and J. L. van Hemmen. Hebbian learning and spiking neurons. *Phys. Rev. E*, 59:4498–4514, 1999.

[KLWvH01] R. Kempter, C. Leibold, H. Wagner, and J. L. van Hemmen. Formation of temporal-feature maps by axonal propagation of synaptic learning. *Proceedings of the National Academy of Sciences*, 98(7):4166–4171, 2001.

[Kre79] H. Kreiss. Problems with different time scales for ordinary differential equations. *SIAM Journal on Numerical Analysis*, 16(6):980–998, 1979.

[KS09] I. G. Kevrekidis and G. Samaey. Equation-free multiscale computation: Algorithms and applications. *Annual Review of Physical Chemistry*, 60(1):321–344, 2009.

[Kuz04] Y. A. Kuznetsov. *Elements of Applied Bifurcation Theory*, volume 112 of *Applied Mathematical Sciences*. Springer, New York, third edition, 2004.

[Lag88] J. L. Lagrange. *Mécanique Analytique*. Desaint, 1788.

[LG88] S. H. Lam and D. A. Goussis. Basic theory and demonstrations of computational singular perturbation for stiff equations. In *12th IMACS World Congress on Scientific Computation*, pages 18–22, 1988.

[LG94] S. H. Lam and D. A. Goussis. The CSP method for simplifying kinetics. *International Journal of Chemical Kinetics*, 26:461–486, 1994.

[Lin94] E. Lindelöf. Sur l'application de la méthode des approximations successives aux équations différentielles ordinaires du premier ordre. *Comptes rendus hebdomadaires des séances de l'Académie des sciences*, 114:454–457, 1894.

[LKGK03] J. Li, P. G. Kevrekidis, C. W. Gear, and I. G. Kevrekidis. Deciding the nature of the coarse equation through microscopic simulations: The baby-bathwater scheme. *Multiscale Modeling & Simulation*, 1(3):391–407, 2003.

[LKvH01] C. Leibold, R. Kempter, and J. L. van Hemmen. Temporal map formation in the barn owl's brain. *Phys. Rev. Lett.*, 87(24):248101, 2001.

[Lor63] E. N. Lorenz. Deterministic non-periodic flow. *J. Atmos. Sci.*, 20, 1963.

[Lor80] E. N. Lorenz. Attractor sets and quasi-geostrophic equilibrium. *J. Atmos. Sci.*, 37(8):1685–1699, 1980.

[Lor86] E. N. Lorenz. On the existence of a slow manifold. *J. Atmos. Sci.*, 43(15):1547–1558, 1986.

[Lot10] A. J. Lotka. Contribution to the theory of periodic reactions. *The Journal of Physical Chemistry*, 14(3):271–274, 1910.

[Mac04] R.S. MacKay. Slow manifolds. *Energy localisation and Transfer*, pages 149–192, 2004.

[Man83] B. B. Mandelbrot. *The fractal geometry of nature*. Macmillan, 1983.

[Max65] J. C. Maxwell. A dynamical theory of the electromagnetic field. *Philosophical Transactions of the Royal Society of London*, 155:459–512, 1865.

[Max67] J. C. Maxwell. On the dynamical theory of gases. *Philosophical Transactions of the Royal Society of London*, 157:49–88, 1867.

[Mei07] J. D. Meiss. *Differential dynamical systems*. SIAM, 2007.

[MFESvH14] C. Marschler, C. Faust-Ellsässer, J. Starke, and J. L. van Hemmen. Bifurcation of learning and structure formation in neuronal maps. *Europhysics Letters*, 2014. Submitted for review.

[MFEvHS14] C. Marschler, C. Faust-Ellsässer, J. L. van Hemmen, and J. Starke. Equation-free bifurcation analysis of a learning process in a neuronal network. *Journal of Mathematical Biology*, 2014. To be submitted.

[MGM+12] M. Moussaïd, E. G. Guillot, M. Moreau, J. Fehrenbach, O. Chabiron, S. Lemercier, J. Pettré, C. Appert-Rolland, P. Degond, and G. Theraulaz. Traffic instabilities in self-organized pedestrian crowds. *PLoS Comput Biol*, 8(3):e1002442, 2012.

[MM13] L. Michaelis and M. L. Menten. Die Kinetik der Invertinwirkung. *Biochem. Z.*, 49:333–369, 1913.

[MP92] U. Maas and S. B. Pope. Simplifying chemical kinetics: Intrinsic low-dimensional manifolds in composition space. *Combustion and Flame*, 88:239 – 264, 1992.

[MSB+14] C. Marschler, J. Sieber, R. Berkemer, A. Kawamoto, and J. Starke. Implicit Methods for Equation-Free Analysis: Convergence Results and Analysis of Emergent Waves in Microscopic Traffic Models. *accepted for publication in: SIAM Journal on Applied Dynamical Systems*, 2014. http://arxiv.org/abs/1301.6044.

[MSHS14] C. Marschler, J. Sieber, P. G. Hjorth, and J. Starke. Equation-free analysis of macroscopic behavior in traffic and pedestrian flow. In *Traffic and Granular Flow '13 (accepted for publication)*, 2014. http://arxiv.org/abs/1402.0314.

[MSLK14] C. Marschler, J. Starke, P. Liu, and I. G. Kevrekidis. Coarse-grained particle model for pedestrian flow using diffusion maps. *Phys. Rev. E*, 89:013304, 2014.

[New87] I. Newton. *Philosophiae Naturalis Principia Mathematica.* , 1687.

[Noe18] E. Noether. Invarianten beliebiger Differentialausdrücke. *Nachrichten von der Gesellschaft der Wissenschaften zu Göttingen, Mathematisch-Physikalische Klasse*, 1918:37–44, 1918.

[OKW05] G. Orosz, B. Krauskopf, and R. E. Wilson. Bifurcations and multiple traffic jams in a car-following model with reaction-time delay. *Physica D: Nonlinear Phenomena*, 211:277–293, 2005.

[OWS10] G. Orosz, R. E. Wilson, and G. Stepan. Traffic jams: dynamics and control. *Philosophical Transactions of the Royal Society A: Mathematical, Physical and Engineering Sciences*, 368(1928):4455–4479, 2010.

[Par89] M. Parmentier. *Gottfried Wilhelm Leibniz: La naissance du calcul différentiel*. J. Vrin, Librarire Philosophique, Paris, 1989.

[PBL78] G. Papanicolau, A. Bensoussan, and J. L. Lions. *Asymptotic analysis for periodic structures.* Elsevier, 1978.

[Pea01] K. Pearson. Philosophical magazine. *Sixth Series*, 2:559–572, 1901.

[Pla00] M. Planck. Über irreversible Strahlungsvorgänge. *Annalen der Physik*, 306(1):69–122, 1900.

[Poi90] H. Poincaré. Sur le problème des trois corps et les équations de la dynamique. *Acta mathematica*, 13(1):A3–A270, 1890.

[RS00] S. T. Roweis and L. K. Saul. Nonlinear dimensionality reduction by locally linear embedding. *Science*, 290(5500):2323–2326, 2000.

[RTK02] O. Runborg, C. Theodoropoulos, and I. G. Kevrekidis. Effective bifurcation analysis: a time-stepper-based approach. *Nonlinearity*, 15(2):491, 2002.

[Sch26] E. Schrödinger. Quantisierung als Eigenwertproblem. *Annalen der Physik*, 385(13):437–490, 1926.

[SFK+08] Y. Sugiyama, M. Fukui, M. Kikuchi, K. Hasebe, A. Nakayama, K. Nishinari, S. Tadaki, and S. Yukawa. Traffic jams without bottlenecks: experimental evidence for the physical mechanism of the formation of a jam. *New J. Phys.*, 10(3), 2008.

[SK93] G. M. Shroff and H. B. Keller. Stabilization of unstable procedures: The recursive projection method. *SIAM Journal on Numerical Analysis*, 30(4):1099–1120, 1993.

[Sma67] S. Smale. Differentiable dynamical systems. *Bulletin of the American mathematical Society*, 73(6):747–817, 1967.

[Smi08] G. Smith. Newton's philosophiae naturalis principia mathematica. In Edward N. Zalta, editor, *The Stanford Encyclopedia of Philosophy*. , 2008.

[SP80] Enrique Sánchez-Palencia. Non-homogeneous media and vibration theory. In *Non-homogeneous media and vibration theory*, volume 127, 1980.

[SR79] J. W. Strutt and Lord Rayleigh. On the instability of jets. In *Proc. R. Soc. London A*, volume 10, pages 4–13, 1879.

[SRK05] G. Samaey, D. Roose, and I. Kevrekidis. The gap-tooth scheme for homogenization problems. *Multiscale Modeling & Simulation*, 4(1):278–306, 2005.

[SRK09] G. Samaey, A. J. Roberts, and I. G. Kevrekidis. Equation-free computation: an overview of patch dynamics. In Jacob Fish, editor, *Multiscale methods : bridging the scales in science and engineering*. Oxford University Press, 2009.

[SSGK10] B. E. Sonday, A. Singer, C. W. Gear, and I. G. Kevrekidis. Manifold learning techniques and model reduction applied to dissipative PDEs. *ArXiv e-prints*, 2010. http://arxiv.org/abs/1011.5197.

[SSM+14] J. Starke, A. Sørensen, C. Marschler, F. Schilder, K. B. Thomsen, and P. Hjorth. Analysis of unstable states in particle models for pedestrian flow. In *Proceedings of 8th European Nonlinear Dynamics Conference (ENOC 2014) in Vienna, Austria*, 2014.

[Sta87] H. E. Stanley. Introduction to phase transitions and critical phenomena. , 1:336, 1987.

[STS+14] J. Starke, K. B. Thomsen, A. Sørensen, C. Marschler, F. Schilder, A. Dederichs, and P. Hjorth. Nonlinear effects in examples of crowd evacuation scenarios. In *17th International IEEE Conference on Intelligent Transportation Systems, Qingdao, China*, 2014. submitted for review.

[Sym] Sympercon. http://sympercon.sourceforge.net/.

[TKF+13] S. Tadaki, M. Kikuchi, M. Fukui, A. Nakayama, K. Nishinari, A. Shibata, Y. Sugiyama, T. Yosida, and S. Yukawa. Phase transition in traffic jam experiment on a circuit. *New Journal of Physics*, 15(10):103034, 2013.

[TQK00] C. Theodoropoulos, Y. H. Qian, and I. G. Kevrekidis. Coarse stability and bifurcation analysis using time-steppers: A reaction-diffusion example. *Proceedings of the National Academy of Sciences*, 97(18):9840–9843, 2000.

[TSL00] J. B. Tenenbaum, V. de Silva, and J. C. Langford. A global geometric framework for nonlinear dimensionality reduction. *Science*, 290(5500):2319–2323, 2000.

[vdP20] B. van der Pol. A theory of the amplitude of free and forced triode vibrations. *Radio Review*, 1(15):754–762, 1920.

[vdP26] B. van der Pol. On "relaxation-oscillations". *Philosophical Magazine Series 7*, 2(11):978–992, 1926.

[VKR09] C. Vandekerckhove, I. Kevrekidis, and D. Roose. An efficient Newton-Krylov implementation of the Constrained Runs Scheme for initializing on a slow manifold. *Journal of Scientific Computing*, 39:167–188, 2009. 10.1007/s10915-008-9256-y.

[VSM+11] C. Vandekerckhove, B. Sonday, A. Makeev, D. Roose, and I. G. Kevrekidis. A common approach to the computation of coarse-scale steady states and to consistent initialization on a slow manifold. *Computers & Chemical Engineering*, 35(10):1949 – 1958, 2011.

[Wig94] S. Wiggins. *Normally hyperbolic invariant manifolds in dynamical systems*. Number 105 in Applied Mathematical Sciences. Springer, 1994.

[Wig03] S. Wiggins. *Introduction to applied nonlinear dynamical systems and chaos*, volume 2. Springer, 2003.

[Wil75] K. G. Wilson. The renormalization group: Critical phenomena and the Kondo problem. *Rev. Mod. Phys.*, 47:773–840, 1975.

[WR02] C. Wulff and M. Roberts. Hamiltonian systems near relative periodic orbits. *SIAM Journal on Applied Dynamical Systems*, 1(1):1–43, 2002.

[ZGKK09] A. Zagaris, C. W. Gear, T. J. Kaper, and I. G. Kevrekidis. Analysis of the accuracy and convergence of equation-free projection to a slow manifold. *ESAIM: Mathematical Modelling and Numerical Analysis*, 43(04):757–784, 2009.

[Zha64] A. M. Zhabotinsky. Periodical oxidation of malonic acid in solution (a study of the Belousov reaction kinetics). *Biofizika*, 9:306–11, 1964.

[ZM71] O. C. Zienkiewicz and P. B. Morice. *The finite element method in engineering science*, volume 1977. McGraw-Hill London, 1971.

[ZVG+12] A. Zagaris, C. Vandekerckhove, C. W. Gear, T. J. Kaper, and I. G. Kevrekidis. Stability and stabilization of the constrained runs schemes for equation-free projection to a slow manifold. *Discrete and Continuous Dynamical Systems - Series A*, 32(8):2759 – 2803, 2012.